

APPLIED COMPUTATIONAL ELECTROMAGNETICS SOCIETY JOURNAL

December 2021

Vol. 36 No. 12

ISSN 1054-4887

The ACES Journal is abstracted in INSPEC, in Engineering Index, DTIC, Science Citation Index Expanded, the Research Alert, and to Current Contents/Engineering, Computing & Technology.

The illustrations on the front cover have been obtained from the research groups at the Department of Electrical Engineering, The University of Mississippi

THE APPLIED COMPUTATIONAL ELECTROMAGNETICS SOCIETY

<http://aces-society.org>

EDITORS-IN-CHIEF

Atef Elsherbeni

Colorado School of Mines, EE Dept.
Golden, CO 80401, USA

Sami Barmada

University of Pisa, ESE Dept.
56122 Pisa, Italy

ASSOCIATE EDITORS

Maokun Li

Tsinghua University
Beijing 100084, China

Wei-Chung Weng

National Chi Nan University, EE Dept.
Puli, Nantou 54561, Taiwan

Paolo Mezzanotte

University of Perugia
I-06125 Perugia, Italy

Mauro Parise

University Campus Bio-Medico of Rome
00128 Rome, Italy

Alessandro Formisano

Seconda Università di Napoli
81031 CE, Italy

Luca Di Rienzo

Politecnico di Milano
20133 Milano, Italy

Yingsong Li

Harbin Engineering University
Harbin 150001, China

Piotr Gas

AGH University of Science and Technology
30-059 Krakow, Poland

Lei Zhao

Jiangsu Normal University
Jiangsu 221116, China

Riyadh Mansoor

Al-Muthanna University
Samawa, Al-Muthanna, Iraq

Long Li

Xidian University
Shaanxi, 710071, China

Sima Noghianian

Commscope
Sunnyvale, CA 94089, USA

Lijun Jiang

University of Hong Kong, EEE Dept.
Hong Kong

Steve J. Weiss

US Army Research Laboratory
Adelphi Laboratory Center (RDRL-SER-M)
Adelphi, MD 20783, USA

Qiang Ren

Beihang University
Beijing 100191, China

Shinshiro Ohnuki

Nihon University
Tokyo, Japan

Jiming Song

Iowa State University, ECE Dept.
Ames, IA 50011, USA

Nunzia Fontana

University of Pisa
56122 Pisa, Italy

Kubilay Sertel

The Ohio State University
Columbus, OH 43210, USA

Toni Bjorninen

Tampere University
Tampere, 33100, Finland

Stefano Selleri

DINFO - University of Florence
50139 Florence, Italy

Giulio Antonini

University of L'Aquila
67040 L'Aquila, Italy

Santanu Kumar Behera

National Institute of Technology
Rourkela-769008, India

Amedeo Capozzoli

Università di Napoli Federico II, DIETI
I-80125 Napoli, Italy

Antonio Musolino

University of Pisa
56126 Pisa, Italy

Daniele Romano

University of L'Aquila
67100 L'Aquila, Italy

Yu Mao Wu

Fudan University
Shanghai 200433, China

Abdul A. Arkadan

Colorado School of Mines, EE Dept.
Golden, CO 80401, USA

Alireza Baghai-Wadji

University of Cape Town
Cape Town, 7701, South Africa

Fatih Kaburcuk

Sivas Cumhuriyet University
Sivas 58140, Turkey

Salvatore Campione

Sandia National Laboratories
Albuquerque, NM 87185, USA

Marco Arjona López

La Laguna Institute of Technology
Torreon, Coahuila 27266, Mexico

Huseyin Savci

Istanbul Medipol University
34810 Beykoz, Istanbul

EDITORIAL ASSISTANTS

Matthew J. Inman
University of Mississippi, EE Dept.
University, MS 38677, USA

Shanell Lopez
Colorado School of Mines, EE Dept.
Golden, CO 80401, USA

EMERITUS EDITORS-IN-CHIEF

Duncan C. Baker
EE Dept. U. of Pretoria
0002 Pretoria, South Africa

Allen Glisson
University of Mississippi, EE Dept.
University, MS 38677, USA

Ahmed Kishk
Concordia University, ECS Dept.
Montreal, QC H3G 1M8, Canada

Robert M. Bevensee
Box 812
Alamo, CA 94507-0516

Ozlem Kilic
Catholic University of America
Washington, DC 20064, USA

David E. Stein
USAF Scientific Advisory Board
Washington, DC 20330, USA

EMERITUS ASSOCIATE EDITORS

Yasushi Kanai
Niigata Inst. of Technology
Kashiwazaki, Japan

Alexander Yakovlev
University of Mississippi, EE Dept.
University, MS 38677, USA

Levent Gurel
Bilkent University
Ankara, Turkey

Mohamed Abouzahra
MIT Lincoln Laboratory
Lexington, MA, USA

Ozlem Kilic
Catholic University of America
Washington, DC 20064, USA

Erdem Topsakal
Mississippi State University, EE Dept.
Mississippi State, MS 39762, USA

Sami Barmada
University of Pisa, ESE Dept.
56122 Pisa, Italy

Fan Yang
Tsinghua University, EE Dept.
Beijing 100084, China

Rocco Rizzo
University of Pisa
56123 Pisa, Italy

William O'Keefe Coburn
US Army Research Laboratory
Adelphi, MD 20783, USA

Mohammed Hadi
Kuwait University, EE Dept.
Safat, Kuwait

Alistair Duffy
De Montfort University
Leicester, UK

Wenxing Li
Harbin Engineering University
Harbin 150001, China

Atif Shamim
King Abdullah University of Science and
Technology (KAUST)
Thuwal 23955, Saudi Arabia

EMERITUS EDITORIAL ASSISTANTS

Khaleb ElMaghoub
Trimble Navigation/MIT
Boston, MA 02125, USA

Kyle Patel
Colorado School of Mines, EE Dept.
Golden, CO 80401, USA

Christina Bonnington
University of Mississippi, EE Dept.
University, MS 38677, USA

Anne Graham
University of Mississippi, EE Dept.
University, MS 38677, USA

Madison Lee
Colorado School of Mines, EE Dept.
Golen, CO 80401, USA

Allison Tanner
Colorado School of Mines, EE Dept.
Golden, CO 80401, USA

Mohamed Al Sharkawy
Arab Academy for Science and Technology, ECE Dept.
Alexandria, Egypt

DECEMBER 2021 REVIEWERS

Behrokh Beiranvand
Billel Bentouhami
Raghvendra Chaudhary
Brinta Chowdhury
Thippesha D.
Biswajit Dwivedy
Piotr Gas
Michael Johnson
Wasi Khan
Vijay Kumar
Brian LaRocca
Yingsong Li
Ivor Morrow
Mahdi Oliaei
Antonio Orlandi

Balendu Kumar Pandey
Mirjana Peric
Mohammd Pourbagher
Umair Rafique
Pavel Roy Paladhi
Slavko Rupcic
Suganthi Santhanam
Giuseppe Vecchi
Marsellas Waller
Chao-Fu Wang
Zhonggen Wang
Peiyu Wu
Yiyang Yu
Xiaoyan Zhang
Zhaojun Zhu

TABLE OF CONTENTS

In Memory of Richard W. (Dick) Adler
Edmond K. Miller, Branislav M. Notaros, and Jim Breakall Intro

FDTD Simulations of Modulated Metasurfaces with Arbitrarily Shaped Meta-atoms by
Surface Impedance Boundary Condition
Yanmeng Hu, Quanen Zhou, Xinyu Fang, and Mengmeng Li 1509

Convergence Acceleration of Infinite Series Involving the Product of Riccati–Bessel
Function and Its Application for the Electromagnetic Field: Using the Continued Fraction
Expansion Method
Zheng Fanghua, Di Qingyun, Yun Zhe, and Gao Ya 1518

Design and Analysis of Multi-Mode Distributed Array with Hybrid Optimization Method
Shutao Fang, Weiming Li, Wu Ren and Zhenghui Xue 1526

Particle Swarm Optimization of Irregular-shaped Hexagon Patch Antenna for 2.4 GHz
WLAN Applications
Wei-Chung Weng and Min-Chi Chang 1535

Equivalent Circuit Approximation to the Connector-Line Transition at High Frequencies
using Two Microstrip Lines and Data Fitting
Duc Le, Nikta Pournoori, Lauri Sydänheimo, Leena Ukkonen, and Toni Björninen 1541

Linear Antenna Array Synthesis by Modified Seagull Optimization Algorithm
Erhan Kurt, Suad Basbug, and Kerim Guney 1552

Pattern Analysis of Conformal Antenna Arrays via the Characteristic Modes of Isolated
Elements
Yuanchen Zeng, Shuo Zhang, and Shunxi Lou 1562

Dual-Band Folded Monopole MIMO Antennas with Enhanced Isolation
Likaa S.Yahya, Loay S.Yahya, and Khalil H. Sayidmarie 1569

A Compact Dual-band Planar Antenna Loaded with Magneto Dielectric Ferrite
Yongwei Li, Quanyuan Feng, and Zongliang Zheng 1579

A Gain-enhanced Dual-band Microstrip Antenna using Metasurface as Superstrate
Configuration
HuQiang Tian, JunLin Wang, Ding Han, and Xin Wang 1586

| | |
|--|------|
| Design Optimization of Ultra-Wideband Vivaldi Antenna using Artificial Intelligence Peyman Mahouti, Ahmet Kızılay, Ozlem Tari, Aysu Belen, Mehmet A. Belen and Alper Çalışkan | 1594 |
| Dual-Band Phased Array 5G Mobile-Phone Antenna with Switchable and Hemispherical Beam Pattern Coverage for MIMO-Diversity Communications Naser Ojaroudi Parchin, Osama M. Dardeer, Ahmed S.I. Amar, Chan Hwang See, Raed Abd-Alhameed | 1602 |
| Design of Planar Directional Coupler using 2-Bit Fragment Structures Yonghui Tao, Wenjuan Zhang, Johan Sidén and Gang Wang | 1610 |
| Compact Dual-Band Bandpass Filter Based on SSL-SIR With Sharp Roll-Off Juan Yue, Guanmao Zhang, Zongge Che, Yupeng Lun, Zhihang Li, and Junhong Suo | 1623 |
| Power Changes of Electromagnetic Waves Across the Temporal Boundary in Simple Polar-Molecule Reactions Xingpeng Liu, Song Zhang, and Kama Huang | 1616 |

In Memory of Richard W. (Dick) Adler

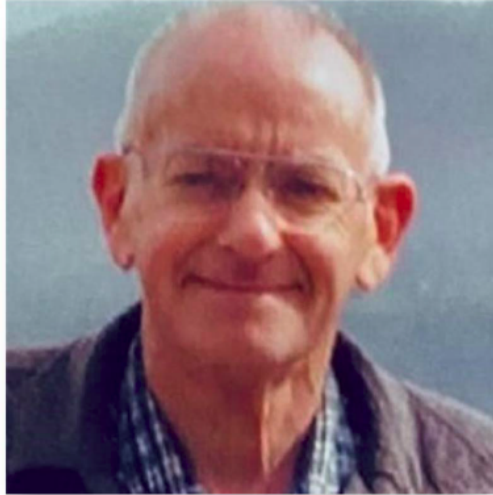


By: Edmund K. Miller

Dick Adler was a long-time mainstay of ACES. Dick, his wife Pat, sometimes with the help of one or two of their children, planned and handled all of the local arrangements during the years that ACES met at the Nave Postgraduate School in Monterey. This arrangement continued at NPS until security concerns required it to be shifted elsewhere in Monterey, a venue that remained a favorite for ACES members. Dick was also one of the founding members of TechEd Associates, a group of NEC users and developers who presented “hands-on” short-course workshops in Monterey for several years. He gave informative and entertaining presentations that could include observations like “epsilon sauce and gamma grease” that lightened up the mathematical details.

Dick himself was a hands-on engineer who contributed to a variety of antenna and communications application for military sponsors. He was an experimentalist as well as an experienced computational modeler who guided many students at the NPS through their degree work. His experimental results influenced modeling developments as well as providing data to validate the computed results. Dick was a valued colleague and friend.

Richard W. (Dick) Adler (1934–2021), a Founder of ACES



Richard W. (Dick) Adler, one of the founders of the Applied Computational Electromagnetics Society, passed away on December 30, 2021, in Bountiful, Utah, USA, at the age of 87, of a combination of causes including COVID-19.

Dick was born on November 28, 1934, in Farrell, Pennsylvania. He attended Penn State University, where he received B.S. and M.S. degrees in electrical engineering, in 1956 and 1958, respectively. He then worked in the industry, at Hughes Aircraft Company and Ford Aeronutronic, and later returned to Penn State as an Instructor in Electrical Engineering and received the Ph.D. in December 1970. In November 1969, he joined the faculty of the Naval Postgraduate School (NPS), in Monterey, California, where he taught in the Department of Electrical Engineering, and pursued research in antennas, propagation, and computational electromagnetics.

The Applied Computational Electromagnetics Society was officially launched on March 19, 1986, at the Second Annual Review of Progress in Applied Computational Electromagnetics, held at NPS in Monterey and organized by Dick Adler. Adler was the first ACES Secretary, serving with Ed Miller, the first ACES President. For decades to come, Richard was a leading force in all ACES activities and accomplishments, including ACES Conferences, Journal, Newsletter, organization, and finances.

Richard Adler will be remembered by all ACES Members and Friends as a leader and visionary without whom the field of applied computational electromagnetics and the ACES Society would not be what they have become during his most active ACES years and today.

We dedicate this issue of ACES Journal in tribute and memory of Dick Adler.

Branislav M. Notaros

President, ACES

Professor, Colorado State University

Fort Collins, Colorado, USA

In Memory of Prof. Richard “Dick” W. Adler, P.E.



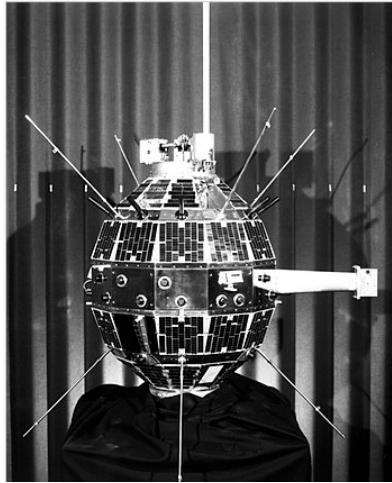
It is with great sadness that I inform ACES of the passing of Prof. Richard W. Adler on December 30th, 2021. R. W. Adler was born in Farrell, PA, in 1934. He received the BSEE and MSEE degrees from Penn State University, University Park, PA, in 1956 and 1958, respectively. He received a Ford Foundation Doctoral Forgivable Loan and completed the Ph.D. degree in electrical engineering in 1970 at the same institution.

He continued graduate studies at the Ohio State University as a Research Assistant in the ElectroScience Laboratory (ESL) until 1960, when he joined the staff at Hughes Ground Systems Group as a Design Engineer in frequency-scanned radar antennas. Graduate studies continued at the University of California, Los Angeles, until 1962, when he became a full-time instructor in the EE Department at Penn State University. In 1970 he accepted a position as an Assistant Professor at the Naval Postgraduate School (NPS), Monterey, CA. He finished as a Senior Lecturer in the Electrical and Computer Engineering Department at NPS, with academic and research interests in antennas, radiowave propagation, and electromagnetic environmental effects. His research projects supported the Naval Security Group (NSG) and later the Naval Information Warfare Activity (NIWA) and the Army Intelligence and Security Command in what was known as the Signal and Noise Enhancement Program (SNEP Team) directed at the enhancement of signal-to-noise ratio in receiving sites and the effects of terrain and platforms on the performance of communication antennas.

Prof. Adler was a licensed professional engineer and served as the Executive Officer and the Managing Editor of publications for the Applied Computational Electromagnetics Society (ACES). His memberships also included the IEEE, Eta Kappa Nu, Tau Beta Pi. and Sigma Xi.

I personally remember meeting Dr. Adler as an undergraduate student at Penn State working in what was called the Ionosphere Research Laboratory (IRL) and was working with Prof. Tony Ferraro on a project of modeling wires on a box like structure for an unnamed government agency. Dick Adler brought a software program on magnetic tape that was

named AMP for Antenna Modeling Program, the predecessor of what would eventually become the Numerical Electromagnetics Code (NEC). The object that we modeled was later declassified in 2005 as a satellite operated by the National Reconnaissance Office (NRO) named POPPY, and we received awards at a ceremony for this work that we never knew what it was at the time. That was the first time I met Dick, and I knew I needed to get to know him a lot more.



POPPY

Fortunately, I kept in touch with him and also developed a close relationship with Jerry Burke and Ed Miller at Lawrence Livermore National Laboratory (LLNL) while I was a Ph.D. student at Case Western Reserve University. LLNL was the originator of NEC, and I knew I had to go there and work with Prof. Adler and those at LLNL. I started at LLNL in 1983 and right away used to travel to Monterey, CA and work with Dick and learn from him how to really model antennas. He and I used to do consulting jobs for AM and FM broadcasting where we would try to optimize placement of antennas on towers and try to increase signal coverage and other projects. It seemed I was spending almost every weekend there in Monterey working with Dick and spending time at his house and with his family. They were so hospitable that I sometimes felt like this was my second family being with him and his wife and kids. Dick and I worked for many radio broadcasting stations in the 1980s and pushed for the use of antenna modeling to be used in addition or in the place of experimental proof antenna pattern measurements. We together presented several papers at IEEE Broadcast Technology Society annual symposiums and won the Matti S. Siukola Memorial Award for Best Paper in 1987.

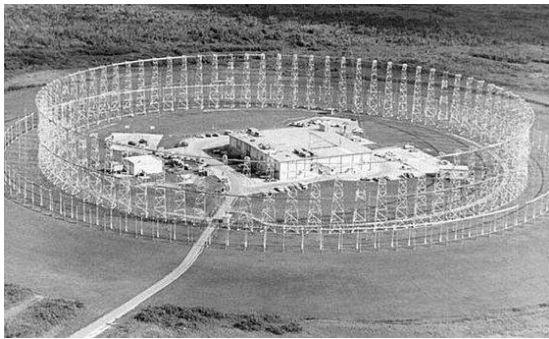
The development of NEC at LLNL was funded and directed from the Army at Ft. Monmouth and Ft. Huachuca and the Navy at San Diego and especially from Prof. Adler at the Naval Postgraduate School (NPS) at Monterey. Dick was always the one instrumental about saying what things were needed to be enhanced and put into the code. Dr. Ed Miller, Jerry Burke, Dick Adler, Jim Logan, Dr. Jay Rockway, and myself and others came up with the idea of starting an organization concerned mainly with antenna modeling and hands-on work, and this became the Applied Computational Electromagnetics Society (ACES) in 1985 with a four-day workshop at LLNL.

ACES became official at the Second Annual Review of Progress, held at NPS in March of 1986. The Review was organized by Prof. Adler, and it became an annual event for many years in March at Monterey. None of this would have ever happened without the painstaking planning and organization of Dick Adler. The first slate of officers included Ed Miller, President; James Logan (Naval Ocean Systems Center or NOSOC), Vice President; Richard W. Adler, (NPS), Secretary; and James K. Breakall (LLNL), Treasurer. Dick was a mainstay for many memorable ACES conferences for many years, an annual event that many including myself really looked forward to. Dick and I both worked a lot behind the scenes to make every part of these meetings something very valuable, not just for the academic part, but also for the social gatherings. Being in Monterey/Carmel did not hurt with its picturesque setting.

Another activity that Dick took charge of for many years was putting on antenna modeling workshop short courses on either NEC or MiniNEC. He was involved in starting an organization named TechEd Associates to put on these courses, and it included Dick, Ed Miller, Jerry Burke, Jim Logan, Jay Rockway, and myself. We would usually put on a week-long series of presentations on the theory of antenna modeling and then hands-on learning how to use the codes with personal computers that were set up by Dick on each desk. Many were held in Monterey, but others would be held around the country too.

There are just too many projects to go into detail that Dick Adler was the catalyst and organizer for, but I will try to touch briefly on a few. Dick and I worked together as a team on many of these, and I know there are others that he did also with others that I was not up on as much. We worked on a multi-volume set of antenna handbooks for both the Army and Marine Corp that would be used by warriors to select the best antennas for the purpose at hand. Some other projects that come to mind are working with some other close colleagues of ours, George Hagn (SRI Intl.) and Steve Faust (Eyring Inst.) to develop and utilize methods to measure ground constants of the earth and characterize antennas in irregular terrain. Dick arranged all of the funding from the Navy and was again the organizer. One of his students, Capt. Hampshire, later took charge of the TACAMO VLF antenna that was on EC-130 and E-6A aircrafts for submarine communication, and Dick work on that with me. Dick was instrumental in a large project from NIWA with CDR Gus Lott, one of his Ph.D. students, named PENEX for Polar Equatorial Near Vertical Incidence Experiment that had the purpose of validating and exploring HF propagation codes through the auroral ionosphere and trans-equatorial paths. I remember fondly of him traveling to Cape Wales in Alaska under some interesting weather conditions to erect antennas and set up equipment. Dick would go anywhere to get the job done. In the 1990s to the 2000s, he arranged for funding to put a really nice graphical user interface (GUI) around NEC2 and NEC4 and helped set up a company, Nittany Scientific, that created NECWIN Basic and GNEC. Many versions of these packages were sold.

In the mid-1980s, Prof. Steve Jauregui at NPS along with Dick and another Prof. Ray Vincent created the Signal to Noise Enhancement Program (SNEP) to help isolate and resolve noise and other EMI issues at the Navy Security Group's large Wullenweber (Elephant Cage) antenna sites around the world. Dick was a key person involved in this work and advised many graduate students and other workers in this effort.



Wullenweber "Elephant Cage" Antenna



SNEP Van Used for Site Surveys

Dick (K6RWA) was an avid Amateur "Ham" Radio operator for many years and was involved in many activities of the Nittany Amateur Radio Club (W3YA) in State College, PA while there at Penn State and also one of the founding and active members of the Naval Postgraduate School Amateur Radio Club (K6LY) in Monterey, CA.

Following are some quotes about the passing of Prof. Adler:

Dean John Volakis of Florida International University said "His photo is exactly as I remember. As the obituary said, a helpful and very active man. I very much enjoyed my visits at Monterey because of him."

Prof. Alan Christman of Grove City College said "Dick was a great guy and a good friend – he will be missed!"

Prof. Emeritus Ronald Marhefka of Ohio State University said "Thanks for letting me know about Dick. I think about him from time to time hoping he was doing well. He had a good productive life living to 87. I too knew him well mostly in the 80's and 90's and appreciated all he did for ACES and many of us early attenders to the conference. Plus, we did a short course at Fort Huachuca for a week one time. I will miss him."

Dr. Jay Rockway (retired Navy NOSC, NRAD, SPAWAR) said "When I became a Federal employee with the Navy, Dick was one of first persons with whom I worked. It was my privilege to know such a creative and honorable person. You were always amazed by what would be the next project/effort."

Prof. Emeritus Ed Miller said "Sad news. We had many good meetings and times at the Postgraduate School over the years. Trying to remember when I first met Dick and think it might have been 1971 at a meeting or short course."

It is hard to believe he is not with us anymore. I would like to speak for all of his friends in ACES, IEEE APS, IEEE Broadcasting, NPS, Penn State, and Amateur Radio to pass on our sincere condolences to Dick's wife and family. We all will really miss him so much. Rest in peace our dear friend Prof. Richard W. Adler.

Jim Breakall
Professor, Electrical Engineering
Penn State University,
University Park, PA 16802

FDTD Simulations of Modulated Metasurfaces with Arbitrarily Shaped Meta-atoms by Surface Impedance Boundary Condition

Yanmeng Hu, Quanen Zhou, Xinyu Fang, and Mengmeng Li

Department of Communication Engineering
Nanjing University of Science and Technology, Nanjing, 210094, China
limengmeng@njjust.edu.cn

Abstract – In this paper, we propose a reduced-complexity finite difference time domain (FDTD) simulations of modulated metasurfaces with arbitrary unit cells. The three dimensional (3D) physical structure of the metasurface is substituted by a spatially varying surface impedance boundary condition (IBC) in the simulation; as the mesh size is not dictated by sub-wavelength details, considerable advantage in space- and time-step is achieved. The local parameters of the IBC are obtained by numerical simulation of the individual unit cells of the physical structure, in a periodic environment approximation, in the frequency domain. As the FDTD requires an appropriate time domain impulse-response, the latter is obtained by broad-band frequency simulations, and vector fitting to an analytic realizable time response. The approach is tested on metasurface structures with complex unit cells and extending over 10×10 wavelengths, using a standard PC with 64GB RAM.

Index Terms – thin-layer model, metasurface, FDTD, impedance boundary condition.

I. INTRODUCTION

Metasurfaces are thin-layer arrays composed of the so called “electromagnetic meta-atoms,” which have been proved to allow unprecedented electromagnetic field manipulations [1, 2]. Due to their advantages of low profile, low cost, easy fabrications, and diverse strategies for realizations, many applications have been reported, such as: radar cross section (RCS) reduction [3], low-scattering antennas [4], planar antennas [5], lenses [6], [7], imaging [8], etc.

The meta-atoms are sub-wavelength in size, and likewise closely spaced; the resulting structure is thus electrically thin, while typically extending over several wavelengths in size; very often, the field manipulation requires meta-atoms with complicated structures. As a result, it is challenging to simulate such multiscale problems with dense discretization and large electrical size by full-wave methods [2], [9], [10].

Most types of field manipulation require that the metasurface be spatially varying over its surface; however, this variability is on the order of the wavelength, i.e. slow with respect to the size of meta-atoms (hence the term “modulated” often employed). Therefore, homogenization yields accurate results, and the effects of sub-wavelength atoms is well described in terms of surface impedance boundary conditions (IBCs) [2], [11–13], that can take different forms [14–26]. This consideration allows a significant reduction of computational load for full-wave analysis; of course it requires that the problem formulation be consistent with the field boundary conditions employed to homogenize the sub-wavelength atoms collectively. In most applications, the underlying lattice of the atoms remains regular, or weakly varying; this allows to use the periodic-medium approximation in relating the surface impedance to the features of the individual meta-atoms.

In this short paper, we propose an FDTD method with surface impedance boundary condition (IBC) for the simulations of spatially varying (i.e. modulated) metasurfaces. Specifically, we address the case of meta-atoms with arbitrary shapes, for which no analytical expression can be found of the equivalent surface impedance. We propose a method to insert numerical characterization of the IBC into the scheme, including the necessity to properly account for frequency dispersion in the time response. The IBC approach reduces mesh density in the *longitudinal* direction by virtue of homogenization into an IBC [24], by de facto removing the meta-atom thickness. However, we would like to stress that in our approach we use the nature of modulation to likewise reduce the necessary mesh density in the *transverse* directions, as modulations are on the order of the wavelength.

To the best of the authors’ knowledge, this use of numerically-derived IBC to solve both thickness and *transverse* meshing issues is novel in FDTD, and applied for the first time to large metasurfaces.

The rest of this paper is organized as follows: in Section II, the background of IBC and FDTD is summarized;

in Section III, the numerical homogenization for wide-band full-wave FDTD simulation of metasurface is proposed; numerical results and discussions in Section IV demonstrate the validity of the proposed method. Finally, a brief conclusion is given in Section V.

II. BACKGROUND

A. Impedance boundary condition (IBC)

When a surface impedance boundary condition is appropriate, the total transverse electric and magnetic fields on the concerned surface are linked as [11–13]

$$\mathbf{E}_t(\omega) = \bar{\bar{Z}}_s(\omega) \cdot [\hat{\mathbf{z}} \times \mathbf{H}_t(\omega)], \quad (1)$$

where \mathbf{E}_t and \mathbf{H}_t are the fields on the outer side of the metasurface, and $\bar{\bar{Z}}_s$ is the equivalent surface impedance, in general of tensor nature. We have explicitly denoted frequency dependence to recall that this is naturally a frequency domain description, while in the following we will address time-domain solution of Maxwell equations. The one-sided description of the homogenized structure in (1) avoids meshing the dielectric (where FDTD would have meshing problems), and is appropriate for thin layers (where spatial dispersion is negligible). Structural symmetry in the meta-atoms generates isotropy in the boundary conditions, and the effective surface impedance is scalar, so that

$$E_x(\omega) = Z_s^{xx}(\omega) \cdot H_y(\omega) \quad (2a)$$

$$E_y(\omega) = -Z_s^{yy}(\omega) \cdot H_x(\omega). \quad (2b)$$

Analytic expressions of the surface impedance can be obtained only for a few simple unit cells [26]. In this paper, we consider meta-atoms with arbitrary structure, and the surface impedances will be extracted from numerical simulation of the meta-atom unit cells, as described below in Secs. III and IV.

B. FDTD with frequency dispersion

In this paper, we follow the classical Yee cell FDTD [27–30], and the usual leap-frog scheme. We will also use FDTD with 2D- or 1D-periodic boundary conditions, which implement the method in [36]. As FDTD is time-domain, it is necessary to express the linear IBC (1) as a time convolution:

$$E_x(t) = \int_0^\infty Z_s^{xx}(t) \cdot H_y(t - \tau) d\tau \quad (3a)$$

$$E_y(t) = - \int_0^\infty Z_s^{yy}(t) \cdot H_x(t - \tau) d\tau, \quad (3b)$$

where now $Z(t)$ represents the impulse responses, i.e. the Fourier (back) transforms of their frequency-domain counterparts in eqn (1).

In the following we will resort to approximations of the dispersion that allow for closed-form expressions of the impulse responses in eqn (3). The piecewise linear recursive convolution (PLRC) method [31] will be employed to evaluate the convolutions in eqn (3). The updating equations for computation domains not

involved in the IBC surface are same as the standard FDTD [27–30].

III. NUMERICAL HOMOGENIZATION

A. Surface impedance extraction from numerical simulation of meta-atoms

As alluded in the Introduction, we will obtain the local values of the (spatially variable) surface impedance via numerical simulation of the local meta-atoms. We will employ the periodicity approximation, which accounts for inter-element coupling, and that has been successfully used in the design of metasurface cells as reported in several publications [1–8]. Here we will call “unit cell” the meta-atom in the periodic lattice; because of the periodic approximation, the simulation is better performed in the frequency domain. The simulation of the unit cell can be carried out with several approaches, most usually finite-elements (FEM) and Method of Moments (MoM); here we will use FEM as implemented in the commercial software HFSS.

In order to reduce the associated numerical cost, we will resort to a method that allows wide-angle response with a limited number (two) of simulations [2], [20]. While the method is general, for the sake of illustration we will consider isotropic meta-atoms constituted by close ring resonators (CRRs) [32] on a grounded dielectric substrate, as in Figure 1.

The approach is based on separating the metal layer (here, the ring) from the grounded slab; as the metal features are sub-wavelength and non-resonant, both their frequency and spatial dispersion (dependence on incidence angle) are weak; as typically higher Floquet modes are deeply evanescent, the equivalent modal circuit is as depicted in Figure 2. As mentioned earlier, we consider explicitly symmetric meta-atoms, which yield an isotropic impedance, and no TE-TM coupling; more general situations are readily accounted for by this coupling and modal network slightly more complex than in Figure 2.

The wide-angle response of the metal feature (ring, here) is conveniently expressed using the generalized sheet transition condition (GSTC) description of the boundary condition [2], [20], i.e. in terms of polarization susceptibility tensors. This yields an expression valid for any incidence angle that however requires only computation of the response for two angles: normal incidence $\theta=0^\circ$, and one oblique incidence $\theta=\theta_0$ encompassing the incidence angle range of interest [2], [20].

The polarization susceptibilities are then expressed in terms of the reflection (R) and transmission (T) coefficients as:

$$\chi_{es}^{xx} = \chi_{es}^{yy} = \frac{2j(T_0 + R_0 - 1)}{k_0(T_0 + R_0 + 1)} \quad (4)$$

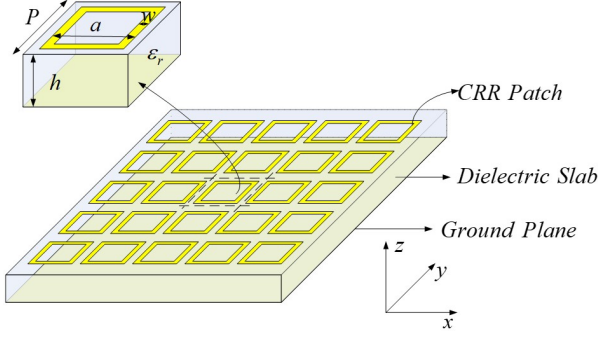


Fig. 1. Example of meta-atoms in a periodic environment: CRR meta-atoms.

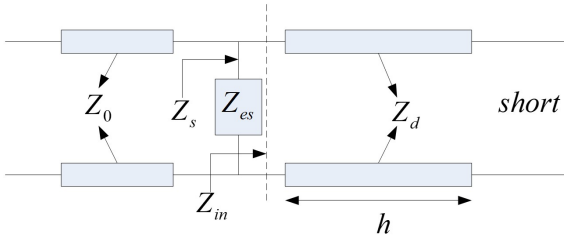


Fig. 2. Equivalent modal transmission line circuit model of the meta-atoms under periodic boundary conditions.

$$\chi_{ms}^{zz} = -\frac{\chi_{es}^{yy}}{\sin^2(\theta_0)} + \frac{2j\cos(\theta_0)(T(\theta_0)+R(\theta_0)-1)}{k_0\sin^2(\theta_0)(T(\theta_0)+R(\theta_0)+1)}, \quad (5)$$

where k_0 denotes the wave number in free space, T_0 and R_0 the transmission and reflection coefficients at normal incidence, $T(\theta_0)$ and $R(\theta_0)$ are the transmission and reflection coefficients for incidence angle θ_0 . The indication of TM or TE polarization has been assumed and omitted in the susceptibilities to avoid notation cluttering, and likewise in reflection (R) and transmission (T) coefficients. One can then pass to the impedance format of the IBC via the following relationships [25]:

$$Z_{es}^{TE} = -\frac{j\eta_{\text{eff}}}{k_{\text{eff}}(\chi_{es}^{yy} + k_0^2\chi_{ms}^{zz}\sin^2\theta/k_{\text{eff}}^2)} \quad (6a)$$

$$Z_{es}^{TM} = -\frac{j\eta_{\text{eff}}}{k_{\text{eff}}\chi_{es}^{xx}} \quad (6b)$$

where $\eta_{\text{eff}} = \eta_0/\sqrt{\epsilon_{\text{eff}}}$, $k_{\text{eff}} = k_0\sqrt{\epsilon_{\text{eff}}}$, $\epsilon_{\text{eff}} = (1 + \epsilon_r)/2$, Z_{es}^{TE} and Z_{es}^{TM} denote the surface impedances of TE and TM polarized plane wave at an oblique incidence angle θ , respectively; note that χ terms in the equations above are also TE and TM although that is not explicitly indicated.

The surface impedances required in eqn (3) are then obtained via the equivalent modal transmission line circuit in Figure 2:

$$Z_s^{xx} = Z_s^{yy} = \frac{Z_{in}Z_{es}^{xx}}{Z_{in} + Z_{es}^{xx}}, \quad (7)$$

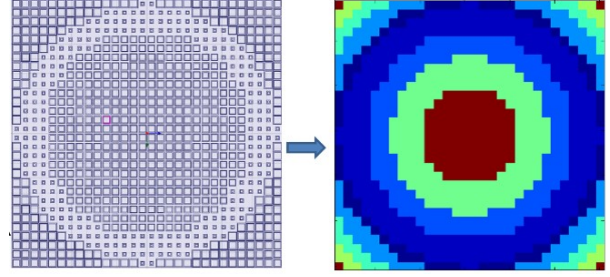


Fig. 3. Modulated metasurface with non-uniform complicated meta-atoms and the corresponding surface impedance.

where $Z_{in} = jZ_d \tan(k_{dz}h)$, Z_0 and Z_d are the characteristic impedances of free space and the dielectric,

$$Z_0 = \begin{cases} \omega_0\mu_0/k_{0z}, & \text{TE} \\ k_{0z}/\omega_0\epsilon_0, & \text{TM} \end{cases} \quad (8)$$

$$Z_d = \begin{cases} \omega_0\mu/k_{dz}, & \text{TE} \\ k_{dz}/\omega_0\epsilon, & \text{TM} \end{cases} \quad (9)$$

$$k_{0z} = \sqrt{k_0^2 - k_x^2}, k_x = k_0 \sin \theta, k_{dz} = \sqrt{k_0^2 \epsilon_r - k_x^2}.$$

For metasurfaces with non-uniform meta-atoms and thus space-varying surface impedance, the projection from the physical structure to its surface impedance description is depicted in Figure 3, where the meta-atoms are substituted by a cell of surface impedance, with values computed as described above. As a result, the metasurface thickness is not meshed at all, and the transverse FDTD mesh density is dictated only by the spatial variability of the meta-atoms (e.g. modulation), which is on the scale of the wavelength; this drastically increases the simulation efficiency of the modulated metasurface; in FDTD, this is even more pronounced than in frequency-domain methods, as time step is related to space discretization by stability, as well known (e.g. [33]).

B. Full-wave simulation with dispersive FDTD

For wideband full-wave simulations of the modulated metasurface, the surface impedances derived in eqn (6) and (7) have complicated relationship with frequency, which cannot be inserted into FDTD directly. As a result, we fit the frequency response with a model that allows closed-form time-domain expressions. As we expect resonances across the bandwidth of interest because of the nature of the meta-atom itself, we employ the following model:

$$Z_s(j\omega) = d + \sum_{n=1}^N \frac{r_n}{j\omega - p_n}, \quad (10)$$

where d is a constant real number, N is the order of rational function, r_n and p_n are n th residue and pole, respectively. The expression above is fit to the actual frequency response (deriving from numerical simulations)

via the vector fitting method [34], in which the nonlinear approximation in eqn (10) can be evaluated with two stages of linear problems.

The time domain expressions read:

$$Z_s^{xx}(t) = Z_s^{yy}(t) = \left(d + \sum_{n=1}^N r_n e^{-Pnt} \right) u(t). \quad (11)$$

Since $Z_s(t)$ has an exponential form, the convolution integrals can be easily solved by the recursive convolution method [35]. Take E_x for example, the surface impedance boundary condition at the m th cell is discretized with FDTD as

$$E_x^n(i + \frac{1}{2}, j, k) = d_m H_y^n(i + \frac{1}{2}, j, k) + \psi_{y,m}^n(i + \frac{1}{2}, j, k), \quad (12a)$$

where

$$\begin{aligned} \psi_{y,m}^n(i + \frac{1}{2}, j, k) &= \sum_{n=1}^N \frac{P_{m,n}}{r_{m,n}} \left[1 + \frac{(e^{-r_{m,n}\Delta t} - 1)}{r_{m,n}\Delta t} \right] H_y^{n-\frac{1}{2}}(i + \frac{1}{2}, j, k + \frac{1}{2}) \\ &+ \sum_{n=1}^N \frac{P_{m,n}}{r_{m,n}} \left[\frac{1}{r_{m,n}\Delta t} - \frac{e^{-r_{m,n}\Delta t}}{r_{m,n}\Delta t} \left(1 + \frac{1}{r_{m,n}\Delta t} \right) \right] H_y^{n-\frac{3}{2}}(i + \frac{1}{2}, j, k + \frac{1}{2}) \\ &+ \sum_{n=1}^N e^{-r_{m,n}\Delta t} \psi_{y,m}^{n-1}(i + \frac{1}{2}, j, k) \end{aligned} \quad (12b)$$

IV. NUMERICAL RESULTS AND DISCUSSION

In this section, numerical examples are presented to validate the accuracy and efficiency of the proposed scheme. In all examples, the incidence angle θ_0 in eqn (4) and (5) is chosen to 45° , which has shown to provide good results in all cases: it is chosen as a tradeoff with respect to the impact of $\sin^2 \theta$ in the denominator of eqn (5) [2], [20]. The proposed algorithm was implemented single thread with Intel Fortran 64-bit compiler, all the computations were carried out on the same computer with an Intel (R) Core (TM) i7-8700 CPU @3.7GHz and 64 GB RAM. The logic here is progressive: (1) first we validate the method against a fully periodic structure (2D periodicity, infinitely extended); (2) we validate on a 1D periodic case, i.e. with periodic boundary conditions along one direction; and (3) we finally show application to a fully 2D variation of the impedance.

A. Uniform infinite metasurface sheet (Meta-atom under periodic boundary conditions)

As a first test, we compare the FDTD-IBC against a standard FDTD and HFSS in a periodic environment. The results are shown in Figure 4, which reports the reflection coefficient phase and amplitude of the CRR meta-atom of Figure 1 from 5 GHz to 10 GHz (note inclusion of nominal substrate losses). The excellent agreement proves the accuracy of the proposed method. Table I lists the necessary grids size, and the related computational requirements, showing significant savings of both the computation time (218 s to 2 s) and memory

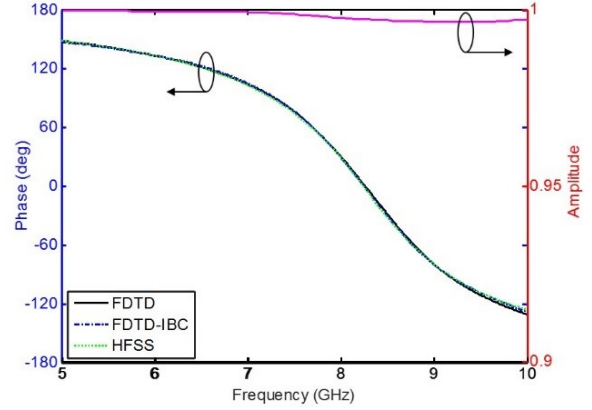


Fig. 4. Accuracy validation: wideband reflection phase and amplitude with (2D) periodic boundary conditions, for the CRR meta-atom shown in Figure 1, with $P = 6$ mm, $a = 4.8$ mm, $h = 2$ mm, $w = 0.5$ mm, and $\epsilon_r = 3.5 - j0.00245$ (note that substrate losses are included).

Table 1: Computation performance comparison of FDTD and FDTD-IBC for the wideband simulation of CRR meta-atom

| | Grid size | Time (s) | Memory (MB) |
|----------|--|----------|-------------|
| FDTD | $0.1 \text{ mm} \times 0.1 \text{ mm} \times 0.1 \text{ mm}$ | 218 | 128.5 |
| FDTD-IBC | $1 \text{ mm} \times 1 \text{ mm} \times 1 \text{ mm}$ | 2 | 4.7 |

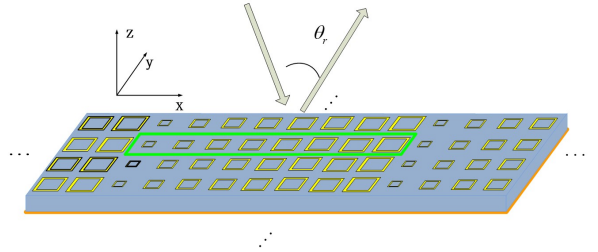


Fig. 5. Gradient metasurface for reflection fields manipulations, the reflection angle θ_r for a given incidence angle θ_i is determined by the phase gradient along \hat{x} .

(128.5 MB to 4.7 MB), which demonstrate the validity of the proposed FDTD-IBC.

B. Wideband reflection field manipulations with gradient metasurface (1D periodicity)

Next, we examine a practical example of metasurface device, yielding the so-called non-Snell reflection via a gradient-phase metasurface, adopting the structure in [1]. For a plane wave with incidence angle θ_i , the reflection angle θ_r from the designed gradient metasurface will follow the generalized law of

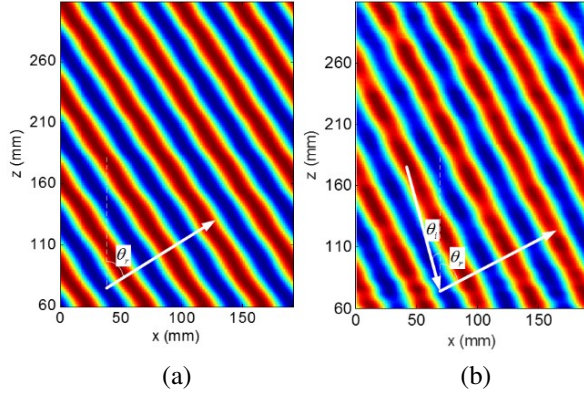


Fig. 6. Validation: reflection fields manipulations by the gradient metasurface at 7.5 GHz under (a) normal incidence, (b) oblique incidence $\theta = 15^\circ$, both of the simulated reflection angles agree well with the analytical values by generalized reflection law [1].

Table 2: Parameters of the 3 bit CRR meta-atoms for reflection fields manipulations at 7.5 GHz

| Meta-atoms $\theta = 0^\circ$ | 1 | 2 | 3 | 4 | 5 | 6 | 7 | 8 |
|-----------------------------------|------|------|------|------|------|------|------|------|
| a (mm) | 3.01 | 4.82 | 5.13 | 5.32 | 5.44 | 5.54 | 5.72 | 5.92 |
| Meta-atoms $\theta = 15^\circ$ | 1 | 2 | 3 | 4 | 5 | 6 | 7 | 8 |
| a (mm) | 3.65 | 5.80 | 6.25 | 6.53 | 6.72 | 6.92 | 7.22 | 7.90 |

reflection [1]

$$\sin \theta_r - \sin \theta_i = \frac{1}{n_0 k_0} \frac{d\phi}{dx}, \quad (13)$$

where $n_0 = 1$, $d\phi/dx$ is the designed phase gradient along \hat{x} . Here we consider periodicity along the y direction. Table II lists the relevant geometric parameters for the reported test cases.

At first, we simulate the reflection fields from the gradient metasurface under normal incidence. Figure 6 (a) shows the simulated reflection fields at 7.5 GHz, the period of the meta-atom is 6 mm. The meta-atoms

Table 3: Computation performance comparison of FDTD and FDTD-IBC for wideband simulation of gradient metasurface.

| | Number of grids | Time | Memory |
|----------|------------------------------|--------|----------|
| FDTD | $1920 \times 60 \times 2900$ | 50.1 h | 27.7 GB |
| FDTD-IBC | $192 \times 6 \times 290$ | 314 s | 639.2 MB |

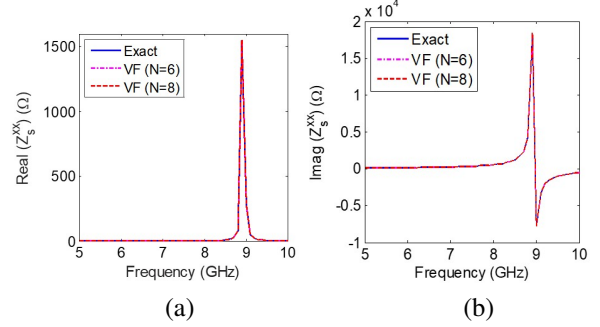


Fig. 7. Vector fitting (VF) for the surface impedances from 5 GHz to 10 GHz for the CRR with $a = 4.8$ mm, (a) real part, (b) imaginary part.

of number 1 to 8 in Table II are placed along \hat{x} with a constant phase difference of $\pi/8$; the length of the metasurface is 192 mm, corresponding to $4.8\lambda_0$, and the y -period is 6 mm. The reflection angle simulated by FDTD-IBC is 56° , which agrees well with the analytical value of 56.4° evaluated by eqn (13). Then, we simulate the reflection fields under oblique incidence angle of 15° as in Figure 6 (b), the period of the meta-atom is 8 mm, the same number of meta-atoms listed in Table II is employed. The reflection angle simulated by FDTD-IBC is 62° , which agrees well with the analytical value of 62.1° evaluated by eqn (13).

For wideband simulations, the surface impedance should be fitted as explained in Sec. III-B. Figure 7 shows the wideband surface impedances of the CRR meta-atom when $a = 4.8$ mm of exact data and vector fitting method [34]. It can be concluded that when $N = 6$ and $N = 8$, the fitted surface impedance converges to the exact data. We choose $N = 6$ in the following simulations, as they employ the same meta-atoms.

Figure 8 shows the reflection angle θ_r from 7.1 GHz to 8.5 GHz for the gradient metasurface in Figure 6 (a) evaluated by generalized reflection law [1] and the proposed FDTD-IBC, very good agreements between them can be found. Table III lists the computation time and memory requirements for the wideband simulation of gradient metasurface. The discretization sizes for FDTD and FDTD-IBC are 0.1 mm and 1mm, respectively, showing the potential for larger surfaces; in this case computation time is reduced from 50.1 hours to 314 seconds, and the memory is reduced from 27.7 GB to 639.2 MB.

C. Reflection fields focusing with 2D metasurface (Metareflector)

As a final application example, we consider a metasurface with two-dimensional variation, designed for reflection field focusing for normal plane-wave incidence. We will call “metareflector” this structure, in

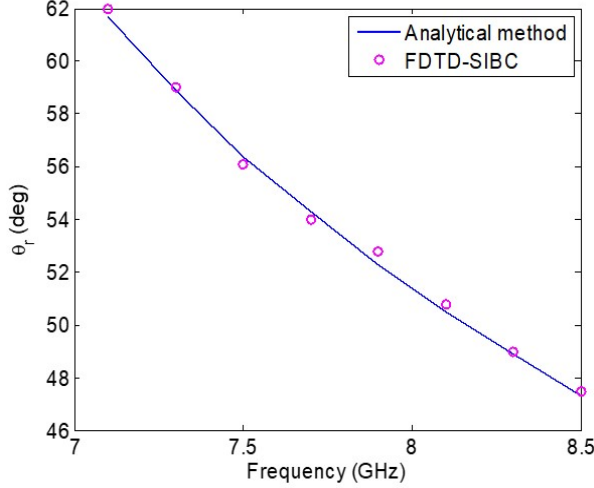


Fig. 8. Wideband simulated reflection angle θ_r of the gradient metasurface with eqn (13) and FDTD-IBC from 7.1 GHz to 8.5 GHz.

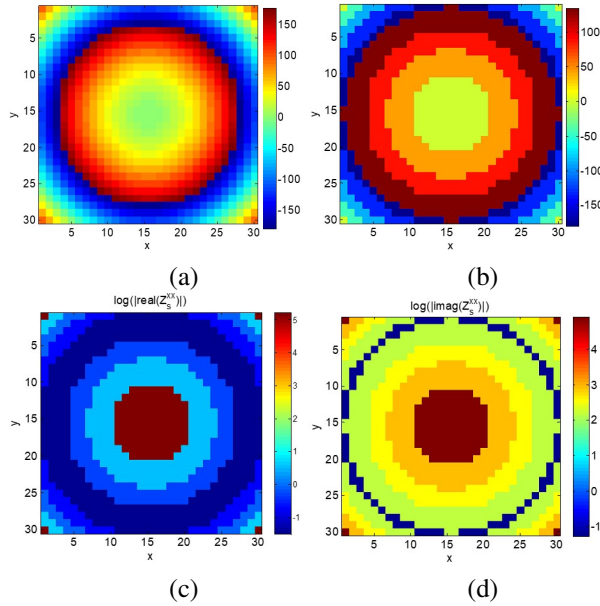


Fig. 9. Phase distributions of the metareflector for reflection fields focusing at 7.5 GHz with the 30×30 CRRs, (a) GO target phase [1], (b) phase compensation with 3 bit meta-atoms, (c) $\log(|\text{real}(Z_s^{xx})|)$, (d) $\log(|\text{imag}(Z_s^{xx})|)$.

analogy to the cognate reflectarrays. The phase distribution is based on the Geometrical Optics (GO) approximation, yielding

$$\varphi(x, y) = k_0(f_c - \sqrt{x^2 + y^2 + f_c^2}), \quad (14)$$

for a focal length f_c ; the surface impedance is again designed so as to yield the desired phase. Figure 9

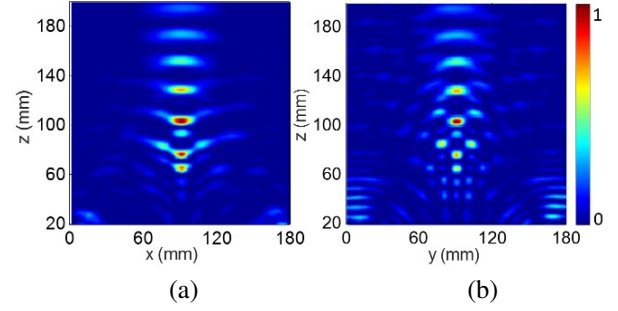


Fig. 10. Normalized focusing fields of the metareflector A i.e. $D = 4.5\lambda$ at 7.5 GHz, (a) xoz plane, (b) $yo z$ plane.

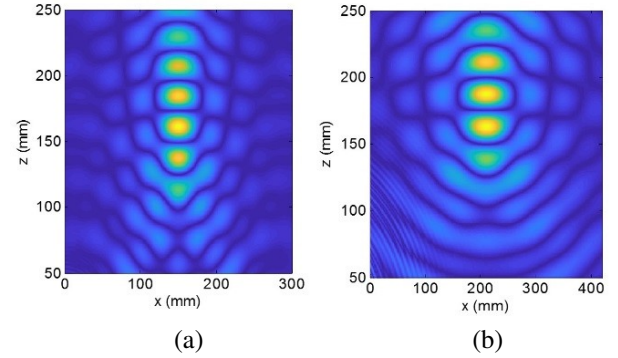


Fig. 11. Normalized focusing fields of xoz plane by the metareflectors B and C at 7.5 GHz, i.e. (a) $D = 300\text{mm} = 7.5\lambda$, with 50×50 meta-atoms and (b) $D = 420\text{mm} = 10.5\lambda$, with 70×70 meta-atoms.

shows the resulting structure for $f_c = 180\text{ mm}$ at 7.5 GHz; Figure 9 (a) plots the ideal (continuous) GO phase compensation at the location of (x, y) , and Figure 9 (b) the realized phase distributions with 3 bit CRR meta-atoms. The effective surface impedances distributions of the metareflector are obtained from the precomputed meta-atoms listed in Table II as in Figure 9 (c) and (d). The physical structures of the metareflector are substituted by homogeneous surface impedances as indicated earlier.

We consider three diameters: (A) $D = 180\text{ mm}$, i.e. 4.5 wavelengths at the operating frequency, and $f_c/D = 1$; (B) $D = 300\text{ mm}$, i.e. 7.5 wavelengths, and $f_c/D = 0.6$; (C) $D = 420\text{ mm}$, i.e. 10.5 wavelengths, and $f_c/D = 0.43$. Figure 10 and Figure 11 show the normalized reflection field manipulations by the designed metasurface reflector at the xoz and $yo z$ plane. For the relatively small structure A in Figure 10, there is a significant discrepancy between the planned focal length (180 mm) and the observed one, 109 mm; this is to be expected from a GO-based design. Indeed, the situation changes with larger sizes, of 7.5 and 10.5

Table 4: Computation time and memory performance of the FDTD-IBC for metareflectors of different dimensions

| Type | Number of meta-atoms | Dimensions [$\lambda \times \lambda$] | Number of grids | Time [h] | Memory [GB] |
|------|----------------------|---|----------------------------|----------|-------------|
| A | 30×30 | 4.5×4.5 | $400 \times 400 \times 80$ | 0.39 | 12.5 |
| B | 50×50 | 7.5×7.5 | $640 \times 640 \times 80$ | 1.75 | 32.6 |
| C | 70×70 | 10.5×10.5 | $880 \times 880 \times 80$ | 3.34 | 54.7 |

wavelengths, as seen in Figure 11 yielding 161 and 175 mm focal lengths, respectively, thus actually nearing the GO prediction [37]. Table IV lists the computation time and memory requirements for the full wave simulations of the proposed method, where the discretization size is 0.5 mm.

V. CONCLUSION

In this short paper, we have presented and validated an effective surface impedance boundary condition (IBC) for FDTD for wideband simulations of modulated metasurface with complicated meta-atoms. The local surface impedance is obtained via frequency domain (FEM) simulation of the meta-atoms in the periodic approximation, and vector fitting method for the frequency dependence not get closed-form time domain impulse responses. With the proposed method, the thickness of the metasurface is not discretized in the FDTD, and the transverse variation only requires space discretization to match the modulation, which is slow. Hence, the multiscale metasurface can be substituted by homogenous surface impedance, and the number of unknowns is reduced significantly. Examples of metasurfaces for reflected field manipulations are shown to demonstrate the validity of the proposed method.

ACKNOWLEDGMENT

This work was supported in part by Natural Science Foundation of China under Grant 61871222 and 61890541, the Fundamental Research Funds for the Central Universities of 30921011101.

REFERENCES

- [1] N. Yu and F. Capasso, "Flat optics with designer metasurfaces," *Nature Materials*, vol. 13, no. 2, pp. 139-150, 2014.
- [2] C. L. Holloway, E. F. Kuester, J. A. Gordon, J. O'Hara, J. Booth, and D. R. Smith, "An overview of the theory and applications of metasurfaces: the two-dimensional equivalents of metamaterials," *IEEE Antennas Propag. Mag.*, vol. 54, no. 2, pp. 10-35, Feb. 2012.
- [3] S. Zhou, X. Fang, M. Li, and R. S. Chen, "S/X dual-band real-time modulated frequency selective surface based absorber," *Acta Physica Sinica*, vol. 69, no. 20, pp. 204101, 2020.
- [4] Y. Liu, K. Li, Y. Jia, Y. Hao, S. X. Gong, and Y. J. Guo, "Wideband RCS reduction of a slot array antenna using polarization conversion metasurfaces," *IEEE Trans. Antennas Propag.*, vol. 64, no. 1, pp. 326-331, Jan. 2016.
- [5] G. Minatti, F. Caminita, M. Casaletti, and S. Maci, "Spiral leakywave antennas based on modulated surface impedance," *IEEE Trans. Antennas Propag.*, vol. 59, no. 12, pp. 4436-4444, Dec. 2011.
- [6] M. Li, S. Li, Y. Yu, X. Ni, and R. S. Chen, "Design of random and sparse metalens with matrix pencil method," *Opt. Express*, vol. 26, no. 19, pp. 24702-24711, Sep. 2018.
- [7] M. Li, S. Li, L. K. Chin, Y. F. Yu, D. P. Tsai, and R. S. Chen, "Dual-layer achromatic metalens design with an effective Abbe number," *Opt. Express*, vol. 28, no. 18, pp. 26041-26055, Aug. 2020.
- [8] L. Li, H. Ruan, C. Liu, Y. Li, Y. Shuang, A. Alù, and T. J. Cui, "Machine-learning reprogrammable metasurface imager," *Nature Communications*, vol. 10, no. 1, pp. 1082, 2019.
- [9] C. L. Holloway, A. Dienstfrey, E. F. Kuester, J. F. OHara, A. K. Azad, and A. J. Taylor, "A discussion on the interpretation and characterization of metafilms/metalsurfaces: the two-dimensional equivalent of metamaterials," *Metamaterials*, vol. 3, no. 2, pp. 100-112, 2009.
- [10] Y. Guo, T. Zhang, W. Y. Yin, and X. H. Wang, "Improved hybrid FDTD method for studying tunable graphene frequency-selective surfaces (GFSS) for THz-wave applications," *IEEE Trans. Terahertz Sci. Technol.*, vol. 5, no. 3, pp. 358-367, May 2015.
- [11] J. G. Maloney, G. S. Smith, "The use of surface impedance concepts in the finite-difference time-domain method," *IEEE Trans. Antennas Propag.*, vol. 40, no. 1, pp. 38-48, Jan. 1992.
- [12] M. A. Francavilla, E. Martini, S. Maci, and G. Vecchi, "On the numerical simulation of metasurfaces with impedance boundary condition integral equations," *IEEE Trans. Antennas Propag.*, vol. 63, no. 5, pp. 2153-2161, May 2015.
- [13] B. Stupfel and D. Poget, "Sufficient uniqueness conditions for the solution of the time harmonic maxwell's equations associated with surface impedance boundary conditions," *J. Comput. Phys.*, vol. 230, no. 12, pp. 4571-4587, Jun. 2011.
- [14] E. F. Kuester, M. A. Mohamed, M. Piket-May and C. L. Holloway, "Averaged Transition Conditions for Electromagnetic Fields at a metafilm," *IEEE Trans. Antennas Propag.*, vol. 51, no. 10, pp. 2641-2651, Oct. 2003.
- [15] C. L. Holloway, D. C. Love, E. F. Kuester, J. A. Gordon, and D. A. Hill, "Use of generalized sheet transition conditions to model guided waves

- on metasurfaces/metafilms,” *IEEE Trans. Antennas Propag.*, vol. 60, no. 11, pp. 5173-5186, Nov. 2012.
- [16] D. González-Ovejero and S. Maci, “Gaussian ring basis functions for the analysis of modulated metasurface antennas,” *IEEE Trans. Antennas Propag.*, vol. 63, no. 9, pp. 3982-3993, Sep. 2015.
- [17] M. Bodehou, D. Gonzalez-Ovejero, C. Craeye, and I. Huynen, “Method of moments simulation of modulated metasurface antennas with a set of orthogonal entire-domain basis functions,” *IEEE Trans. Antennas Propag.*, vol. 67, no. 2, pp. 1119-1130, Feb. 2018.
- [18] M. Bodehou, C. Craeye, and I. Huynen, “Electric field integral equation-based synthesis of elliptical-domain metasurface antennas,” *IEEE Trans. Antennas Propag.*, vol. 67, no. 2, pp. 1270-1274, Feb. 2019.
- [19] Q. Wu, “Characteristic mode analysis of composite metallic–dielectric structures using impedance boundary condition,” *IEEE Trans. Antennas Propag.*, vol. 67, no. 12, pp. 7415-7424, Dec. 2019.
- [20] K. Achouri, M. A. Salem, and C. Caloz, “General metasurface synthesis based on susceptibility tensors,” *IEEE Trans. Antennas Propag.*, vol. 63, no. 7, pp. 2977-2991, Jul. 2015.
- [21] C. Pfeiffer and A. Grbic, “Bianisotropic metasurfaces for optimal polarization control: Analysis and synthesis,” *Phys. Rev. Appl.*, vol. 2, no. 4, p. 044011, Oct. 2014.
- [22] X. Du, H. Yu, and M. Li, “Effective modeling of tunable graphene with dispersive FDTD-GSTC method,” *Applied Computational Electromagnetics Society Journal, (Special Issue of ACES, Beijing, 2018)*, vol. 31, no. 6, pp. 851-856, 2019.
- [23] X. Jia, F. Yang, X. Liu, M. Li, and S. Xu, “Fast nonuniform metasurface analysis in FDTD using surface susceptibility model,” *IEEE Trans. Antennas Propag.*, vol. 68, no. 10, pp. 7121-7130, Oct. 2020.
- [24] V. Nayyeri, M. Soleimani, O. M. Ramahi, “Modeling graphene in the finite-difference time-domain method using a surface boundary condition,” *IEEE Trans. Antennas Propag.*, vol. 61, no. 8, pp. 4176-4182, May 2013.
- [25] X. Liu, F. Yang, M. Li, and S. Xu, “Analysis of reflectarray antenna elements under arbitrary incident angles and polarizations using generalized boundary conditions,” *IEEE Antennas Wirel. Propag. Lett.*, vol. 17, pp. 2208-2212, 2018.
- [26] O. Luukkonen, C. Simovski, G. Granet, G. Goussetis, D. Lioubtchenko, A. V. Räsänen, and S. A. Tretyakov, “Simple and accurate analytical model of planar grids and high-impedance surfaces comprising metal strips or patches,” *IEEE Trans. Antennas Propag.*, vol. 56, no. 6, pp. 1624-1632, Jun. 2008.
- [27] K. Yee, “Numerical solution of initial boundary value problems involving Maxwell’s equations in isotropic media,” *IEEE Trans. Antennas Propag.*, vol. 14, no. 3, pp. 302-307, May 1966.
- [28] A. Taflove and S. C. Hagness, *Computational Electrodynamics: The Finite-Difference Time-Domain Method*, 3rd edition. Norwood, MA: Artech House, 2017.
- [29] K. Niu, Z. X. Huang, M. Li, and X. L. Wu, “Optimization of the artificially anisotropic parameters in WCS-FDTD method for reducing numerical dispersion,” *IEEE Trans. Antennas Propag.*, vol. 65, no. 12, pp. 7389-7394, Dec. 2017.
- [30] K. Niu, Z. X. Huang, X. Ren, M. Li, B. Wu and X. L. Wu, “An optimized 3-D HIE-FDTD method with reduced numerical dispersion,” *IEEE Trans. Antennas Propag.*, vol. 66, no. 11, pp. 6435-6440, Nov. 2018.
- [31] D. F. Kelley and R. J. Luebbers, “Piecewise Linear Recursive Convolution for Dispersive Media Using FDTD,” *IEEE Trans. Antennas Propag.*, vol. 44, no. 6, pp. 792-797, Jun. 1996.
- [32] Y. Yang, L. Jing, B. Zheng, R. Hao, W. Yin, E. Li, C. M. Soukoulis, and H. Chen, “Full-polarization 3D metasurface cloak with preserved amplitude and phase,” *Advanced Materials*, vol. 28, no. 32, pp. 6866-6871, 2016.
- [33] S. A. Cummer, “An analysis of new and existing FDTD methods for isotropic cold plasma and a method for improving their accuracy,” *IEEE Trans. Antennas Propag.*, vol. 45, pp. 392-400, 1997.
- [34] B. Gustavsen and A. Semlyen, “Rational approximation of frequency domain responses by vector fitting,” *IEEE Transactions on Power Delivery*, vol. 14, no. 3, pp. 1052-1061, Mar. 1999.
- [35] R. Luebbers, F. P. Hunsberger, K. S. Kunz, R. B. Standler, and M. Schaneider, “A frequency-dependent time-domain formulation for dispersive materials,” *IEEE Trans. Electromagn. Compat.*, vol. 37, pp. 222-227, Aug. 1990.
- [36] J. A. Roden, S. D. Gedney, M. P. Kesler, J. G. Maloney, and P. H. Harms, “Time-domain analysis of periodic structures at oblique incidence: Orthogonal and nonorthogonal FDTD implementations,” *IEEE Trans. Microwave Theory Tech.*, vol. 46, pp. 420-427, Apr. 1998.
- [37] X. Li, S. Xiao, B. Cai, Q. He, T. J. Cui, and L. Zhou, “Flat metasurfaces to focus electromagnetic waves in reflection geometry,” *Opt. Letters*, vol. 37, no. 23, pp. 4940-4942, 2012.



Yanmeng Hu received the B.S. degree in Electronic Information Science and Technology from the Henan University Minshen College, Kaifeng China, in 2017. She is pursuing the master's degree in integrated circuit engineering in the Nanjing University of Science and Technology, Nanjing, China. Ms. Hu's current research interest is electromagnetic analysis of multiscale problems.



Mengmeng Li received the B.S. degree (Hons.) in physics from Huaiyin Normal College, Huai'an, China, in 2007, and the Ph.D. degree in electromagnetic field and microwave technology from the Nanjing University of Science and Technology, Nanjing, China, in 2014. From 2012 to 2014, he was a Visiting Student

with the Electronics Department, Politecnico di Torino, Turin, Italy, and also with the Antenna and EMC Laboratory (LACE), Istituto Superiore Mario Boella, Turin, where he carried out fast solver for multiscale simulations. Since 2014, he has been with the Department of Communication Engineering, Nanjing University of Science and Technology, where he has been an Assistant Professor, Associate Professor, and Professor since 2020. In 2017, he was a Visiting Scholar with Pennsylvania State University, Pennsylvania, PA, USA. His current research interests include fast solver algorithms, computational electromagnetic solvers for circuits, signal integrity analysis, and multiscale simulations.

Dr. Li was a recipient of the Doctoral Dissertation Award of Jiangsu Province in 2016, the Young Scientist Award at the ACES-China Conference in 2019, and five student paper/contest awards at the international conferences with the students. He is an active reviewer for many IEEE journals and conferences. He is an Associate Editor of the IEEE Antennas and Propagation Magazine, IEEE Open Journal of Antennas and Propagation (OJAP), and IEEE Access, and a Guest Editor of OJAP.

Convergence Acceleration of Infinite Series Involving the Product of Riccati–Bessel Function and Its Application for the Electromagnetic Field: Using the Continued Fraction Expansion Method

Zheng Fanghua^{1,2,3}, Di Qingyun^{1,2,3}, Yun Zhe^{1,2,3}, and Gao Ya^{1,2,3}

¹CAS Engineering Laboratory for Deep Resources Equipment and Technology, Institute of Geology and Geophysics, Chinese Academy of Sciences, Beijing 100029, China

²Innovation Academy for Earth Science, Chinese Academy of Sciences, Beijing 100029, China

³University of Chinese Academy of Sciences, Beijing 100049, China

Zhengfanghua18@mails.ucas.ac.cn; qydi@mail.iggcas.ac.cn; yz791161833@163.com; gaoya171@mails.ucas.ac.cn

Abstract – A summation technique has been developed based on the continuous fractional expansion to accelerate the convergence of infinite series involving the product of Riccati–Bessel functions, which are common to electromagnetic applications. The series is transformed into a new and faster convergent sequence with a continued fraction form, and then the continued fraction approximation is used to accelerate the calculation. The well-known addition theorem formula for spherical wave function is used to verify the correctness of the algorithm. Then, some fundamental aspects of the practical application of continuous fractional expansion for Mie scattering theory and electromagnetic exploration are considered. The results of different models show that this new technique can be applied reliably, especially in the electromagnetic field excited by the vertical electric dipole (VED) source in the “earth-ionospheric” cavity. The comparison among the new technology, the Watson-transform, and the spherical harmonic series summation algorithm shows that this new technology only needs less than 120 series items which is already enough to obtain a small relative error, which greatly improves the convergence speed, and provides a new way to solve the problem.

Index Terms – infinite series; Riccati–Bessel function; Mie scattering; electromagnetic prospecting.

I. INTRODUCTION

The study of electromagnetism can be applied in many areas, such as electromagnetic scattering [1–5], plasmonics [6–8], seismo-ionospheric disturbance [9–11], radio communication [12–15], and earth science [16–20] studies. Following the pioneering work of Lorenz-Mie [21], the subject of electromagnetic wave propagation under spherical boundary has become a hot

spot in the fields of electromagnetism [1–5, 14–16, 22]. Since the spherical Bessel function is often used as the eigenfunction for the spherical coordinate system, the numerical calculation including the integral or series of the spherical Bessel function is extremely important in the fields of scientific calculation and engineering applications [23, 24]. Theoretically, the analytical solution of the Helmholtz equation in the spherical coordinate system can be obtained by the method of separating variables. However, even if modern high-performance computers are used to calculate the sum of the series directly item by item, the spherical Bessel function of high-order complex parameters can easily lead to a numerical overflow in the calculation process [25, 26]. As a result, the series expression does not converge, and it is time-consuming to directly calculate the infinite sum.

To overcome this computational burden, predecessors proposed different solutions to specific series problems [27–29]. For the Mie scattering series, for example, Wiscombe [30] proposed to truncate the series and give the maximum summation term N_{\max} . The Wiscombe criterion is by far the most widely used, but the criterion is based on a priori estimation [31], and N_{\max} is positively correlated with the frequency and the radius of the sphere. That is, the truncation terms will increase with the increase in frequency and radius. In addition, the truncation formula cannot be fully applied to the spherical vector wave function. For earth-scale models, it is time-consuming to directly calculate the infinite sum. Fock [32] put forward the Watson-transform technique to transform the infinite series summation into a contour integral and obtained the expression that is convenient for engineering calculations. But the realization of the Watson-transform depends on the solution of the poles of the summation function in the series, which is complicated. Wang [22] developed the spherical harmonic

series acceleration convergence algorithm proposed by Barrick, but it needs to subtract an appropriate closed-form expression from the original accurate series, and then add the same closed-form expression to improve the convergence.

The principle of the infinite series acceleration method is to transform a slowly convergent sequence into a new, faster converging sequence. Since there is not any general algorithm that could work well for every type of sequence, we should try different algorithms to obtain the optimum result for the problem under investigation [28]. Continued fraction expansion has wide application in the numerical calculation of special analytic functions. Hänggi [27] applied the method of the continued fraction expansion for the slow convergent series which occurs in quantum mechanics and statistical mechanics. In this paper, the author tries to apply the continued fraction expansion to improve the convergence of infinite series containing the product of spherical Bessel functions, aiming to find a simpler and more efficient method to converge the series. The comparison with previous results shows that this new technology can be reliably applied, especially for the calculation of the field excited by the electric dipole source in the “earth-ionospheric” cavity, and provides a new way to solve the problems.

II. BASIC PROPERTIES OF THE CONTINUED FRACTIONS

A. Continued fraction expansion of the series

If the infinite series S_∞ satisfies the form:

$$S_\infty = \frac{1}{y} \sum_{n=1}^{\infty} \frac{g_n(x)}{y^{2n-1}}. \quad (1)$$

Expand the series (1) into continued fraction form at $y=1$, we have:

$$S_n = \frac{d_1}{1 + \frac{d_2}{1 + \frac{\dots}{1 + d_n}}}, \quad (2)$$

where d_n is the n th continued fraction factor [27], n is the total number of factors, and eqn (2) is named the limit periodic continued fraction. Define a global array X with an initial value of “0,” intermediate variables D_n and L , then the relationship between the continued fraction factor d_n and the series g_n is [27]: when $n < 5$,

$$\begin{aligned} n = 1, D_1 &= g_1, d_1 = D_1 \\ n = 2, D_2 &= g_2, d_2 = -D_2/D_1 \\ n = 3, D_3 &= g_3 + g_2 d_2, d_3 = -D_3/D_2 \\ n = 4, D_4 &= g_4 + g_3 (d_2 + d_3), d_4 = -D_4/D_3 \\ n &\geq 5, \\ L &= 2 * INT [(n-1)/2] \end{aligned}$$

$$\begin{aligned} X(k) &= X(k-1) + d_{n-1} * X(k-2) \quad (k = L, L-2, \dots, 4) \\ X(2) &= X(1) + d_{n-1} \\ X(k) &\leftrightarrow X(k+1) \quad (k = 1, 3, 5, \dots, L-1) \\ D_n &= g_n + \sum_{i=1}^{L/2} g_{n-i} X(2i-1) \\ d_n &= -D_n/D_{n-1}, \end{aligned} \quad (3)$$

where k and i are loop variables, INT is a rounding function, and $X(k) \leftrightarrow X(k+1)$ means interchange $X(k)$ and $X(k+1)$.

B. Convergence algorithm for continued fractions

Starting from the right side of eqn (2), one can gradually approach the convergence value of the series S_∞ , but each additional term in the calculation means recalculating the entire continued fraction. Therefore, Wallis [33] proposed a fast recursive algorithm, define the array A_n and B_n with an initial value: $A_{-1} = 1, B_{-1} = 0, A_0 = 1, B_0 = 1$. And the relationship between A_n, B_n and d_n is:

$$\begin{aligned} A_n &= A_{n-1} + d_n A_{n-2} \\ B_n &= B_{n-1} + d_n B_{n-2} \end{aligned} \quad (4)$$

And we have:

$$f_n = 1 + S_n = \frac{A_n}{B_n}. \quad (5)$$

From eqn (2), (4), and (5), the successive approximation to infinite continued fraction can be calculated until the required accuracy is obtained. But the recursive algorithm is easy to cause calculation overflow because the values of A_n and B_n are too large or too small. Define $C_n = A_n/A_{n-1}, D_n = B_n/B_{n-1}$, we have [34]:

$$C_n = 1 + \frac{d_n}{A_{n-1}/A_{n-2}} = 1 + \frac{d_n}{C_{n-1}} \quad (6)$$

$$D_n = 1 + \frac{d_n}{B_{n-1}/B_{n-2}} = 1 + \frac{d_n}{D_{n-1}} \quad (7)$$

$$\frac{C_n}{D_n} = \frac{A_n/A_{n-1}}{B_n/B_{n-1}} = \frac{A_n/B_n}{A_{n-1}/B_{n-1}}. \quad (8)$$

Define $C_1 = 1 + d_1, D_1 = 1, f_0 = 1$, from eqn (5) and (8) we have:

$$f_n = \frac{C_n}{D_n} \cdot f_{n-1}. \quad (9)$$

Eqn (9) describes the n th approximate value represented by the continued fraction, where the value of n depends on the oscillation of the Bessel function and the required accuracy. Therefore, it is necessary to specify a small positive number ε according to the required calculation accuracy. When the relative error of the last two calculation results is less than or equal to ε , that is, when the eqn (10) is established, the series is considered to be convergent, and $S_\infty \cong f_n - 1$.

$$\frac{f_n}{f_{n-1}} - 1 \leq \varepsilon. \quad (10)$$

III. EXAMPLES

To investigate the approximation effect of the continued fraction expansion of infinite series containing Bessel function, we choose the addition theorem formula [15] of the spherical wave function in free space to verify the correctness of the algorithm:

$$\frac{e^{-ikR}}{R} = \sum_{n=0}^{\infty} -ik(2n+1)j_n(kr)h_n^{(2)}(kr_s)P_n(\cos\theta), r < r_s, \quad (11)$$

where j_n and $h_n^{(2)}$ are the spherical Bessel functions, $k = 2\pi f \cdot \sqrt{\mu\epsilon}$ is the wavenumber of free space, r is the radius of the earth, r_s is the position of the field source, $R = \sqrt{r^2 - 2rr_s \cos\theta + r_s^2}$ is the distance from the observation point to the source.

Figure 1 shows the calculation results of direct series summation and continued fraction expansion summation. The frequency $f = 1 \text{ Hz}$ (a), 300 Hz (b), $r = 6371 \text{ km}$, $r_s = r + 10 \text{ m}$. To further show the numerical characteristics of the technique in this paper, in Figure 2, we show the number of items in the continued fraction expansion required at different frequencies and different observation positions and the number of terms required for the direct summation of the series.

It can be seen from Figure 1 and Figure 2 that the result of the continued fraction expansion is completely consistent with the analytical solution. As the frequency increases, the oscillation of the spherical Bessel function increases. It is necessary to increase the calculation items to obtain higher accuracy. It is worth noting that even at 300 Hz , the continued fraction expansion method only needs no more than 100 items, the effect and speed are much better than the direct summation method. At the same frequency, the farther away from the field source, the faster the series converges, and the closer to the field source, the slower the convergence

speed. That is, we need to accurately calculate the high-order spherical Bessel function.

IV. APPLICATION OF CONTINUED FRACTION EXPANSIONS FOR ELECTROMAGNETIC FIELD

A. Expressions for Mie series

The Lorenz-Mie theory [21] is a complete theoretical framework for studying the electromagnetic scattering of plane waves by a uniform isotropic media sphere. Consider a uniform sphere of radius a and embedded in a non-absorbing medium with a dielectric constant of ϵM . For an incident monochromatic plane wave of wavelength λ , the electromagnetic characteristics of the incident beam can be described by a set of dimensionless scattering coefficients Q_{sca} , extinction coefficients Q_{ext} , absorption coefficients Q_{abs} , and backscattering coefficients Q_b [5]:

$$\begin{aligned} Q_{\text{sca}} &= \frac{2}{x^2} \sum_{n=1}^{\infty} (2n+1) (|a_n|^2 + |b_n|^2) \\ Q_{\text{ext}} &= \frac{2}{x^2} \sum_{n=1}^{\infty} (2n+1) (\text{Re}(a_n) + \text{Re}(b_n)) \\ Q_{\text{abs}} &= Q_{\text{sca}} - Q_{\text{ext}} \\ Q_b &= \frac{1}{x^2} \left| \sum_{n=1}^{\infty} (2n+1) (-1)^n (a_n - b_n) \right|^2, \end{aligned} \quad (12)$$

where a_n and b_n are the Mie coefficients that characterize the optical response of the sphere:

$$\begin{aligned} a_n &= \frac{m\hat{J}_n(mx)\hat{J}_n'(x) - \hat{J}_n(x)\hat{J}_n'(mx)}{m\hat{J}_n(mx)\hat{H}_n^{(1)'}(x) - \hat{H}_n^{(1)}(x)\hat{J}_n'(mx)}, \\ b_n &= \frac{\hat{J}_n(mx)\hat{J}_n'(x) - m\hat{J}_n(x)\hat{J}_n'(mx)}{\hat{J}_n(mx)\hat{H}_n^{(1)'}(x) - m\hat{H}_n^{(1)}(x)\hat{J}_n'(mx)}, \end{aligned}$$

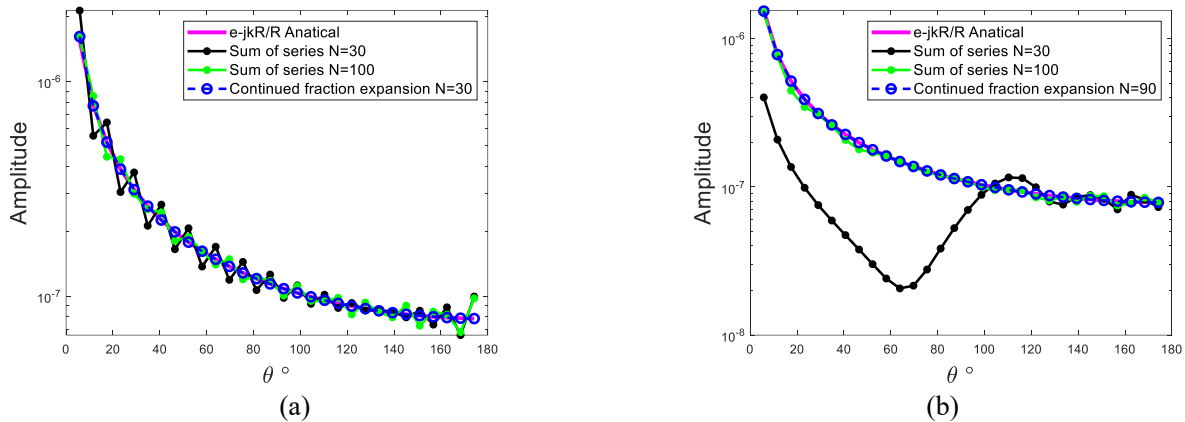


Fig. 1. Comparison of the free-space spherical wave function obtained by the continued fraction expansion method and the direct summation. N is the number of items, and the relative accuracy is 10^{-10} . (a) $f = 1 \text{ Hz}$, (b) $f = 300 \text{ Hz}$.

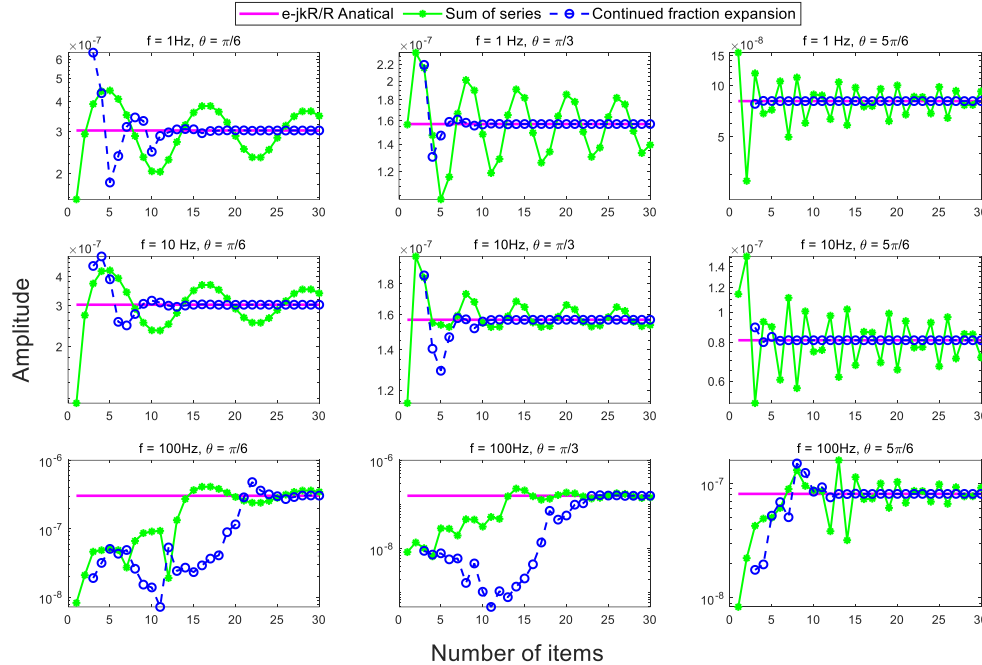


Fig. 2. Comparison of the number of items required for the continued fraction expansion and the direct summation.

where $x = 2\pi R/\lambda$ is the particle size parameter, m is the relative refractive index, \hat{J}_n and \hat{H}_n^1 are the Riccati-Bessel functions.

Figure 3 shows the calculation results of metal materials ($m = 50+50i$) in the range of particle size parameter x from 0 to 30 and compares them with the calculation results of Christian Mätzler [5]. It can be seen from Figure 3 that the two algorithms are in good agreement. The parameter with the maximum value and the maximum fluctuation is Q_b . The curves of Q_{ext} and Q_{sca} are closely connected near the value 2 and increase rapidly. For $x = 30$, $N_{wis} = 44$, and $N_{cf} = 58$. For the Mie series, the convergence of the original series is good enough, so the application of the continued fraction method does not bring a significant improvement in convergence, but it proves the correctness and practicability of our method. Note that as the particle size parameter x increases, the number of truncation items required for the series will increase. In Mätzler [5], for large parameters, the high-order spherical Bessel function leads to the overflow. The accurate calculation of high-order spherical Bessel functions can be found in the literature [25], [26].

B. Propagation of ELF/SLF electromagnetic waves

In recent years, the propagation of ELF/SLF electromagnetic waves in the “earth-ionospheric” cavity has attracted much attention in the fields of submarine communication, resource exploration, earthquake precursor

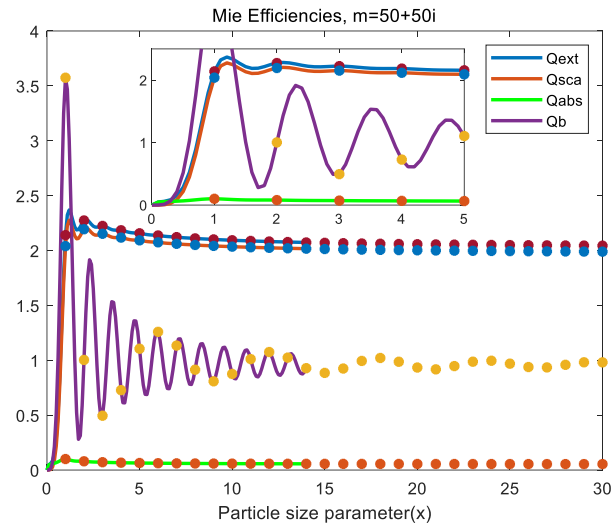


Fig. 3. Mie Efficiencies for a metal-like material ($m=50+50i$) over the x range from 0 to 30. The solid lines are computed with the Wiscombe criterion, the dotted lines are calculated using the continued fraction expansion.

monitoring, and space weather disaster investigation [14, 15, 19, 22, 35].

Considering the vertical electric dipole source (VED) located near the spherical surface, the electromagnetic field on the earth’s surface can be represented

as [14]:

$$\begin{aligned}
 E_r &= \frac{-\eta k^2 I d l}{4\pi v_s^2 v} \cdot \sum_{n=1}^{\infty} \left\{ \frac{n(n+1) \cdot (2n+1) \cdot P_n(\cos \theta) \cdot \left[\hat{J}_n(v) \hat{H}_n^1(v_s) + b_n \hat{J}_n(v) + c_n \hat{H}_n^1(v) \right]}{\left[\hat{J}_n(v) \hat{H}_n^1(v_s) + b_n \hat{J}_n(v) + c_n \hat{H}_n^1(v) \right]} \right\} \\
 E_\theta &= \frac{\eta k^2 I d l}{4\pi v_s^2 v} \cdot \sum_{n=1}^{\infty} \left\{ \frac{(2n+1) \cdot P_n'(\cos \theta) \cdot \left[\hat{J}_n(v) \hat{H}_n^1(v_s) + b_n \hat{J}_n'(v) + c_n \hat{H}_n^1(v) \right]}{\left[\hat{J}_n(v) \hat{H}_n^1(v_s) + b_n \hat{J}_n(v) + c_n \hat{H}_n^1(v) \right]} \right\} \\
 H_\phi &= \frac{i k^2 I d l}{4\pi v_s^2 v} \cdot \sum_{n=1}^{\infty} \left\{ \frac{(2n+1) \cdot P_n'(\cos \theta) \cdot \left[\hat{J}_n(v) \hat{H}_n^1(v_s) + b_n \hat{J}_n(v) + c_n \hat{H}_n^1(v) \right]}{\left[\hat{J}_n(v) \hat{H}_n^1(v_s) + b_n \hat{J}_n(v) + c_n \hat{H}_n^1(v) \right]} \right\}, \quad (13)
 \end{aligned}$$

where b_n and c_n are coefficients related to the electrical characteristics of the ionosphere and the earth, and \hat{J}_n and \hat{H}_n^1 are the Riccati-Bessel function.

Different from the Mie scattering series, which only contains the product of the spherical Bessel function once, the ELF/SLF electromagnetic field excited by an electric dipole contains the product of the spherical Bessel function multiple times and the product of the Legendre function. Due to the scale of the earth, it is difficult to obtain accurate spherical Bessel function values of high-order complex parameter unless it is properly approximated [36]. Therefore, even with a high-performance computer, it is hard to converge the series by calculating the sum of the sequence item by item. Wait [15] adopted the classical modal theory and applied the Watson-transform to solve the radial electric field excited by a VED. Barrick [36] derived the spherical harmonic series expression of ELF/SLF electromagnetic wave field under ideal boundary conditions. Wang [22] developed Barrick's method and proposed a numerical convergence algorithm, but it needs to subtract a closed-form expression from the original exact series, and then add the same closed expression to modify the summation.

To verify the correctness and practicability of the new sequence, Figure 4 compares the radial electric field strength at 5 and 50 Hz with the asymptotic solution of Wait [15] and the numerical sum of Barrick [36]. At 50 Hz, the approximate solution obtained by Wait [15] using the classic Watson transform works well far away from the source, but it fails to show the rapid attenuation trend of the field in the region closer to the source. That is, near the source point, the electromagnetic field has the largest value and then decays rapidly, and finally shows the well-known resonance phenomenon. At 5 Hz, the difference of approximate solution increases significantly. Since both the paper and Barrick's research adopt precise series solutions, the two curves are in good agreement, and the electromagnetic field near the source shows a clear downward trend. However, Barrick achieved sufficient accuracy and convergence by taking 650 items in the sequence, while it only needs no more than 120 items to obtain a relative accuracy of 10^{-15} by the algorithm

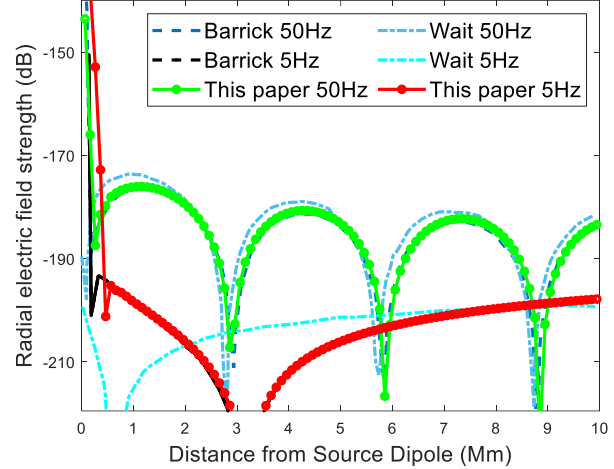


Fig. 4. Compare the radial electric field strength at 5 and 50 Hz with the asymptotic solution of Wait [15] and the numerical sum of Barrick [36].

in this paper, of which no more than 50 items in the far-field. Therefore, the algorithm in this paper can greatly improve the convergence speed. Therefore, only a few items are already enough to obtain a small relative error, which greatly improves the convergence speed.

C. Application in electromagnetic prospecting

As one of the important methods of resource and energy exploration, electromagnetic exploration is based on the difference in resistivity and polarizability between the ore body and the surrounding rock. Different from signal transmission in the communication field, geophysical prospecting needs to construct the electrical parameters of underground media from the information carried by electromagnetic waves.

As a new electromagnetic exploration method, the wireless electromagnetic method (WEM) has the advantages of high signal strength, good consistency, wide application range, large exploration depth, etc., and has a broad application prospect in deep resource exploration [19]. By measuring the spatial distribution of electromagnetic fields caused by different rocks and ores, the electrical parameters of underground media can be constructed, thus to detect underground targets. Following the expression (13), define the ratio of the orthogonal electric field to the magnetic field on the earth's surface as the spherical wave impedance [15]: $|Z_e| = |E_\theta/H_\phi|$, in the extremely low-frequency range: $|Z_e| \approx \sqrt{\omega\mu_0/\sigma_e}$ [35]. Although it is not possible to define an idealized plane wave source on the spherical earth model, fortunately, Di [19] pointed out that when the transmission distance is greater than six skin depths, the ELF/SLF electromagnetic wave field can be regarded as a plane

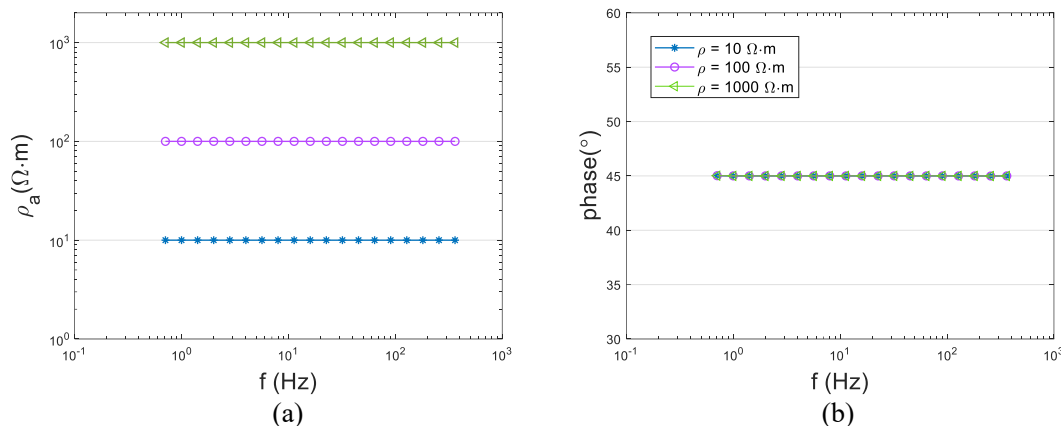


Fig. 5. WEM apparent resistivity (a) and phase (b) calculated for the homogeneous models. The transmit frequency is 2^n Hz, $n = -0.5:0.5:8.5$, and the interval is 0.5, and the observation azimuth is 10 degrees.

wave source. And the apparent resistivity and phase in the spherical coordinate are:

$$\rho_a = \frac{1}{\omega\mu} |Z_e|^2, \phi = \tan^{-1} \left| \frac{Im(Z_e)}{Re(Z_e)} \right|. \quad (14)$$

To verify the feasibility of WEM in the spherical earth and analyze its response characteristics, Figure 5 shows the apparent resistivity and phase of the WEM in the homogeneous earth model with earth resistivity of $10\Omega \cdot m$, $100\Omega \cdot m$ and $1000\Omega \cdot m$.

Figure 5(a) shows that in the ELF/SLF range, the apparent resistivity curve of WEM at different frequencies is completely coincident with the resistivity of the earth. Because in eqn (14), it can be seen that the ratio of the electric field and the magnetic field is closely related to the emission frequency and the resistivity of the underground medium. Therefore, when the emission frequency is known, the resistivity of the underground medium can be obtained, which reveals that WEM can detect the electrical parameters of underground targets. In addition, following the definition of skin depth $\delta = \sqrt{2/\omega\mu\sigma}$, it can be known that in the earth media, the attenuation rate of electromagnetic waves is proportional to the square root of its working frequency. Therefore, WEM has obvious advantages in deep resource exploration due to its lower operating frequency. Figure 5 (b) shows that for a homogeneous earth model, the phase is $\pi/4$, which is independent of the frequency and the electrical parameters of the underground media. This is consistent with the conclusion that the phase of the magnetic field in a homogeneous medium lags the phase of the electric field by $\pi/4$, and further proves the correctness of WEM.

V. CONCLUSION

In this paper, a summation technique based on Continued fraction is developed to accelerate the convergence of infinite series containing the product of

Riccati–Bessel functions, which are common in electromagnetic problems. And the recursive algorithm needed for effective calculation of Continued fraction coefficients is presented, so that the series is transformed into a new and faster convergent sequence in the form of continued fractions, then the Continued fraction approximation is used to accelerate the calculation. In addition, some main aspects of the practical application of continuous fractional expansion in Mie scattering theory and electromagnetic exploration are considered. The results show that in the Mie scattering model, since the convergence of the original series is good enough, the application of the Continued fraction expansion does not bring significant improvement. However, the new technology has powerful advantages for the calculation of extremely low-frequency electromagnetic fields. It only needs no more than 120 series items to obtain a relative accuracy of 10^{-15} , of which no more than 50 items in the far-field. Therefore, only a few operations can be performed to obtain a small relative error, which greatly improves the convergence speed.

ACKNOWLEDGEMENTS

This work was supported part by the Scientific Instrument Developing Project of the Chinese Academy of Sciences under Grant ZDZBGCH2018006, and in part by the National Natural Science Foundation of China under grant number 41874088.

REFERENCES

- [1] G. Ruello and R. Lattanzi, "Scattering from spheres: A new look into an old problem," *Electronics*, vol. 10, no. 2, pp. 216, 2021.
- [2] W. Zhuang, R. Li, J. Liang, and Y. Jia, "Debye series expansion for light scattering by a charged sphere," *Applied Optics*, vol. 60, no. 7, pp. 1903-1915, 2021.

- [3] C. Gao, B. Sun, and Y. Zhang, "Electromagnetic wave scattering by charged coated spheres," *Journal of Quantitative Spectroscopy and Radiative Transfer*, vol. 272, pp. 107757, 2021.
- [4] S. Batool, F. Frezza, F. Mangini, and X. Yu-Lin, "Scattering from multiple PEC sphere using translation addition theorems for spherical vector wave function," *Journal of Quantitative Spectroscopy and Radiative Transfer*, vol. 248, pp. 106905, 2020.
- [5] C. Mätzler, *MATLAB Functions for Mie Scattering and Absorption, Version 2*, 2002.
- [6] M. E. Nazari and W. Huang, "Asymptotic solution for the electromagnetic scattering of a vertical dipole over plasmonic and non-plasmonic half-spaces," *IET Microwaves, Antennas & Propagation*, vol. 15, pp. 704-717, 2021.
- [7] B. Beiranvand, A. S. Sobolev, and A. Sheikholeslami, "A proposal for a dual-band tunable plasmonic absorber using concentric-rings resonators and mono-layer graphene," *Optik*, vol. 223, pp. 165587, 2020.
- [8] M. Gingsins, M. Cuevas, and R. Depine, "Surface plasmon dispersion engineering for optimizing scattering, emission, and radiation properties on a graphene spherical device," *Applied Optics*, vol. 59, no. 14, pp. 4254-4262, 2020.
- [9] S. Zhao, X. Shen, C. Zhou, L. Liao, Z. Zhima, and F. Wang, "The influence of the ionospheric disturbance on the ground based VLF transmitter signal recorded by LEO satellite—Insight from full wave simulation," *Results in Physics*, vol. 19, pp. 103391, 2020.
- [10] M. Hayakawa, A. P. Nickolaenko, Y. P. Galuk, and I. G. Kudintseva, "Scattering of extremely low frequency electromagnetic waves by a localized seismogenic ionospheric perturbation: observation and interpretation," *Radio Science*, vol. 55, no. 12, pp. 1-26, 2020.
- [11] R. Song, K. Hattori, X. Zhang, and S. Sanaka, "Seismic-ionospheric effects prior to four earthquakes in Indonesia detected by the China seismo-electromagnetic satellite," *Journal of Atmospheric and Solar-Terrestrial Physics*, vol. 205, pp. 105291, 2020.
- [12] S. Chowdhury, S. Kundu, T. Basak, S. Ghosh, M. Hayakawa, S. Chakraborty, and S. Sasmal, "Numerical simulation of lower ionospheric reflection parameters by using international reference ionosphere (IRI) model and validation with very low frequency (VLF) radio signal characteristics," *Advances in Space Research*, vol. 67, no. 5, pp. 1599-1611, 2021.
- [13] C. Dong, Y. He, M. Li, C. Tu, Z. Chu, X. Liang, and N. X. Sun, "A portable very low frequency (VLF) communication system based on acoustically actuated magnetoelectric antennas," *IEEE Antennas and Wireless Propagation Letters*, vol. 19, no. 3, pp. 398-402, 2020.
- [14] W. Pan and K. Li, *Propagation of SLF/ELF Electromagnetic Waves*. Springer Science & Business Media, 2014.
- [15] J. R. Wait, *Electromagnetic Waves in Stratified Media: Revised Edition Including Supplemented Material*. Elsevier, 2013.
- [16] Y. Gao, Q. Di, R. Wang, C. Fu, et al., "Strength of the electric dipole source field in multilayer spherical media," *IEEE Transactions on Geoscience and Remote Sensing*, 2021.
- [17] Q. Di, C. Fu, Z. An, et al., "An application of CSAMT for detecting weak geological structures near the deeply buried long tunnel of the Shijiazhuang-Taiyuan passenger railway line in the Taihang Mountains," *Engineering Geology*, vol. 268, pp. 105517, 2020.
- [18] Q. Di, G. Xue, C. Fu, and R. Wang, "An alternative tool to controlled-source audio-frequency magnetotellurics method for prospecting deeply buried ore deposits," *Science Bulletin*, vol. 65, no. 8, pp. 611-615, 2020.
- [19] Q. Di, M. Wang, C. Fu, et al., *Study on the Characteristics of Electromagnetic Wave Propagation in Earth-Ionosphere Mode*, Science Press, 2013.
- [20] D. Shreeja, et al. "Application of Fracture Induced Electromagnetic Radiation (FEMR) technique to detect landslide-prone slip planes," *Natural Hazards*, vol. 101, no. 2, 2020.
- [21] G. Mie, "Articles on the optical characteristics of turbid tubes, especially colloidal metal solutions," *Ann. Phys.*, vol. 330, pp. 377-445, 1908.
- [22] Y. X. Wang, R. H. Jin, J. P. Geng, et al., "Exact SLF/ELF underground HED field strengths in earth-ionosphere cavity and Schumann resonance," *IEEE Transactions on Antennas and Propagation*, vol. 59, no. 8, pp. 3031-3039, 2011.
- [23] M. Tezer, "On the numerical evaluation of an oscillating infinite series," *Journal of Computational and Applied Mathematics*, vol. 28, pp. 383-390, 1989.
- [24] M. Toyoda and T. Ozaki, "Fast spherical Bessel transform via fast Fourier transform and recurrence formula," *Computer Physics Communications*, vol. 181, no. 2, pp. 277-282, 2010.
- [25] W. J. Lentz, "Generating Bessel functions in Mie scattering calculations using continued fractions," *Applied Optics*, vol. 15, no. 3, pp. 668-671, 1976.
- [26] D. M. O'Brien, "Spherical Bessel functions of large order," *Journal of Computational Physics*, vol. 36, no. 1, pp. 128-132, 1980.

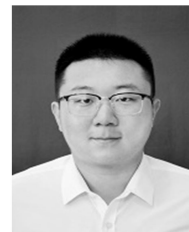
- [27] P. Hänggi, F. Rösler, and D. Trautmann, "Continued fraction expansions in scattering theory and statistical non-equilibrium mechanics," *Zeitschrift Für Naturforschung A*, vol. 33, no. 4, pp. 402-417, 1978.
- [28] N. Kinayman and M. I. Aksun, "Comparative study of acceleration techniques for integrals and series in electromagnetic problems," *Radio Science*, vol. 30, no. 6, pp. 1713-1722, 1995.
- [29] F. G. Mitri, "Partial-wave series expansions in spherical coordinates for the acoustic field of vortex beams generated from a finite circular aperture," *IEEE Transactions on Ultrasonics, Ferroelectrics, and Frequency Control*, vol. 61, no. 12, pp. 2089-2097, 2014.
- [30] W. J. Wiscombe, "Improved Mie scattering algorithms," *Applied Optics*, vol. 19, no. 9, pp. 1505-1509, 1980.
- [31] J. R. Allardice and R. E. C. Le, "Convergence of Mie theory series: criteria for far-field and near-field properties," *Applied Optics*, vol. 53, no. 31, pp. 7224-7229, 2014.
- [32] V. A. Fock, *Electromagnetic Diffraction and Propagation Problems*, Pergamon Press, 1965.
- [33] W. H. Press, W. H. Press, B. P. Flannery, et al., *Numerical Recipes in Pascal: The Art of Scientific Computing*, Cambridge University Press, 1989.
- [34] J. Wallis and W. Johannis, *Opera Mathematica*, vol. 3, 1972.
- [35] Y. Yuan, *Propagation and Noise of Ultra-Low Frequency and Extremely Low Frequency Electromagnetic Waves*, National Defense Industry Press, 2011.
- [36] D. E. Barrick, "Exact ULF/ELF dipole field strengths in the earth-ionosphere cavity over the Schumann resonance region: idealized boundaries," *Radio Science*, vol. 34, no. 1, pp. 209-227, 1999.



Fang-hua Zheng was born in Luzhou, Sichuan, China, in 1995. He received a bachelor's degree in exploration technology and engineering from the Southwest Petroleum University in Chengdu, China, in 2018. He is currently pursuing the Ph.D. degree in geophysics at University of Chinese Academy of Sciences, Beijing, China. His current research interests include the propagation of SLF/ELF electromagnetic waves in the "earth-ionosphere" cavity and its applications in geophysical prospecting.



Qing-yun Di received the bachelor's and master's degrees from the Changchun College of Geology (now Jilin University), Jilin, China, in 1987 and 1990, respectively, and the Ph.D. degree from the Institute of Geology and Geophysics (IGG), Chinese Academy of Sciences (CAS), Beijing, China, in 1998. Dr. Di is a research fellow of geophysics at the CAS Engineering Laboratory for Deep Resources Equipment and Technology, IGGCAS. She has received a number of awards from the Chinese Government and CAS, including the National Science and Technology Progress Second Prize and the Outstanding Science and Technology Achievement Prize of CAS. She is researching the propagation characteristics of controlled-source EM waves, putting into consideration the ionosphere, atmosphere, and the earth. Her research activities are mainly devoted to research and development of EM method instruments, forward modeling, and inversion of controlled source audio-frequency magnetotellurics (CSAMT), electrical resistivity tomography (ERT), and ground-penetrating radar (GPR) methods.



Zhe Yun received the B.S. degree in Geo-exploration Technology and Engineering from the Ocean University of China, Qingdao, China, in 2020. He is currently pursuing the M.S. degree in geophysics at the Institute of Geology and Geophysics (subordinate to the Innovation Academy for Earth Science), and the College of Earth and Planetary Sciences, University of the Chinese Academy of Sciences. His research interests include the controlled source electromagnetic data forward modeling and inversion.



Ya Gao received the B.S. degree in Geophysics from the Jilin University, Jilin, China, in 2017. She is currently pursuing the Ph.D. degree at the Key Laboratory of Shale Gas and Engineering, Institute of Geology and Geophysics (subordinate to the Innovation Academy for Earth Science), and the College of Earth and Planetary Sciences, University of the Chinese Academy of Sciences. Her research interests cover the controlled source electromagnetic data forward modeling and inversion.

Design and Analysis of Multi-Mode Distributed Array with Hybrid Optimization Method

Shutao Fang, Weiming Li, Wu Ren, and Zhenghui Xue

School of Information and Electronics
Beijing Institute of Technology, Beijing, 100081, China
bit_fst@163.com, wml@bit.edu.cn, renwu@bit.edu.cn, zhxue@bit.edu.cn

Abstract – In this paper, we presented an improved hybrid optimization method to construct distributed array with two identical sub-arrays, which is mainly applied on airplanes as the front-end of communication and detection system. According to different demands on array's gain and operating distances, the proposed method presents a scheme of implementation of two operate modes by optimizing elements' positions and excitations. Two sub-arrays are able to work together to realize high gain when the object is quite far away, and one sub-array is able to work alone when the object is relatively close. This method is presented based on Particle Swarm Optimization (PSO) method and convex method, accomplishing that peak sidelobe level (PSLL) of whole array is lowered under -10 dB, and PSLLs of sub-arrays are lowered under -20 dB by supplementing some auxiliary units and re-optimizing array's excitation distribution. In the procedure of optimization, the hybrid method is designed catering to multiple constraints according to the requirements of practical application. A specific example for synthesizing reconfigurable distributed array is provided and the sensitivity of obtained performance affected by interference of optimized results is discussed.

Index Terms – convex optimization, differential evolution algorithm, distributed array synthesis, grating lobe suppression, PSO Optimization Algorithm.

I. INTRODUCTION

With the requirements of radar and communication systems applied on complex platform, distributed array is attracting more and more attention and research nowadays[1, 2]. Different from traditional array, distributed array has better flexibility of array configuration and enlarges array's aperture on account of the cooperation of sub-arrays. With large array aperture, distributed array has higher directivity and narrower main lobe width, realizing desirable features like good spatial resolution and angular accuracy[3]. As for distributed array with a few sub-arrays, it has broad application

prospects because of its good flexibility on array arrangement. For example, when applied on airplane as the front-end of radar system, distributed array is able to be arranged on a side of the fuselage, taking full advantage of the available space to make the aperture as large as possible. In [4], we have proposed a hybrid method to optimize distributed array, the optimized PSLL is -10 dB.

Considering that optimized distributed array's PSLL is still higher than traditional antenna array, it will be helpful to enhance array's applicability if it can operate in different modes in which array's PSLL can be suppressed lower. For example, when the target is relatively close to the plane, the detecting result obtained from a single sub-array might be better since the sub-array has the potential of reaching lower PSLL, ensuring sub-arrays' ability of isolated operation would be a good way of improvement. However, performance of sub-arrays with elements' locations and excitation distribution presented in [4] is not good enough to put into practical application. Therefore, the optimized distributed array should be further improved to cater to the demand.

Nowadays, a lot of optimization researches have been done to improve the performance of large-spaced antenna array. Many global optimization algorithms are used on array synthesis, such as Genetic Algorithm (GA), Simulated Annealing (SA), Particle Swarm Optimization (PSO) and Differential Evolution (DE) [5–15]. Considering that array optimization problem has high degree of freedom, global optimization methods will be helpful to improve array's performance. Furthermore, distributed array synthesis is a high-dimensional nonlinear problem, convex optimization method has been considered and widely researched for array synthesis. As proposed in [16–19], convex optimization is usually applied to improve the sparsity of array. According to its optimization principle of using l_1 -norm, convex optimization is also able to be leverage to solve the problem of distributed array synthesis.

In this paper, based on the result in [4], we propose a hybrid optimization method specially for designing

and constructing distributed array with multiple operating modes. Considering that the array to be modified is sparse, and only change the locations and excitations of original elements will badly affect the whole array's pattern, it is possible to improve sub-arrays' performance by interpolating elements and adjusting their parameters. To accomplish the model switch of array, binary codes are adopted to control the on-off state of array elements to make the whole array reconfigurable and normally operate in different mode. Meanwhile, in order to guarantee both whole array and sub-arrays perform well, the distributed array should be holistically optimized after sub-array construction. With this method, the performance of sub-arrays are significantly improved and the pattern of the whole array is almost unaffected. Since elements' positions and excitations are optimized and fixed, it is also convenient to switch operation mode by just changing the on-off state of array elements.

The paper is organized as follows: In Section II, configuration and performance of array to be improved are introduced and the hybrid method to design reconfigurable distributed array are proposed. Optimized numerical results are presented in Section III. Array's tolerance to excitation error and element position error are statistically analyzed in Section IV. Conclusions are given in Section V.

II. ARRAY'S CONFIGURATION AND HYBRID METHOD TO DESIGN MULTI-MODE DISTRIBUTED ARRAY

Uniform distributed array is formed by two identical sub-arrays arranged in line, as shown in Figure 1. Each sub-array has N isotropic elements, and the distance between two adjacent units equals to half wavelength. The far-field pattern of distributed array can be calculated by

$$S(\theta) = \sum_{n=0}^{2N-1} I_n e^{-jkx_n \sin\theta} \quad (1)$$

$$= S_e(\theta)(1 + e^{-jkD \sin\theta}),$$

where $S_e(\theta)$ represents sub-arrays' pattern and D is the distance between two sub-arrays. The whole distributed

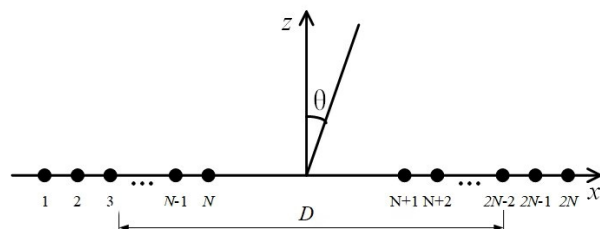


Fig. 1. Model of distributed array with two identical sub-arrays.

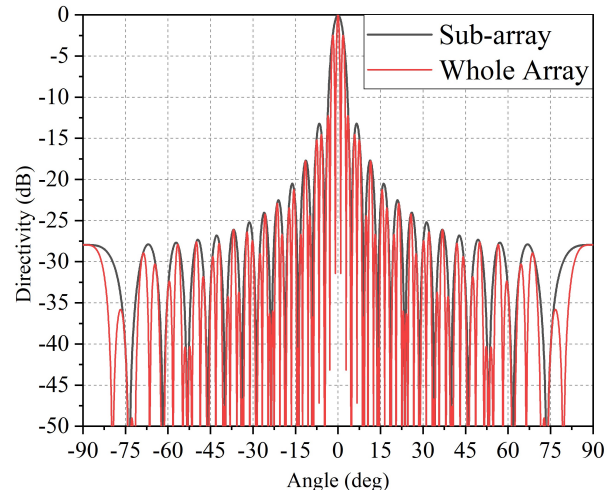


Fig. 2. Normalized Patterns of distributed array and sub-array. All elements are evenly spaced arranged and uniformly excited.

array can be regarded as a large binary array. The radiation performance of the distributed array factor is coherent with the typical pattern of a binary array. If all elements in every sub-array are evenly spaced arranged and uniformly excited, patterns of whole array and sub-array are shown in Figure 2. PSLL of distributed array is -2.47 dB.

In [4], we proposed a new hybrid method to optimize the global performance of distributed array, in which every sub-array has 25 elements. PSLL of the whole array is lower than -10 dB, exactly equal to -10.6624 dB, far lower than original PSLL of -2.1594 dB. However, both sub-arrays are badly deteriorated, where the PSLL of left and right sub-arrays are respectively equal to -6.5776 dB and -2.5718 dB. The patterns of two sub-arrays resulted from global optimization are shown in Figure 3.

In order to accomplish the reconfiguration of distributed array, sub-arrays' performance should be improved first. Based on the sparsity of sub-arrays, we present a hybrid method to improve the performance of sub-array method by adding supplementary units into sub-arrays and presenting binary code to control the on-off state of array's elements.

A. Reconfigurable sub-array design

For the optimized distributed array, inter-element distances of sub-arrays are enlarged, the sparsity of which gives enough space to interpolate more elements. After presetting minimum inter-element spacing, supplementary elements should be added as much as possible to ensure enough degrees of freedom of sub-array optimization. According to test, not all elements are

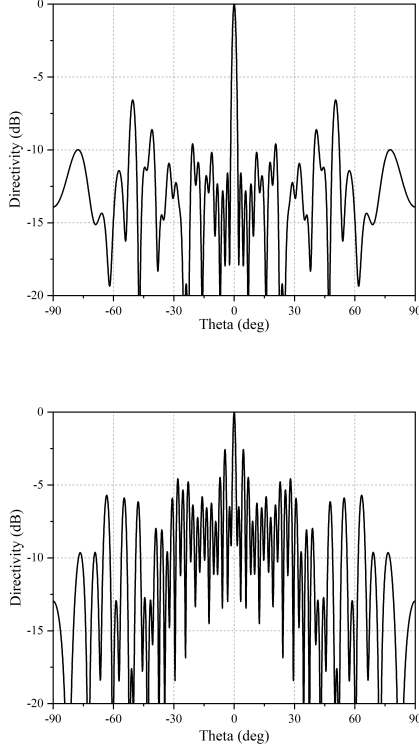


Fig. 3. Normalized directivity pattern of left and right sub-arrays. Elements' positions and excitations are respectively as Table 1 and Table 2 shows.

required to get involved in sub-arrays. Therefore, sub-arrays with added elements should be thinned in the next step to find optimal sparse scheme.

During the process, global optimization algorithms will be helpful to interpolate elements. In this paper, PSO is adopted with advantages of simpleness and quickness. To accomplish optimization of sub-arrays, we take PSLL as an indicator to search the optimal result. Therefore, PSLL and the fitness function are

$$PSLL = \max_{\theta \in \Omega_{SL}} [20 \log_{10} \frac{S_{\Delta}(\theta)}{S_{\Delta_{max}}}], \quad (2)$$

$$f(x) = \min(PSLL). \quad (3)$$

The iterative formula of PSO is shown as

$$\begin{aligned} v_{id}(t+1) &= w \times v_{id}(t) + c_1 \times rand_1 \times \\ & (p_{best}(t) - x_{id}(t)) + c_2 \times rand_2 \\ & \times (g_{best} - x_{id}(t)), \end{aligned} \quad (4)$$

where v_{id} and x_{id} are velocity vector position vector of i th element, p_{best} is the best individual in one iteration and g_{best} is the best individual during the whole process of optimization, and k is the inertia weight to control the search capability of algorithm.

During the process, we set that the interval between two adjacent elements is no less than 0.4λ . The fitness

function and constraints are described as

$$\begin{aligned} f(x) &= \min(PSLL) \\ s.t. \quad d_{id}(n) - d_{id}(n-1) &\geq 0.4\lambda \\ d_{id}(n+1) - d_{id}(n) &\geq 0.4\lambda. \end{aligned} \quad (5)$$

After this procedure, optimal result of element interpolation is obtained. All added elements are temporarily uniform excited in the result. In the next step, both original elements and added elements are getting involved in the selection to form new sub-arrays. In this process, binary PSO (BPSO) is used to determine the selection of sub-arrays' elements, which is presented by Kennedy in 1997 [20] and used for antenna and array design to get better radiation performance[21–24].

Here a logistic transformation $\text{sigmoid}(x)$ is used to constrain x_{id} to the integer 1 or 0, and the relationship between the value of x_{id} and $\text{sigmoid}(x)$ is shown as follow.

$$\text{sigmoid}(v_{id}) = (1 + \exp(v_{id}))^{-1}, \quad (6)$$

$$x_{id} = \begin{cases} 0, & \text{if } rand() \geq \text{sigmoid}(v_{id}) \\ 1, & \text{otherwise} \end{cases}. \quad (7)$$

During the interpolation and selection of elements, two weight vectors should be recorded. One is the thinning weight vector describing sub-arrays' sparsity, named as w_s . The other is to mark interpolated elements, named as w_i . Two vectors are defined as follows.

$$w_i(n) = \begin{cases} 1, & \text{if the element is turned on} \\ 0, & \text{otherwise} \end{cases}, \quad (8)$$

$$w_s(n) = \begin{cases} 0, & \text{if the element is added} \\ 1, & \text{otherwise} \end{cases}. \quad (9)$$

Assuming that the sum of elements making up new sub-array is N , the pattern of new sub-array will be calculated by

$$S(\theta) = \sum_{n=0}^{N-1} w_i(n) I_n e^{-jkx_n \sin \theta}. \quad (10)$$

B. Excitation Optimization

In order to get optimal performance of sub-arrays, elements' excitations should be optimized as well. Assuming D_{ini} is the directivity of sub-array before optimized, the constraints can be expressed as

$$\begin{cases} R\{S(\theta_{max})\} = D_{ini} \\ |S(\theta)| \leq PSLL - q \quad \forall \theta \in \Omega_{SL}, \end{cases} \quad (11)$$

where q is the preset parameter to help finding the lowest PSLL. Assuming sub-arrays' excitation vector is w . To identify elements whose excitations should be optimized, weight vector w_1 are obtained by

$$w_1 = w_r \cap w_i. \quad (12)$$

By vectorizing eqn (10) and adding the weight vector w_1 , constraints in eqn (11) can be rewritten as

$$\begin{cases} R\{A(\theta_0^T w_1 w)\} = D_{ini} \\ A(\theta^T w_1 w) \leq PSLL - q \quad \forall \theta \in \Omega_{SL}. \end{cases} \quad (13)$$

The optimization problem is described as

$$\min_w \|w\|_1 \quad \text{under eqn (13)}. \quad (14)$$

Here l_1 minimization optimization is considered to optimize the excitations of array. To get a better solution, a range of favorable weighting matrices α for a fixed w when w is unknown and iterative computation procedure that alternates between obtained w and redefining new weights are adopted. The optimization problem in i th iteration is

$$\min_{w^i} \sum_{n=0}^{2N-1} \alpha_n^i w_0 w_n \quad \text{under eqn (13)}, \quad (15)$$

$$\alpha_n^i = 1/(|w_n^{i-1}| + \varepsilon) \quad \text{for } i > 1. \quad (16)$$

It should be noticed that excitation optimization is supposed to proceed simultaneously with element selection to find the optimal result. After this process, excitations of original elements getting involved in restructuring sub-arrays are changed, resulting in bad influence to the performance of the whole array. Therefore, original elements not involved in new sub-arrays will be helpful to reduce the deterioration by tweaking their excitations. Here, convex optimization method is also suitable for the operation. Assume that w_h is the weight vector to mark elements to be adjusted, in which 1 represents elements whose excitations will be tweaked and 0 represents elements which remain unchanged. The adjustment problem is described as

$$\min_{w^i} \sum_{n=0}^{2N-1} \alpha_n^i w_h w_n \quad \text{under eqn (13)}. \quad (17)$$

The iteration during the process is the same as eqn (16).

After all procedures proposed above, the design of distributed array with multiple operation modes is finished. Binary codes controlling elements' on-off state are also obtained. The design process is summarized as follows:

1. Add supplemental elements into sub-arrays as much as possible and adjust their locations.
2. Select proper elements to reassemble new sub-arrays.
3. Solve convex problem (15) to get optimal result under arrangement designed in step 2.
4. If the optimal result meet the demand, end the iteration.
5. If not, repeat steps 1 to 3 until the desirable PSLL is obtained or the number of iterations is reached.
6. Get weight vectors to control the working state of elements.
7. Solve convex problem (17) to optimize performance of the whole array.

III. NUMERICAL RESULTS

Here, results of designing the multi-mode distributed array are presented to assess the capability and effectiveness of the hybrid method. Distance between

two sub-arrays is 30λ . The number of elements in the whole array is 50 and both original sub-arrays contain 25 elements.

To keep the scale of reconstructed sub-arrays as the same as the original, the number of elements getting involved in new sub-arrays are artificially preset as 25. During the process, the desired PSLLs of sub-arrays are set as -20 dB and the PSLL of the whole array after sub-array design is hoped to be maintained under -10 dB. In the procedure of element interpolation, the minimum inter-element distance is preset as 0.4λ . According to practical calculation tests, 100 times of PSO iterations and 20 times of convex optimization iterations are enough to get optimal result.

Figure 4 shows the comparisons of original sub-arrays and the optimized reconstructed sub-arrays. Optimization results of elements' positions and excitations of reconstructed two sub-arrays are presented in Table 1 and Table 2, in which the supplementary elements are marked "1" and original elements

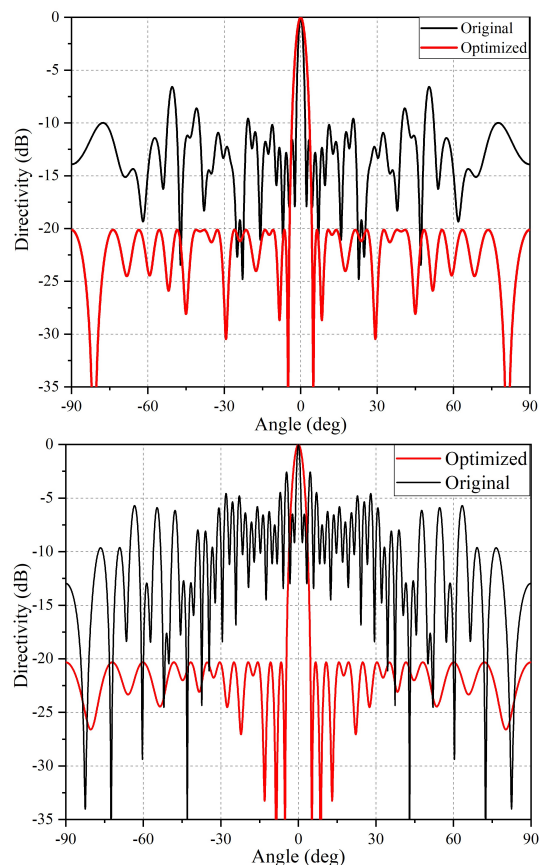


Fig. 4. Comparison of normalized original pattern and optimized pattern of two sub-arrays. First figure is pattern of left sub-array and the other is pattern of right sub-array.

Table 1: Optimized positions and excitations of left sub-array

| No. | Posit. | Excit. | If added |
|-----|--------|--------|----------|
| 1 | 8.50 | 0.0758 | 0 |
| 2 | 9.69 | 0.4898 | 0 |
| 3 | 10.84 | 0.7541 | 0 |
| 4 | 11.24 | 0.2145 | 1 |
| 5 | 11.64 | 1.0805 | 1 |
| 6 | 12.05 | 0.1824 | 0 |
| 7 | 12.47 | 0.8190 | 1 |
| 8 | 12.91 | 0.3002 | 1 |
| 9 | 13.50 | 0.8716 | 0 |
| 10 | 13.99 | 0.2831 | 1 |
| 11 | 14.40 | 0.9619 | 1 |
| 12 | 15.37 | 1.0704 | 1 |
| 13 | 16.21 | 0.9172 | 0 |
| 14 | 17.20 | 1.1829 | 0 |
| 15 | 17.70 | 0.8281 | 1 |
| 16 | 18.12 | 0.9002 | 0 |
| 17 | 18.63 | 0.3515 | 1 |
| 18 | 19.10 | 0.7759 | 1 |
| 19 | 19.57 | 0.0726 | 0 |
| 20 | 20.16 | 0.7240 | 0 |
| 21 | 20.76 | 0.6283 | 1 |
| 22 | 21.23 | 0.4384 | 0 |
| 23 | 21.89 | 0.4468 | 0 |
| 24 | 22.41 | 0.2567 | 0 |
| 25 | 22.95 | 0.6680 | 0 |

Table 2: Optimized positions and excitations of right sub-array

| No. | Posit. | Excit. | If added |
|-----|--------|--------|----------|
| 1 | 43.30 | 0.4787 | 0 |
| 2 | 43.81 | 0.4661 | 0 |
| 3 | 44.44 | 0.3169 | 0 |
| 4 | 44.99 | 0.5370 | 0 |
| 5 | 45.60 | 0.6914 | 0 |
| 6 | 46.42 | 0.9867 | 0 |
| 7 | 47.59 | 0.8062 | 0 |
| 8 | 48.06 | 0.5422 | 1 |
| 9 | 48.51 | 0.9421 | 1 |
| 10 | 48.98 | 0.1754 | 0 |
| 11 | 49.39 | 0.9837 | 1 |
| 12 | 49.80 | 0.0306 | 1 |
| 13 | 50.20 | 1.0501 | 0 |
| 14 | 50.71 | 0.1044 | 1 |
| 15 | 51.17 | 0.8562 | 1 |
| 16 | 51.59 | 0.4388 | 0 |
| 17 | 52.19 | 1.1783 | 1 |
| 18 | 52.61 | 0.3757 | 1 |
| 19 | 53.02 | 1.1090 | 0 |
| 20 | 53.45 | 0.3466 | 1 |
| 21 | 53.85 | 0.9394 | 1 |
| 22 | 54.25 | 0.1085 | 0 |
| 23 | 54.78 | 0.7255 | 1 |
| 24 | 55.20 | 0.0366 | 1 |
| 25 | 55.61 | 0.5992 | 0 |

are marked "0". The unit of element position is D/λ .

For the left sub-array, PSLL of original pattern is -6.5776 dB, while the PSLL of optimized pattern is -20.1245 dB. For the right sub-array, PSLL of original pattern is -2.5718 dB, and PSLL of optimized pattern is -20.3247 dB. Compared with original sub-arrays, performance of reconstructed sub-arrays has significantly improved.

Affected pattern and optimized pattern of whole array are shown in Figure 5. The PSLL of affected pattern is equals to -6.91 dB. By optimizing excitations of other elements, PSLL of the whole array is lowered to -10.12 dB. Optimized results are listed in Table 3. Compared with original distributed array, whose PSLL is -10.6624 dB, result obtained from design method proposed in this paper is slightly higher, which is acceptable.

To research if optimized pattern would be affected when main beam points at different angles, we calculated distributed array's pattern when directions of main beam are 15 deg, 30 deg and 60 deg. Results are shown in Figure 6. It clearly shows that when array's elements

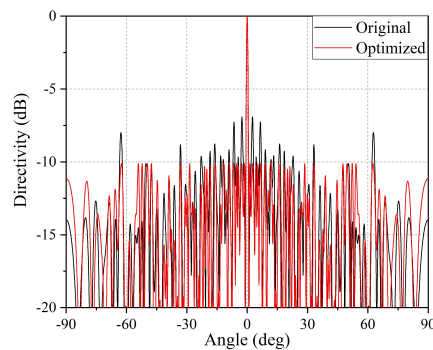


Fig. 5. Comparison of normalized pattern of distributed array. The black line shows the deteriorated pattern of distributed array without second optimization, and the red line shows optimized pattern.

are isotropic, main beam deflection is of no influence on PSLL of optimized distributed array.

The entire process of optimization is based on MATLAB 2018b on Windows 10, with hardware

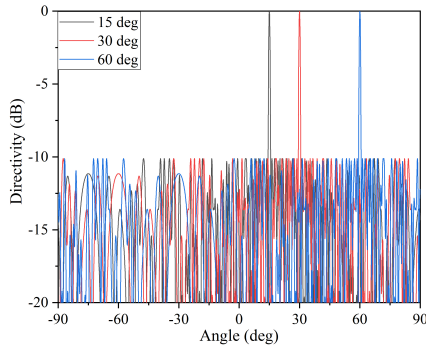


Fig. 6. Normalized pattern of distributed array when its main beam points at 15 deg, 30 deg, and 60 deg respectively.

configuration of Intel Core i7-8700 CPU @ 3.20GHz and 48.0GB RAM. The convex optimization problems discussed above can be solved by professional MATLAB toolbox efficiently, such as CVX Toolbox.

With sufficient sampling point on array's pattern, computation time of a single circulation from step 1 to step 3 is around 55 seconds. Meanwhile, the process in step 7 with 20 iterations needs around 17 seconds.

IV. INFLUENCE OF POSITION AND EXCITATION ERRORS

Considering that all results obtained from the method proposed before are too accurate, when designed distributed array works in different modes, performances of both sub-arrays and whole array will be sensitively affected by errors in elements' positions and excitations, which should be estimated to further analyze the stability of distributed array. Therefore, we will give error analysis on array performance in this section.

Based on optimized results in Tables 1, 2 and 3, random errors obeying Gaussian distribution are added. The mean value μ of Gaussian distribution is set as 0. As for variance, We set 3δ of excitation errors respectively equaling to 0.05, 0.1, and 0.5, and 3δ of position errors respectively equaling to 0.1, 0.5, and 1 (d/λ), where δ is the variance of Gaussian distribution.

Statistical results including mean value, median, and standard deviation are calculated and presented to measure the sensitivity in varying degrees of random errors. Each result is obtained by 100 repetitive calculations considering the particularity of single experiment.

Table 4 shows how far the performance of the whole array is affected by excitation errors, Table 5 and Table 6 show the impacts on sub-arrays. According to these results, with errors becoming larger, performances of whole array and sub-arrays are all deteriorated more seriously. Meanwhile, performances of sub-arrays are more

Table 3: Optimized positions and excitations of right sub-array

| No. | Posit. | Excit. | No. | Posit. | Excit. |
|-----|--------|--------|-----|--------|--------|
| 1 | 0 | 0.2673 | 26 | 42.01 | 4.1974 |
| 2 | 1.00 | 1.3577 | 27 | 42.60 | 1.9057 |
| 3 | 1.81 | 0.7584 | 28 | 43.30 | 0.4787 |
| 4 | 2.82 | 0.2774 | 29 | 43.81 | 0.4661 |
| 5 | 3.62 | 0.8353 | 30 | 44.44 | 0.3169 |
| 6 | 4.35 | 0.4523 | 31 | 44.99 | 0.5370 |
| 7 | 5.58 | 0.6042 | 32 | 45.60 | 0.6914 |
| 8 | 7.07 | 0.6341 | 33 | 46.42 | 0.9867 |
| 9 | 8.50 | 0.0758 | 34 | 47.59 | 0.8062 |
| 10 | 9.69 | 0.4898 | 35 | 48.97 | 0.1754 |
| 11 | 10.84 | 0.7541 | 36 | 50.20 | 1.0501 |
| 12 | 12.05 | 0.1824 | 37 | 51.59 | 0.4388 |
| 13 | 13.50 | 0.8716 | 38 | 53.02 | 1.1090 |
| 14 | 14.91 | 1.7641 | 39 | 54.25 | 0.1085 |
| 15 | 16.21 | 0.9172 | 40 | 55.60 | 0.5992 |
| 16 | 17.20 | 1.1829 | 41 | 56.73 | 2.5817 |
| 17 | 18.12 | 0.9002 | 42 | 57.79 | 1.8934 |
| 18 | 19.57 | 0.0726 | 43 | 59.26 | 0.9398 |
| 19 | 20.16 | 0.7240 | 44 | 60.42 | 0.9546 |
| 20 | 21.23 | 0.4384 | 45 | 61.84 | 0.7879 |
| 21 | 21.89 | 0.4468 | 46 | 63.32 | 0.0533 |
| 22 | 22.41 | 0.2567 | 47 | 64.47 | 0.5555 |
| 23 | 22.95 | 0.6680 | 48 | 65.61 | 0.2845 |
| 24 | 23.51 | 2.1102 | 49 | 66.51 | 0.3983 |
| 25 | 24.01 | 2.3182 | 50 | 67.71 | 3.5303 |

Table 4: Statistical results of influence of performance of whole array affected by excitation errors

| 3σ | Mean | Median | STD |
|-----------|------------|------------|--------|
| 0.05 | -9.5865 dB | -9.5899 dB | 0.0297 |
| 0.1 | -9.5887 dB | -9.5849 dB | 0.0513 |
| 0.5 | -9.2738 dB | -9.3218 dB | 0.2327 |

Table 5: Statistical results of influence of performance of left sub-array affected by excitation errors

| 3σ | Mean | Median | STD |
|-----------|-------------|-------------|--------|
| 0.05 | -19.5693 dB | -19.5953 dB | 0.1879 |
| 0.1 | -18.9642 dB | -19.0321 dB | 0.3873 |
| 0.5 | -15.0161 dB | -15.1379 dB | 1.0454 |

Table 6: Statistical results of influence of performance of right sub-array affected by excitations with errors

| 3σ | Mean | Median | STD |
|-----------|-------------|-------------|--------|
| 0.05 | -19.6902 dB | -19.6956 dB | 0.1983 |
| 0.1 | -19.0137 dB | -19.0164 dB | 0.3547 |
| 0.5 | -14.8955 dB | -14.8412 dB | 1.2031 |

Table 7: Statistical results of influence of performance of whole array affected by position errors

| 3σ | Mean | Median | STD |
|-----------|------------|------------|--------|
| 0.1 | -9.3233 dB | -9.4196 dB | 0.3074 |
| 0.5 | -7.9334 dB | -8.0707 dB | 1.0199 |
| 1 | -7.3616 dB | -7.4806 dB | 0.9001 |

Table 8: Statistical results of influence of performance of left sub-array affected by position errors

| 3σ | Mean | Median | STD |
|-----------|-------------|-------------|--------|
| 0.1 | -16.6991 dB | -16.8060 dB | 1.1429 |
| 0.5 | -10.2251 dB | -10.4522 dB | 1.9255 |
| 1 | -7.9909 dB | -7.4586 dB | 1.5969 |

Table 9: Statistical results of influence of performance of right sub-array affected by position errors

| 3σ | Mean | Median | STD |
|-----------|-------------|-------------|--------|
| 0.1 | -17.0452 dB | -17.2262 dB | 1.2713 |
| 0.5 | -9.9021 dB | -9.8193 dB | 1.7144 |
| 1 | -7.6588 dB | -7.7431 dB | 1.6792 |

easily to be affected. Compared with optimized results in Table 3, it is indicated that the optimized distributed array can tolerate excitation errors to some extent.

Then the statistical results of influence caused by element position errors are displayed in Tables 7, 8 and 9. According to the results, obviously element position error can lead to more serious deterioration of array's performance than excitation error. With the variance of error becoming larger, PSLL of optimized whole array and sub-arrays are rapidly increased, especially for sub-arrays, their PSLs are raised over 10 dB. As shown in these three tables, when 3δ equals to $1(d/\lambda)$, PSLs of whole array and sub-arrays are all higher than -8 dB, the optimized performances of every operating mode are deteriorated.

V. CONCLUSION

In this paper, a hybrid method for designing distributed array with different operating modes is proposed. The working modes are conveniently switched by changing on-off state of elements. After array optimizing, PSLs of sub-arrays can be lowered under -20 dB, making their patterns significantly improved. Meanwhile, performance of the whole array is hardly influenced, PSL of which maintains under -10 dB. Then, array's sensitivity to excitation errors and element position errors are tested, and its tolerance to these two errors are given via statistical results, in which the effectiveness and capability of proposed method are proved. Therefore, the proposed method gives a new solution

of designing distributed array with multiple operating modes, improving performance of distributed array and broadening its applicability on a variety of practical applications.

REFERENCES

- [1] S. Rao, A. Pandya, and C. Oostroot, "Phased array antennas for aircraft applications," *IEEE Indian Conf. Antennas Propag. (InCAP)*, pp. 1-4, Dec. 2018.
- [2] K. Buchanan, C. Flores-Molina, O. Sternberg, D. Overturf, S. Wheeland, and N. Johnson, "Near-field receive beamforming analysis using circularly distributed random arrays," *IEEE Int. Symp. Antennas Propag. USNC/URSI National Radio Science Meeting*, pp. 1591-1592, Jul. 2017.
- [3] P. Chatterjee and J. A. Nanzer, "Using platform motion for improved spatial filtering in distributed antenna arrays," *IEEE Radio Wirel. Symp., RWS*, pp. 253-255, Jan. 2018.
- [4] S. Fang, W. Li, Z. Xue, and W. Ren, "Synthesis of distributed array consisting of two subarrays via hybrid method of differential evolution optimization and convex optimization," *IEEE Antennas Wirel. Propag. Lett.*, vol. 20, no. 2, pp. 125-129, Feb. 2021.
- [5] B. Feng and D. C. Jenn, "Grating lobe suppression for distributed digital subarrays using virtual filling," *IEEE Antennas Wirel. Propag. Lett.*, vol. 12, pp. 1323-1326, 2013.
- [6] S. Fang, Z. Xue, W. Li, and W. Ren, "Grating lobe suppression of planar array with large inter-element spacing by using genetic algorithm," *Int. Conf. Microw. Millim. Wave Technol., ICMMT - Proc.*, pp. 1-3, May 2018.
- [7] P. Chakravorty and D. Mandal, "Grating lobe suppression with discrete dipole element antenna arrays," *IEEE Antennas Wirel. Propag. Lett.*, vol. 15, pp. 1234-1237, 2016.
- [8] S. Jayaprakasam, S. K. A. Rahim, L. C. Yen, and K. R. Ramanathan, "Genetic Algorithm based weight optimization for minimizing sidelobes in distributed random array beamforming," *Int. Conf. Parallel Distrib. Syst., ICPADS*, pp. 623-627, Dec. 2013.
- [9] Y. V. Krivosheev, A. V. Shishlov, and V. V. Denisenko, "Grating lobe suppression in aperiodic phased array antennas composed of periodic sub-arrays with large element spacing," *IEEE Antennas Propag. Mag.*, vol. 57, no. 1, pp. 76-85, Feb. 2015.
- [10] H. Xiaojian, T. Xinhui, Y. Jinyuan, and W. Jianguo, "Distributed genetic algorithm for optimal

- planar arrays of aperture synthesis telescope," *J. Syst. Eng. Electron.*, vol. 15, no. 3, pp. 419-425, Sep. 2004.
- [11] A. Trucco, "Synthesizing wide-band sparse arrays by simulated annealing," in *MTS/IEEE Oceans 2001. An Ocean Odyssey. Conf. Proc. (IEEE Cat. No.01CH37295)*, vol. 2, pp. 989-994, Nov. 2001.
- [12] N. Jin and Y. Rahmat-Samii, "Advances in particle swarm optimization for antenna designs: Real-number, binary, single-objective and multiobjective implementations," *IEEE Trans. Antennas Propag.*, vol. 55, no. 3, pp. 556-567, Mar. 2007.
- [13] D. G. Kurup, M. Himdi, and A. Rydberg, "Synthesis of uniform amplitude unequally spaced antenna arrays using the differential evolution algorithm," *IEEE Trans. Antennas Propag.*, vol. 51, no. 9, pp. 2210-2217, Sep. 2003.
- [14] A. Massa, M. Pastorino, and A. Randazzo, "Optimization of the directivity of a monopulse antenna with a subarray weighting by a hybrid differential evolution method," *IEEE Antennas Wirel. Propag. Lett.*, vol. 5, pp. 155-158, 2006.
- [15] D. Mandal, A. K. Bhattacharjee, and S. P. Ghoshal, "Application of bio-inspired optimization technique for finding the optimal set of concentric circular antenna array," in *World Congr. Nat. Biol. Inspired Comput., NABIC*, pp. 1247-1252, Dec. 2009.
- [16] E. J. Candès, M. B. Wakin, and S. P. Boyd, "Enhancing sparsity by reweighted L1 minimization," *J. Fourier Anal. Appl.*, vol. 14, no. 5-6, pp. 877-905, 2008.
- [17] S. E. Nai, W. Ser, Z. L. Yu, and H. Chen, "Beam-pattern synthesis for linear and planar arrays with antenna selection by convex optimization," *IEEE Trans. Antennas Propag.*, vol. 58, no. 12, pp. 3923-3930, Dec. 2010.
- [18] B. Fuchs, "Synthesis of sparse arrays with focused or shaped beam pattern via sequential convex optimizations," *IEEE Trans. Antennas Propag.*, vol. 60, no. 7, pp. 3499-3503, Jul. 2012.
- [19] Y. Liu, L. Zhang, L. Ye, Z. Nie, and Q. H. Liu, "Synthesis of sparse arrays with frequency-invariant-focused beam patterns under accurate sidelobe control by iterative second-order cone programming," *IEEE Trans. Antennas Propag.*, vol. 63, no. 12, pp. 5826-5832, Dec. 2015.
- [20] J. Kennedy and R. C. Eberhart, "A discrete binary version of the particle swarm algorithm," *Conf. Proc. IEEE Int. Conf. Syst. Man Cybern. Comput. Cybern. Simul.*, vol. 5, pp. 4104-4108, Oct. 1997.
- [21] X. Jia and G. Lu, "A hybrid taguchi binary particle swarm optimization for antenna designs," *IEEE Antennas Wirel. Propag. Lett.*, vol. 18, no. 8, pp. 1581-1585, Aug. 2019.
- [22] W. Weng, W. Ho, and M. Chang, "Optimal design of a planar antenna using binary particle swarm optimization," *IEEE Int. Workshop Electromagn., (iWEM)*, pp. 68-69, Aug. 2014.
- [23] F. Afshinmanesh, A. Marandi, and M. Shahabadi, "Design of a single-feed dual-band dual-polarized printed microstrip antenna using a boolean particle swarm optimization," *IEEE Trans. Antennas Propag.*, vol. 56, no. 7, pp. 1845-1852, Jul. 2008.
- [24] X. Jun and H. Chang, "The discrete binary version of the improved particle swarm optimization algorithm," in *2009 Int. Conf. Manage. Serv. Sci.*, pp. 1-6, Sep. 2009.



Shutao Fang received the B.S. degree in Information and Electronics from Beijing Institute of Technology, Beijing, China, in 2017. He is currently pursuing the Ph.D. degree in Electronic Science and Technology at the same university. His research interests include antenna array analysis and synthesis, array design and optimization method.



Weiming Li received the B.S. degree in Mathematics from the Jiangxi Normal University, Nanchang, China, in 1988, and the Ph.D. degree in electromagnetic field and microwave technology from the Beijing Institute of Technology, Beijing, China, in 2001. He is currently an associate professor with the Electronic Engineering Department, Beijing Institute of Technology. Mr. Li's current research interests are computational electromagnetics, wideband antenna techniques. He has authored or coauthored over 20 papers.



Wu Ren received the B.S. and Ph.D. degrees in electromagnetic field and microwave technology from the Beijing Institute of Technology, Beijing, China, in 1998 and 2003, respectively. Now, Mr. Ren is an associate professor with the School of Information and Electronics, Beijing Institute of Technology. He has authored or coauthored over 60 papers. He has been in charge of more than 15 projects, including National Natural Science Foundation of China (NSFC) and other scientific research projects. His current research interests are computational electromagnetics, microwave and millimeter-wave techniques, electromagnetic compatibility, and metamaterials.



Zhenghui Xue received the B.S. and Ph.D degrees from the School of Information and Electronics, Beijing Institute of Technology. Now, he is a professor, doctoral supervisor and a discipline leader of the Institute of electronic science and technology at the School of Information and Electronics, Beijing Institute of Technology. He has been in charge of more than 20 projects including National Natural Science Foundation of China (NSFC) and other scientific research projects. Mr. Xue has authored or coauthored over 60 papers. His research interests include theory of electromagnetic field, microwave device design, and research of antenna array.

Particle Swarm Optimization of Irregular-shaped Hexagon Patch Antenna for 2.4 GHz WLAN Applications

Wei-Chung Weng and Min-Chi Chang

Department of Electrical Engineering
National Chi Nan University, 301, University Rd., Puli, Nantou 54561, Taiwan
weweng@ncnu.edu.tw, s100323910@mail1.ncnu.edu.tw

Abstract – This study proposes a patch antenna with an irregular shape on a radiating metal patch for 2.4 GHz WLAN applications. The proposed antenna is optimized using our in-house designed particle swarm optimization (PSO) method. By optimizing the coordinates of each vertex of the hexagon radiating metal patch, the PSO algorithm successfully extends the impedance bandwidth and antenna gain without increasing the size, cost, and complexity of the antenna. The optimized antenna has a unique and irregular shape. Measured impedance bandwidth of 7.71% (2.37–2.56 GHz) and peak gain of 2.84 dBi of the proposed irregular-shaped patch antenna are obtained. The simulated and measured results of reflection coefficient, gain, and far-field radiation are found to be in good agreement with each other, hence evidently confirming the validity of the proposed method. The proposed irregular shaped hexagon patch antenna demonstrates superior performance of impedance bandwidth and antenna gain compared to those of the regular-shaped hexagon patch antenna.

Index Terms – antennas, optimization methods, PSO, and wireless LAN.

I. INTRODUCTION

Patch antennas have been widely applied for wireless communication systems. Patch antennas have advantages of light weight, low profile, and easy fabrication. However, one of the drawbacks of patch antennas is their narrow impedance bandwidth (typically 3–5%). To overcome this drawback, broadening band techniques, such as stacking layers, adding parasitic elements, using slots and short pins, and increasing the thickness of the substrate, can be used. However, these broadening band techniques will complicate the antenna configuration.

The shape of the radiating element on conventional patch antennas is usually regular, such as square, rectangle, circle, triangle, and polygon, on a radiating metal patch. However, irregular shapes and curve shapes can provide more flexibility to achieve wide band specifica-

tions. To date, irregular shapes have been less applied to radiators since they are difficult to design.

Transmission-line and cavity models [1] have been commonly used to analyze and design conventional patch antennas. An alternative method is to apply an optimization algorithm in conjunction with a full-wave electromagnetic (EM) simulator to design patch antennas. Using this method, complicated configuration and satisfactory performance of an antenna can be achieved. Many optimization algorithms have been applied to design antennas. In [2] and [3], the numerical electromagnetics code (NEC) was used as the EM simulator for the genetic algorithm (GA) [4, 5] for the design and optimization of a planar monopole antenna and an electrically small wire antenna. In [6], Taguchi's method [7] in conjunction with a method of moments (MoM)-based EM simulator, IE3D, was applied to optimize CPW-fed slot antennas. Particle swarm optimization (PSO) method [8] is another popular and effective algorithm to optimize patch antennas [8–12]. Recently, invasive weed optimization (IWO) algorithm was also applied to optimize a U-slot patch antenna [13] and a meander-shaped MIMO antenna [14].

In this design, we employed our in-house designed PSO method in conjunction with the finite element method (FEM) based EM simulator, HFSS, to design and optimize a regular-shaped hexagon patch antenna. The focus of the proposed approach is to apply the PSO optimizing the coordinates of six vertices of the hexagon radiating patch to extend the impedance bandwidth (BW) and increase gain of the regular-shaped hexagon patch antenna for 2.4 GHz WLAN applications without using any broadening band techniques. In contrast to other optimization works that optimize dimensions of the antenna, the proposed approach, which optimizes the coordinates of vertices, provides more flexibility to design the antenna, since the dimensions and shape of the radiating structure are simultaneously changed by the PSO. This approach does not constrain the shape of the antenna during optimization, and the PSO algorithm is free to produce the optimized antenna.

The optimized antenna will have the characteristics of low cost, compact size, and simple configuration. Therefore, this design can be considered a challenging task. After optimization, the optimized patch antenna will have a unique and irregular shape on the radiating metal patch. The proposed design method successfully extends the impedance bandwidth and antenna gain. Compared with the regular-shaped hexagon patch antenna, the optimized irregular-shaped patch antenna has wider impedance bandwidth and higher antenna gain. Therefore, the proposed irregular hexagon patch antenna can be considered as a novel patch antenna. The optimization settings of the PSO method and characteristics of the proposed irregular-shaped hexagon patch antenna are presented and discussed. Moreover, this study could serve as a helpful example to design a new patch antenna with satisfactory performance using an optimization method.

II. ANTENNA DESIGN AND PSO OPTIMIZATION

Figure 1 shows a regular-shaped hexagon patch antenna, which is denoted as the initial antenna here. The initial antenna is to be fabricated on a cheap FR4 substrate with a thickness of 0.8 mm, a relative dielectric constant of 4.4, and a loss tangent of 0.02. The initial antenna consists of a ground plane printed on the bottom side of the substrate and a metal hexagon patch with six vertices or edges printed on the upper side of the substrate. The center of the antenna structure is located at the origin of the coordinates. The coordinates of the six vertices are located on the x-y plane and measured in millimeters (mm). The initial antenna was

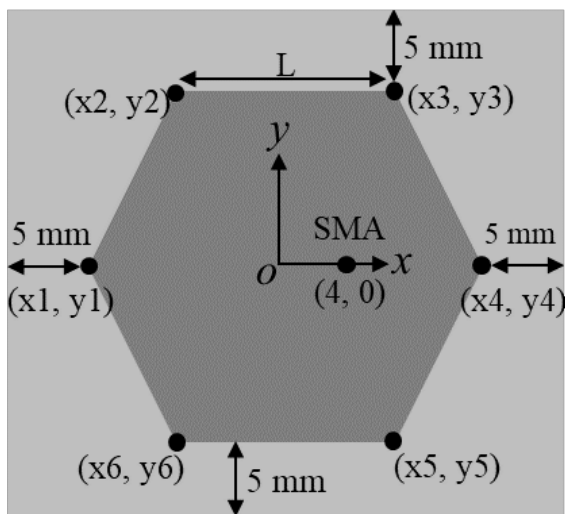


Fig. 1. The geometry of initial antenna with a regular hexagon patch.

Table 1: Coordinates of six vertices for the initial and optimized hexagon patch antenna

| Coordinates (x, y) | Initial (mm) | Optimized (mm) |
|--------------------|------------------|--------------------|
| (x_1, y_1) | $(-18.0, 0)$ | $(-22.81, 6.46)$ |
| (x_2, y_2) | $(-9.0, 15.59)$ | $(-14.03, 10.65)$ |
| (x_3, y_3) | $(9.0, 15.59)$ | $(1.86, 13.69)$ |
| (x_4, y_4) | $(18.0, 0)$ | $(13.96, -3.14)$ |
| (x_5, y_5) | $(9.0, -15.59)$ | $(9.07, -7.74)$ |
| (x_6, y_6) | $(-9.0, -15.59)$ | $(-12.74, -23.67)$ |

designed using the trial-and-error approach. Each edge has a length of L (18 mm) so that the initial antenna can operate in the 2.45 GHz WLAN band with a good impedance matching less than -25 dB. The coordinates of the six vertices for the initial antenna are shown in Table 1.

In our optimization approach, the coordinates of six vertices are to be optimized by using our in-house designed PSO method, which was performed using Matlab version R2016b, to achieve the desired specifications. The main reason of choosing a hexagon-shaped radiating patch instead of a rectangular-shaped radiating patch for the initial antenna is that the hexagon-shaped shape has six vertices, which are two vertices more than the rectangular shape, and can offer more degrees of freedom for optimization. Although a greater number of vertices for the patch shape, such as octagon or decagon, can be utilized, the solution dimensions will also be increased. And it will cause more complexity of the problem. Hence, it is appropriate to use the hexagon shape patch in this design. The optimization range of each vertex is set to be $0.5 L$, which can be considered as the radius of the circle in solution space and hence for searching the optimal antenna shape the center of the circle is located at each vertex. This arrangement prevents the edges of the patch from overlapping. It is worth noting that the initial values of the vertices are only applied to easily create the geometry of the initial antenna in a full-wave electromagnetic (EM) simulator and to set the optimization range for each vertex. It is not necessary to require the initial antenna to perform well. The PSO method will try to find the optimal solution in the given optimization range, since the PSO method is a global optimizer. The interval between each vertex and the edge of the substrate for clearance is set to be 5 mm as shown in Figure 1. This interval setting can ensure that the location of each vertex will not exceed the edge of the substrate. The metal patch is excited by an SMA connector. The location of the SMA connector is fixed at the coordinates $(4, 0)$.

The desired specifications of the proposed hexagon patch antenna are that the magnitude of reflection coefficient of the antenna ($|S_{11}(f)|$) should be less than

-10 dB, while the antenna gain ($\text{gain}(f)$) should be at least 3 dBi at frequencies between 2.35 and 2.55 GHz. Therefore, based on the desired specifications, the fitness function for the PSO method is described as follows:

$$\begin{aligned} \text{Fitness} &= \sum_{f=2.35 \text{ GHz}}^{f=2.55 \text{ GHz}} (|S_{11}(f)| - |S_{11d}|) \left[\frac{1 + \text{sgn}(|S_{11}(f)| - |S_{11d}|)}{2} \right] \Delta f_1 \\ &+ 2 (\text{gain}_d - \text{gain}(f)) \left[\frac{1 + \text{sgn}(\text{gain}_d - \text{gain}(f))}{2} \right] \Delta f_2, \end{aligned} \quad (1)$$

where, Δf_1 and Δf_2 are the frequency interval set to be 0.05 GHz and 0.1 GHz, respectively; $|S_{11d}|$ is -10 dB; is 3 dBi. $\text{sgn}()$ equals 1 if the entry is positive, whereas $\text{sgn}()$ equals -1 if the entry is negative. The fitness value is a parameter related to the antenna to be designed, such as the reflection coefficient and the antenna gain of the antenna. If $|S_{11}(f)|$ is higher than $|S_{11d}|$, computing the fitness value is calculated at frequencies between 2.35 GHz and 2.55 GHz. However, computing the fitness value is not performed when $|S_{11}(f)|$ is less than -10 dB. The same process is applied to the calculation of the fitness value for the antenna gain. Therefore, a smaller fitness value reflects better antenna performance. In the PSO optimization process, the coordinates of each vertex are varied on the basis of the fitness value in each EM simulation performed by HFSS, and the final solution of the present simulation is then obtained after the iterative operation is completed. In the PSO settings, the maximum number of iterations is set to be 50. The reflecting boundary condition [8] and 36 particles were used.

This study focuses on the design and optimization of the proposed hexagon patch antenna. Therefore, for

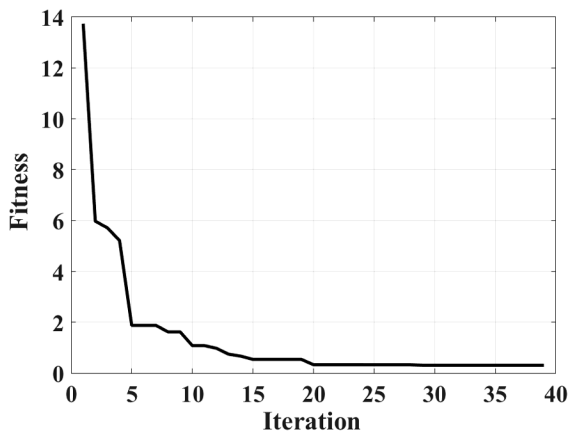


Fig. 2. Fitness curve of the PSO optimization for the hexagon patch antenna design. The embedded figure is the geometry of the optimized patch antenna.

a concise reason, other detailed concepts and procedures of the PSO method are not shown here and they can be found in [8] and [10].

III. RESULTS AND DISCUSSIONS

The antenna optimization was performed on a personal computer with a 2.9 GHz Intel i7 870 CPU and 8 GB of memory. Figure 2 shows the fitness curve of the PSO optimization for the hexagon patch antenna design. The PSO process was terminated after 39 iterations since the fitness value was convergent. The optimized antenna was then fabricated on the FR4 substrate based on the optimized vertices coordinates presented in Table 1. Figure 2 also reveals the geometry of the optimized hexagon patch antenna, which shows that the shape of its metal radiating patch is irregular. The overall antenna size with 5 mm clearance in each direction of the optimized antenna is 46.7 mm (in the x direction) by 47.4 mm (in the y direction). Measured $|S_{11}|$ and radiation patterns were obtained using an Agilent N5230A vector network analyzer (VNA) and an MVG SG-24 antenna measurement system, respectively. Figure 3 exhibits the $|S_{11}|$ curves of the optimized antenna and the initial antenna. The embedded photograph shown in Figure 3 is the optimized patch antenna. Good agreements between measured and simulated $|S_{11}|$ of the two antennas are observed, which demonstrates the validity of the proposed design. The measured impedance bandwidth (below -10 dB) of the optimized antenna is 0.19 GHz (7.71%, 2.37–2.56 GHz), which is 2.6 times wider than that of the initial antenna.

To better understand the operating principle of the optimized antenna, the input impedance Z_{in} and surface currents of the optimized antenna were simulated.

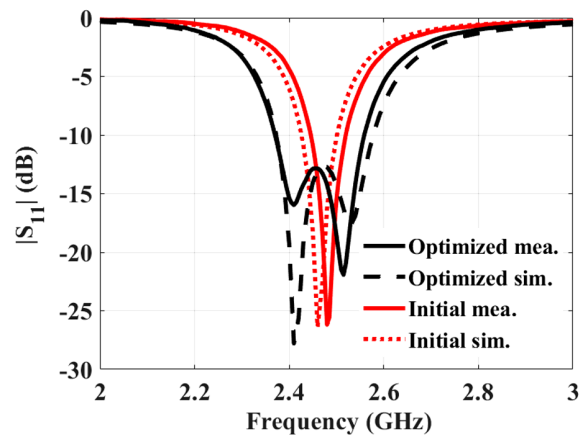


Fig. 3. Reflection coefficients $|S_{11}|$ of the initial and optimized antennas. The embedded photograph is the optimized patch antenna fabricated on the FR4 substrate.

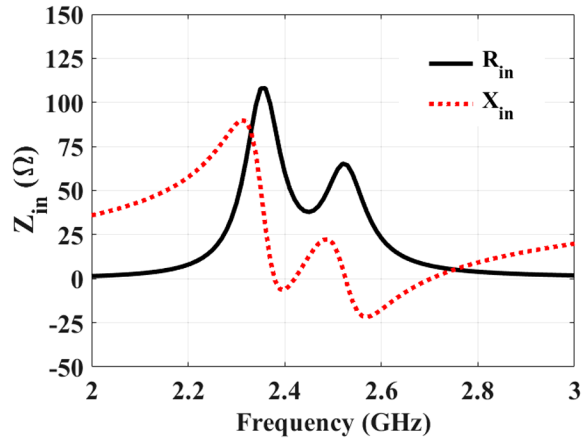


Fig. 4. Simulated input impedance of the optimized antenna.

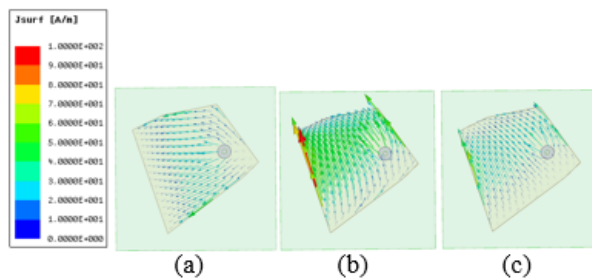


Fig. 5. Simulated surface currents of the optimized antenna at (a) 2.38 GHz, (b) 2.45 GHz, and (c) 2.55 GHz.

Figure 4 shows the input impedance Z_{in} of the antenna, where $Z_{in} = R_{in} + jX_{in}$. Three resonant frequencies (at $X_{in} = 0$) excite at 2.38, 2.42, and 2.52 GHz close to the design frequency at 2.45 GHz, while the real parts (R_{in}) of Z_{in} are near 50 ohms. Hence, the irregular radiating patch excites multi-resonant frequencies around the center frequency of 2.45 GHz resulting in a wide impedance bandwidth.

Figure 5 reveals the simulated surface currents of the optimized antenna at 2.38 GHz, 2.45 GHz, and 2.55 GHz, respectively. There are two modes in the operating band. One mode exists at 2.38 GHz, which is the dominant resonant frequency, and the other one exists around 2.45 GHz to 2.55 GHz. The directions of surface currents in each mode are almost orthogonal to each other.

Figure 6 exhibits the simulated three-dimensional (3D) gain patterns of the initial antenna and the optimized antenna at 2.45 GHz, respectively. Three-dimensional gain patterns of the two antennas are similar to each other. Two antennas have a wide beamwidth and a symmetric pattern in the boresight direction. Figure 7 (a), (b) reveals two-dimensional radiation patterns of the optimized antenna in the x-z and y-z planes, respectively.

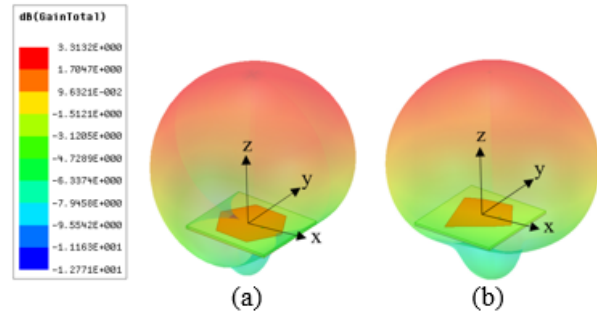


Fig. 6. Simulated three-dimensional gain patterns of (a) initial antenna and (b) optimized antenna at 2.45 GHz.

In addition to 2.45 GHz, two frequency points 2.38 and 2.55 GHz are chosen based on the -10 dB limit of $|S_{11}|$. Again, good agreements between simulated and measured gain patterns at 2.45 GHz are observed, as shown in Figure 7 (a). The measured 3 dB beamwidth is 100 degrees in both the x-z and y-z planes. Meanwhile, the radiation patterns of the optimized antenna do not change much, with the frequencies at 2.38, 2.45, and 2.55 GHz

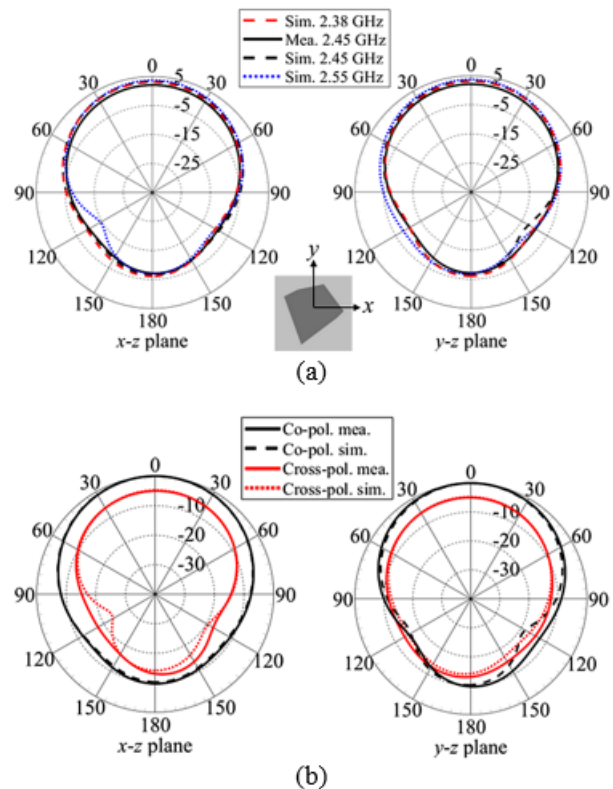


Fig. 7. Radiation patterns of the optimized antenna in the x-z and y-z planes, respectively. (a) Gain patterns with different frequencies and (b) normalized co- and cross-polarization radiation patterns at 2.45 GHz.

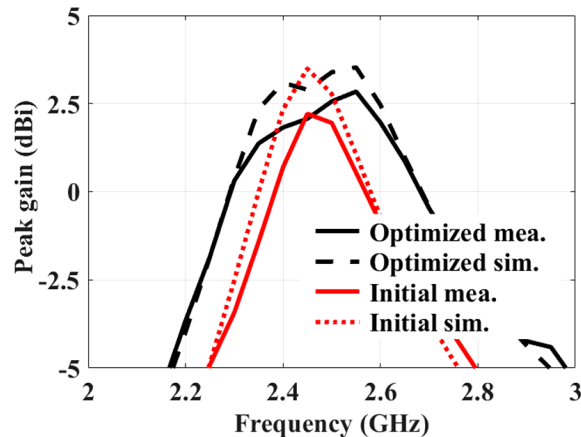


Fig. 8. Measured and simulated peak gains of the initial and optimized antennas.

Table 2: Measured results comparison between initial and optimized hexagon patch antennas

| Antenna | Bandwidth (GHz) | Peak gain (dBi) | Size (mm) |
|-----------|---------------------|-----------------|-------------|
| Initial | 3.02 %,2.44-2.52 | 2.21 | 46.0 × 41.2 |
| Optimized | 7.71 %,2.37-2.56 | 2.84 | 46.7 × 47.4 |

showing stable patterns over the working band.

For the normalized co- and cross-polarization fields of the optimized antenna at 2.45 GHz shown in Figure 7 (b), the level difference between co-polarization and cross-polarization is around 5 dB in the bore sight direction. The cross polarization level in the x-z and y-z planes is higher than that of the regular shape initial antenna. The high level of cross-polarization fields is mainly due to the irregular radiating structure of the antenna [15, 16]. Meanwhile, the polarization conditions are not included in the fitness function shown in (1) when optimizing the proposed antenna. Ideally, the level difference of the two orthogonal fields should be maximal for linear polarization. However, these high cross-polarization fields could be an advantage in WLAN communications [16] and a potential property for designing a circularly polarized antenna.

The measured peak gains of the optimized antenna are 2.07 dBi at 2.45 GHz and 2.84 dBi at 2.55 GHz, which are usually higher than those of the initial antenna, as shown in Figure 8. Additionally, the bandwidth of peak gain of the optimized antenna is also wider than that of the initial antenna, while the optimized antenna almost maintains the same antenna size. Comparisons of measured results, such as impedance bandwidth, peak gain, and overall size of the two antennas at 2.45 GHz, are

tabulated in Table 2. Apparently, the performance of the optimized irregular-shaped hexagon patch antenna outperforms the initial antenna in impedance bandwidth and antenna gain. The proposed optimization approach successfully achieves the desired specifications of the proposed antenna. The optimized irregular-shaped hexagon patch antenna is suitable for 2.4 GHz WLAN applications.

IV. CONCLUSION

This paper presents a novel irregular-shaped hexagon patch antenna for 2.4 GHz WLAN applications. The in-house designed PSO code has been combined with the electromagnetic simulator, HFSS, to design and optimize the proposed antenna. By optimizing the coordinates of the vertices, the proposed irregular-shaped hexagon patch antenna has been designed via the PSO method on the unconstrained shape of the antenna. Optimization settings for the PSO method have been provided. The proposed approach successfully extends the impedance bandwidth and antenna gain without using any other broadening band techniques, such as stacking layers, adding parasitic elements, using slots and shorting pins, and increasing the thickness of the substrate. Therefore, the proposed approach has achieved the characteristics of compact size, low profile, simple structure, and low cost of the proposed antenna. The proposed irregular hexagon patch antenna has exhibited superior performance in impedance bandwidth and antenna gain compared to those of the regular hexagon patch antenna. Meanwhile, the fabrication process of the proposed irregular-shaped patch antenna is the same as that of regular-shaped patch antennas. Hence, there are no extra costs or challenges in the antenna fabrication process. This study also shows that the irregular shapes adopted for antenna designs can provide better antenna performance in the case of the proposed antenna. The proposed irregular-shaped hexagon patch antenna can be a promising candidate for applications in 2.4 GHz WLAN systems.

ACKNOWLEDGMENT

The authors thank the National Center for High-performance Computing for providing software and facilities. This work was supported in part by the MOST under Grant 110-2221-E-260-007.

REFERENCES

- [1] C. A. Balanis, *Antenna Theory Analysis and Design*, 3rd ed., John Wiley & Sons Inc., pp. 816-839, 2005
- [2] A. J. Kerckhoff, R. L. Rogers, and H. Ling, "Design and analysis of planar monopole antennas using a genetic algorithm approach," *IEEE Trans. Antennas Propag.*, vol. 52, no. 10, pp. 2709-2718, Oct. 2004.

- [3] H. Choo, R. L. Rogers, and H. Ling, "Design of electrically small wire antennas using a pareto genetic algorithm," *IEEE Trans. Antennas Propag.*, vol. 53, no. 3, pp. 1038-1046, Mar. 2005.
- [4] R. L. Haupt, "An introduction to genetic algorithms for electromagnetics," *IEEE Antennas Propag. Mag.*, vol. 37, pp. 7-15, Apr. 1995.
- [5] Y. Rahmat-Samii and E. Michielssen, *Electromagnetic Optimization by Genetic Algorithms*. New York: Wiley, 1999.
- [6] W. C. Weng and C. T. M. Choi, "Optimal design of CPW slot antennas using Taguchi's method," *IEEE Trans. Magn.*, vol. 45, no. 3, pp. 1542-1545, Mar. 2009.
- [7] W. C. Weng, F. Yang, and A. Z. Elsherbeni, *Electromagnetics and Antenna Optimization Using Taguchi's Method*, Morgan and Claypool Publishers, pp. 1-84, 2007.
- [8] J. Robinson and Y. Rahmat-Samii, "Particle swarm optimization in electromagnetics," *IEEE Trans. Antennas Propag.*, vol. 52, no. 2, pp. 397-407, Feb. 2004.
- [9] M. C. Tang, X. Chen, M. Li, and R. W. Ziolkowski, "Particle swarm optimized, 3-D-printed, wideband, compact hemispherical antenna," *IEEE Antennas Wireless Propag. Lett.*, vol. 17, pp. 2031-3035, 2018.
- [10] W. C. Weng, "Optimal design of an ultra-wideband antenna with the irregular shape on radiator using particle swarm optimization," *Applied Computational Electromagnetic Society (ACES) Journal*, vol. 27, no 5, pp. 427-434, May 2012.
- [11] W. C. Weng and C. L. Hung, "An H-fractal antenna for multiband applications," *IEEE Antennas Wireless Propag. Lett.*, vol. 13, pp. 1705-1708, 2014.
- [12] L. Lizzi and A. Massa, "Dual-band printed fractal monopole antenna for LTE applications," *IEEE Antennas Wireless Propag. Lett.*, vol. 10, pp. 760-763, 2011.
- [13] S. Karimkashi and A. A. Kishk, "Invasive weed optimization and its features in electromagnetics," *IEEE Trans. Antennas Propag.*, vol. 58, no. 4, pp. 1269-1278, Apr. 2010.
- [14] B. Bahreini, A. Mallahzadeh, and M. Soleimani, "Design of a meander-shaped MIMO antenna using IWO algorithm for wireless applications," *Applied Computational Electromagnetic Society (ACES) Journal*, vol. 25, no 7, pp. 631-638, Jul. 2010.
- [15] A. A. Minasian and T. S. Bird, "Particle swarm optimization of microstrip antennas for wireless communication systems," *IEEE Trans. Antennas Propag.*, vol. 61, no. 12, pp. 6214-6217, Dec. 2013.
- [16] K. Bahadori and Y. Rahmat-Samii, "A miniaturized elliptic-card UWB antenna with WLAN band rejection for wireless communications," *IEEE Trans. Antennas Propag.*, vol. 55, no. 11, pp. 3326-3332, Nov. 2007.



Wei-Chung Weng received the B.S. degree in electronic engineering from National Changhua University of Education, Changhua, Taiwan, in 1993, the M.S. degree in electrical engineering from I-Shou University, Kaohsiung, Taiwan, in 2001, and the Ph.D. degree in electrical engineering from The University of Mississippi, MS, USA, in 2007.

In 2008, he joined the Department of Electrical Engineering, National Chi Nan University, Puli, Taiwan, where he is currently an Associate Professor. From 2017 to 2018, he was a Visiting Scholar at the Department of Electrical Engineering, Colorado School of Mines, Golden, CO, USA. From 2004 to 2007, he was a Graduate Research Assistant in the Department of Electrical Engineering, The University of Mississippi. He has authored or coauthored more than 50 journal articles and conference papers and a book entitled *Electromagnetics and Antenna Optimization Using Taguchi Method* (Morgan & Claypool, 2007). His research interests include antenna and microwave circuit design, computational electro magnetics, electromagnetic compatibility, and optimization techniques in electro magnetics.

Dr. Weng is the Associate Editor-in-Chief for *Applied Computational Electromagnetics Society (ACES) Journal*. He has served many journals as a reviewer for years. He is a Member of ACES, a Senior Member of IEEE, and a Life Member of the Institute of Antenna Engineers of Taiwan (IAET). He was the recipient of the Outstanding Teaching Award of National Chi Nan University in 2013, 2016, and 2019 and the Teaching Contribution Award of the same university in 2020.



Min-Chi Chang Min-Chi Chang was born in Yunlin, Taiwan. He received the B.S. degree in electrical engineering from National United University, Miaoli, Taiwan, in 2009. He is currently working toward the Ph.D. degree in the Department of Electrical Engineering, National Chi Nan University, Puli, Taiwan. His research interests focus on antenna design, computational electro magnetics, and optimization techniques in electro magnetics.

Equivalent Circuit Approximation to the Connector-Line Transition at High Frequencies using Two Microstrip Lines and Data Fitting

Duc Le¹, Nikta Pournoori¹, Lauri Sydänheimo¹, Leena Ukkonen¹, and Toni Björninen²

¹Faculty of Medicine and Health Technology

Tampere University, Tampere, Finland

duc.le, nikta.pournoori, lauri.sydanheimo, leena.ukkonen@tuni.fi

²Faculty of Information Technology and Communication Sciences

Tampere University, Tampere, Finland

toni.bjorninen@tuni.fi

Abstract – This article presents a method of obtaining an equivalent lumped element circuit to model the electrical connector-line transitions in the ultra-high frequency (UHF) band. First, the scattering matrices of two microstrip transmission lines that are otherwise identical but have the physical lengths of d and $2d$ are measured. Next, the theoretical model of the lines cascaded with the connector-line transitions modeled as lumped element circuits is established. The selection of the line lengths to be d and $2d$ results in an over determined system of equations that links the circuit component values to the two-port network parameters of the cascaded system. Finally, the least-squares data fitting procedure yields the best-fit component values. The results show that in our tested scenario, 3-component reactive circuit models well the transitions. Compared with the previous methods, the proposed approach does not require knowledge of the dielectric properties of the substrate of the measured transmission lines. This property integrates the method with our previous work on estimating a microstrip line substrate's relative permittivity and loss tangent. The obtained transition circuit model is also validated through the testing of two quarter-wave transformers. The lines and transformers are implemented on a textile substrate to highlight the method's applicability to wearable textile-based electronics.

Index Terms – microstrip line, electrical transitions, equivalent circuit, data fitting, least-squares method, over determined system, ABCD parameters, SMA connector, textile electronics.

I. INTRODUCTION

The research and development of high-frequency electronic and electromagnetic systems rely heavily on computer-aided engineering to predict and optimize

their electrical response. In this process, the electrical responses are typically observed at the terminals that are internal to the modeled structure. In experiments, however, the signals are recorded through connectors. Although the physical distance to the system's internal terminal through the connector is usually very short, its impact on the high-frequency signal transmission can be appreciable. The discontinuity in waveguide characteristics between the connector and the transmission line configuration internal to the system exacerbates the effect of this non-ideality further [1, 3].

Depending on the target application and the required precision of the numerical prediction of the system's electrical response, the assumption that the connectors have a negligible impact on the high-frequency signal may be acceptable. Alternatively, the effect on the impedance matching, for instance, can be handled through post-manufacturing tuning. On the other hand, the connectors could be characterized with full-wave electromagnetic field simulations, but this is time-consuming and requires accurate knowledge of the structure and materials of the connector.

Finally, the measurement-based de-embedding process could be used to characterize the connectors and subsequently remove their influence on the system's electrical response. However, this requires custom-built test fixtures where the connector is mounted on and then measured with a vector network analyzer (VNA) under the conditions of various pre-determined terminations, such as short, open, and matched load. The terminations, however, are challenging to implement with high precision at high frequencies over significant bandwidths. Moreover, the method is subject to the accuracy of the fixture characterizations, and in general, it is not straightforward to apply in practice [1, 2].

Recent literature proposes several approaches to more effectively characterize the electrical transitions

due to connectors [2–6]. Most of the works ([2], [4–6]) incorporate simulations in the process of identifying the suitable model parameters that match the simulation outcome with the experiments. The authors of [5] used a semi-analytical approach tailored to the studied scenario of a Sub-Minature type A (SMA) connector, including a 90° corner. In the article [6], the authors considered a hybrid lumped-distributed circuit as a coupling model between a transverse electromagnetic (TEM) wave and two types of transmission lines. Still, they used a pre-defined numerical model of the entire SMA connector based on its structure and materials to account for its contribution to the electrical response. The article [2] presents a broadband model for the electrical transition through SMA connectors based on the cascade of several hybrid lumped-distributed circuits. However, the resources and expertise needed for the numerical optimization of the multi-stage circuit model and the implementation and testing of several fixtures are significant.

In contrast to the methods presented in [2], [4]–[6], the authors of [3] proposed a direct approach, which does not involve simulations or data fitting. The method is based on measuring two transmission lines of different lengths and using algebraic manipulations on the governing equation system comprising the cascade of the connectors and the lines to invert it. Consequently, they obtained the two-port network parameters for the electrical transitions due to the connectors. The method was demonstrated up to a notably high frequency of 30 GHz.

However, similar to the works [2], [4]–[6], where the dielectric properties of the test structures need to be accurately known, the approach [3] requires the exact knowledge of the characteristic impedance and propagation constant of the transmission lines as a function of frequency. Still, they are not straightforwardly measured [7, 8]. Similarly, the measurement of the dielectric properties of materials at high frequencies remains a challenging task [9, 10]. As a result, with these approaches, significant time and effort must be dedicated to prior experiments, and combining the results with the characterization of the electrical transitions leads to the accumulation of uncertainty.

This article presents a new method of obtaining an equivalent circuit model to the connector-line transition and demonstrates it in the UHF band. Our method uses two transmission lines, but in contrast to the prior art, it is entirely independent of the EM properties of the materials involved in the lines. Therefore, the line width can be selected considering the ease of manufacturing, e.g., avoiding excessively narrow lines instead of optimizing the width to provide a particular characteristic impedance. These features make the method compelling

for the emerging textile electronics applications, where the high-precision manufacturing and material characterization are even more challenging than the conventional high-frequency electronics applications [9–10]. The proposed method is simple to apply as it requires only the VNA measurement of two transmission lines and data fitting based on the well-known least-squares method. The fitting is based on basic circuit analysis considerations and does not involve circuit or EM field simulations.

II. METHOD

A. Data fitting approach

The method we propose for characterizing the connector-line transitions as lumped element equivalent circuits is two-fold. First, we implemented the two microstrip transmission line structures, MSL1 and MSL2 illustrated in Figure 1, and measured their two-port S-parameters with a VNA. Second, we performed the least-squares type model fitting for several circuit topologies to determine the type of the equivalent circuit and its component values that best represents the connector-line transitions. As illustrated in Figure 1, the two microstrip transmission line structures comprise identical RF connectors and the internal lines L1 and L2 with

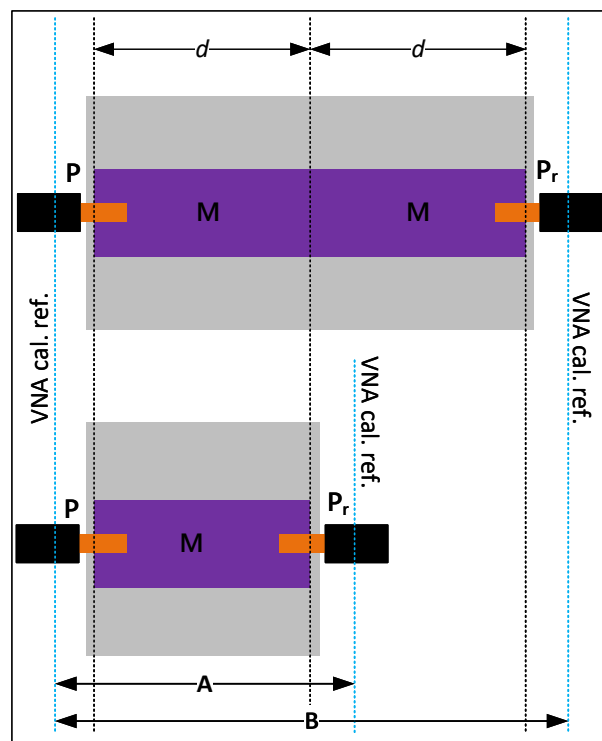


Fig. 1. Top view of the microstrip line structures of the proposed two-line method. The boldface symbols denote the associated chain matrices used in the analysis.

the respective physical lengths of d and $2d$. All the other aspects of the lines, i.e., the substrate and conductor materials and the line widths, are equal. Importantly, we note that, in addition to this, no other properties, such as the substrate dielectric properties, need not be known. Overall, no numerical simulations are involved in the process.

For further analysis, we denote the chain (or ABCD) matrix of L1 as \mathbf{M} so that using the cascading property of the chain parameters [11], [12, pp. 188–190], the chain matrix of L2 is given by the matrix product $\mathbf{M}\mathbf{M}$. Referring to Figure 1, we denote the chain matrix of the connector-to-line transition as $\mathbf{P} = (P_{ij}), i, j = 1, 2$. Given the assumption of identical connectors, we have for the chain matrix of the reverse, i.e., line-to-connector transition,

$$\mathbf{P}_r = \begin{pmatrix} P_{22} & P_{12} \\ P_{21} & P_{11} \end{pmatrix}. \quad (1)$$

Thus,

$$\mathbf{A} = \mathbf{P}\mathbf{M}\mathbf{P}_r \text{ and } \mathbf{B} = \mathbf{P}\mathbf{M}\mathbf{M}\mathbf{P}_r = (\mathbf{P}\mathbf{M})(\mathbf{M}\mathbf{P}_r) \quad (2)$$

from which we can solve

$$\mathbf{P}\mathbf{M} = \mathbf{A}\mathbf{P}_r^{-1} \text{ and } \mathbf{M}\mathbf{P}_r = \mathbf{P}^{-1}\mathbf{A}, \quad (3)$$

so that

$$\mathbf{B} = (\mathbf{A}\mathbf{P}_r^{-1})(\mathbf{P}^{-1}\mathbf{A}). \quad (4)$$

Consequently,

$$\mathbf{P}_r^{-1}\mathbf{P}^{-1} = \mathbf{A}^{-1}\mathbf{B}\mathbf{A}^{-1} \implies \mathbf{P}\mathbf{P}_r = \mathbf{A}\mathbf{B}^{-1}\mathbf{A} \stackrel{\text{def}}{=} \mathbf{U}. \quad (5)$$

This equation links the connector-line transition to the measured two-port network parameters of MSL1 and MSL2 through the matrix \mathbf{U} .

Next, we note that \mathbf{M} , \mathbf{P} , and \mathbf{P}_r are reciprocal two-port networks because they are passive and are expected to comprise only regular bulk conductor and linear isotropic dielectric materials. Therefore, they exhibit determinants equal to one [11]. Moreover, since \mathbf{M} is symmetric, \mathbf{A} , \mathbf{B} , and \mathbf{U} are reciprocal and symmetric. Using these facts we obtain

$$\mathbf{P} = \begin{pmatrix} P_{11} & P_{12} \\ P_{21} & P_{22} \end{pmatrix} = \begin{pmatrix} P_{11} & P_{12} \\ P_{21} & \frac{1+P_{12}P_{21}}{P_{11}} \end{pmatrix}, \quad (6a)$$

$$\mathbf{P}_r = \begin{pmatrix} P_{22} & P_{12} \\ P_{21} & P_{11} \end{pmatrix} = \begin{pmatrix} \frac{1+P_{12}P_{21}}{P_{11}} & P_{12} \\ P_{21} & P_{11} \end{pmatrix}, \quad (6b)$$

$$\mathbf{U} = \begin{pmatrix} U_{11} & U_{12} \\ U_{21} & U_{11} \end{pmatrix} = \begin{pmatrix} U_{11} & U_{12} \\ \frac{U_{11}^2-1}{U_{12}} & U_{11} \end{pmatrix}, \quad (6c)$$

and

$$\mathbf{P}\mathbf{P}_r = \begin{pmatrix} 1+2P_{12}P_{21} & 2P_{11}P_{12} \\ 2P_{21}\frac{1+P_{12}P_{21}}{P_{11}} & 1+2P_{12}P_{21} \end{pmatrix}. \quad (6d)$$

The entry-wise comparison of the left- and right-hand sides of the matrix equation $\mathbf{P}\mathbf{P}_r = \mathbf{U}$ (eqn (5)) reveals that we can express three of the entries of \mathbf{P} as functions of the fourth. However, the number of the independent equations does not suffice for solving all the elements of \mathbf{P} . In other words, $\mathbf{P}\mathbf{P}_r = \mathbf{U}$ defines an over determined

system of equations. By defining $x \stackrel{\text{def}}{=} P_{21}$ as a free variable and applying regular algebraic manipulations on the equation $\mathbf{P}\mathbf{P}_r = \mathbf{U}$, we obtain

$$\mathbf{P}(x) = \begin{pmatrix} \frac{xU_{12}}{U_{11}-1} & \frac{U_{11}-1}{2x} \\ x & \frac{U_{11}^2-1}{2U_{12}x} \end{pmatrix}, \quad (7)$$

where x is an arbitrary non-zero complex number.

Because the connector-line transitions must be passive two-port networks, we hypothesize that they can be approximated as passive lumped element equivalent circuits over a range of frequencies. We denote the chain matrix modeling the forward, i.e., connector-to-line transition, as $\mathbf{Q} = (Q_{ij}), i, j = 1, 2$. Because we model the transition as a passive lumped element circuit, it is a reciprocal two-port network that satisfies $\det(\mathbf{Q}) = 1$ [11]. Consequently, an entry-wise inspection of the matrix equation $\mathbf{P}(x) = \mathbf{Q}$, where $\mathbf{P}(x)$ is given in eqn (7), yields four solutions for the variable x :

$$x_1 = \frac{Q_{11}(U_{11}-1)}{U_{12}}, \quad x_2 = \frac{U_{11}-1}{2Q_{12}}, \quad (8)$$

$$x_3 = Q_{21}, \quad x_4 = \frac{U_{11}^2-1}{2U_{12}Q_{22}}.$$

Ideally, for perfectly identical connectors, in the absence of any measurement uncertainty, and with a perfect agreement between the circuit model and reality, all four equations would yield the same solution for x . In practice, however, this is not possible. Therefore, we seek the component values that bring the four solutions as close as possible to each in the complex plane.

The centroid of the solution quadruplet is given by the mean value

$$C(\omega_k) \stackrel{\text{def}}{=} \frac{1}{4} \sum_{m=1}^4 x_m(\omega_k), \quad (9)$$

where k is the frequency index in the list of N measured frequency points. Now, the least-squares type estimate for the solution can be obtained by identifying the set of circuit component values that minimizes the sum of the squared residuals defined as the sum of the squared distances from the centroid given by

$$E = \sum_{k=1}^N |C(\omega_k) - x_1(\omega_k)|^2 + |C(\omega_k) - x_2(\omega_k)|^2$$

$$+ |C(\omega_k) - x_3(\omega_k)|^2 + |C(\omega_k) - x_4(\omega_k)|^2 \quad (10)$$

$$= \frac{1}{16} \sum_{k=1}^N \sum_{n=1}^4 \sum_{\substack{m=1 \\ m \neq n}}^4 |x_m(\omega_k) - 3x_n(\omega_k)|^2.$$

The implementation of the model fitting for particular circuit topologies will be discussed further in Section III

B. Preconditioning of the measured data

The initial assumption of our analysis is that MSL1 and MSL2 are symmetric two-port networks. Still, in practice this assumption cannot be satisfied precisely due to the measurement uncertainty and manufacturing tolerances. This non-ideality could lead to unexpected propagation of error through the governing system of

non-linear equations. Therefore, we precondition the measured S-matrices of MSL1 and MSL2 by enforcing the symmetry condition (equal diagonal and anti-diagonal entries). Let $\mathbf{S}_{\text{mes}}^{(1)}$ and $\mathbf{S}_{\text{mes}}^{(2)}$ be the measured S-matrices of MSL1 and MSL2, respectively. Now, the entries of the corresponding symmetrized matrices can be estimated as the mean values of the relevant entries of the measured matrices

$$\mathbf{S}^{(i)} \stackrel{\text{def}}{=} \frac{1}{2} \begin{pmatrix} \mathbf{S}_{\text{mes},11}^{(i)} + \mathbf{S}_{\text{mes},22}^{(i)} & \mathbf{S}_{\text{mes},12}^{(i)} + \mathbf{S}_{\text{mes},21}^{(i)} \\ \mathbf{S}_{\text{mes},21}^{(i)} + \mathbf{S}_{\text{mes},12}^{(i)} & \mathbf{S}_{\text{mes},22}^{(i)} + \mathbf{S}_{\text{mes},11}^{(i)} \end{pmatrix}, \quad (11)$$

where $i = 1, 2$. By using $\mathbf{S}^{(1)}$ and $\mathbf{S}^{(2)}$ as the source data for computing the corresponding chain matrices \mathbf{A} and \mathbf{B} for the model fitting procedure through the well-known two-port network parameter transformations [12, p. 192], the numerical values of the entries of \mathbf{U} will necessarily follow the form defined in eqn (6c).

For assessing how much the symmetrized data differs from the original raw measured data at each frequency, we can inspect the value

$$W_i(\omega_k) \stackrel{\text{def}}{=} \frac{1}{\|\mathbf{S}_{\text{mes}}^{(i)}(\omega_k) - \mathbf{S}^{(i)}(\omega_k)\|}, \quad i = 1, 2, \quad (12)$$

where $\|\cdot\|$ denotes the matrix 2-norm [13, Ch. 2]. The larger the value, the better the initial symmetric network assumption holds in the original measured data. Thus, we can use this information to form weights for each frequency point in the model fitting. For this purpose, let N_T be the number of elements of a subset T of the measured frequency indices ($1 \leq N_T \leq N$) such that

$$t_i \leq W_i(\omega_k) \quad \text{for all } k \in T. \quad (13)$$

By this definition, for a particular portion of the measured frequency points, we have $t_i \leq W_i$. For example, if $t_1 = 15$ and $t_2 = 20$, and one would list W_1 and W_2 in the ascending order, then for more than N_T frequency points on the lists, W_1 and W_2 would take values greater than 15 and 20, respectively.

For the measured data that would fulfill the initial assumption of symmetric S-matrix very closely, t_i would take large values throughout the frequency range. Still, in practice t_i may also take very low values at some frequencies. Consequently, these frequencies should have proportionally less influence on the outcome of the model fitting. On the other hand, considering only the frequencies among the highest values of W_i would not be a balanced approach because it could over-emphasize the data from a limited sub-band of the total frequency range of interest in the model fitting. Given this, in the definition of t_i , we consider N_T to be rounded to the integer nearest to $N/2$. This way, considering at least half of the measured frequency points, if $t_1 \leq t_2$, then the measurement of MSL1 was in a relatively closer agreement with the initial assumption than MSL2, and vice versa.

Thus, we can first use the threshold numbers t_1 and t_2 , to compare for which one of the measured structures, the symmetrization yields smaller/larger deviation from the original data considering the whole frequency range. Second, with this information, we can compute the weighted average

$$W(\omega_k) \stackrel{\text{def}}{=} \frac{t_1 W_1(\omega_k) + t_2 W_2(\omega_k)}{t_1 + t_2}, \quad k = 1, 2, \dots, N, \quad (14)$$

which measures the fitness of the initial assumption of MSL1 and MSL2 both being symmetric two-port networks. This approach considers both structures but places proportionally more weight on the one for which the assumption holds true closer for 50% of the measured frequencies. Therefore, we can incorporate values $W(\omega_k)$ as frequency weights in the computation of the sum of the squared residuals for the model fitting as

$$E_W \stackrel{\text{def}}{=} \sum_{k=1}^N W(\omega_k) \sum_{n=1}^4 \sum_{\substack{m=1 \\ m \neq n}}^4 \left| \frac{x_m(\omega_k)}{-3x_n(\omega_k)} \right|^2, \quad (15)$$

where, for simplicity, we have left out the multiplication with the constant scaling factor of 1/16 of the whole sum that appeared in the non-weighted eqn (10).

III. RESULTS FROM THE MODEL FITTING

A. Candidate circuit for the model fitting

Transmission line theory establishes that over an infinitesimal length, a transmission line can be approximated as a lumped element equivalent circuit made up of series inductance and shunt capacitance [12, pp. 48–50]. The component values are determined by the structure and materials of the cross-section of the line. Series resistance and shunt conductance can be included in the model to account for the energy dissipation in the conductor and the dielectric material, respectively. Still, for electrically short lines, they are often negligible. Motivated by this and the fact that the connectors are certain types of transmission line or waveguide structures, we considered lumped element circuits that are combinations of series inductance and shunt capacitance as viable candidates to model the connector-to-line transition. In addition, we limit the study to the six cases listed in Figure 2, which are all the combinations of series inductance–shunt capacitance circuits with the number of components between two and four. The circuit for the reverse transition, i.e., line-to-connector, is obtained by reversing the order of the components.

As an example, we derive here the chain matrix \mathbf{Q} of Circuit 3 by cascading the three two-port networks representing shunt-connected capacitance C_s , series-connected inductance L , and shunt-connected capacitance C_e , in left-to-right order [12, p. 199]:

$$\mathbf{Q} = \begin{pmatrix} 1 & 0 \\ j\omega C_s & 1 \end{pmatrix} \begin{pmatrix} 1 & j\omega L \\ 0 & 1 \end{pmatrix} \begin{pmatrix} 1 & 0 \\ j\omega C_e & 1 \end{pmatrix}. \quad (16a)$$

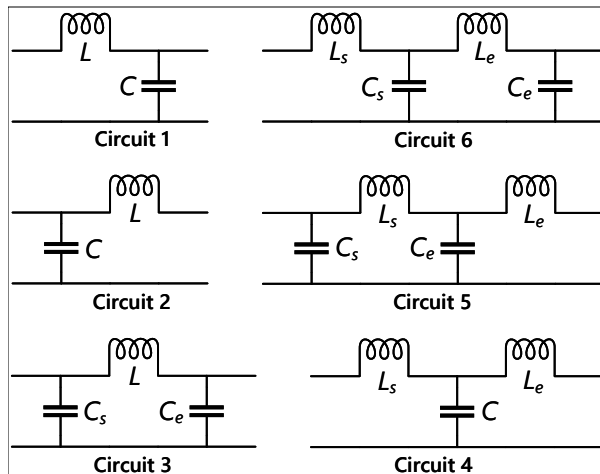


Fig. 2. Circuits considered for modeling the connector-to-line transition. The connector is on the left and the line is on the right side of each circuit.

Regular algebraic manipulations yield

$$\mathbf{Q} = \begin{pmatrix} 1 - \omega^2 LC_e & j\omega L \\ j\omega(C_s + C_e - \omega^2 LC_s C_e) & 1 - \omega^2 LC_s \end{pmatrix}. \quad (16b)$$

By substituting the elements of \mathbf{Q} into eqn (8), we obtain

$$x_1 = \frac{(U_{11} - 1)(1 - \omega^2 LC_e)}{U_{12}} \quad (17a)$$

$$x_2 = \frac{U_{11} - 1}{j2\omega L}, \quad (17b)$$

$$x_3 = j\omega(C_s + C_e - \omega^2 LC_s C_e), \quad (17c)$$

$$\text{and } x_4 = \frac{U_{11}^2 - 1}{2U_{12}(1 - \omega^2 LC_s)}. \quad (17d)$$

These are the four solutions for the variable x that will determine the sum of the squared residuals for any given circuit component values from eqn (15). The chain matrices of all considered circuits and the corresponding solution quadruplets for x are found analogously. We list them in Tables A.1 and A.2 in the Appendix.

B. Implementation and results

In this work, we targeted characterizing the connector-line transitions in the ultra-high frequency (UHF) range. For the experiments, we chose the frequency range from 800 MHz to 3 GHz. It covers several critical modern wireless applications, such as the UHF radio-frequency identification (RFID) at 866/915 MHz bands, L1-signal of the global positioning system (GPS) at 1575.42 MHz, and the industrial, scientific, and medical (ISM) band at 2.45 GHz. To highlight the fact that we do not need to know the electromagnetic properties of the line substrate for applying the proposed two-line method, we implemented the test structures MSL1 and MSL2 on textile type of material, ethylene-propylene-diene-monomer (EPDM) foam [14]. The connectors were

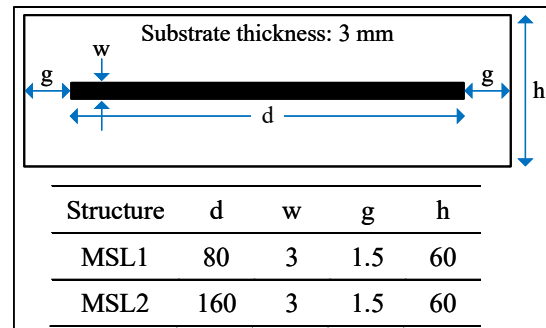


Fig. 3. Top view of the microstrip line structures used in the measurement with the geometrical parameters reported in millimetres.

SMA connectors used in the mounted-through configuration, i.e., the connectors' body soldered to the ground plane and the center pin inserted through the substrate to the line terminal. Figure 3 shows the tested structures and their dimensions.

The S-parameter measurements were conducted with Keysight ENA Network Analyzer E5080A. For implementing the model fitting procedure, we used Mathworks MATLAB version R2018a. The search of the equivalent circuit component values that minimize the sum of the squared residuals was based on the direct computation of the residual given in eqn (15) over a uniformly spanned grid of the component values. The search was initiated considering the range of 0–800 fF and 0–2500 pH for the capacitors and inductors. Figure 4 illustrates the relationship between the component values and the residual error of the model fitting in the case of Circuit 3.

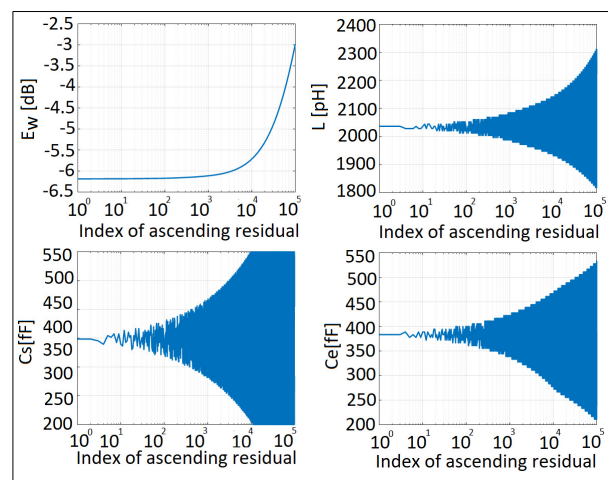


Fig. 4. The residual (top left) from fitting the component values to Circuit 3 in the ascending order and the correspondingly ordered component values L , C_s , and C_e .

Table 1: Component values of the field circuits in [pH] and [fF]

| Circuit | L or L_s | C or C_s | L_e | C_e | E_w [dB] |
|---------|------------|------------|-------|-------|------------|
| 1 | 3724 | 537 | N/A | N/A | 2.64 |
| 2 | 2131 | 964 | N/A | N/A | -0.4 |
| 3 | 2033 | 398 | N/A | 383 | -6.1 |
| 4 | 661 | 763 | 1383 | N/A | -5.5 |
| 5 | 2027 | 397 | 6 | 385 | -6.1 |
| 6 | 71 | 412 | 1973 | 368 | -6.1 |

For the best 10,000 indices, E_w remains within 0.5 dB from the optimum. Thus, the fit is not highly sensitive toward the component values. The minimum-to-maximum variation of the component values for the best 10,000 induces are approximately 350 fF, 200 fF, and 300 pH, for C_s , C_e , and L , respectively. Comparison of the deviations relative to the optimum values indicates that the fit is most sensitive toward L and least sensitive toward C_s .

Table 1 shows the outcome of the model fitting for all the studied circuits. The conclusions we draw from the results are summarized as follows:

1. The residual for Circuits 1 and 2 is large compared with others.
2. Circuit 4 achieved a notably smaller residual than Circuits 1 and 2 but higher than Circuits 3, 5, and 6.
3. Circuits 3, 5, and 6 achieved low and nearly equal residuals.
4. For Circuit 5, the value of the ending inductor (L_e) is small. Thus, Circuit 5 is approximately Circuit 3.
5. For Circuit 6, the value of the starting inductor (L_s) is small. Thus, Circuit 6 is approximately Circuit 3.

Based on these observations, we conclude that Circuit 3 is the best choice for modeling the connector-line transitions for our studied microstrip line structures. Additionally, we note that our analysis converged to the same circuit topology adopted for a coaxial-to-microstrip transition by the authors of [3]. In the next section, we will demonstrate the applicability of the equivalent circuit in two microwave engineering scenarios.

IV. EXPERIMENTAL DEMONSTRATIONS

A. Estimation of the dielectric properties of the line substrate

In our previous work [10], we presented a method of estimating the frequency-dependent relative permittivity and loss tangent of the substrate of a microstrip transmission line. We did this by parameterizing the numerical simulation model of a transmission line as a function of these quantities, sweeping them over a range of values in the simulator, and then fitting the results to the measured data using the least-squares method. Since

obtaining the equivalent circuit models for the connector-line transitions using the approach presented in this work does not require any prior knowledge of the dielectric properties of the substrate material, we can re-use the measured S-parameters of MSL1 and MSL2 for estimating the dielectric properties of the substrate material. This way, we can enhance the accuracy of our previous method [10] in two ways: first, by having the equivalent circuit models of the connector-line transitions, we can remove their parasitic contribution, and second, since we measure two lines as compared with a single one in [10], we can combine the data to reduce uncertainty.

The procedure described in Sections II and III provides the equivalent circuit models for the connector-to-line (chain matrix \mathbf{Q}) and the reverse transition (chain matrix \mathbf{Q}_r), such that we have $\mathbf{P} \approx \mathbf{Q}$ and $\mathbf{P}_r \approx \mathbf{Q}_r$ in eqn (2). Thus, we obtain

$$\mathbf{M} \approx \mathbf{Q}^{-1} \mathbf{A} \mathbf{Q}_r^{-1} \quad \text{and} \quad \mathbf{M} \mathbf{M} \approx \mathbf{Q}^{-1} \mathbf{B} \mathbf{Q}_r^{-1}, \quad (18)$$

which approximate the chain matrices of the transmission lines L1 and L2 internal to the measured structures MSL1 and MSL2 in Figure 1, respectively. Here \mathbf{A} and \mathbf{B} are the chain matrices corresponding with the symmetrized measured S-parameters of MSL1 and MSL2, respectively (eqn (11)).

Following the procedure described in [10], we sweep the values of the relative permittivity and loss tangent of the line substrate in a numerical simulation to find the values that provide the best fit between the simulation and measurement in the least-squares-sense. Moreover, the frequency-dependency of the relative permittivity and loss tangent will be defined by the Svensson/Djordjevic model based on the dielectric relaxation phenomenon [15, 16]. Thus, for parameterizing the simulation model, we sweep the values of the relative permittivity (ϵ_{r0}) and loss tangent (t_{d0}), which define the dielectric properties of the substrate material at the given center frequency of the Svensson/Djordjevic model.

For most engineering applications, the critical features of transmission line circuits and components are the reflection coefficient, signal attenuation due to the internal power loss of the line given by the maximum attainable gain of the two-port network (G_{\max}) [12, pp. 571–575], and the transmission phase angle. In this regard, at each frequency, we can define the following percentage differences

$$e_{i,1}(\omega_k) = \left| \frac{\tilde{S}_{11}^{(i)}(\omega_k) - S_{11}^{(i)}(\omega_k)}{S_{11}^{(i)}(\omega_k)} \right|, \quad (19a)$$

$$e_{i,2}(\omega_k) = \left| \frac{\tilde{G}_{\max}^{(i)}(\omega_k) - G_{\max}^{(i)}(\omega_k)}{G_{\max}^{(i)}(\omega_k)} \right|, \quad (19b)$$

$$\text{and } e_{i,3}(\omega_k) = \left| \frac{\text{Arg}(\tilde{S}_{21}^{(i)}(\omega_k)) - \text{Arg}(S_{21}^{(i)}(\omega_k))}{\text{Arg}(S_{21}^{(i)}(\omega_k))} \right|, \quad (19c)$$

where the accent mark “~” identifies the simulated quantities while the other quantities are derived from \mathbf{M} and \mathbf{MM} . Further, $1 \leq k \leq N$ is the frequency index, and $i = 1, 2$ refers to L1 and L2, respectively. Any of these three percentage differences can be used to form the sum of squared residuals for the model fitting as

$$E_{i,m}(\epsilon_{r0}, t_{d0}) = \sum_{k=1}^N W_i(\omega_k) |e_{i,m}(\omega_k)|^2, \quad (20)$$

where $i = 1, 2$ and $m = 1, 2, 3$. In eqn (20), the weights W_i computed from eqn (11) give relatively more importance to the frequencies where the initial assumption of the symmetric two-port network holds true closer in the original measured data.

To consider $E_{i,1}$, $E_{i,2}$, and $E_{i,3}$ simultaneously, we can combine them as the sum

$$E_i(\epsilon_{r0}, t_{d0}) = \sum_{m=1}^3 \frac{E_{i,m}(\epsilon_{r0}, t_{d0})}{\max_{\{\epsilon_{r0}, t_{d0}\}} E_{i,m}(\epsilon_{r0}, t_{d0})}, \quad (21)$$

where $i = 1, 2$, and the three summands are normalized to their respective maxima over the considered model variations to uniformize their impact on the combined residual E_i . For each line, the pair of values ϵ_{r0} and t_{d0} that minimizes E_i is the least-squares estimate to the substrate material properties. However, for achieving a single estimate for ϵ_{r0} and t_{d0} , we can define the total residual E as the weighted average

$$E(\epsilon_{r0}, t_{d0}) = \frac{E_1 / \left(\min_{\{\epsilon_{r0}, t_{d0}\}} E_1 \right) + E_2 / \left(\min_{\{\epsilon_{r0}, t_{d0}\}} E_2 \right)}{1 / \left(\min_{\{\epsilon_{r0}, t_{d0}\}} E_1 \right) + 1 / \left(\min_{\{\epsilon_{r0}, t_{d0}\}} E_2 \right)}, \quad (22)$$

which gives proportionally more weight to the data measured from the line that yields a smaller residual. The pair of values ϵ_{r0} and t_{d0} that minimizes E is the least-squares estimate to the substrate material properties at the center frequency of the Svensson/Djordjevic model with respect to the measured data from both lines.

We implemented the model fitting routine in Mathworks MATLAB version R2018a using Circuit 3 (Figure 2) with the component values listed in Table 1 to model the connector-line transitions. The frequency range we considered was from 800 MHz to 3 GHz, and the center frequency for the Svensson/Djordjevic dielectric relaxation model was set to 1 GHz. The transmission line simulations were performed using Keysight Advanced Design System (ADS) version 2013.06, where the relaxation model is internally implemented [17]. In the simulation, we swept ϵ_{r0} and t_{d0} over the intervals 1–3 (25 points) and 0.01–0.025 (20 points), respectively. The outcome is presented in Table 2 with a comparison to other works. Overall, the estimated values agree with the reported values in the literature. In comparison with our previous estimate [10], we note that removing the connector-line transitions through eqn (18) brought the estimated dielectric properties closer to the other works.

Table 2: The dielectric properties of EPDM

| Reference | Frequency | Relative permittivity | Loss tangent |
|-----------|-----------|-----------------------|--------------|
| [10] | 1GHz | 1.534 | 0.01 |
| [18] | 900MHz | 1.23 | 0.02 |
| [19] | 868MHz | 1.21 | N/A |
| This work | 1GHz | 1.2821 | 0.0195 |

B. Computer-aided design and design verification of two quarter-wave transformers

Quarter-wave transformer is a typical passive transmission line component that transforms a given load resistance (R_L) to desired input resistance (R_{in}). It comprises a single transmission line section, which has an electrical length of 90° and the characteristic impedance of $Z_0 = \sqrt{R_{in}R_L}$ [12, pp. 246–249]. Thus, optimizing the transformer requires accurate knowledge of the dielectric properties of the line substrate to enable finding the required physical width and length of the line that yields the targeted Z_0 and the electrical length of 90° . As an example, we considered transforming $R_L = 50 \Omega$ $R_{in} = 200 \Omega$ at 1 GHz and 2.45 GHz. For this transformation, we need $Z_0 = 100 \Omega$.

Next, we designed the transformers in Keysight Advanced Design System (ADS) version 2013.06 using the estimated dielectric properties of the substrate presented in the previous sub-section. Figure 5 shows the tested structures and their dimensions. Following the standard engineering practice, we optimized the transformers, excluding the connector-line transition circuits, and inspect their impact later by comparing the simulated and measured performance of the transformers. Figures 6 and 7 show the simulated and measured input impedance. The results show that the simulation without the connector-line transition circuits does not accurately predict the measured input impedance.

In contrast, the simulation, including the transition circuits, is in excellent agreement with the measurement.

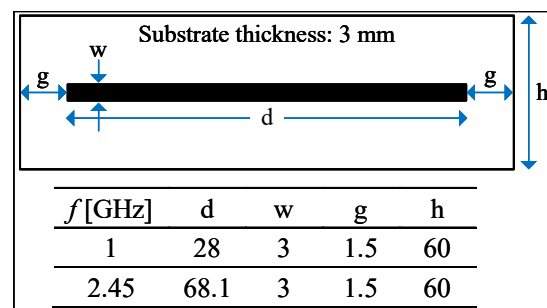


Fig. 5. Top view of the implemented quarter-wave transformers with the geometrical parameters reported in millimeters.

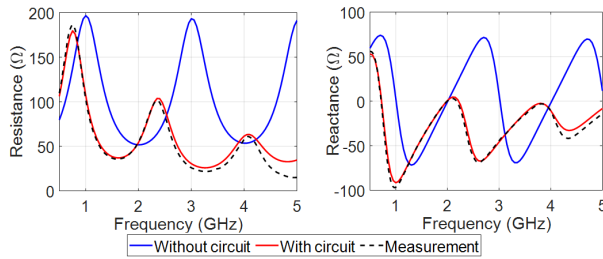


Fig. 6. Input impedance of the quarter-wave transformer operating at 1 GHz.

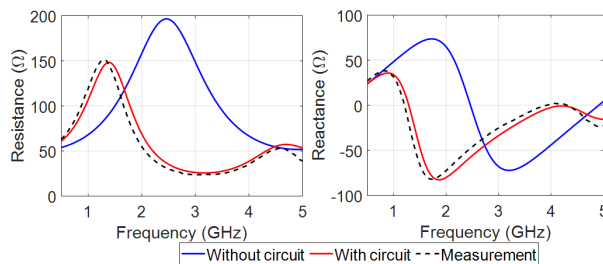


Fig. 7. Input impedance of the quarter-wave transformer operating at 2.45 GHz.

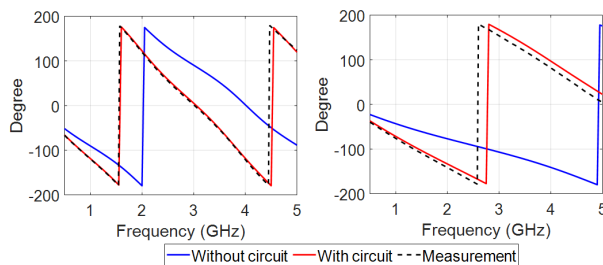


Fig. 8. Electrical length of the quarter-wave transformer operating at 1 GHz (left) and 2.45 GHz (right).

A similar conclusion holds for the measured electrical length of the transformers presented in Figure 8. Furthermore, the agreement in the results extends well beyond the frequency range of 800 MHz to 3 GHz, which was considered in the data fitting to obtain the transition circuit model and the dielectric properties of the substrate. Thus, we conclude that including the connector-line transition equivalent circuit in the simulation model notably improves the computer-aided design process and is readily applicable to the textile electronics application.

V. CONCLUSION

The VNA is a standard tool for the electrical characterization of high-frequency circuits and devices. Despite the device calibration, any residual physical separation between the VNA's calibrated electrical contact point and the actual input terminal of the device under

test causes a residual error in the measurement. We presented a new method of obtaining a lumped element equivalent circuit to model the electrical transition due to the connector. The method is based on the analysis and measurement of two microstrip transmission lines, one of which has precisely double the physical length of the other. It does not require knowledge of the dielectric properties of the line substrate or numerical simulations but relies on basic circuit analysis and the least-squares data fitting.

In the experiments, we found a 3-component reactive circuit to model well the electrical transition due to an SMA connector in a through mount configuration on a 3 mm thick textile substrate in the UHF band. Further, we applied the transition circuit model to augment our previously proposed method of estimating the relative permittivity and the loss tangent of the line substrate. Finally, we tested two quarter-wave transformers. The results showed that including the transition circuits in the computer-aided design process significantly improved the agreement between the simulated and measured results.

In our future work, we will consider replacing the transmission line as a test structure with a reconfigurable transmission line component to produce a larger set of data for the model fitting.

ACKNOWLEDGMENT

D. Le and T. Björninen were funded by Academy of Finland (funding decisions 294616 and 327789). N. Pournoori was funded by the Doctoral Programme in Biomedical Sciences and Engineering under the Faculty of Medicine and Health Technology of Tampere University. Additionally, D. Le was supported by Nokia Foundation, and N. Pournoori was supported by The Finnish Foundation for Technology Promotion (TES) and Nokia Foundation.

REFERENCES

- [1] A. J. Lozano-Guerrero, F. J. Clemente-Fernandez, J. Monzo-Cabrera, J. L. Pedreno-Molina, and A. Diaz-Morcillo, "Precise evaluation of coaxial to waveguide transitions by means of inverse techniques," *IEEE Trans. Microw. Theory Techn.*, vol. 58, no. 1, pp. 229-235, Jan. 2010.
- [2] T. Mandic, M. Magerl, and A. Baric, "Sequential buildup of broadband equivalent circuit model for low-cost SMA connectors," *IEEE Trans. Electromagn. Compatib.*, vol. 61, no. 1, pp. 242-250, Feb. 2019.
- [3] R. Torres-Torres, G. Hernandez-Sosa, G. Romo, and A. Sánchez, "Characterization of electrical transitions using transmission line measurements," *IEEE Trans. Adv. Packag.*, vol. 32, no. 1, pp. 45-52, Feb. 2009.

- [4] S. A. Wartenberg and Qing Huo Liu, "A coaxial-to-microstrip transition for multilayer substrates," *IEEE Trans. Microw. Theory Techn.*, vol. 52, no. 2, pp. 584-588, Feb. 2004.
- [5] H. Zha, D. Lu, W. Wang, and F. Lin, "RF modeling and optimization of end-launch SMA to trace transition," in *Proc. IEEE Electronics Packaging and Technology Conference*, Singapore, pp. 4, 2015.
- [6] T. Mandic, R. Gillon, B. Nauwelaers, and A. Baric, "Characterizing the TEM cell electric and magnetic field coupling to PCB transmission lines," *IEEE Trans. Electromagn. Compatib.*, vol. 54, no. 5, pp. 976-985, Oct. 2012.
- [7] J. A. Reynoso-Hernandez, "Unified method for determining the complex propagation constant of reflecting and nonreflecting transmission lines," *IEEE Microw. Wireless Compon. Lett.*, vol. 13, no. 8, pp. 351-353, Aug. 2003.
- [8] R. B. Marks and D. F. Williams, "Characteristic impedance determination using propagation constant measurement," *IEEE Microw. Guided Wave Lett.*, vol. 1, no. 6, pp. 141-143, Jun. 1991.
- [9] F. Declercq, H. Rogier, and C. Hertleer, "Permittivity and loss tangent characterization for garment antennas based on a new matrix-pencil two-line method," *IEEE Trans. Antennas Propag.*, vol. 56, no. 8, pp. 2548-2554, Aug. 2008.
- [10] D. Le, Y. Kuang, L. Ukkonen, and T. Björninen, "Microstrip transmission line model fitting approach for characterization of textile materials as dielectrics and conductors for wearable electronics," *Int. J. Numerical Modelling Electronic Netw., Dev. Fields*, vol. 32, no. 6, pp. 10, Feb. 2019.
- [11] P. L. D. Peres, I. S. Bonatti, and A. Lopes, "Transmission line modeling: A circuit theory approach," *SIAM Review*, vol. 40, no. 2, pp. 347-352, Jun. 1998.
- [12] David M. Pozar, *Microwave Engineering*, 4th Ed., Hoboken, NJ, USA: Wiley, 2012.
- [13] Gene. H. Golub, *Matrix Computations*, 2nd Ed., Baltimore, MD, USA: Johns Hopkins University Press, 1989.
- [14] Johannes Birkenstock GmbH. Wuppertal, Germany. Available: <http://www.johannesbirkenstock.de/index.html>
- [15] C. Svensson and G. E. Dermer, "Time domain modeling of lossy interconnects," *IEEE Trans. Adv. Packag.*, vol. 24, no. 2, pp. 191-196, May 2001.
- [16] A. R. Djordjevic, R. M. Biljic, V. D. Likar-Smiljanic, and T. K. Sarkar, "Wideband frequency-domain characterization of FR-4 and time-domain causality," *IEEE Trans. Electromag. Compatib.*, vol. 43, no. 4, pp. 662-667, Nov. 2001.
- [17] Keysight Technology, "About dielectric loss models," Keysight Online Knowledge Center 2009. Available: <http://edadocs.software.keysight.com/display/ads2009/Conductor+Loss+Models+in+Momentum>.
- [18] Koski K, Sydänheimo L, Rahmat-Samii Y, and Ukkonen L, "Fundamental characteristics of electro-textiles in wearable UHF RFID patch antennas for body-centric sensing systems," *IEEE Trans. Antennas Propag.*, vol. 62, no. 12, pp. 6454-6462, Dec. 2014.
- [19] S. Manzari, S. Pettinari, G. Marrocco, "Miniaturized and tunable wearable RFID tag for body-centric applications," in *Proc. IEEE Int. Conf. RFID-Technologies and Applications*, Nice, Italy, 5-7 Nov. 2012, pp. 239-243.

APPENDIX

Table A.1 Chain matrices (\mathbf{Q}) of the lumped element equivalent circuits listed in Figure 2

| | |
|-----------|---|
| Circuit 1 | $\begin{pmatrix} 1 & j\omega L \\ j\omega C & 1 - \omega^2 LC \end{pmatrix}$ |
| Circuit 2 | $\begin{pmatrix} 1 - \omega^2 LC & j\omega L \\ j\omega C & 1 \end{pmatrix}$ |
| Circuit 3 | $\begin{pmatrix} 1 - \omega^2 LC_e & j\omega L \\ j\omega (C_s + C_e - \omega^2 LC_s C_e) & 1 - \omega^2 LC_s \end{pmatrix}$ |
| Circuit 4 | $\begin{pmatrix} 1 - \omega^2 L_s C & j\omega (L_s + L_e - \omega^2 L_s L_e C) \\ j\omega C & 1 - \omega^2 C L_e \end{pmatrix}$ |
| Circuit 5 | $\begin{pmatrix} 1 - \omega^2 L_s C_e & j\omega (L_s + L_e - \omega^2 L_s L_e C_e) \\ j\omega (C_s + C_e - \omega^2 L_s C_s C_e) & 1 - \omega^2 (L_e (C_s + C_e) + L_s C_s) + \omega^4 L_s L_e C_s C_e \end{pmatrix}$ |
| Circuit 6 | $\begin{pmatrix} 1 - \omega^2 (L_s (C_s + C_e) + L_e C_e) + \omega^4 L_s L_e C_s C_e & j\omega (L_s + L_e - \omega^2 L_s L_e C_s) \\ j\omega (C_s + C_e - \omega^2 L_e C_s C_e) & 1 - \omega^2 C_s L_e \end{pmatrix}$ |

Table A.2 Solution quadruplets to equation $\mathbf{P}(x) = \mathbf{Q}$, where $\mathbf{P}(x)$ and \mathbf{Q} are given in equation (7) and Table A.1

| | | |
|---------|--|---|
| Circ. 1 | $x_1 = \frac{(1-\omega^2 LC)(U_{11}-1)}{U_{12}}$ $x_3 = j\omega C$ | $x_2 = \frac{U_{11}-1}{j2\omega L}$ $x_4 = \frac{U_{11}^2-1}{2U_{12}}$ |
| Circ. 2 | $x_1 = \frac{U_{11}-1}{U_{12}}$ $x_3 = j\omega C$ | $x_2 = \frac{U_{11}-1}{j2\omega L}$ $x_4 = \frac{U_{11}^2-1}{2U_{12}(1-\omega^2 LC)}$ |
| Circ. 3 | $x_1 = \frac{(U_{11}-1)(1-\omega^2 LC_e)}{U_{12}}$ $x_3 = j\omega (C_s + C_e - \omega^2 LC_s C_e)$ | $x_2 = \frac{U_{11}-1}{j2\omega L}$ $x_4 = \frac{U_{11}^2-1}{2U_{12}(1-\omega^2 LC_s)}$ |
| Circ. 4 | $x_1 = \frac{(U_{11}-1)(1-\omega^2 L_s C)}{U_{12}}$ $x_3 = j\omega C$ | $x_2 = \frac{U_{11}-1}{j2\omega (L_s + L_e - \omega^2 L_s L_e C)}$ $x_4 = \frac{U_{11}^2-1}{2U_{12}(1-\omega^2 L_e C)}$ |
| Circ. 5 | $x_1 = \frac{(U_{11}-1)(1-\omega^2 L_s C_e)}{U_{12}}$ $x_3 = j\omega (C_s + C_e - \omega^2 L_s C_s C_e)$ | $x_2 = \frac{U_{11}-1}{j2\omega (L_s + L_e - \omega^2 L_s L_e C_e)}$ $x_4 = \frac{U_{11}^2-1}{2U_{12}(1-\omega^2 (L_e (C_s + C_e) + L_s C_s) + \omega^4 L_s L_e C_s C_e)}$ |
| Circ. 6 | $x_1 = \frac{(U_{11}-1)(1-\omega^2 (L_s (C_s + C_e) + L_e C_e) + \omega^4 L_s L_e C_s C_e)}{U_{12}}$ $x_3 = j\omega (C_s + C_e - \omega^2 L_e C_s C_e)$ | $x_2 = \frac{U_{11}-1}{j2\omega (L_s + L_e - \omega^2 L_s L_e C_s)}$ $x_4 = \frac{U_{11}^2-1}{2U_{12}(1-\omega^2 C_s L_e)}$ |



Duc Le received the B.Sc. degree in electrical engineering from HCMC University of Technology and Education, Ho Chi Minh City, Vietnam, in 2014 with excellent degree and the M.Sc. degree with distinction in Electrical Engineering from Tampere University of Technology (TAU), Tampere, Finland, in 2018.

Currently, Mr. Le pursues a Ph.D. degree with the Faculty of Medicine and Health Technology, Tampere University, Tampere. His research interests include wireless health technology, wearable antennas, electromagnetic modeling, RF circuits, RFID tags, and low-profile antennas. Mr. Le is a recipient of prestigious awards, including HPY Research Foundation of Elisa and the Nokia Foundation Scholarship.



Nikta Pournoori received the M.Sc. degree in electrical engineering specializing in RF-electronics from the Tampere University of Technology, Tampere, Finland, with distinction in 2018.

Currently, she pursues a Ph.D. degree with the Faculty of Medicine and Health Technology, Tampere University, Tampere. Her research interests include implantable antenna design and sensors for biomedical telemetry systems, RF energy harvesting systems, wireless power transfer, and RFID systems. She is a recipient of prestigious awards, including the Nokia Foundation Scholar-

ship and the Finnish Foundation for Technology Promotion (TES).



Lauri Sydänheimo received the M.Sc. and Ph.D. degrees in electrical engineering from the Tampere University of Technology (TUT), Tampere, Finland. He is currently a Professor with the Faculty of Medicine and Health Technology, Tampere University, Tampere, Finland. He has authored more than 250 publications in radio-frequency identification tag and reader antenna design and wireless system performance improvement. His current research interests include wireless data communication and wireless identification and sensing.



Leena Ukkonen received the M.Sc. and Ph.D. degrees in electrical engineering from the Tampere University of Technology, Tampere, Finland, in 2003 and 2006, respectively. She is currently a Professor with the Faculty of Medicine and Health Technology, Tampere University, Tampere, Finland, and is leading the Wireless Identification and Sensing Systems Research Group. She has authored more than 300 scientific publications in radio-frequency identification (RFID), antenna design, and biomedical and wearable sensors. Her current research interests include RFID antennas, RFID sensors, implantable biomedical systems, and wearable antennas.



Toni Björninen received the M.Sc. and Ph.D. degrees in electrical engineering from Tampere University of Technology (TUT), Tampere, Finland, in 2009 and 2012, respectively.

He works as a University Lecturer at the Faculty of Information Technology and Communication Sciences, Tampere University (TAU), Tampere, Finland. During 2013–2016 he held the post of Academy of Finland Postdoctoral Researcher at TUT and, subsequently, the Academy of Finland Research Fellow post during 2016–2021 at TUT and TAU. He has been a Visiting Postdoctoral Scholar in Berkeley Wireless Research Center at UC Berkeley and

Microwave and Antenna Institute in Electronic Engineering Department at Tsinghua University, Beijing, China. Dr. Björninen's research focuses on microwave technology for wireless health, including implantable and wearable antennas, wireless power transfer, sensors, and RFID-inspired wireless solutions. He is an author of 185 peer-reviewed scientific articles and a Senior Member of the IEEE.

Dr. Björninen serves as an Associate Editor in Applied Computational Electromagnetics Society Journal. Previously, he has been a member of the editorial boards of IEEE Journal of Radio Frequency Identification (2017–2020), IET Electronics Letters (2016–2018) and International Journal of Antennas and Propagation (2014–2018).

Linear Antenna Array Synthesis by Modified Seagull Optimization Algorithm

Erhan Kurt¹, Suad Basbug², and Kerim Guney¹

¹Department of Electrical and Electronics Engineering,
Nuh Naci Yazgan University, Kayseri, 38170, Turkey

²Department of Electrical and Electronics Engineering,
Nevsehir Haci Bektas Veli University, Nevsehir, 50300, Turkey
E-Mail: ekurt@nny.edu.tr; kguney@nny.edu.tr ; suad@nevsehir.edu.tr

Abstract – This paper presents a study of linear antenna array (LAA) synthesis with a seagull optimization algorithm (SOA) to achieve radiation patterns having low maximum sidelobe levels (MSLs) with and without nulls. The SOA is a new optimization technique based on the moving and attacking behaviors of the seagull in the nature. In this study, the original mathematical model of SOA is modified by compensating the exploration and exploitation features to improve the optimization performance. The optimization ability of the modified SOA (MSOA) is tested with seven numerical examples of LAA. In the first three examples, the amplitude values of the array elements are optimized by MSOA whereas the element position values are calculated by MSOA for the last four examples. The numerical results obtained by MSOA are compared with those of different algorithms from the literature. The results reveal that MSOA algorithm is very good at optimizing antenna array parameters to obtain a desired radiation pattern. Additionally, it is seen that MSOA finds better results than the compared algorithms in terms of MSL and single and multiple null depth levels (NDLs). The contribution of the modification of MSOA is shown with a convergence curve to compare with the original one.

Index Terms – antenna array synthesis, linear antenna arrays, maximum sidelobe level, null depth level, seagull optimization algorithm.

I. INTRODUCTION

Antenna arrays are widely used in many communication and radar systems to improve the quality of the signal [1]. The quality of antenna array design significantly affects the performance of these array systems. In recent years, a lot of research has been carried out on the design of antenna arrays to achieve desired radiation pattern synthesis. These parameters are mainly amplitude, phase, and position values of array elements. From this perspective, calculating proper array parameters is

an optimization problem. Therefore, many optimization methods have been used to obtain the desired antenna array radiation pattern. Modifications on the radiation pattern are performed for different purposes. Maximum sidelobe level (MSL) reductions are basically used to diminish the negative effect of the electromagnetic pollution. Additionally, the radiated power can be better focused on the main beam direction with the help of sidelobe reduction. Placing nulls on the radiation pattern are generally used to prevent interferences caused by unwanted signals received from other communication systems.

There are several different geometrical structures of antenna arrays used in the wireless systems such as linear [2–12], circular [13–18], elliptical [19–21], and planar antenna arrays [22, 24]. Linear antenna arrays (LAAs) are very common geometry among the array systems. Several antenna elements are placed in a straight line for this geometry. Because of its simple structure, LAAs are used in a wide range of applications. Hence, the synthesis problem of LAA has received remarkable attention throughout the years. Different optimization methods such as grey wolf optimizer (GWO) [2], moth-flame optimization (MFO) [3], ant lion optimization (ALO) [4], biogeography-based optimization (BBO)[5], tabu search algorithm (TSA) [6], memetic algorithm (MA) [6], genetic algorithm (GA) [6], fitness-adaptive differential evolution algorithm (FiADE) [7], particle swarm optimization (PSO) [7, 8], harmony search algorithm (HSA) [9], backtracking search algorithm (BSA) [10], comprehensive learning particle swarm optimizer (CLPSO) [11], and mean variance mapping optimization (MVMO) [12] have been proposed and employed to solve these synthesis problems. GWO is used to obtain an optimal pattern synthesis of LAA with a reduced MSL and nulls in the desired directions [2]. The side lobes of two LAAs with different sizes are suppressed by MFO algorithm [3]. Sidelobe reduction and null placement are also carried out by means of ALO

evolutionary algorithm in [4]. BBO is employed in [5] to achieve an optimum pattern synthesis with low MSLs by using amplitude as well as phase and position values of array elements. Cengiz and Tokat [6] have employed TSA, MA, and GA to synthesis three LAAs with different number of array elements. FiADE by Chowdhury et al. [7], which is a modified version of the classical DE algorithm, is also used for LAA. The element positions of the LAA elements are determined by using PSO algorithm to get a low MSL and null placement [8]. HSA is also employed to obtain lower MSLs and deeper null levels [9]. Guney and Durmus [10] have used BSA for pattern nulling of LAA. CLPSO, an improved variant of PSO, is employed by Goudos et al. to optimize three different LAAs [11], and MVMO has been applied to LAA synthesis by Guney and Basbug [12].

This paper presents a simple and effective method using the seagull optimization algorithm (SOA) to design an LAA by optimizing only the amplitude and position values of the antenna array elements. Generally, variable attenuators are used to control amplitude values of the array elements in practice. A symmetrical linear array ensures cheaper practical implementations and less computational effort for calculations. If the design is desired to be dynamic, mechanical driving systems are needed to move antenna array elements for the position-only control techniques. The SOA is a novel bio-inspired metaheuristic algorithm proposed by Dhi-man and Kumar [25]. The simple structure of SOA with few parameters makes it applicable to different engineering problems [26–28]. Nine well-known optimization algorithms are chosen for different benchmark comparisons with SOA to validate its performance [25]. The algorithms compared with SOA are GA, differential evolution algorithm, PSO, spotted hyena optimizer, multi-verse optimizer, MFO, sine cosine algorithm, GWO, and gravitational search algorithm [25]. In this paper, a modified version of SOA (MSOA) is employed. The modification is on the step size of SOA that defines the movement behavior of population elements. The original version of SOA has already a linear changing strategy for the parameter of the movement behavior. However, this strategy is limited with a linear decrease. In this paper, a nonlinear changing is proposed to improve search quality of SOA with a better exploration in the early phase of the algorithm and a better exploitation in its later phases. The enhancement that achieved by the modification is shown with two pairs of convergence curve comparisons in the first and second examples.

In this paper, seven different LAA optimization examples are considered. For the first three examples, the amplitude values of LAA are calculated by MSOA to achieve low MSLs. The fourth example includes the optimization of the element positions in the LAA to

reduce sidelobe levels. In the last three examples, element positions are determined by MSOA to locate nulls at the desired directions of the radiation pattern. The results of MSOA are compared with those of GWO [2], MFO [3], ALO [4], BBO[5], MA [6], GA [6], TSA [6], FiADE [7], PSO [8], HSA [9], BSA [10], CLPSO [11], and MVMO [12]. It was shown that MSOA can obtain better results than those of the other compared algorithms.

II. PROBLEM FORMULATION

A symmetrical LAA that consists of even number ($2N$) isotropic elements is illustrated in Figure 1. The array elements are placed symmetrically along the x -axis. Because of the symmetrical structure, LAA has a symmetrical radiation pattern. The elements placed symmetrically can also reduce the computational cost since it is sufficient to optimize only N elements. The array factor of LAA shown in Figure 1 is given by [1]:

$$AF(\theta) = 2 \sum_{n=1}^N I_n \cos(kd_n \sin \theta + \delta_n), \quad (1)$$

where I_n and δ_n are amplitude and phase of n_{th} element, respectively. d_n is the distance from the array center to the n_{th} element. θ is the scanning angle from broadside and k is the wave number which equals to $2\pi/\lambda$. In the first three examples of this study, the main purpose is to obtain optimum amplitude values (I_n) of equally spaced antenna array elements to generate diagrams with low MSL values. For the fourth example, the position values (d_n) of the array elements are optimized by using MSOA to obtain patterns with low MSL values. In the last three examples, in order to achieve radiation patterns with low MSLs and deep nulls placed in desired directions, the element positions (d_n) of the antenna arrays with constant excitations are calculated by means of MSOA.

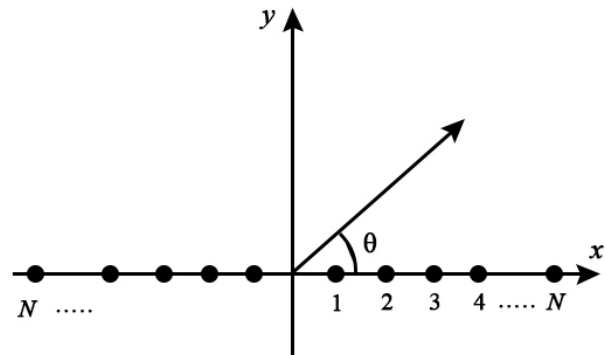


Fig. 1. Geometry of a symmetric linear antenna array with elements positioned along x -axis.

A general fitness function is formulated for the all examples as

$$Fitness = f_{MSL} + f_{FNBW} + f_{NULL}, \quad (2)$$

where f_{MSL} , f_{FNBW} , and f_{NULL} functions are used to suppress the MSL, limit the first null beamwidth (FNBW), and place nulls at desired directions, respectively. The function f_{MSL} can be formulated as follows:

$$f_{MSL} = \int_{\theta_{NULL}}^{\pi/2} E_{MSL}(\theta) d\theta, \quad (3)$$

where θ_{NULL} is the first null point in degree on the right side of the main beam. $E_{MSL}(\theta)$ is formulated as follows to calculate the values that are greater than the desired MSL (MSL_d) on the sidelobes:

$$E_{MSL}(\theta) = \begin{cases} (AF_{dB}(\theta) - MSL_d)^2, & \text{for } AF_{dB}(\theta) > MSL_d \\ 0, & \text{elsewhere,} \end{cases} \quad (4)$$

where

$$AF_{dB}(\theta) = 20 \log(AF(\theta)_{\text{normalized}}). \quad (5)$$

The function f_{FNBW} in (2) can be given by

$$f_{FNBW} = \begin{cases} (FNBW_0 - f_{FNBW_{\max}})^2, & \text{for } FNBW_0 > f_{FNBW_{\max}} \\ 0, & \text{elsewhere,} \end{cases} \quad (6)$$

where $FNBW_0$ and $f_{FNBW_{\max}}$ are the FNBW calculated by MSOA and the desired maximum FNBW, respectively. f_{NULL} in (2) is defined as

$$f_{NULL}(\theta) = \begin{cases} (AF_{dB}(\theta) - NULL_d)^2, & \text{for } AF_{dB}(\theta) > NULL_d \\ 0, & \text{elsewhere,} \end{cases} \quad (7)$$

where $NULL_d$ is the desired NDL at the predetermined null angle.

III. METHOD

A. Seagull optimization algorithm

Seagulls are sea birds with many species with different masses and lengths that can live all over the planet. They are omnivores that feed on insects, fish, lizards, frogs, and eggs. The body of seagulls is generally covered with white plumages. Seagulls are highly intelligent animals. They use their intelligence to find and attack the prey. For example, they use breadcrumbs to attract and hunt the fishes. They can also produce sounds like rain to deceive and catch the earthworms. Generally, seagulls live in colonies and there are two most important behaviors for seagulls in terms of swarming. They migrate to other locations and attack their preys together according to a plan. The migration and hunting behaviors of the seagulls are illustrated in Figure 2 [25]. During the migration, the seagulls instinctively consider three different points. First, they try to avoid collision with other population members. Second, each seagull tends to approach the neighbor that has better fitness. Lastly,

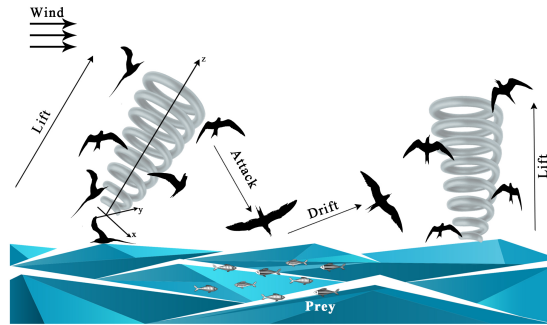


Fig. 2. Schematic models of seagulls for their migration and attacking behaviors.

all seagulls try to sustain their near positions to the seagull which has the best fitness in the flock. When one of the seagulls searches and attacks the prey, it follows a spiral path in the air.

The mathematical model of SOA [25] is based on the pattern of seagull behavior. First of all, the seagulls in the population are distributed randomly as population members through the solution space. The cost function values are calculated for each seagull by using their positions. The cost function as an objective function for the metaheuristic optimization algorithms is the reciprocity of fitness function. In this study, the cost function specialized for antenna array synthesis problems is used.

The migration is a movement of seagulls to find a better hunting place in terms of rich prey populations. The members of seagull population try to avoid a collision with the other members. To model this behavior α parameter is used as follows:

$$\vec{C}_s = \alpha \cdot \vec{P}_s(x), \quad (8)$$

where \vec{C}_s denotes the position of the seagull that tries to prevent from colliding with other search member. \vec{P}_s , x , and α represent the current position of search member, the current iteration, and the movement behavior of the search member in a given search space, respectively. The parameter α is given by

$$\alpha = f_c - \left(x \left(\frac{f_c}{Max_{\text{iteration}}} \right) \right), \quad x = 0, 1, 2, \dots, Max_{\text{iteration}}, \quad (9)$$

where f_c is the starting value for the parameter α . α linearly decreases as iteration progress to 0 as defined in eqn (9). After the collision avoidance mechanism is assured, the search members fly in the direction of the best neighbor. The next position of the search member \vec{M}_s can be written as

$$\vec{M}_s = B \cdot (\vec{P}_{bs}(x) - \vec{P}_s(x)), \quad (10)$$

where B , \vec{P}_{bs} , and \vec{P}_s represent scaling factor, member having the best cost function value, and current position of search member, respectively. B value is randomized

as follows:

$$B = 2 \cdot \alpha^2 \cdot rd, \quad (11)$$

where rd is a pseudo random number in $[0, 1]$. After these processes, the search member changes its position according to the best search member in the population with the following distance formula between the search member and the best member:

$$\vec{D}_s = \left| \vec{M}_s + \vec{C}_s \right|. \quad (12)$$

The attack is performed by the seagulls to the prey through a spiral-shaped track. This path is modeled as the following formula:

$$\vec{P}_s(x) = (\vec{D}_s x' y' z') + \vec{P}_{bs}(x), \quad (13)$$

where $\vec{P}_s(x)$ is the best solution. x' , y' , and z' in eqn are used to generate the spiral motion:

$$\begin{aligned} x' &= r \cos(k) \\ y' &= r \sin(k), \\ z' &= r \cdot k \end{aligned} \quad (14)$$

with

$$r = u e^{kv}, \quad (15)$$

where r , k , u , and v are variable radius of each turn, random number in $[0, 2\pi]$, scaler, and power constants, respectively.

B. Modification on seagull optimization algorithm

This paper also proposes a modification to improve the searching ability of SOA in terms of exploration and exploitation. For this purpose, instead of using eqn (9), α parameter in eqn (8) is decreased gradually by tracing a special nonlinear curve defined as follows:

$$\alpha = f_c \cdot e^{\left(\frac{-7x}{2Max_{iteration}}\right)^2}, \quad x = 0, 1, 2, \dots, Max_{iteration}, \quad (16)$$

The main idea of this modification is providing a better exploration in the beginning of the iteration process and a finer tuning at the rest of the optimization. In order to achieve this aim, the formulation in eqn (16) is used to provide large steps in the beginning and small steps through the rest of the process as shown in Figure 3. The performance contribution of this modification is validated by comparing the convergence curves of SOA and MSOA solutions for the first example in the following section.

IV. NUMERICAL RESULTS

The results of seven LAA synthesis examples obtained by MSOA are presented in this section. The computer hardware used for the simulations is a Core i5 microprocessor with 16 GB RAM and 2.10 GHz clock speed. The MSOA is implemented on MATLAB version R2020a. The number of iterations for each run is set to 1000. The simulation results for the first three examples and the last four examples are obtained within 35–40 and 50–55 seconds, respectively. The algorithm is run 20 times for each example and the best results are evaluated.

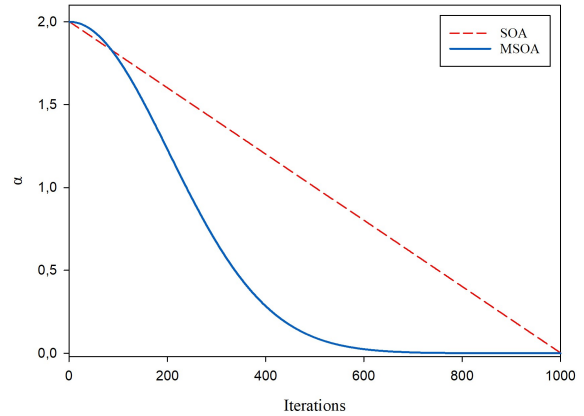


Fig. 3. The changes of α that models the movement behavior of the search member for the MSOA and SOA.

The movement behavior (α) and control frequency (f_c) parameter of MSOA are set to $[2, 0]$ and 2, respectively. The population size is fixed to 30. Schematic models of seagulls for their migration and attacking behaviors.

The synthesis results of MSOA are compared with those of 13 different algorithms, GWO [2], MFO [3], ALO [4], BBO [5], MA [6], GA [6], TSA [6], FiADE [7], PSO [7, 8], HSA [9], BSA [10], CLPSO [11], and MVMO [12]. In the first three examples, MSOA is used to calculate the amplitude values of the array elements to achieve radiation patterns with low MSL values and the results are compared with those of GWO [2], MFO [3], ALO [4], and BBO [5]. For the last four examples, the position values of the array elements are optimized by MSOA and the achieved results are compared with MA [6], GA [6], TSA [6], FiADE [7], PSO [7, 8], HSA [9], BSA [10], CLPSO [11], and MVMO [12].

A. Amplitude only control

In this section, three examples that demonstrate the LAA synthesis with MSL reduction by controlling amplitude-only are given. The phase and interelement position values of the array elements are fixed to $\delta_n = 0$ and $\lambda/2$, respectively. The radiation patterns are plotted by using the best amplitude values achieved by 20 different optimization runs.

For the first example, the synthesis of 10-element LAA is considered to achieve low MSL values. The cost function given by eqn (2) is used to optimize with MSOA. Thanks to the array symmetry, it is enough to consider only five elements to optimize their amplitude values. The radiation pattern with low MSL value obtained by MSOA is given in Figure 4. For a comparison, the radiation patterns of GWO [2], MFO [3], and ALO [4] are also given in Figure 4. The MSL results achieved by MSOA are compared with those of

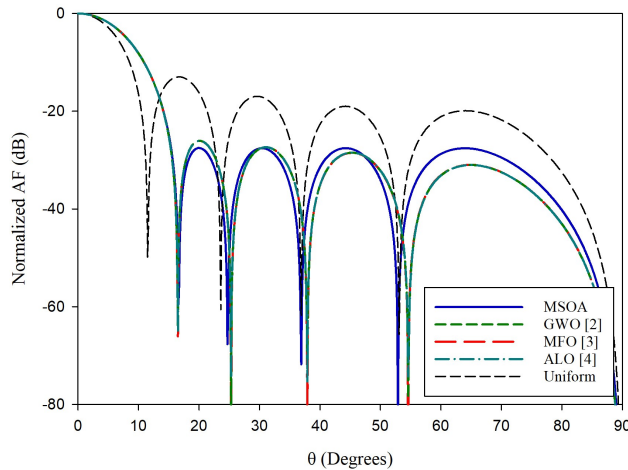


Fig. 4. Radiation patterns optimized by MSOA and the compared algorithms GWO [2], MFO [3], and ALO [4] for 10-element LAA.

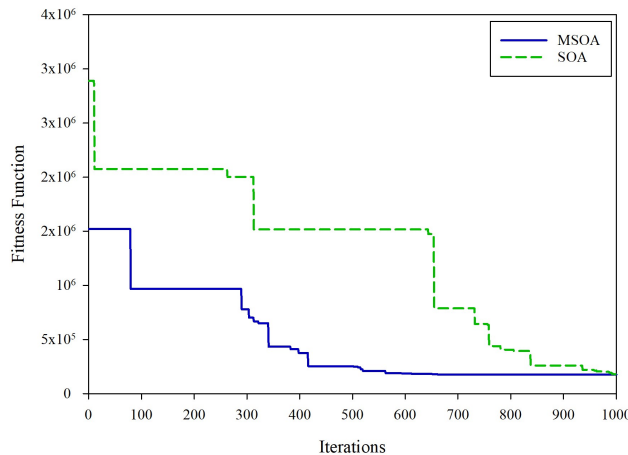


Fig. 5. Convergence curve plots of MSOA and SOA for the first example with 10-element LAA.

GWO [2], MFO [3], ALO [4], and uniform array in Table 1. From the table, it can be said that the MSL value achieved by MSOA is better than those of GWO [2], MFO [3], and ALO [4]. For this example, the convergence curves of the original SOA and MSOA can be seen in Figure 5. It can be concluded from the figure that MSOA can converge faster than the original SOA.

In the second example, a 16-element LAA is optimized by using MSOA method to obtain radiation pattern with low MSL. Figure 6 shows the patterns obtained by MSOA, GWO [2], and MFO [3]. Table 2 presents a comparison between the MSL results achieved by MSOA and those of GWO [2], MFO [3], and uniform array. As shown in Figure 6 and Table 2, the MSL value calculated by MSOA is -40.65 dB which is better than

Table 1: Comparison of the MSL values for 10-element symmetrical LAA design

| Algorithm | MSL (dB) |
|-----------|----------|
| MSOA | -27.52 |
| GWO [2] | -26.05 |
| MFO [3] | -26.07 |
| ALO [4] | -26.08 |
| Uniform | -12.97 |

Table 2: Comparison of the MSL values for 16-element symmetrical LAA design

| Algorithm | MSL (dB) |
|-----------|----------|
| MSOA | -40.65 |
| GWO [2] | -40.50 |
| MFO [3] | -40.25 |
| Uniform | -13.15 |

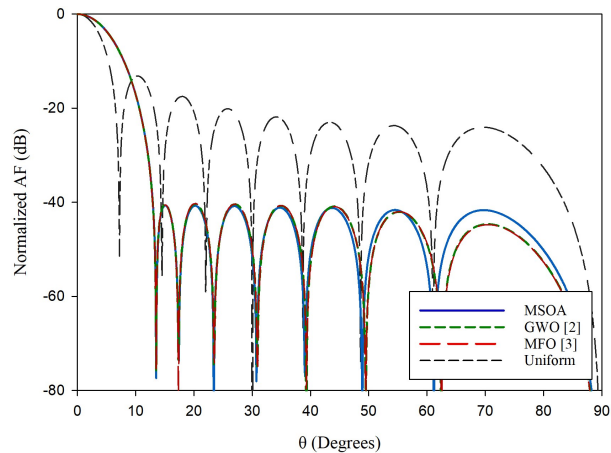


Fig. 6. Radiation patterns optimized by MSOA and compared algorithms GWO [2] and MFO [3] for 16-element LAA.

the other compared values. In Figure 7, the convergence curves of the MSOA suggested in this article and original SOA are illustrated. It is very clear from Figure 7 that the MSOA leads to better convergence and that 1000 iterations are needed to find the optimal solutions.

The difference of the third example from the second example is only that the main beam is limited in a fixed region. The third example is designed for a fair comparison with the similar examples from the literature. The main beam is confined as another optimization constraint in addition to the sidelobe restriction. The radiation pattern obtained by MSOA is shown in Figure 8 in comparison with ALO [4] and BBO [5]. The MSL value obtained by MSOA is given in Table 3. In the same table, the MSL results from the literature obtained by

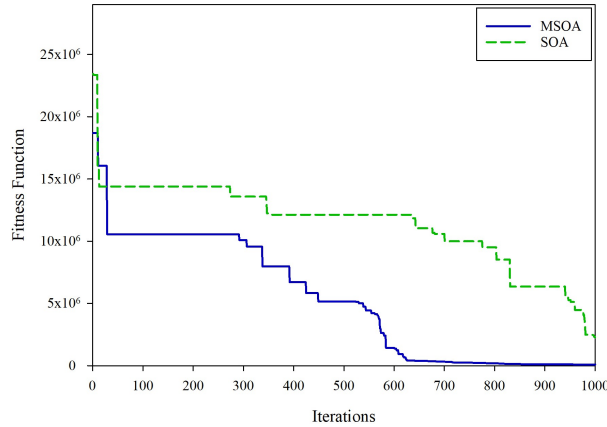


Fig. 7. Convergence curve plots of MSOA and SOA for the second example with 16-element LAA.

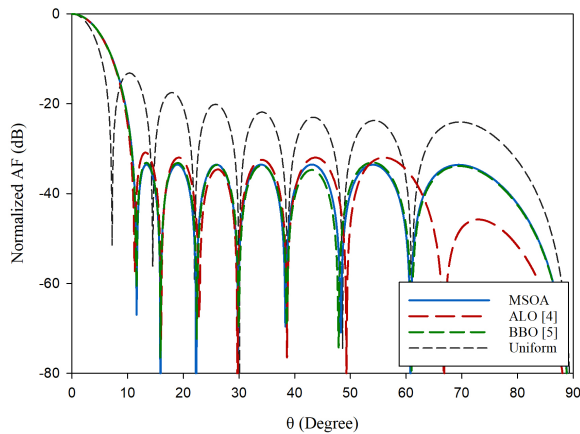


Fig. 8. Radiation patterns optimized by MSOA and compared algorithms ALO [4] and BBO [5] for 16-element LAA with constraint FNBW.

other compared algorithms can also be seen. From the table, it can be noted that MSOA has found better MSL value than ALO [4] and BBO [5] algorithms.

The amplitude values of array elements obtained by MSOA for the patterns in Figures 4, 6, and 8 are listed in Table 4.

B. Position only control

In this section, four examples in which position values of the array elements are adjusted by MSOA are given. The amplitude (I_n) and phase (δ_n) values of the array elements are fixed to 1 and 0° , respectively.

For the fourth example, $2N = 12$ element linear array is considered to achieve a radiation pattern with low MSL values. The cost function given in eqn (2) is used to obtain low MSL by calculating the position values

Table 3: Comparison of the MSL values for 16-element symmetrical LAA with constraint FNBW

| Algorithm | MSL (dB) |
|-----------|----------|
| MSOA | -33.53 |
| ALO [4] | -30.85 |
| BBO [5] | -33.06 |

Table 4: The element amplitudes (I_n) for the array patterns given in Figures 4, 6, and 8

| Number of elements | Optimized amplitude values |
|--------------------|---|
| 10 (Figure 4) | [1.0000 0.8887 0.6944 0.4657 0.3154] |
| 16 (Figure 6) | [1.0000 0.9342 0.8121 0.6543 0.4835 0.3220 0.1888 0.1026] |
| 16 (Figure 8) | [1.0000 0.9466 0.8465 0.7125 0.5606 0.4071 0.2681 0.2055] |

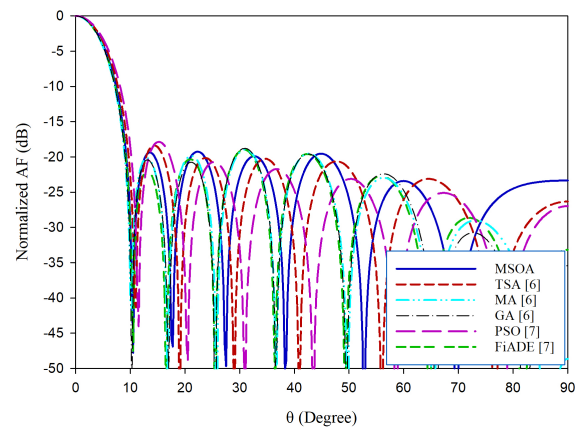


Fig. 9. Radiation patterns optimized by MSOA and compared algorithms TSA [6], MA [6], GA [6], PSO [7], and FiADE [7] for 12-element LAA.

of array elements (d_n). Figure 9 illustrates the array radiation patterns achieved by using MSOA, TSA [6], MA [6], GA [6], PSO [7], and FiADE [7]. Table 5 presents the MSL values of the radiation patterns calculated by MSOA and the other compared algorithms. From Table 5, it is clear that MSOA has achieved a better MSL value than the other algorithms. It is observed that the physical dimension of antenna array synthesized by MSOA in this work is more compact than those of other antenna arrays optimized by TSA [6], MA [6], GA [6], PSO [7], and FiADE [7].

In the fifth example, the element positions of $2N = 22$ element LAA are optimized by means of MSOA to obtain a radiation pattern with nulls at 9° as well as the low MSL values. Figure 10 presents the radiation pattern

Table 5: Comparison of the MSL values for 12-element LAA design by controlling the positions of array elements

| Algorithm | MSOA | TSA [6] | MA [6] | GA [6] | PSO [7] | FiADE [7] |
|-----------|--------|---------|--------|--------|---------|-----------|
| MSL (dB) | -19.25 | -18.40 | -19.10 | -18.77 | -17.90 | -18.96 |

Table 6: MSL and NDL values of the patterns achieved by MSOA and other optimization algorithms for 22-element LAA with null at 9°

| Algorithm | MSOA | TSA [6] | MA [6] | PSO [7] | HSA [9] | BSA [10] |
|---------------|---------|---------|--------|---------|---------|----------|
| MSL (dB) | -23.90 | -17.17 | -18.11 | -20.68 | -23.28 | -23.54 |
| NDL (dB) (9°) | -119.80 | -67.94 | -73.92 | -49.94 | -103.30 | -104.61 |

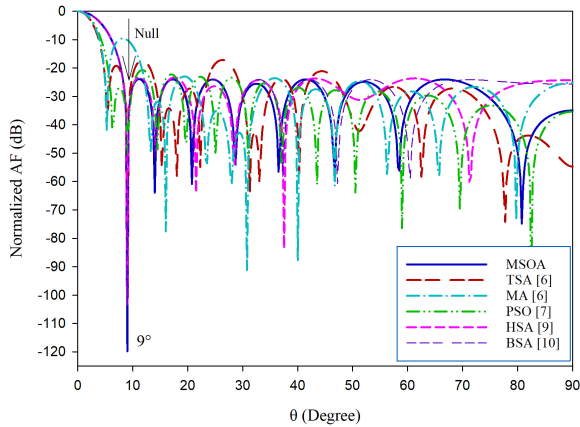


Fig. 10. Radiation patterns with null at 9° optimized by MSOA and compared algorithms TSA [6], MA [6], PSO [7], HSA [9], and BSA [10] for 22-element LAA.

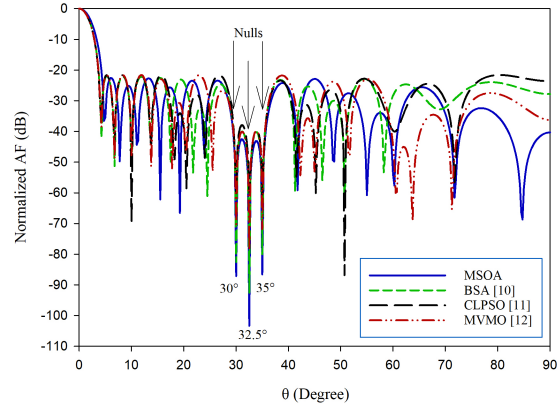


Fig. 11. Radiation patterns with nulls at 30°, 32.5°, and 35° optimized by MSOA and compared algorithms BSA [10], CLPSO [11], and MVMO [12] for 28-element LAA.

calculated by MSOA. The figure also includes the radiation patterns produced by TSA [6], MA [6], PSO [7], HSA [9], and BSA [10]. Table 6 gives the MSL and NDL comparisons between MSOA and the other algorithms. From the table, it can be said that MSOA achieved better MSL and NDL values than the other algorithms.

There are two differences between the fifth and sixth examples. The first one is that the LAA considered in the sixth example is $2N = 28$ element antenna array. As a second difference from the fifth example, in the sixth example, multiple nulls (30°, 32.5°, and 35°) are placed on the radiation pattern instead of a single null. The

resultant array pattern with a low MSL value and multiple nulls at 30°, 32.5°, and 35° is given in Figure 11. The figure also owns the array patterns obtained by BSA [10], CLPSO [11], and MVMO [12]. For a more precise comparison, The MSL and NDL values obtained by MSOA and the other algorithms are tabulated in Table 7. From Table 7, it can be concluded that MSOA has achieved better values than the other algorithms in terms of MSL and NDL parameters.

For the last example, the number of elements is increased to $2N = 32$ to test MSOA for a larger parametric dimension. The target in this example is to achieve a

Table 7: NDL and MSL values of the patterns obtained by MSOA, BSA [10], CLPSO [11], and MVMO [12] for 28-element LAA with nulls at 30°, 32.5°, and 35°

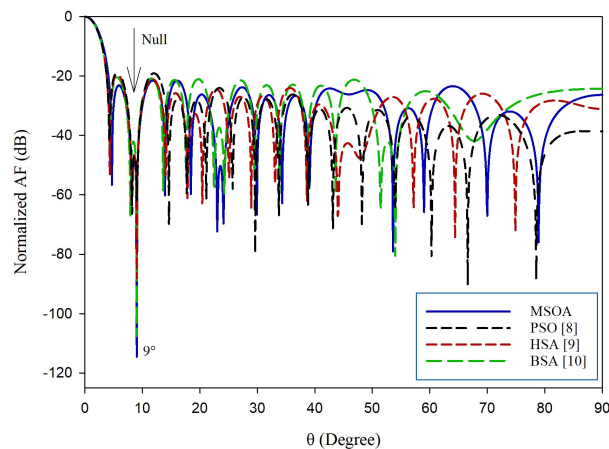
| Algorithm | MSOA | BSA [10] | CLPSO [11] | MVMO [12] |
|------------------|---------|----------|------------|-----------|
| MSL (dB) | -22.57 | -21.90 | -21.63 | -21.63 |
| NDL (dB) (30°) | -87.10 | -82.49 | -60.04 | -70.19 |
| NDL (dB) (32.5°) | -103.30 | -93.59 | -60.01 | -78.79 |
| NDL (dB) (35°) | -86.56 | -80.49 | -60.00 | -71.79 |

Table 8: Comparison of results of different algorithms for 32-element LAA with null at 9°

| Algorithm | MSOA | PSO [8] | HSA [9] | BSA [10] |
|------------------------|---------|---------|---------|----------|
| MSL (dB) | -21.49 | -18.80 | -19.51 | -20.50 |
| NDL (dB) (9°) | -114.50 | -62.20 | -88.08 | -107.50 |

Table 9: Element positions optimized by MSOA for the array patterns given in Figures 9–12

| Number of elements | $[d_1, d_2, \dots, d_N]$ |
|--------------------|--|
| 12 (Figure 9) | [0.4206 1.2580 2.2039 3.1671 4.4298 5.7448] |
| 22 (Figure 10) | [0.2804 0.8094 1.3807 1.9663 2.4326 3.2601 3.7161 4.6507 5.3881 6.5371 7.6742] |
| 28 (Figure 11) | [0.5756 1.0542 2.1406 2.7600 3.7187 4.4164 5.3123 6.1621 7.3610 8.2936 9.3923 11.0114 12.5343 14.0927] |
| 32 (Figure 12) | [0.2150 1.2795 1.9403 2.7564 3.2846 4.2449 5.0273 5.7899 6.4887 7.2680 8.1098 8.9617 10.4744 11.9414 13.7327 15.3084] |

Fig. 12. Radiation patterns with null at 9° optimized by MSOA and compared algorithms PSO [8], HSA [9], and BSA [10] for 32-element LAA.

pattern with a low MSL and a deep NDL at 9° . Figure 12 presents the radiation patterns calculated by MSOA and the other algorithms including PSO [8], HSA [9], and BSA [10] from the literature. Table 8 gives the MSL and NDL values of the radiation patterns given in Figure 12. It is apparent from the figure and the table that MSOA has obtained better MSL and NDL results than the compared algorithms.

The element position values calculated by the MSOA for the patterns given in Figures 9, 10, 11, 12 are tabulated in Table 9.

V. CONCLUSION

In this paper, MSOA, a modified version of SOA, is employed to optimize the array amplitude and position values in order to achieve desired radiation patterns. Seven examples including 10-, 12-, 16-, 22-, 28-, and 32-elements LAA are considered for different purposes. The

main idea in this work is to produce radiation patterns with low MSL and deep NDL values. From the overall results, it can be concluded that MSOA has a good performance to synthesize LAA radiation patterns.

It is also shown that the modification on SOA proposed in this article ensures that the algorithm converges faster. The comparisons with the other algorithms from the literature show that MSOA is a very good competitor in the engineering optimization field. Although MSOA is used for LAAs in this study, it can be apparently said that the algorithm is suitable to be used for the other array geometries such as circular, elliptical, and planar.

REFERENCES

- [1] C. A. Balanis, *Antenna Theory: Analysis and Design*, vol. 1, John Wiley & Sons, 2005.
- [2] P. Saxena and A. Kothari, "Optimal pattern synthesis of linear antenna array using grey wolf optimization algorithm," *International Journal of Antennas and Propagation*, vol. 2016, 2016.
- [3] A. Das, D. Mandal, S. P. Ghoshal, and R. Kar, "Moth flame optimization based design of linear and circular antenna array for side lobe reduction," *International Journal of Numerical Modelling: Electronic Networks, Devices and Fields*, vol. 32, no. 1, e2486, 2019.
- [4] P. Saxena and A. Kothari, "Ant lion optimization algorithm to control side lobe level and null depths in linear antenna arrays," *AEU-International Journal of Electronics and Communications*, vol. 70, no. 9, pp. 1339-1349, 2016.
- [5] A. Sharaqa and N. Dib, "Design of linear and elliptical antenna arrays using biogeography based optimization," *Arabian Journal for Science and Engineering*, vol. 39, pp. 2929-2939, 2014.
- [6] Y. Cengiz and H. Tokat, "Linear antenna array design with use of genetic, memetic and tabu search

- optimization algorithms,” *Progress in Electromagnetics Research C*, vol. 1, pp. 63-72, 2008.
- [7] A. Chowdhury, R. Giri, A. Ghosh, S. Das, A. Abraham, and V. Snasel, “Linear antenna array synthesis using fitness-adaptive differential evolution algorithm,” *In IEEE Congress on Evolutionary Computation*, IEEE, pp. 1-8, July 2010.
- [8] M. M. Khodier and C. G. Christodoulou, “Linear array geometry synthesis with minimum side-lobe level and null control using particle swarm optimization,” *IEEE Transactions on Antennas and Propagation*, vol. 53, no. 8, pp. 2674-2679, 2005.
- [9] K. Guney and M. Onay, “Optimal synthesis of linear antenna arrays using a harmony search algorithm,” *Expert Systems with Applications*, vol. 38, no. 12, pp. 15455-15462, 2011.
- [10] K. Guney and A. Durmus, “Pattern nulling of linear antenna arrays using backtracking search optimization algorithm,” *International Journal of Antennas and Propagation*, vol. 2015, 2015.
- [11] S. K. Goudos, V. Moysiadou, T. Samaras, K. Siakavara, and J. N. Sahalos, “Application of a comprehensive learning particle swarm optimizer to unequally spaced linear array synthesis with sidelobe level suppression and null control,” *IEEE Antennas and Wireless Propagation Letters*, vol. 9, pp. 125-129, 2010.
- [12] K. Guney and S. Basbug, “Linear antenna array synthesis using mean variance mapping method,” *Electromagnetics*, vol. 34, no. 2, pp. 67-84, 2014.
- [13] K. Guney and S. Basbug, “Null synthesis of time-modulated circular antenna arrays using an improved differential evolution algorithm,” *IEEE Antennas and Wireless Propagation Letters*, vol. 12, pp. 817-820, 2013.
- [14] A. Sharaqa and N. Dib, “Circular antenna array synthesis using firefly algorithm,” *International Journal of RF and Microwave Computer-Aided Engineering*, vol. 24, no. 2, pp. 139-146, 2014.
- [15] A. E. Taser, K. Guney, and E. Kurt, “Circular antenna array synthesis using multiverse optimizer,” *International Journal of Antennas and Propagation*, vol. 2020, 2020.
- [16] G. Ram, D. Mandal, R. Kar, and S. P. Ghoshal, “Circular and concentric circular antenna array synthesis using cat swarm optimization,” *IETE Technical Review*, vol. 32, no. 3, pp. 204-217, 2015.
- [17] P. Civicioglu, “Circular antenna array design by using evolutionary search algorithms,” *Progress in Electromagnetics Research B*, vol. 54, pp. 265-284, 2013.
- [18] A. S. Zare and S. Baghaiee, “Application of ant colony optimization algorithm to pattern synthesis of uniform circular antenna array,” *Applied Computational Electromagnetics Society Journal*, vol. 30, no. 8, pp. 810-818, 2015.
- [19] N. Dib, A. Amaisreh, and A. Al-Zoubi, “On the optimal synthesis of elliptical antenna arrays,” *International Journal of Electronics*, vol. 106, no. 1, pp. 121-133, 2019.
- [20] A. A. Amaisreh, N. Dib, and A. S. Al-Zoubi, “The optimal synthesis of concentric elliptical antenna arrays,” *International Journal of Electronics*, vol. 107, no. 3, pp. 461-479, 2020.
- [21] V. V. S. S. Chakravarthy, P. S. R. Chowdary, N. Dib, and J. Anguera, “Elliptical antenna array synthesis using evolutionary computing tools,” *Arabian Journal for Science and Engineering*, pp. 1-18, 2021.
- [22] A. Smida, R. Ghayoula, A. Ferchichi, A. Gharsallah, and D. Grenier, “Planar antenna array pattern synthesis using a taguchi optimization method,” *International Journal on Communications Antenna and Propagation*, vol. 3, no. 3, pp. 158-162, 2013.
- [23] L. Zhang, Y. C. Jiao, B. Chen, and H. Li, “Orthogonal genetic algorithm for planar thinned array designs,” *International Journal of Antennas and Propagation*, vol. 2012, 2012.
- [24] T. Sallam and M. A. Attiya, “Different array synthesis techniques for planar antenna array,” *Applied Computational Electromagnetics Society Journal*, vol. 34, no. 5, pp. 716-723, 2019.
- [25] G. Dhiman and V. Kumar, “Seagull optimization algorithm: Theory and its applications for large-scale industrial engineering problems,” *Knowledge-Based Systems*, vol. 165, pp. 169-196, 2019.
- [26] Y. Cao, Y. Li, G. Zhang, K. Jermsittiparsert, and N. Razmjooy, “Experimental modeling of PEM fuel cells using a new improved seagull optimization algorithm,” *Energy Reports*, vol. 5, pp. 1616-1625, 2019.
- [27] H. Jiang, Y. Yang, W. Ping, and Y. Dong, “A Novel Hybrid Classification Method Based on the Opposition-Based Seagull Optimization Algorithm,” *IEEE Access*, vol. 8, pp. 100778-100790, 2020.
- [28] G. Lei, H. Song, and D. Rodriguez, “Power generation cost minimization of the grid-connected hybrid renewable energy system through optimal sizing using the modified seagull optimization technique,” *Energy Reports*, vol. 6, pp. 3365-3376, 2020.



Erhan Kurt was born in 1988. He received his M.Sc. from the Erciyes University in 2014. He is currently employed as a research assistant at Nuh Naci Yazgan University, Electrical and Electronics Engineering Department and working towards the Ph.D. degree in Electrical and Electronics Engineering at Erciyes University. His research interests include antennas and antenna arrays.



Suad Basbug received the B.S. and Ph.D. degrees in electrical and electronics engineering from Erciyes University, Kayseri, in 2008 and 2014, respectively. He has been an assistant professor at Nevsehir Haci Bektas Veli University since 2014. His current research interests

include antennas, antenna arrays, conformal antennas, evolutionary algorithms, and computational electromagnetics.



Kerim Guney received the B.S. degree from Erciyes University, in 1983, the M.S. degree from Istanbul Technical University, in 1988, and the Ph.D. degree from Erciyes University, in 1991, all in electronics engineering. He is now a Professor in the Department of Electrical and Electronics Engineering, Nuh Naci Yazgan University. His research interests include antennas, planar transmission lines, optimization algorithms, and target tracking.

Pattern Analysis of Conformal Antenna Arrays via the Characteristic Modes of Isolated Elements

Yuanchen Zeng, Shuo Zhang, and Shunxi Lou

Key Laboratory of Electronic Equipment Structure Design of Ministry of Education
Xidian University, Xi'an, Shaanxi 710071, China
zengyuanchen123@qq.com, 18392027103@163.com, sxlou_xd@126.com

Abstract – A simple pattern analysis method is presented for conformal antenna arrays, considering mutual coupling effects based on the characteristic modes of isolated elements. There are many methods to analyze the performance of conformal antenna arrays, but they seldom provide a clear insight into the coupling mechanism. Thus, the overall characteristic modes of the conformal array are calculated from the characteristic modes of the isolated elements and coordinate transformation, which are different from the traditional modal analysis for the entire array. And the radiation field of the conformal array is given. The modal coupling matrix which depends on the structural parameters and relative pose of conformal elements is used to characterize the mutual coupling effect between elements and explain the coupling mechanism from the perspective of the characteristic currents. Finally, the effectiveness and efficiency of the proposed method is verified by some numerical examples.

Index Terms – conformal array, characteristic modes, coordinate transformation, mutual coupling.

I. INTRODUCTION

Conformal antennas have been widely used in radio communications and avionics due to their remarkable electrical performance [1, 2]. Although a wealth of research has been conducted on the analysis of the electromagnetic characteristics of conformal antennas, they rarely provide a clear insight into the coupling mechanism. The simple and intuitive understanding of the mutual coupling mechanism of the conformal array antenna is helpful for further research on its radiation performance [1].

State-of-the-art conformal array analysis methods fall under two main categories. The first one includes use of an approximate method that can serve as a reference for the pattern analysis of the conformal array. The simplest technique is to apply coordinate transformation into the classical pattern theory [3]. But it can only be applied in the absence of mutual coupling effects. The

diffraction ray solution based on the uniform geometrical theory of diffraction (UTD) is often used to analyze conformal arrays on the surface of typical geometric models [1, 4]. UTD can analyze the pattern of conformal antenna arrays including mutual coupling, as a high-frequency approximation method, but it has higher requirements for antenna operating frequency. The higher the frequency is, the more accurate the result is. In addition, there are special analysis methods for conformal antennas, such as cavity model analysis which is discussed in detail. The microstrip antenna is equivalent to a 2×2 dipole array. The relative pose of dipoles is optimized to simplify pattern analysis of the conformal antenna [5]. The other strategy includes an accurate analysis method that can help achieve the pattern analysis according to the electromagnetic field control equation and boundary conditions, for example, the method of moments (MoM) is used to model the conformal array as a whole system and analyze its radiation performance [6].

However, the methods mentioned above do not show a clear insight into the coupling mechanism. Thus, an analysis method to explore the coupling relationship between radiating elements has been developed. For example, domain decomposition method combined with generalized scattering matrix (GSM) is used to analyze the conformal antennas performance on aircraft [7]. Although the overall generalized scattering matrix of an array constructed by the GSM of an isolated radiating element can accurately characterize the electromagnetic field of the array, it requires that the minimum spheres surrounding each radiating element do not overlap [8]. Further analysis is needed if the minimum spheres overlap [9, 10], which increases the difficulty of using this method in conformal arrays. And the coupling matrix given in GSM can only represent the position relationship of elements. That is, the coupling mechanism is mathematically perfect, but its physical insight is still unclear. A method of sampling the far-field data of an isolated element to analyze the mutual interactions between the array elements in the far-field region is mentioned [11]; it does not present

a clear physical insight into the coupling mechanism either.

The theory of characteristic modes has been widely used in antenna analysis and design lately, providing a physical explanation for the antenna radiation mechanism [12–14]. However, these applications treat the array or antenna as a multiport network and analyze the entire array or antenna. Then we do a research on the characteristic modes of a planar array; the correlation model between the electrical performance parameters of an entire array and the characteristic modes of isolated radiating elements is established [15]. On the basis of this solution strategy and coordinate transformation, this paper analyzes the overall characteristic modes of conformal arrays and describes the coupling mechanism from the perspective of the characteristic currents clearly.

This paper is organized as follows. First, the radiation pattern and modal coupling matrix of conformal antenna arrays are analyzed based on the characteristic modes of an isolated conformal element and coordinate transformation. Second, the proposed method is verified by some numerical experiments. Finally, some meaning conclusions are given.

II. THEORY

A. Process of the proposed method

Figure 1 shows the flow chart of the application of the proposed method to the analysis of conformal arrays. The process is as follows.

Firstly, the characteristic modes of the isolated radiating element are analyzed using the MoM. Secondly, the modal coupling matrix is constructed based on the modal current and coordinate transformation. On this basis, the modal excitation matrix is constructed, and then the modes are superimposed to obtain the radiation field of the conformal array.

B. Modal excitation matrix of a conformal array

Considering a conformal array on an arbitrary surface in the coordinate system shown in Figure 2 (a), refer to the planar array [15], under the influence of other elements, the incident field of the n th element can be expressed as

$$\mathbf{E}_n^{\text{inc}} = \mathbf{E}_{dn} + \sum_{\substack{k=1 \\ k \neq n}}^N T_{nk} \mathbf{E}_{nk}, \quad (1)$$

where \mathbf{E}_{dn} is the incident field of the n th isolated element. \mathbf{E}_{nk} is the scattered field from other elements in the corresponding local coordinate system. N defines the number of elements. And T_{nk} which requires three Euler rotations is the rotation matrix of the k th element relative to the n th element. Rotate \mathbf{E}_{nk} around x , y and z by α_{nk} , β_{nk} and χ_{nk} , respectively. The three angles are the rotation angles of the outside nor-

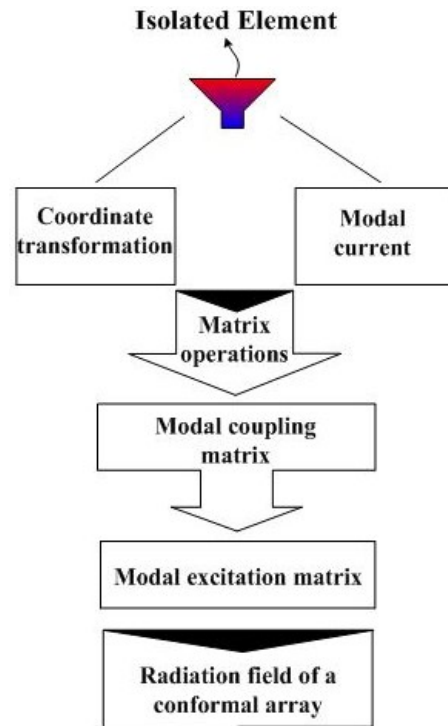


Fig. 1. Process of the proposed method.

mal vector of the k th element relative to the n th element, as shown in Figure 2 (b). The coordinate transformation process can be expressed as [16]

$$T_{nk} = T^{s1}(\chi_{nk}) T^{s2}(\beta_{nk}) T^{s3}(\alpha_{nk}), \quad (2)$$

where

$$T^{s1}(\chi_{nk}) = \begin{bmatrix} \cos \chi_{nk} & \sin \chi_{nk} & 0 \\ -\sin \chi_{nk} & \cos \chi_{nk} & 0 \\ 0 & 0 & 1 \end{bmatrix}, \quad (3)$$

$$T^{s2}(\beta_{nk}) = \begin{bmatrix} \cos \beta_{nk} & 0 & -\sin \beta_{nk} \\ 0 & 1 & 0 \\ \sin \beta_{nk} & 0 & \cos \beta_{nk} \end{bmatrix}, \quad (4)$$

$$T^{s3}(\alpha_{nk}) = \begin{bmatrix} 1 & 0 & 0 \\ 0 & \cos \alpha_{nk} & \sin \alpha_{nk} \\ 0 & -\sin \alpha_{nk} & \cos \alpha_{nk} \end{bmatrix}. \quad (5)$$

Refer to [15], the modal excitation coefficient of m th mode for the n th element in a conformal array environment can be written as

$$V_n^m = \int_{S_n} \mathbf{J}_n^m \cdot \left(\mathbf{E}_{dn} + \sum_{\substack{k=1 \\ k \neq n}}^N T_{nk} \mathbf{E}_{nk} \right) dS, \quad (6)$$

where \mathbf{J}_n^m is the characteristic current of m th mode for the n th element.

The scattered field of the k th element is [15]

$$\mathbf{E}_{nk} = \sum_{l=1}^L \frac{V_k^l \mathbf{E}_k^l}{1 + j\lambda_k^l}, \quad (7)$$

where V_k^l , \mathbf{E}_k^l and λ_k^l are the modal excitation coefficient, characteristic field and eigenvalue of l th mode for the k th element, respectively. L represents the number of modes for the k th element.

Substituting eqn (7) into (6), the modal excitation coefficient of m th mode for the n th element in an array environment is composed of two parts: the initial modal excitation coefficient of the isolated element and the modal excitation coefficient affected by other elements, which can be further expressed as

$$V_n^m = V_{dn}^m + \sum_{k \neq n}^N \sum_{l=1}^L \frac{V_k^l C_{nk}^{ml}}{1 + j\lambda_k^l}, \quad (8)$$

wherein

$$V_{dn}^m = \int_{S_n} \mathbf{J}_n^m \cdot \mathbf{E}_{dn} dS, \quad (9)$$

$$C_{nk}^{ml} = \int_{S_n} \mathbf{J}_n^m \cdot (T_{nk} \mathbf{E}_k^l) dS, \quad (10)$$

where V_{dn}^m is the initial modal excitation coefficient of m th mode for the n th element, and C_{nk}^{ml} is the modal coupling coefficient between the elements.

Further, eqn (9) and (10) can be written as

$$V_{dn}^m = v_n^{\text{port}} I_n^m, \quad (11)$$

$$C_{nk}^{ml} = \int_{S_n} \mathbf{J}_n^m Z (\mathbf{J}_k^l) dS, \quad (12)$$

where v_n^{port} is the delta-gap voltage at the feeding port of the n th element. I_n^m is the modal electric current at feeding port of m th mode for the n th element, details shown in [17]. Z represents an operator that converts \mathbf{J}_k^l into $T_{nk} \mathbf{E}_k^l$ [18] which has the dimension of impedance. \mathbf{J}_k^l is the characteristic current of l th mode for the k th element. Eqn (10) shows the mutual coupling is related to the characteristic current.

Extending eqn (8) to the conformal array, we can get

$$\mathbf{V} = \mathbf{V}_d + \mathbf{C} \mathbf{A} \mathbf{V}, \quad (13)$$

where \mathbf{V} , \mathbf{V}_d , \mathbf{C} and \mathbf{A} are respectively given by the following matrix.

$$\mathbf{V} = [V_1 \cdots V_n \cdots V_N]^T, \quad (14)$$

$$\mathbf{V}_d = [V_{d1} \cdots V_{dn} \cdots V_{dN}]^T, \quad (15)$$

$$\mathbf{C} = \begin{bmatrix} 0 & C_{12} & \cdots & \cdots & C_{1N} \\ C_{21} & 0 & \ddots & C_{nk} & \vdots \\ \vdots & \ddots & \ddots & \ddots & \vdots \\ \vdots & C_{kn} & \ddots & 0 & C_{N-1N} \\ C_{N1} & \cdots & \cdots & C_{NN-1} & 0 \end{bmatrix}, \quad (16)$$

$$\mathbf{A} = \text{diag}(\mathbf{A}_n). \quad (17)$$

and

$$V_n = [V_n^1 \ V_n^2 \ \cdots \ V_n^M]^T, \quad (18)$$

$$V_{dn} = [V_{dn}^1 \ V_{dn}^2 \ \cdots \ V_{dn}^M]^T, \quad (19)$$

$$\mathbf{A}_n = \text{diag} \left(\frac{1}{1 + j\lambda_k^l} \right), \quad (20)$$

$$C_{nk} = \begin{bmatrix} C_{nk}^{11} & C_{nk}^{12} & \cdots & C_{nk}^{1L} \\ C_{nk}^{21} & C_{nk}^{22} & \cdots & C_{nk}^{2L} \\ \vdots & \vdots & \ddots & \vdots \\ C_{nk}^{M1} & C_{nk}^{M2} & \cdots & C_{nk}^{ML} \end{bmatrix}. \quad (21)$$

where M represents the number of modes for the n th element.

In practical applications, the number of modes cannot be infinite, so the empirical truncation rule is given by [15]

$$M = N_0 \left(MS \geq 1/\sqrt{2} \right) + n_0, \quad (22)$$

where N_0 is the number of modes with the modal significance MS not less than $1/\sqrt{2}$, and a positive integer n_0 depends on the required accuracy of the solution.

Further solving the implicit equation (13), the modal excitation matrix of the array can be obtained

$$\mathbf{V} = (\mathbf{I} - \mathbf{C} \mathbf{A})^{-1} \mathbf{V}_d, \quad (23)$$

where \mathbf{I} is the identity matrix.

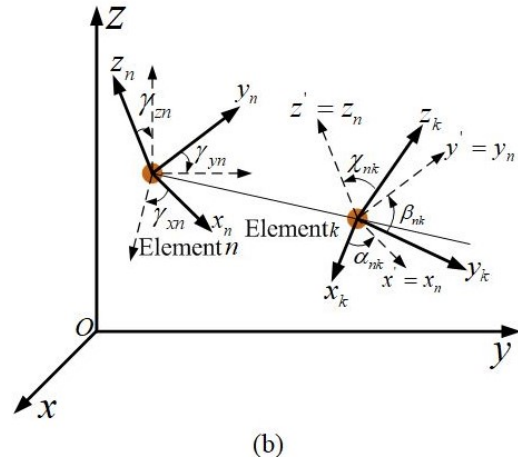
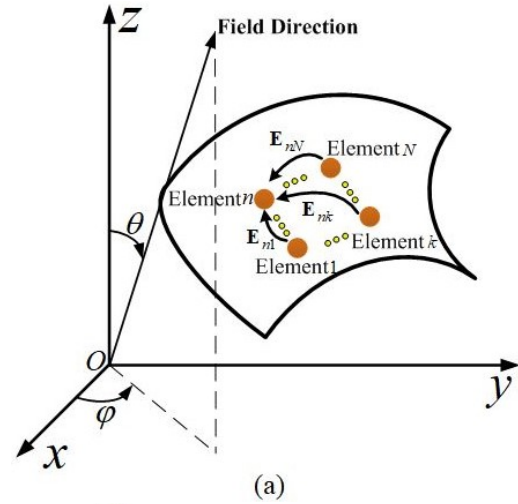


Fig. 2. Mutual coupling of conformal elements, (a) conformal array on an arbitrary surface, (b) position relationship of two elements.

C. Radiation field of a conformal array

Thus, the radiation field of the conformal array on arbitrary curved surface at R is

$$\mathbf{E}(R, \theta, \varphi) = \mathbf{T}(\mathbf{F}) \mathbf{A} \mathbf{V} \frac{e^{-j\beta R}}{R}, \quad (24)$$

where

$$\mathbf{T}(\mathbf{F}) = \left[T_1 \mathbf{F}_1 e^{j\beta \mathbf{r}_1 \cdot \mathbf{r}}, \dots, T_n \mathbf{F}_n e^{j\beta \mathbf{r}_n \cdot \mathbf{r}}, \dots, T_N \mathbf{F}_N e^{j\beta \mathbf{r}_N \cdot \mathbf{r}} \right], \quad (25)$$

and

$$\mathbf{F}_n = \left[\mathbf{F}_n^1(R, \theta, \varphi) \dots \mathbf{F}_n^m(R, \theta, \varphi) \dots \mathbf{F}_n^M(R, \theta, \varphi) \right], \quad (26)$$

herein β is the free-space wave number. \mathbf{r}_n is the position vector. \mathbf{r} is the unit vector of the observation direction. $\mathbf{F}_n^m(R, \theta, \varphi)$ is the characteristic field of m th mode for the n th element. T_n represents the transformation matrix between the local coordinate system (x_n, y_n, z_n) and the global coordinate system (x, y, z) , which can be expressed as

$$T_n = T^{s3}(\gamma_{xn}) T^{s2}(\gamma_{yn}) T^{s1}(\gamma_{zn}), \quad (27)$$

where the definition of $T^{s3}(\gamma_{xn})$, $T^{s2}(\gamma_{yn})$ and $T^{s1}(\gamma_{zn})$ is similar to eqn (3), (4) and (5). γ_{xn} , γ_{yn} and γ_{zn} are the angles between x_n , y_n , z_n and x , y , z respectively, as shown in Figure 2 (b).

III. NUMERICAL RESULTS AND VALIDATION

This section presents two numerical examples to verify the effectiveness of the proposed method. The numerical results are compared with those of the MoM [19] and the finite element method (FEM) [20].

A. Example 1

The structure of the element with the feed amplitude of 1 V and the phase of 0 degree is shown in Figure 3. A symmetrical 5×5 antenna array conformal on a parabolic cylinder at 2 GHz with a spacing of 0.5λ between elements was analyzed, as shown in Figure 4 (a). λ is the wavelength and the number of modes is $M = 1$. The circumferential curve equation is

$$z^2 = -0.02(x - 0.1). \quad (28)$$

where the variable unit is m and $x \leq 0.1$.

The parabolic cylinder has different circumferential curvatures, so conformal radiating elements are not identical in the circumferential direction. Considering the symmetry of the 5×5 array, three types of Rao–Wilton–Glisson (RWG) basis function need to be processed, and then extended to axial elements through rotation and translation.

Figure 4 (b), (c) and (d) show the normalized electric-field pattern analysis results of a 5×5 conformal array calculated by the proposed method, FEM and MoM considering mutual coupling effects at planes $\phi = 0^\circ$, $\phi = 90^\circ$ and $\theta = 90^\circ$. Observing the pattern of the

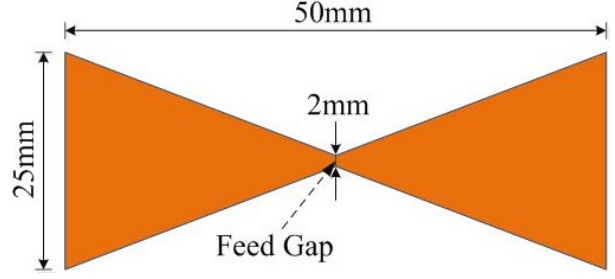


Fig. 3. Geometry and dimensions of the bowtie antenna before conformed to the surface [15].

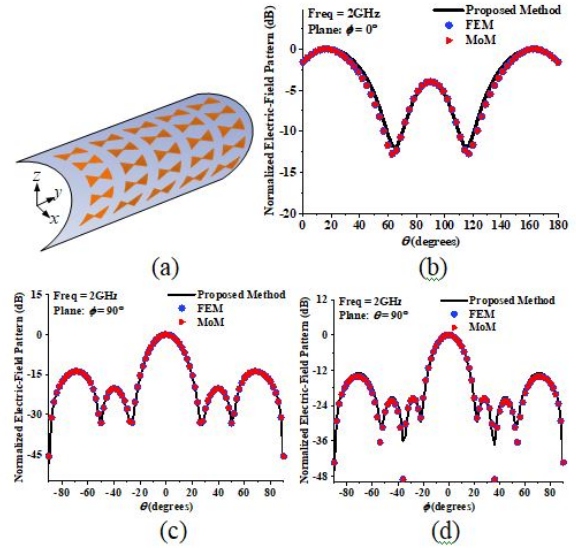


Fig. 4. Parabolic conformal array and normalized electric-field pattern, (a) parabolic cylindrical conformal array, (b) $\phi = 0^\circ$ cut, (c) $\phi = 90^\circ$ cut, (d) $\theta = 90^\circ$ cut.

three main planes, we found that the results analyzed by the proposed method are basically the same as those of FEM and MoM. This demonstrates the effectiveness of the proposed method in multiple conformal elements of different curvatures.

To further verify the effectiveness of the proposed method, the array shown in Figure 4 (a) is still used and only the element spacing is changed. Table 1 shows the errors of radiation fields obtained by the proposed method, FEM and MoM. The error [15] of radiation fields were calculated by

$$Err_R = \sqrt{\sum_{i=1}^{N_{\text{sam}}} \left| \frac{E_i}{E_{\text{max}}} - \frac{E_i^{\text{tar}}}{E_{\text{max}}^{\text{tar}}} \right|^2}, \quad (29)$$

where N_{sam} is the number of sample points in three main cuts. E_i and E_i^{tar} are the electric field values obtained by the proposed and existing methods, respectively. E_{max}

Table 1: The errors of radiation fields obtained by different methods

| Spacing | $Err_R^{\text{MoM}}(\%)$ | $Err_R^{\text{FEM}}(\%)$ |
|--------------|--------------------------|--------------------------|
| 0.5λ | 1.46 | 1.42 |
| 0.6λ | 2.15 | 2.17 |
| 0.7λ | 1.83 | 1.79 |
| 0.8λ | 2.31 | 2.19 |

Table 2: Computation cost for the conformal arrays (CPU: i5-6500 3.20 GHz, RAM:8.00 GB)

| Size | Number of RWG | CPU Time with FEKO (sec.) | CPU Time with the proposed method (sec.) |
|----------------|---------------|---------------------------|--|
| 9×9 | 1863 | 8.42 | 0.46 |
| 15×15 | 5175 | 63.77 | 4.94 |
| 21×21 | 10143 | 270.30 | 21.25 |
| 27×27 | 16767 | 815.44 | 97.90 |

and E_{\max}^{tar} are the maximum values of E_i and E_i^{tar} , respectively.

In order to validate the efficiency of the proposed method, according to Figure 1, the proposed method is divided into three steps in general. Firstly, the generalized characteristic equation is solved to obtain the modal current of the isolated radiating element by the implicitly restarted Arnoldi method [21, 22]. The number of basis functions is set as N_e , and the time complexity of this step is $O(N_e^3)$. Secondly, the modal coupling matrix is constructed to derive the modal excitation matrix, and the time complexity of this step is $O((NMN_e)^2 + (NM)^3)$. Finally, the superposition principle is used to obtain the radiation field of the entire conformal array, and its time complexity is $O(NM)$. Therefore, when the number of array elements is $N \rightarrow \infty$, $NM \gg N_e^2$, the time complexity of the entire algorithm is $O((NM)^3)$. The time complexity is $O((NN_e)^3)$ for the classical MoM. So, the proposed method is more efficient than the method of moments for electrically small-sized radiating elements ($N_e \gg M$).

The following takes the calculation time of different sizes of array composed of bowtie antenna shown in Figure 3 as an example to illustrate the efficiency of the proposed method, as shown in Table 2.

B. Example 2

The ground effect is not considered in the above example. So, we consider a more complex array. The coaxially fed microstrip antenna is used as conformal array elements, as shown in Figure 5 (a). The feed amplitude is 1 V, and the phase is 0° ; the array element works

Table 3: Optimized parameters of the equivalent model for the microstrip antenna

| X_s (mm) | Y_s (mm) | θ_t ($^\circ$) |
|------------|------------|-------------------------|
| 31.31 | 35.66 | 14.86 |

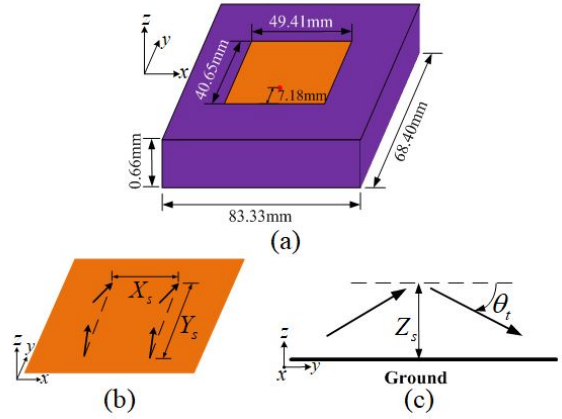


Fig. 5. A microstrip antenna and its equivalent model, (a) the microstrip antenna, (b) its equivalent 2×2 dipole array model, (c) side view of the equivalent model.

at 2.4 GHz. The geometrical parameters of a microstrip antenna are consistent with those of [5].

An equivalent method of a microstrip antenna is proposed in [5] on the basis of the cavity model method. The microstrip antenna can be equivalent to the 2×2 electric dipoles on the ground of a perfect electrical conductor, as shown in Figure 5 (b) and (c).

It's noted that the dipole in the equivalent model adopts a strip dipole with a width of 2 mm to apply the proposed method, which is different from [5]. The optimized parameters of the equivalent model for a microstrip antenna are shown in Table 3. The root-mean-square error of normalized electric-field pattern for the abovementioned equivalent model is 0.45%. And the normalized near-field distribution of the microstrip patch antenna and its equivalent model are shown in Figure 6.

A 3×5 microstrip antenna array is conformal on a cylinder with a radius of 83.33 mm, as shown in Figure 7 (a). The element spacing is 0.5λ . Then, we feed the 2×2 equivalent model with the uniform amplitude and the number of modes is $M = 6$. It is clear that the results calculated by the proposed method, MoM and FEM are consistent on the three main planes from Figure 7 (b), (c) and (d), which shows the effectiveness of the proposed method. The abovementioned model has a certain deviation in the region that is far from the main lobe. This occurs owing to the error caused by the equivalent model of the microstrip antenna.

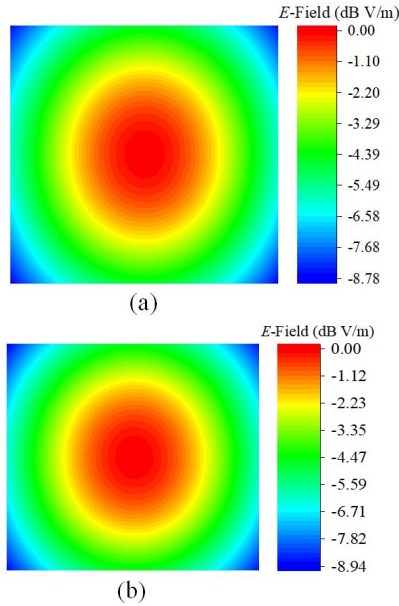


Fig. 6. The normalized near-field distribution, (a) the microstrip antenna, (b) its equivalent 2×2 dipole array model.

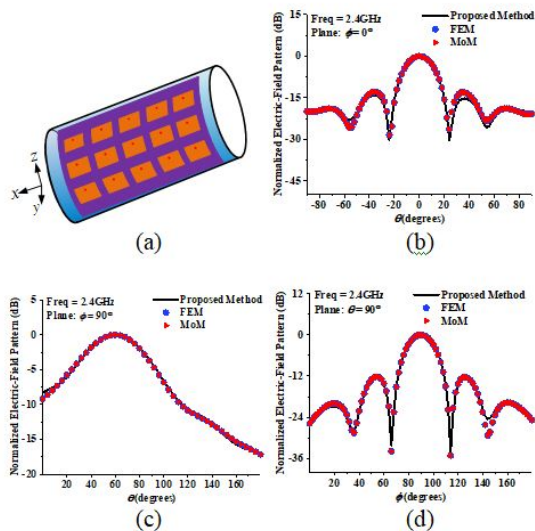


Fig. 7. Microstrip conformal array and normalized electric-field pattern, (a) cylindrical conformal array, (b) $\phi = 0^\circ$ cut, (c) $\phi = 90^\circ$ cut, (d) $\theta = 90^\circ$ cut.

IV. CONCLUSION

This paper presents a method for analyzing the performances of conformal array antennas based on the characteristic modes of isolated elements. Combining the coordinate transformation, the modal coupling matrix is constructed to derive the field formula of the conformal array. The modal coupling matrix is only

related to the structural parameters of the elements and relative pose, and presents a clear physical insight into the coupling mechanism of conformal radiating elements from the perspective of the characteristic currents. Finally, some examples are used to validate the proposed method. This provides a basis for further research on the conformal array.

ACKNOWLEDGMENT

The paper is supported by the Fundamental Research Funds for the Central Universities and the Innovation Fund of Xidian University (Grant No. U1931139).

REFERENCES

- [1] L. Josefsson, *Conformal Array Antenna Theory And Design*, Hoboken, NJ, USA: Wiley, 2006.
- [2] Y. Li, "Synthesis of conical conformal array antenna using invasive weed optimization method," *Applied Computational Electromagnetics Society (ACES) Journal*, vol. 28, no. 11, pp. 1025-1030, Nov. 2013.
- [3] H. M. Bernety, S. Venkatesh, and D. Schurig, "Analytical phasing of arbitrarily oriented arrays using a fast, analytical far-field calculation method," *IEEE Trans. Antennas Propagat.*, vol. 66, no. 6, pp. 2911-2922, Jun. 2018.
- [4] P. H. Pathak, "A collective UTD ray analysis for the radiation from conformal linear phased array antennas on large cylindrical surfaces," *In EUCAP*, Paris, France, 2017.
- [5] S. P. Gao, "Installed radiation pattern of patch antennas: prediction based on a novel equivalent model," *IEEE Trans. Antennas Propagat Mag.*, vol. 57, no. 3, pp. 81-94, Jun. 2015.
- [6] W. J. Zhao, "Analysis of radiation characteristics of conformal microstrip arrays using adaptive Integral Method," *IEEE Trans. Antennas Propagat.*, vol. 60, no. 2, pp. 1176-1181, Feb. 2012.
- [7] B. Andr and P. Caudrillier, "Domain decomposition method based on Generalized Scattering Matrix for installed performance of antennas on aircraft," *IEEE Trans. Antennas Propagat.*, vol. 55, no. 6, pp. 1833-1842, Jun. 2007.
- [8] J. Rubio, "Array thinning of coupled antennas based on the orthogonal matching pursuit method and a spherical-wave expansion for far-field synthesis," *IEEE Trans. Antennas Propagat.*, vol. 63, no. 12, pp. 5425-5432, Dec. 2015.
- [9] J. F. Izquierdo, "Efficient radiation antenna modeling via orthogonal matching pursuit in terms of infinitesimal dipoles," *IEEE Antennas Wireless Propagat Lett.*, vol. 15, pp. 444-447, 2015.
- [10] J. Rubio, "Mutual coupling of antennas with overlapping minimum spheres based on the

- transformation between spherical and plane vector waves," *IEEE Trans. Antennas Propagat.*, vol. 69, no. 4, pp. 2103-2111, Apr. 2021.
- [11] T. Marinovic, "Fast characterization of mutually-coupled array antennas using isolated antenna far-field data," *IEEE Trans. Antennas Propagat.*, vol. 69, no. 1, pp. 206-218, Jan. 2021.
- [12] Z. Ma and Q. Wu, "Reduction of mutual coupling for broadband vivaldi antennas using characteristic modes analysis and lumped loads," *Applied Computational Electromagnetics Society (ACES) Journal*, vol. 34, no. 6, pp. 921-926, Jun. 2019.
- [13] A. Nikfal, G. Dadashzadeh, and M. Naser-Moghadas, "A reconfigurable crossed dipole antenna for polarization diversity using characteristic mode theory," *Applied Computational Electromagnetics Society (ACES) Journal*, vol. 34, no. 9, pp. 1320-1326, Sep. 2019.
- [14] L. Ling, "Efficient characteristic mode analysis for radiation problems of antenna arrays," *IEEE Trans. Antennas Propagat.*, vol. 67, no. 1, pp. 199-206, Jan. 2019.
- [15] S. X. Lou, "Analysis of finite antenna arrays using the characteristic modes of isolated radiating elements," *IEEE Trans. Antennas Propagat.*, vol. 67, no. 3, pp. 1582-1589, Mar. 2019.
- [16] T. Milligan, "More application of Euler rotation angles," *IEEE Trans. Antennas Propagat Mag.*, vol. 41, no. 4, pp.78-83, Aug. 1999.
- [17] Q. Wu and W. Su, "Reduction of out-of-band antenna coupling using characteristic mode analysis," *IEEE Trans. Antennas Propagat.*, vol. 64, no. 7, pp. 2732-2742, Jul. 2016.
- [18] S. D. Rao, "Electromagnetic scattering by surfaces of arbitrary shape," *IEEE Trans. Antennas Propagat.*, vol. 30, no. 3, pp. 409-418, May. 1982.
- [19] S. N. Makarov, *Antenna and EM modeling with Matlab*. New York, 2002.
- [20] J. M. Jin, *The Finite Element Method in Electromagnetics*. New York: Wiley, 2002.
- [21] Y. Chen and C. F. Wang, *Characteristic Modes: Theory and Applications in Antenna Engineering*. Hoboken, NJ, USA: Wiley, 2015.
- [22] R. B. Lehoucp, D. C. Sorensen, and C. Yang, *ARPACK Users Guide: Solution of Large-Scale Eigenvalue Problems with Implicitly Restarted Arnoldi Methods*. Philadelphia, PA: SIAM, 1998.



Yuanchen Zeng was born in Shaanxi, China, in 1996. He received the B.S. degree in mechanical design manufacture and automation major from Xidian University, Xi'an, China, in 2017, where he is currently pursuing the Ph.D. degree in electromechanical engineering. His current research interests include conformal arrays and computational electromagnetics.



Shuo Zhang was born in Heilongjiang, China, in 1993. She received the B.S. degree in automation technology from Xidian University, Xi'an, China, in 2016, where she is currently pursuing the Ph.D. degree in electromechanical engineering. Her current research interests include the theory of microwave power transmission, antenna arrays, and aperture antennas.



Shunxi Lou was born in Hebei, China, in 1992. He received the B.S. and Ph.D. degrees from Xidian University, Xi'an, China, in 2015, and 2021, respectively. His current research interests include the theory of characteristic modes, antenna arrays, and computational electromagnetics.

Dual-Band Folded Monopole MIMO Antennas with Enhanced Isolation

Likaa S. Yahya¹, Loay S. Yahya¹, and Khalil H. Sayidmarie²

¹Institute of Technology
Northern Technical University, Mosul, Iraq
likaasalim@ntu.edu.iq, loaysalim@ntu.edu.iq

²College of Electronics Engineering
Ninevah University, Mosul, Iraq
kh.sayidmarie@uoninevah.edu.iq

Abstract – In this paper, a compact dual-band multiple-input multiple-output (MIMO) diversity antenna is proposed. Each of the two MIMO antennas consists of two folded strips working as radiating elements that are fed by a microstrip line. The antennas operate in three WLAN bands: ISM 2.45 GHz, 5.25 GHz, and ISM 5.775 GHz. To improve the isolation at WLAN (2.4–2.48 GHz), two L-shaped slots are etched in the ground plane while a U-shaped slot is cut in the ground plane to enhance isolation at WLAN (5.15–5.35 GHz and 5.725–5.825 GHz). Three slots on the substrate between radiating patches are also employed for an extra reduction in the mutual coupling at 2.45 GHz. The antenna performance was examined by simulation employing CST Microwave Studio Software. The proposed antenna offers minimum isolation of more than 19.5 dB, a low envelope correlation coefficient (ECC) of less than 0.0016, and good radiation efficiency (~80%) through the operating frequency bands. The antenna is compact, thin, and suitable for portable devices.

Index Terms – dual-band antennas, folded monopoles, L-slots, mutual coupling, U-slot.

I. INTRODUCTION

The use of high-bit-rate wireless communication systems is rapidly increasing. To increase channel capacity and reduce multipath fading effects, multiple-input-multiple-output (MIMO) systems are desirable. The MIMO antenna array requires a compact structure, high isolation between the signal ports, low envelope correlation, and high radiation efficiency [1]. The mutual coupling and antenna size are the major challenges for MIMO antenna design. As the mutual coupling and correlation between the elements increase, the performance of the MIMO antenna systems degrades [2]. Various techniques have been recommended by the researchers

to reduce the mutual coupling between antenna elements. Threefold fork-shaped stubs are employed for mutual coupling reduction in MIMO antenna applications [3]. A coupled strip resonator is loaded at the top hybrid two-antenna system for isolation enhancement was demonstrated in [4], while a fractal-shaped EBG and a mushroom-shaped electromagnetic bandgap (EBG) have been explored in [5] to improve the isolation between the elements in 2×2 MIMO antenna system. A line slot DGS (Defective Ground Structure) was used to reduce the mutual coupling between the antenna elements [6]. A dumbbell-shaped parasitic element is inserted between the circular patches to suppress the unavoidable mutual coupling [7]. A parasitic element was implanted between two band antennas to improve port-to-port isolation in the 2.4–2.5 GHz and 5.15–5.825 GHz WLAN bands [8]. The use of parasitic elements and defected ground structure was presented in [9]. A slot splitting the meandered lines defected ground was developed in [10] to reduce the mutual coupling between two microstrip antennas. The proposed structure was improved and expounded by the common and differential mode theory. A rectangular parasitic element with ten square slots was proposed to minimize the mutual coupling to about -25 dB at 2.4 GHz in [11]. A dual-band coupled resonator structure was suggested to decouple a pair of dual-band closely spaced MIMO monopole antennas employed for the WLAN 2.45/5.25 GHz bands. The edge-to-edge distance is set to be 9 mm and is $0.0735\lambda_0$ at 2.45 GHz and $0.1575\lambda_0$ at 5.25 GHz [12]. A slotted complementary split-ring resonator (CSRR) was inserted on the ground plane to enhance the isolation for WLAN applications [13]. A modified U-shaped resonator as decoupling structure between the two MIMO elements to reduce the undesired coupling was presented in [14]. The MIMO elements were kept at a distance of $\lambda_0/10$ (edge to edge) and a coupling suppression of 14 dB was achieved.

Four monopole antenna elements were placed orthogonally at the corners of the substrate in [15]. A decoupling structure composed of a circular patch and four L-shaped branches placed counterclockwise is printed on the upper surface of the substrate to reduce coupling between antenna elements. A two-port dual-band characteristics MIMO antenna was reported in [16]. Each radiator of the MIMO configuration consists of a dome-shaped monopole antenna element. A T-shaped stub is placed between the two radiators to achieve high isolation. In [17], the decoupling element for enhancing the port isolation is based on the neutralization line, where two series lumped capacitors are inserted in the structure to enhance the isolation between the two strongly coupled antennas. An open stub meandered (OSM) band stop filter (BSF) design for MIMO applications has been implemented in [18]. This technique demonstrated high isolation of 60 dB at 2.4 GHz across the 30% bandwidth and ECC of 0.0093 at 2.42 GHz, while maintaining edge-to-edge spacing as $0.19\lambda_0$. The method of the parasitic structure to improve antenna isolation has been studied in [19]. Two-port MIMO antennas were designed in [20] for the sub-6 GHz 5G band covering the 3.3–5 GHz frequency range. A connected meander ground slot was introduced as a decoupling structure. A technique to reduce mutual coupling between two antennas for WLAN and WIMAX applications with fractional wavelength spacing has been proposed in [21]. An S-shaped slot is inserted into the feed line of each antenna, and it is tuned to resonate at the same frequency as the other antenna. Despite the tiny antenna spacing of 9 mm (0.0735 wavelengths at 2.45 GHz frequency), the slots were able to reduce the coupling sufficiently. In [22], two interlaced U-shaped slots are etching in the feed line of each antenna to reduce the effect of mutual coupling. A simple microstrip C-shaped resonator between the radiating patches and an inverted C-shaped slot DGS on the ground plane have been proposed in [23] to increase the isolation between two microstrip patch antennas operating at dual-frequency. In [24], a multi-layered electromagnetic bandgap (ML-EBG) structure was incorporated into two MIMO antenna array elements to confirm its usefulness in surface wave suppression, and enhance the isolation. Three EBG layers were stacked on top of the antenna layer resulting in a 9.6 mm thick antenna, and three stacks were placed between the two microstrip patch antennas.

In this paper, a compact two-element MIMO antenna for WLAN applications at 2.45, 5.25, and 5.775 GHz is proposed. Each of the two MIMO antennas consists of two folded strips working as radiating elements. The overall volume of the MIMO antenna is equal to $0.33\lambda_0 \times 0.2\lambda_0 \times 0.012\lambda_0$ and the edge-to-edge distance is $0.055\lambda_0$, where λ_0 is the free space wavelength at 2.45

GHz. The proposed MIMO antenna has isolation greater than 20 dB in the two operating frequency bands and a peak gain of 1.99 dBi for the first band and 3.49 dBi for the second band. The envelope correlation coefficient (ECC) is less than 0.0016.

II. DESIGN OF THE TWO-ELEMENT MIMO ANTENNA

A compact two-element MIMO folded antenna is designed on an FR4 substrate of dielectric constant 4.3 and loss tangent 0.02 as shown in Figure 1 and the parameters of the proposed antenna are shown in Table 1. The overall dimensions of the MIMO antenna are $41 \text{ mm} \times 25.5 \text{ mm} \times 1.5 \text{ mm}$. The design steps are explained in the following sections.

A. Single-element folded strip antenna.

The basic radiating part of the antenna is a monopole formed of two conducting strips for the two desired bands. To achieve a miniaturized design, the radiating strips were folded. Figure 2 shows a single-element folded strip antenna (SEFSA) which is used in the proposed MIMO system. The overall size of the antenna is $24 \text{ mm} \times 18 \text{ mm}$. The upper strip of the antenna is used to excite a resonance at the first operating frequency ($f_{r1} = 2.45 \text{ GHz}$) band while the lower strip is used to excite the second resonance frequency ($f_{r2} = 5.25 \text{ GHz}$) band. The effective relative permittivity ϵ_e and effective wavelength λ_e were calculated using the following relations

$$\epsilon_e = (1 + \epsilon_r)/2, \quad (1)$$

$$\lambda_e = C/\sqrt{\epsilon_e}. \quad (2)$$

where ϵ_r is the relative permittivity of the used substrate. The total average length of the upper strip ($L_{s1} + L_p$) was set to be $\lambda_e/2$ and optimized to $37.77 \text{ mm} \cong \lambda_e/2$ (where λ_e is the effective wavelength at 2.45 GHz). The total average length of the lower strip ($L_{s2} + L_p$) was set to be

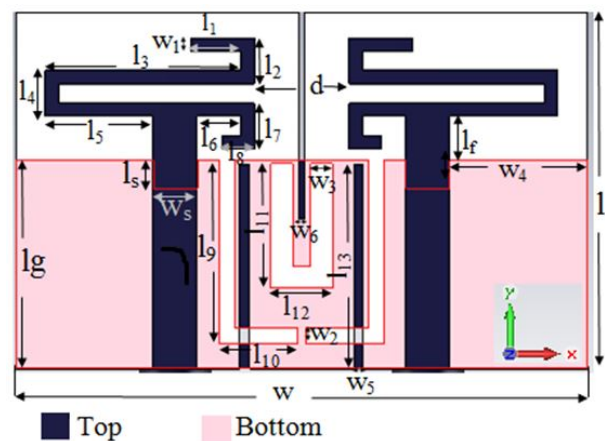


Fig. 1. Configuration of the proposed MIMO antenna.

Table 1: Dimensions of the proposed MIMO antenna (in millimeters)

| Parameters | | Values | |
|------------|-----------|------------|-----------|
| Length (l) | Width (w) | Length (l) | Width (w) |
| l_1 | w_1 | 3.7 | 0.95 |
| l_2 | w_2 | 3.3 | 1.3 |
| l_3 | w_3 | 14.25 | 1.7 |
| l_4 | w_4 | 3.3 | 9.7 |
| l_5 | w_5 | 7.85 | 0.7 |
| l_6 | w_6 | 3.2 | 0.5 |
| l_7 | w_s | 3.3 | 3.2 |
| l_8 | w | 2.3 | 41 |
| l_9 | d | 13.2 | 6.8 |
| l_{10} | | 5.8 | |
| l_{11} | | 9 | |
| l_{12} | | 4.48 | |
| l_{13} | | 14.8 | |
| l_s | | 2 | |
| l | | 25.5 | |
| l_g | | 15 | |
| l_f | | 3.2 | |

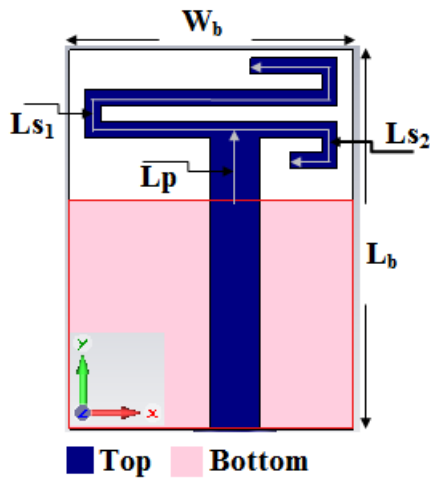


Fig. 2. Geometry of the dual-band antenna element.

$\lambda_c/2$ and optimized to $15.63 \text{ mm} = 0.45\lambda_c$ at 5.25 GHz. The feed line position is adjusted carefully to obtain the required dual-band property. The antenna performance was examined and optimized by extensive simulations employing the CST Microwave Studio Software. The Transient Solver was used. The reflection coefficient plot in Figure 3 shows two operating bands within $S_{11} < -10 \text{ dB}$ limit. These bands have bandwidths of 120 MHz (2.39–2.51 GHz) and 2.05 GHz (4.13–6.18 GHz), which cover all the 2.4/5.25/5.775 GHz WLAN bands. In the upper frequency band, the resonance frequency is determined by a combination of two factors. The first is the

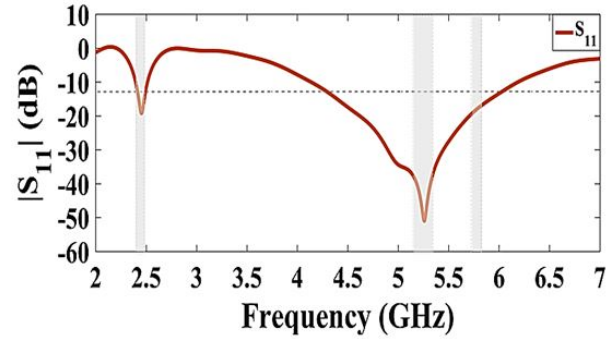


Fig. 3. Variation of the antenna reflection coefficient with frequency for the proposed antenna element SEFSA.

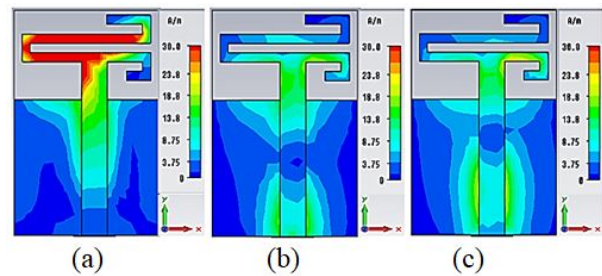


Fig. 4. Simulated surface current distributions at; (a) 2.45 GHz, (b) 5.25 GHz, and (c) 5.775 GHz.

second resonant frequency due to the lower strip while the other frequency corresponds to the higher mode of the upper strip.

The surface current distributions in Figure 4 show that the folded strip antenna is resonating at 2.45 GHz and 5.25 GHz frequencies. The upper (long) strip has a higher current density at the lower band (2.45 GHz), while the lower (short) strip carries a high current density at the upper band. The radiation patterns of the SEFSA antenna are displayed in Figure 5 which shows that the radiation pattern in the XZ-plane is omnidirectional and in the YZ-plane is bidirectional. Moreover, the radiation patterns are stable for the three desired frequencies.

B. Two-element MIMO antenna

Using the above SEFSA as a reference unit, the two-element MIMO antenna is designed. At first (step 1), two SEFSA antennas are located in adjacent face to face positions with edge to edge distance of 6.8 mm as shown in Figure 6 (a). The overall size of antenna1 in step 1 is $39 \text{ mm} \times 24.5 \text{ mm}$.

The surface current distribution in Figure 7 (a) and the S-parameters plot in Figure 8 (a) show that this antenna has a high mutual coupling of -4 dB for the first band and -10 dB for the second band. In order to reduce the mutual coupling at the first band, two L-shaped slots

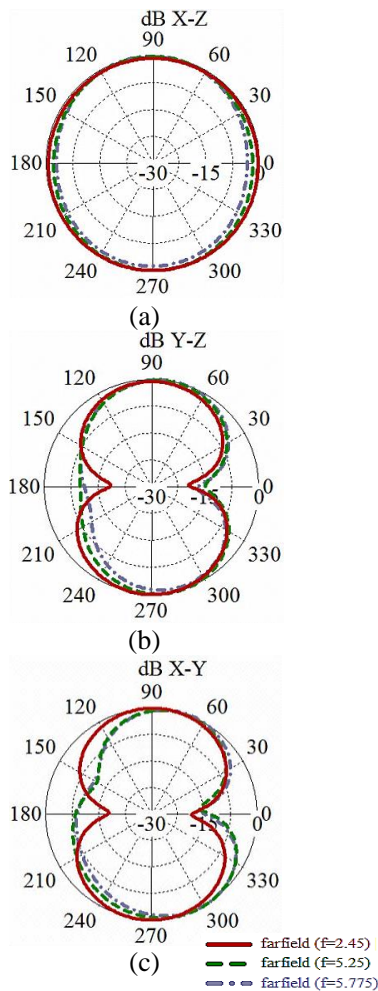


Fig. 5. Simulated radiation patterns of the SEFSA at the frequency of 2.45 GHz, 5.25 GHz, and 5.775 GHz for the; (a) XZ plane, (b) YZ plane, and (c) XY plane.

were cut in the ground plane. These L-shaped slots introduce a high impedance region between the feeding lines of the two antennas and enhance the isolation. The length of each slot is set at $\lambda/4$ at the frequency of 2.45 GHz that is desired to have higher isolation. Thus, the

length of the slot L can be calculated using the following relations [25], and found to be 17.9 mm.

$$L = \frac{C}{4f_{\text{center}} \cdot \sqrt{\epsilon_e}}, \quad (3)$$

$$\epsilon_e = \frac{\epsilon_{r+1} + \epsilon_{r-1}}{2} + \frac{\epsilon_{r-1}}{2} \left(1 + \frac{12h}{w_3}\right)^{-\frac{1}{2}}. \quad (4)$$

To increase the isolation at the frequency of 5.25 GHz a U-shaped slot in the middle of the ground plane was introduced. The U-shaped slot changes the current distribution on the ground plane resulting in higher isolation between the two antennas at 5.25 GHz (Fig. 6 (b)). The length of the U-shaped slot was calculated using eqn (4) and eqn (5), and found to be 16.1 mm. Thus, the MIMO antenna2 is obtained in step 2

$$L = \frac{C}{2f_{\text{center}} \sqrt{\epsilon_e}}. \quad (5)$$

The surface current distribution in Figure 7 (b) proves that the mutual coupling due to the surface current propagation and near-field coupling between the antenna elements has been reduced. The S-parameters plot of the proposed MIMO antenna2 in Figure 8 (b) shows that good impedance matching is obtained in the two frequency bands and isolation greater than 19 dB between elements is obtained in the two operating frequency bands. At the 2.45 GHz frequency, the mutual coupling decreased from -4 dB to -24.26 dB, while at the 5.25 GHz band the mutual coupling decreased from -10 dB to -60.37 dB, but at 5.775 GHz it drops from -14.5 dB to -19.9 dB. To obtain a further reduction in the mutual coupling at 2.45 GHz, three slots between the two patches were inserted in the substrate. The length of each slot is equal to 14.8 mm, which is approximately about $\lambda_0/4$ at 2.45 GHz isolated frequency, thus the proposed MIMO antenna3 is obtained in step3. Figure 8 (c) displays the simulated S-parameters for double-antenna3. The minimum mutual couplings are -47.8 dB, -61 dB, at 2.47 GHz and 5.2 GHz, respectively. Better isolation has been obtained at the lower band in this case as compared with the previous case. It is 36.86 dB at 2.45 GHz,

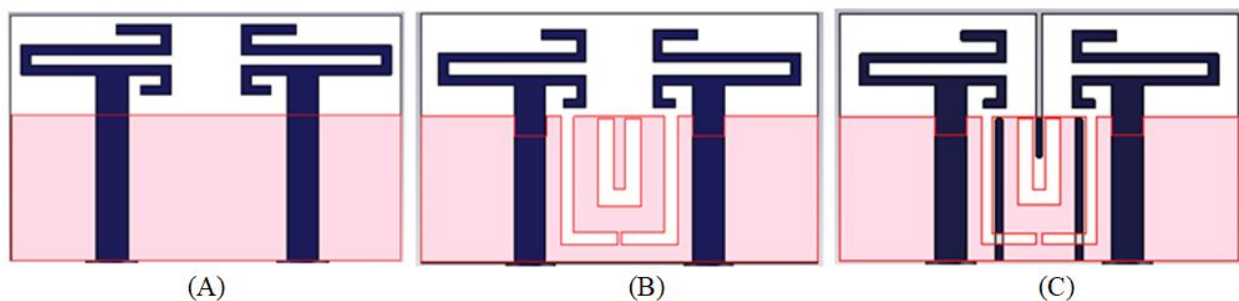


Fig. 6. Evolution of the proposed MIMO antenna; (A) Antenna1, (B) Antenna2, and (C) Antenna3.

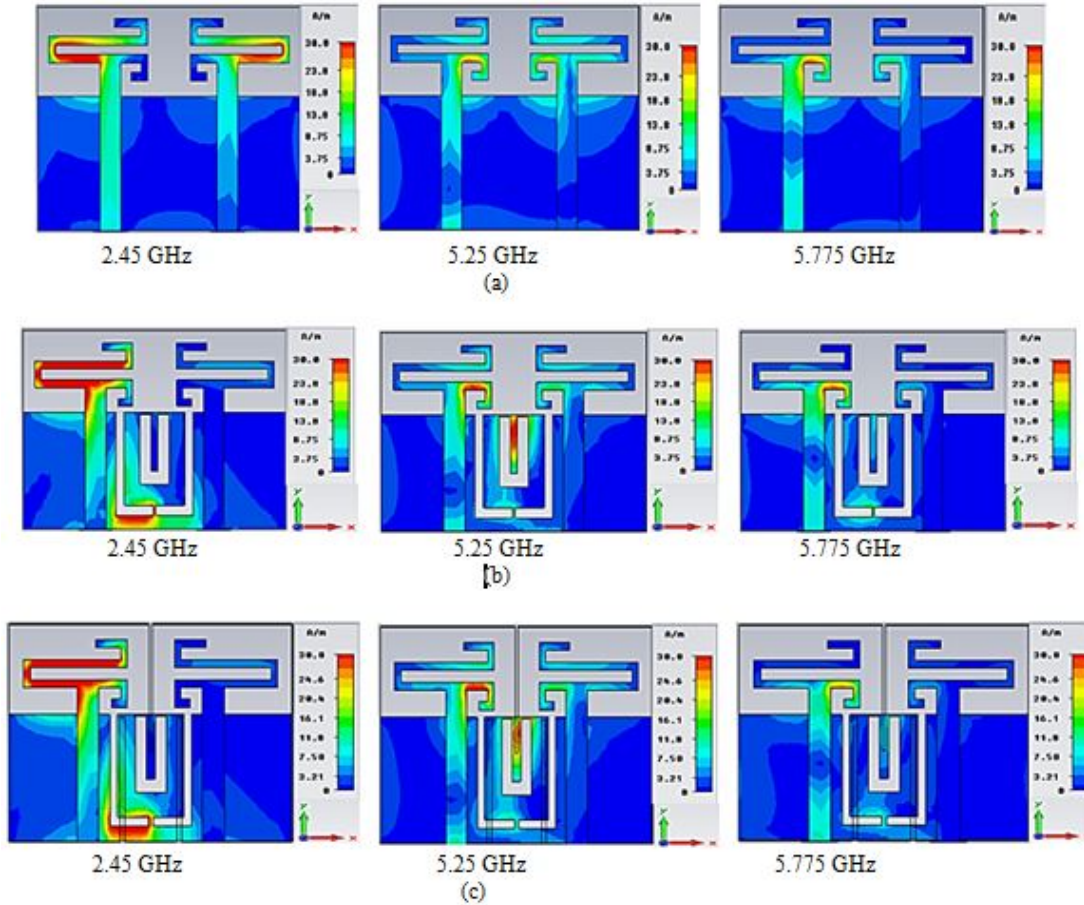


Fig. 7. The surface current distributions at 2.45, 5.25, and 5.775 GHz when port 1 is excited and port 2 is terminated to 50Ω load. (a) Antenna1, (b) Antenna2, and (c) Antenna3.

which represents a 12.6 dB enhancement over the performance of antenna2.

The simulated radiation pattern of the proposed antenna is shown in Figure 9. Due to the symmetrical structure, the radiation pattern is obtained by exciting one antenna element with the other terminated to a 50Ω matched load. The results show similar performance at the three bands. Figure 10 shows the simulated efficiency and gain. In the lower band, the minimum efficiency is 81.1% and the minimum gain is 1.84 dBi. In the upper band, the minimum efficiency is 72.3% and the minimum gain is 3.14 dBi.

III. DIVERSITY PERFORMANCE

The performance of the proposed antenna3 was further evaluated by studying the following figure of merits. In each case the antenna performance results were taken from the CST software and applied to codes written in MATLAB to determine, Envelope Correlation Coefficient, Mean Effective Gain, and Total Active Reflection Coefficient, as shown in the next subsections:

A. ECC (Envelope Correlation Coefficient).

For MIMO systems, ECC is an important figure of merit in characterizing the mutual coupling effect between the antenna elements. The value of ECC was calculated from the obtained S-parameters using the following relation:

$$ECC = \frac{|S_{11}^* S_{12} + S_{21}^* S_{22}|^2}{\left[1 - (|S_{11}|^2 + |S_{21}|^2)\right] \left[1 - (|S_{22}|^2 + |S_{12}|^2)\right]} \quad (6)$$

The ECC must be below 0.5 for good diversity performance [26].

Figure 11 shows the obtained values of ECC. It can be seen that the ECC is less than 0.0043 for the first band (2.4–2.48) GHz, less than 0.00037 for the second band (5.15–5.35) GHz, and less than 0.0023 for the third band (5.725–5.825) GHz. Considerable improvement has been achieved by antenna3 in comparison with antenna1.

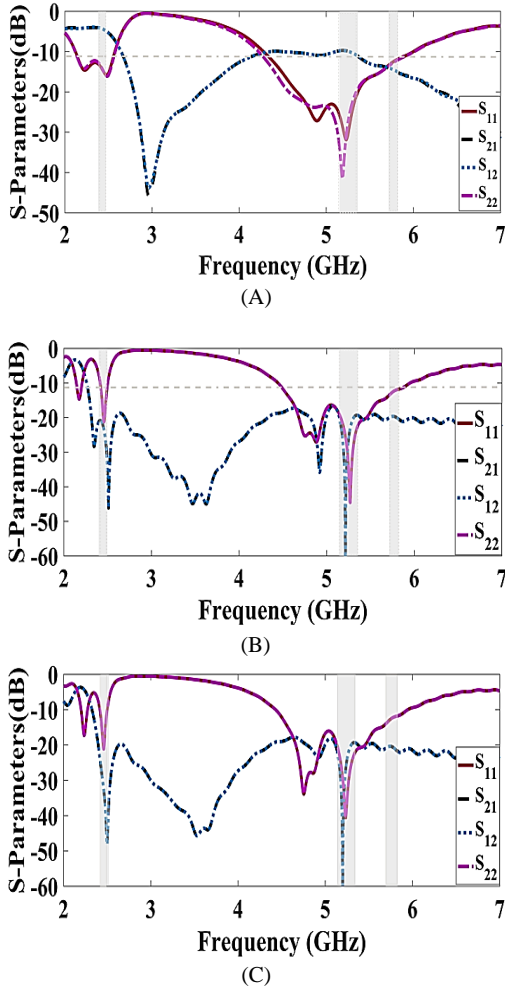


Fig. 8. S-parameters of the MIMO antenna; (a) Antenna1, (b) Antenna2, and (c) Antenna3.

B. MEG (Mean Effective Gain).

When contrasted to an isotropic antenna, the mean effective gain (MEG) is the ratio of accepted mean power to average incident power by the radiating element of MIMO. The following equations were used to calculate MEG [27]:

$$MEG_1 = 0.5 \left[1 - \sum_{j=1}^N |S_{ij}|^2 \right] < -3\text{dB}, \quad (7)$$

$$|MEG_1 - MEG_j| < 3\text{dB}. \quad (8)$$

MEG1 and MEG2 can be written as,

$$MEG_1 = 0.5 \left[1 - |S_{11}|^2 - |S_{12}|^2 \right], \quad (9)$$

$$MEG_2 = 0.5 \left[1 - |S_{21}|^2 - |S_{22}|^2 \right]. \quad (10)$$

As can be seen from Figure 12, the MEG is under -3 dB.

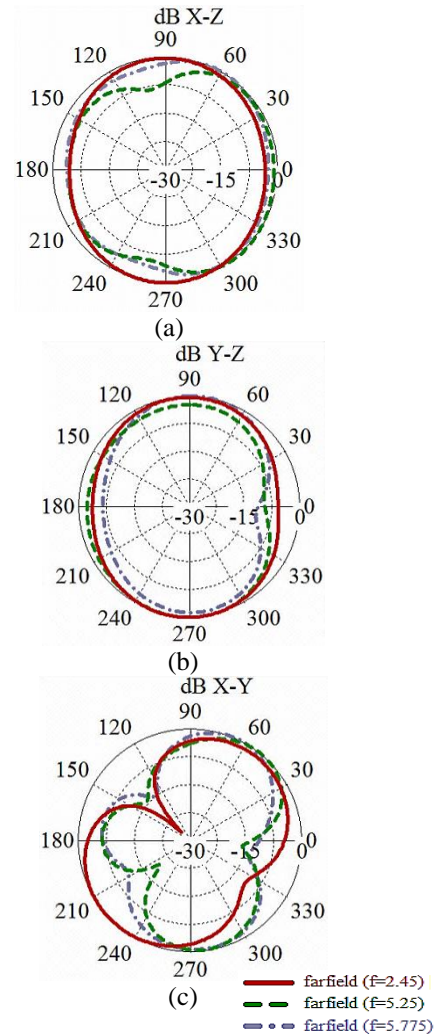


Fig. 9. Simulated radiation patterns of the MIMO antenna3 at frequencies of 2.45 GHz, 5.25 GHz, and 5.775 GHz for the; (a) XZ plane, (b) YZ plane, and (c) XY plane.

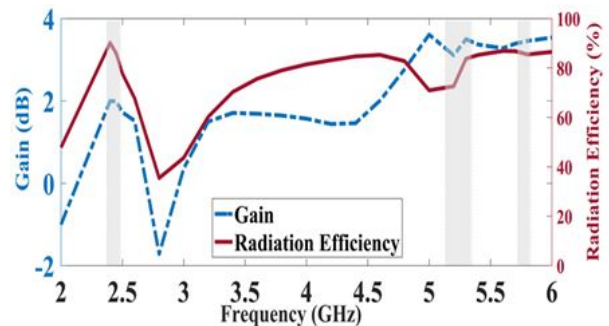


Fig. 10. Simulated gain and efficiency of proposed MIMO antenna3.

Table 2: Comparison of the performance of the proposed MIMO antenna with some published work

| Ref. | f_0 (GHz) | Edge to edge spacing (mm) | Overall antenna dimensions & volume (mm) | Isolation (dB) | Gain (dBi) | Radiation efficiency [%] | ECC |
|-----------|-------------|---------------------------|---|----------------|-----------------|--------------------------|---|
| [2] | 5.7 | 4 | $26 \times 26 \times 0.8 = 540$ | 15.4 | 1.6 | NA | 0.01 |
| [3] | 8.97 | 1 | $34 \times 22 \times 1.5 = 1122$ | 43 | 4.5 | 86.96 | 0.018 |
| [5] | 2.44 | 8.4 | $38.2 \times 95.94 \times 1.6 = 5863$ | 24 | 4.68 | 54.99 | 0.008 |
| [9] | 2.45, 5.5 | 17.9 | $50 \times 30 \times 1.59 = 2385$ | 24, 27 | 0.26, 3.1 | 32.9, 63.8 | 0.027, 0.005 |
| [12] | 2.45, 5.25 | 9 | $100 \times 55 \times 1.5 = 8250$ | 30, 35 | | 68, 74 | 0.0003, 0.0001 |
| [16] | 2.45, 5.5 | 4.8 | $20 \times 34 \times 1.6 = 1088$ | 21, 25 | 2.75–4.19 | >70% | <0.004 |
| [17] | 2.4, 5 | 18 | $60 \times 7.5 \times 4.5 = 2025$ | 16, 23 | 3.6, 4.1 5–6 | 70 67–78% | NA |
| [18] | 2.42 | 18 | $120 \times 60 \times 1.52 = 10944$ | 60 | 6.95 | 90 | 0.0093 |
| [19] | 16.05 | 6 | $15 \times 30 \times 1.57 = 7065$ | 23.92 | 7.28 | 80.4 | 0.00016 |
| [23] | 2.78, 4.12 | 7 | $75 \times 60 \times 1.6 = 7200$ | 22, 40 | N.A | N.A | N.A |
| [24] | 2.55 | 15.29 | $\approx 57 \times 47 \times 9.6 = 25718$ | 31 | N.A | N.A | N.A |
| This work | 2.45, 5.25 | 6.8 | $25.5 \times 41 \times 1.5 = 1568.25$ | 36.8, 60.37 | 1.9, 3.26 | 82.22, 79.78 | 1.9×10^{-5} , 8.58×10^{-7} |

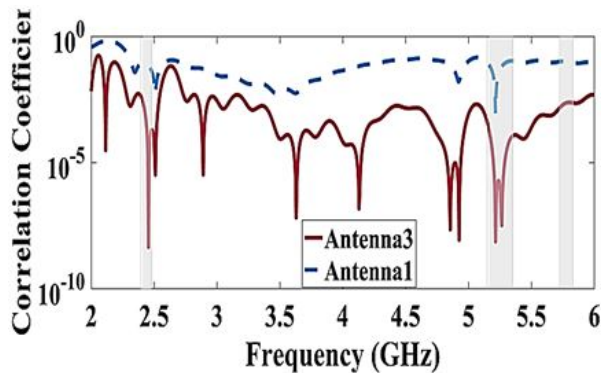


Fig. 11. The calculated envelope correlation coefficient of the proposed MIMO antenna.

C. TARC (Total Active Reflection Coefficient)

The total active reflection coefficient (TARC) denotes the significance of non-variance of the resonance frequency and IBW (Impedance Bandwidth) even when the phase of the input signals, for example, θ , varies with regard to the other antenna elements [27]. The following formulae can be used to calculate it.

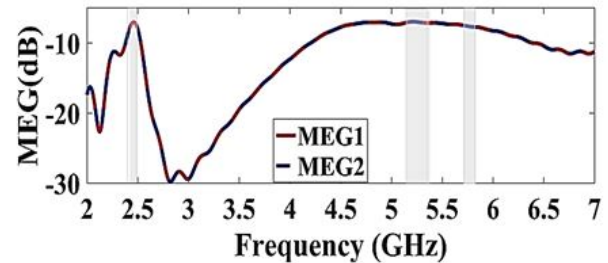


Fig. 12. The calculated mean effective gain of antenna3.

$$\text{TARC} = \frac{\sqrt{|S_{11} + S_{12}e^{j\theta}|^2 + |S_{21} + S_{22}e^{j\theta}|^2}}{\sqrt{2}}. \quad (11)$$

In Figure 13, θ is consistently changed by 30° steps, but the calculated TARC preserves the reflection coefficient pattern in each case, preserving the resonance characteristic even when the phase of the signal changes.

The comparisons between the proposed antenna and the previously reported MIMO antennas are listed in Table 2. Compared with [5,9,12,17,18,23,24] the pro-

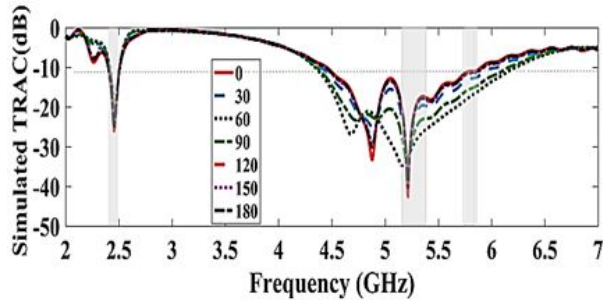


Fig. 13. Variation of total active reflection coefficient with a phase angle of antenna3.

posed MIMO antenna has a smaller edge-to-edge distance and size. Compared with [2,5,9,16,17,19,23,24] the proposed MIMO antenna shows higher isolation and efficiency. It is clear that the proposed design provides a low correlation coefficient as compared to those achieved by the other listed works.

IV. CONCLUSIONS

A proposed design of a multi-input multi-output (MIMO) antenna system for wireless devices operating at WLAN (2.45, and 5.25 GHz) bands has been demonstrated in this paper. Each of the two antennas has the shape of two-folded monopoles that cover the 2.45 GHz, and the 5.25–5.775 GHz bands. A new decoupling mechanism in the form of two L-shaped slots and a U-shaped slot is investigated. Three slots on the substrate are inserted between the radiating patches of the MIMO antenna to provide a further reduction in the mutual coupling. The MIMO elements were placed at a small distance of $0.055\lambda_0$ (edge to edge). The mutual coupling at the 2.45, 5.2, and 5.775 GHz bands was suppressed to -36.86 dB, -60.3 , and -20.61 dB, respectively. The simulated antenna gain is equal to 1.96 dB and the efficiency is 85.85% within the WLAN 2.45 GHz band while the gain is 3.3 dB and the efficiency is 78.16% within the WLAN 5.25 GHz band. The proposed MIMO antenna provides compact size, simple structure, high isolation, and low ECC.

REFERENCES

- [1] D.-L. Shen, L. Zhang, Y.-C. Jiao, and Y.-D. Yan, "Dual-element antenna with high isolation operating at the WLAN bands," *Microwave Optical Technology Letters*, vol. 61, pp. 2323-2328, 2019.
- [2] S. Pandit, A. Mohan, and P. Ray, "A compact four-element MIMO antenna for WLAN applications," *Microwave Optical Technology Letters*, vol. 60, pp. 289-295, 2018.
- [3] C. Hao, H. Zheng, J. Zhang, and X. Sun., "The deployment of stub structures for mutual coupling reduction in MIMO antenna applications," *Progress In Electromagnetics Research Letters*, vol. 92, pp. 39-45, 2020.
- [4] W.-H. Chang and S.-W. Su, "Very-low-profile, decoupled, hybrid two-antenna system using top-loaded, coupled strip resonator for notebook computer applications," *Progress In Electromagnetics Research M*, vol. 84, pp. 63-72, 2019.
- [5] K. Sharma, and G. P. Pandey, "Two-port compact MIMO antenna for ISM band applications," *Progress In Electromagnetics Research C*, vol. 100, pp. 173-185, 2020.
- [6] T. Agrawal and S. Srivastava, "Compact MIMO antenna for multiband mobile applications," *Journal of Microwaves, Optoelectronics, and Electromagnetic Applications*, vol. 16, no. 2, pp. 542-552, Jun. 2017.
- [7] K. V. Babu, and B. Anuradha, "Analysis of multi-band circle MIMO antenna design for C-band applications," *Progress In Electromagnetics Research C*, vol. 91, pp. 185-196, 2019.
- [8] R. Addaci, A. Diallo, C. Luxey, P. L. Thuc, and R. Staraj., "Dual-band WLAN diversity antenna system with high port-to-port isolation," *IEEE Antenna and Wireless Propagation Letters*, vol. 11, pp. 244-247, 2012.
- [9] W. Wu, R. Zhi, Y. Chen, H. Li, Y. Tan, and G. Liu., "A compact multiband MIMO antenna for IEEE 802.11 a/b/g/n applications," *Progress In Electromagnetics Research Letters*, vol. 84, pp. 59-65, 2019.
- [10] B. Qian, X. Chen, and A. A. Kishk, "Decoupling of microstrip antennas with defected ground structure using the common/differential mode theory," *IEEE Antennas and Wireless Propagation Letters*, vol. 20, no. 5, pp. 828-832, Mar. 2021.
- [11] A. A. Abdulhammed, A. S. Abdullah, H. M. Al Sabbagh, and H. K. Bashir., "Mutual coupling reduction of a (2×1) MIMO antenna system using parasitic element structure for WLAN applications," *Journal of Emerging Trends in Computing and Information Sciences*, vol. 6, no. 11, pp. 605-613, Nov. 2015.
- [12] X. Zou, G. M. Wang, Y. W. Wang and B. F. Zong, "Decoupling of dual-band closely spaced MIMO antennas based on novel coupled resonator structure," *Frequenz*, vol. 72, no. 9-10, pp. 437-441, 2018.
- [13] D.-G. Yang, D. O. Kim, and C.-Y. Kim, "Design of dual-band MIMO monopole antenna with high isolation using slotted CSRR for WLAN," *Microwave and Optical Technology Letters*, vol. 56, no. 10, pp. 2252-2257, Oct. 2014.

- [14] A. Iqbal, A. Altaf, M. Abdullah, M. Alibakhshikari, E. Limiti, and S. Kim, "Modified U-shaped resonator as decoupling structure in MIMO antenna," *Electronics*, vol. 9, no. 8, pp. 1-13, Aug. 2020.
- [15] M. Yang, and J. Zhou, "A compact pattern diversity MIMO antenna with enhanced bandwidth and high-isolation characteristics for WLAN/5G/ WiFi applications," *Microwave Optical Technology Letters*, vol. 62, no. 6, pp. 2353-2364, 2020.
- [16] R. N. Tiwari, P. Singh, B. K. Kanaujia, S. Kumar and S. K. Gupta "A low profile dual band MIMO antenna for LTE/Bluetooth/Wi-Fi/WLAN applications," *Journal of Electromagnetic Waves and Applications*, vol. 34, no. 9, pp. 1239-1253, Jan. 2020.
- [17] J.-H. Chou, J.-F. Chang, D.-B. Lin, and T.-L. Wu, "Dual-band WLAN MIMO antenna with a decoupling element for full-metallic bottom cover tablet computer applications," *Microwave Optical Technology Letters*, vol. 60, pp. 1245-1251, 2018.
- [18] S. R. Govindarajulu, A. Jenkel, R. Hokayem, and E. A. Alwan, "Mutual coupling suppression in antenna arrays using meandered open stub filtering technique," *IEEE open journal of Antenna and Propagation*, vol. 1, pp. 379-386, Jul. 2020.
- [19] H. Yon, N. H. Abd Rahman, M. A. Aris, M. H. Jamaluddin, and H. Jumaat, "Parametric Study on Mutual Coupling Reduction for MIMO Future 5G Antennas," *Journal of Electrical and Electronic Systems Research*, vol. 16, pp. 59-64, Jun. 2020.
- [20] S. P. Biswal, S. K. Sharma, and S. Dasi, "Collocated microstrip slot MIMO antennas for cellular bands along with 5G phased array antenna for user equipment (UEs)," *IEEE Access*, vol. 8, pp. 209138-209152, 2020.
- [21] K. H. Sayidmarie and L. S. Yahya, "Double-monopole crescent-shaped antennas with high isolation for WLAN and WIMAX applications," *Antenna Fundamentals for Legacy Mobile Applications and Beyond*, Springer International Publishing, pp. 53-70, 2018.
- [22] L. S. Yahya, K. H. Sayidmarie, F. Elmegri and R. A. Abd-Alhameed, "Arc-shaped monopole antennas with reduced coupling for WLAN and WIMAX applications," *IEEE Internet Technologies and Applications (ITA)*, Wrexham, UK, pp. 218-223, 2017.
- [23] Y. Yu, L. Yi, X. Liu, and Z. Gu, "Mutual coupling reduction of dual-frequency patch antenna arrays," *Applied Computational Electromagnetics Society (ACES) Journal*, vol. 31, no. 9, pp. 1092-1099, Sep. 2016.
- [24] T. Jiang, T. Jiao, and Y. Li., "A Low mutual coupling MIMO antenna using periodic multi-layered electromagnetic band gap structures," *Applied Computational Electromagnetics Society (ACES) Journal*, vol. 33, no. 3, pp. 305-311, Mar. 2018.
- [25] G. Kumer and K. P. Ray, "Broadband Microstrip Antennas," *Artech House*, 2003.
- [26] H. U. Iddi, M. R. Kamarudin, T. Abdrahman, A. Y. Abdurahman, R. Dewan, and A. S. Azin, "Triple band planar monopole antenna for MIMO application," *Progress In Electromagnetics Research Symposium Proceedings*, Sweden, Aug. 12-15, pp. 1421-1424, 2013.
- [27] A. Kumar, A. Q. Ansari, B. K. Anaujia, J. Kishor, and N. Tewari, "Design of triple-band MIMO antenna with one band-notched Characteristic" *Progress In Electromagnetics Research C*, vol. 86, pp. 41-53, 2018.



Likaa S. Yahya was born in Mosul, Iraq, in 1970. She received a B.Sc. degree in Electrical Engineering from the University of Mosul, Iraq, in 1992, and an M.Sc. degree in Communication Engineering from the University of Mosul, in 2002 and Ph.D. Degree in Communication

Engineering from the University of Mosul, in 2017. She is currently a Lecturer at the Dept. of Electronic Techniques, Northern Technical University, Mosul, Iraq. Her interest includes multiband antenna design and antenna modeling.



Loay S. Yahya was born in Mosul, Iraq, in 1963. He received a B.Sc. degree in Electrical Engineering from the University of Mosul, Iraq, in 1985, and an M.Sc. degree in Computer Engineering, University of Mosul, in 2005. He is currently an Assistant-Lecturer at the

Dept. of Electronic Techniques, Northern Technical University, Mosul, Iraq. His interest includes Neural Network, Recognition Systems, and antenna design.



Khalil H. Sayidmarie received a B.Sc. degree in Electronics and Communication Engineering from Mosul University, Iraq, in 1976, and Ph.D. Degree in Antennas and Propagation from Sheffield University, U.K. in 1981. Then he joined the College of Engineering at Mosul University in 1983 and was promoted to full professor in 1992. He worked as the head of the electrical engineering department for 9 years. Mr. Sayidmarie

served as Prof. of communication engineering at the College of Engineering, University of Amman, Jordan from October 2006 to September 2009, and as the Dean of that college from September 2008 to September 2009. He has been Prof of communication engineering at the college of electronic engineering, Ninevah University since July 2002. He is now Professor Emeritus with the college of electronics engineering, Ninevah University. His research interests cover antennas, propagation, and microwaves, and he has published more than 130 papers in international journals and conferences.

A Compact Dual-band Planar Antenna Loaded with Magneto Dielectric Ferrite

Yongwei Li, Quanyuan Feng, and Zongliang Zheng

School of Information Science and Technology, Southwest Jiaotong University, Chengdu 611756, China
liyongwei_101@qq.com, fengquanyuan@163.com, zlzheng@swjtu.edu.cn

Abstract – In this paper, a compact dual-band planar antenna loaded with magnetodielectric ferrite is proposed for ISM/GSM/UMTS. Slot and ring structures are dual-resonant mode generators of the antenna. And the characteristic mode analysis is used for the modeling, analysis, and optimization of the proposed antenna. Because of the loading of a piece of rectangular Co₂W hexaferrite medium, this antenna can be used in lower frequency bands. The electromagnetic parameters of this ferrite are measured by the transmission line method. Finally, the antenna is fabricated and measured. The operation frequency band ($S_{11} < -10$ dB) is determined to be 80 MHz (890–970 MHz) and 370 MHz (1.87–2.24 GHz) with the dual resonance frequencies of 925 MHz and 2.175 GHz, respectively, which is capable for ISM (915 MHz)/GSM900/UMTS applications.

Index Terms – dual-band, miniaturized antenna, magnetodielectric ferrite, characteristic mode analysis, planar antenna.

I. INTRODUCTION

With the arrival of 5G, wireless communication equipment integrates more and more applications. A communication device needs to work in multiple frequency bands. Many multiple-input–multiple-output (MIMO) antennas have been proposed to solve this problem [1–4]. MIMO antenna conforms to the development trend of communication. At the same time, the compatibility design of MIMO antenna elements is relatively complex. And broadband antenna is also an inevitable trend [5–7]. The design of a miniaturized planar broadband antenna is very difficult and demanding. Therefore, to make full and accurate use of spectrum resources, the design of a multi-frequency antenna is more in line with the actual needs. In recent years, many types of research on multi-frequency antennas have been proposed. In comparison with patch antennas, slot antennas have advantages including easier implementation of multiband, wider potential bandwidth, and more stability to fabrication tolerances [8]. Among them, the slot struc-

ture composed of multiple rings is widely used. A compact multiband circularly polarized (CP) slot antenna loaded with metallic strips and a split-ring resonator (SRR) is proposed in [9]. The use of SRR or new structures derived from SRR can enlarge bandwidth, produce resonance frequency, and change radiation polarization, etc. In [10], a ring monopole antenna coupled with an electric-inductive-capacitive (ELC) meta material element achieves better return loss characteristics. In [11], the use of a hexagonal complementary split-ring resonator (HCSRR) is capable of creating a new resonance frequency for an antenna. The paper [12] shows that the combination of multiple structures can produce multi-frequency characteristics. The change of the ground plane can also affect the resonance characteristics of the antenna. In article [13], the design of using SRRs on the partial ground plane generates multiple circularly polarized bands. In [14], the metasurface (MS)-based artificial ground composed of CRRS is loaded on the dual-band antenna. SRR and MS structures have great advantages for the design of multi-frequency antennas.

With the rapid development of circuit integration, the size of wireless communication equipment is getting smaller and smaller, leaving less and less space for the antenna. The existing miniaturized antenna has been difficult to meet the space given by the increasingly highly integrated equipment. The dielectric material loading method is a useful and promising technique to make a better performance for antennas [15]. Magnetic and dielectric properties are the two main physical properties used by many electronic components. In the past, the research on the miniaturization of microwave devices relatively focuses on the innovation of device structure and advanced manufacturing and packaging technology. More attention should be paid to new media materials with high performance. Ferrite with both dielectric and magnetic properties deserves attention. At present, the research of antenna miniaturization by improving the structure has reached the bottleneck, and the research of antenna miniaturization by using high-performance media is becoming more and more important. Recently, some novel

high-frequency magnetodielectric properties ferrites for RF and microwave device applications have been synthesized [16, 17].

The research of high-frequency magnetodielectric properties ferrites loaded antenna will be of great significance. In this paper, a compact dual-band antenna with magnetodielectric ferrite loaded is proposed for ISM (915 MHz)/GSM900/UMTS. Because of the loading of a piece of magnetodielectric ferrite, the presented antenna can be used in lower frequency bands. The arrangement of ferrite affects the radiation characteristics of an antenna. The proposed antenna is fabricated and measured. For the operation band, the proposed antenna provides very relatively small size and good performance. The antenna is designed and analyzed in Section II. The results of the antenna are analyzed in Section III, followed by conclusion in Section IV.

II. DESIGN AND ANALYSIS OF DUAL-BAND ANTENNA

The configuration of the proposed compact dual-band antenna with magnetodielectric ferrite loaded is illustrated in Figure 1. The antenna is fabricated in an FR4 substrate with the thickness of 1.6 mm, dielectric constant of 4.4 and dielectric loss of 0.02. The top layer of the antenna as shown in Figure 1 (a) consists of two square rings (TSRs) and a patch connected by stubs. The feed mode of the antenna is side feed, and the feed line is also on the upper surface of the antenna. The bottom layer of the antenna as shown in Figure 1 (b) consists of a square ring ground plane (SRGND) and an H-shaped structure with an angle of 45.0° to the feed line. Figure 1 (c) is the side view of this antenna. A rectangular Co_2W hexaferrite medium with thickness of 0.6 mm, relative dielectric constant of 14, and relative permeability fre-

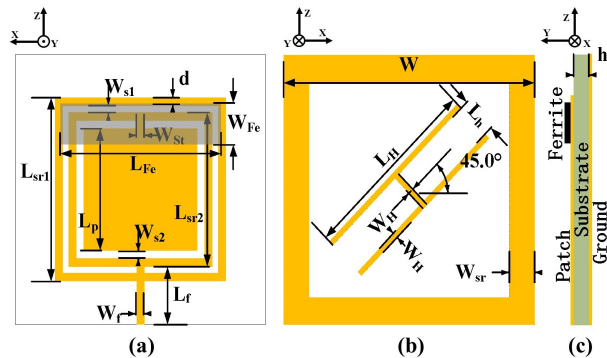


Fig. 1. Configuration of the proposed antenna. (a) top view, (b) bottom view, (c) side view. (Unit: mm $W = 50$, $H = 1.6$, $L_{Fe} = 33$, $W_{Fe} = 7$, $L_{sr1} = 34$, $L_{sr2} = 28.6$, $d = 1.5$, $W_{st} = 1.5$, $L_f = 10.7$, $W_f = 1.5$, $W_{sr1} = 5$, $L_H = 18$, $L_p = 22.6$, $W_{s1} = 1.2$, $W_{s2} = 1.7$, $W_H = 1$, $L_h = 7$.)

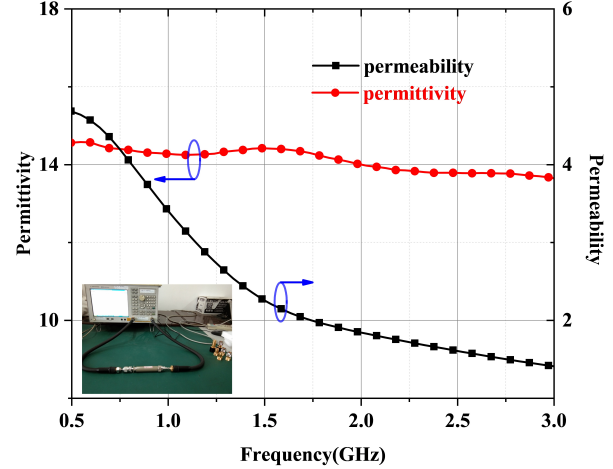


Fig. 2. The measurement results of the permittivity and permeability of the ferrite used in this paper.

quency dependent was loaded at the gap of TSRs on the upper surface. The Key sight materials measurement suite is used to measure the electromagnetic parameters of this ferrite. The result of the measurement is shown in Figure 2.

A. Analysis of the dual-band antenna without ferrite

The resonant mode generated by the discrete elements of the antenna is the basis for generating dual bands [8, 18]. This can be analyzed by applying the theory of characteristic mode (TCM) to the elements under consideration. A more convenient way to measure the resonant frequency and potential contribution to the radiation of a mode is to define the Modal Significance (MS) whose range is 0 to 1. The mode resonates and radiates the most efficiently when $MS = 1$ [19, 20].

TSR and SRGND structures are designed to apply the ferrites mentioned above. As shown in Figure 3, the resonant mode of the TSR is at 2.4 GHz, which is a half-wavelength resonance, and that of the SRGND are at 1.6 GHz and 2.7 GHz, which are a half-wavelength resonance and a full-wavelength resonance. It can be observed that the resonant modes of the two main elements are distributed at about 1.6 GHz and 2.5 GHz. In order to make the resonant modes of the two elements work together, a patch is designed in the center of the TSR, forming a TSR + Patch structure (TSRP). Two square slots formed by TSRP can generate two resonant modes [8]. It can be seen from Figure 3 that the resonant modes of TSRP designed in this paper are 2.13 GHz and 1.68 GHz. According to the reference [21, 22], an asymmetric structure can affect the mechanism of dual-band resonance; this paper designs a tilted H-shaped structure at the bottom to form an asymmetric ground plane and adjust the dual-band res-

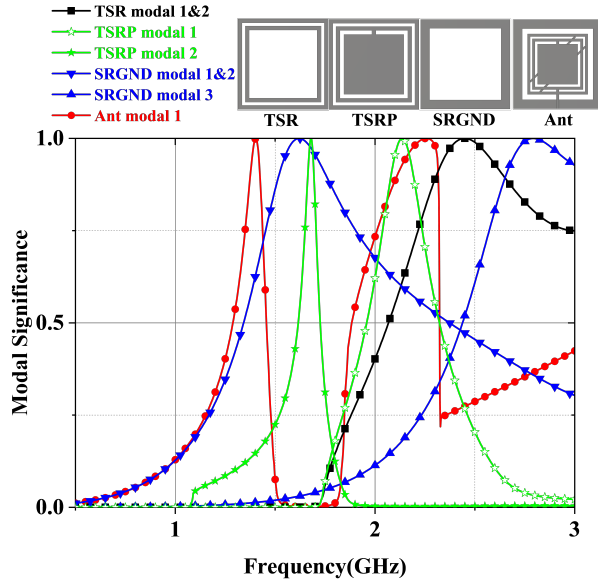


Fig. 3. The modal significance of TSR, SRGND, and the antenna without ferrite. (The frequency range from 0.5 GHz to 3 GHz.).

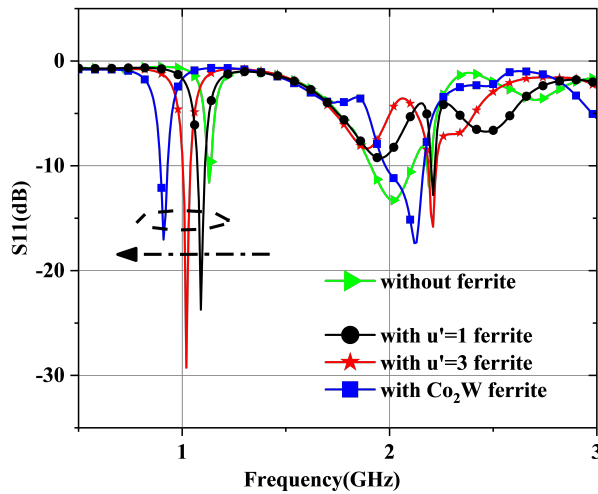


Fig. 4. The simulation S_{11} of the proposed antenna without ferrite and the simulation S_{11} of the antenna with different permeability ferrite (Other parameters of ferrite keep the same as the Co_2W hexaferrite).

onance point of the antenna. Finally, Ant is obtained. It can be seen from Figure 3 that there are two resonant modes of the Ant, one at 1.4 GHz and the other at 2.2 GHz. It can be seen that the resonant frequency of the whole antenna migrates toward the lower frequency. Through the above method we design a dual-band antenna, and the simulation S_{11} parameters are shown in Figure 4.

B. Compact dual-band planar antenna with ferrite loading

The wavelength of the electromagnetic wave in a medium is largely affected by a factor ($n = n(\mu' \epsilon')^{1/2}$, where μ' is the real part of permeability and ϵ' is the real part of permittivity). The size of the antenna is also closely related to the n of the loaded medium [17]. In this paper, a Co_2W hexaferrite is used. As can be seen from Figure 2, the value of permittivity is relatively stable with frequency, while the permeability decreases sharply with the increase of frequency. Therefore, the ferrite load should have a greater impact on the antenna's low-frequency operating band. The simulation S_{11} of the antenna loaded with a ferrite having the same permittivity and different permeability is shown in Figure 4. In the simulation, only the permeability of ferrite is changed. As the permeability increases, the resonance frequency of the antenna in the low frequency operation band shifts to the left. When Co_2W hexaferrite is loaded on the proposed antenna, the low frequency operation band of the antenna will move to a lower frequency band. The miniaturization of the antenna is realized in this way. To study the effect of ferrite loading on the radiation characteristics of the antenna, the current distribution comparison of the antenna before and after ferrite loading is shown in Figure 5. Through the comparison of Figure 5 (a) and (b), it can be concluded that the current of the antenna with the proposed structure is concentrated near the ferrite when the ferrite is loaded. It can be seen from Figure 5 (c) and (d) that the effect

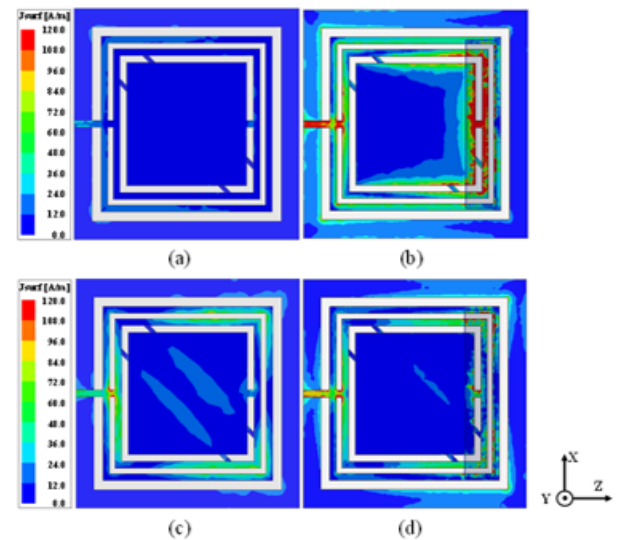


Fig. 5. The current distribution comparison of the presented antenna. (a) at 0.925 GHz, without ferrite, (b) at 0.925 GHz, with ferrite, (c) at 2.175 GHz, without ferrite, (d) at 2.175 GHz, with ferrite.

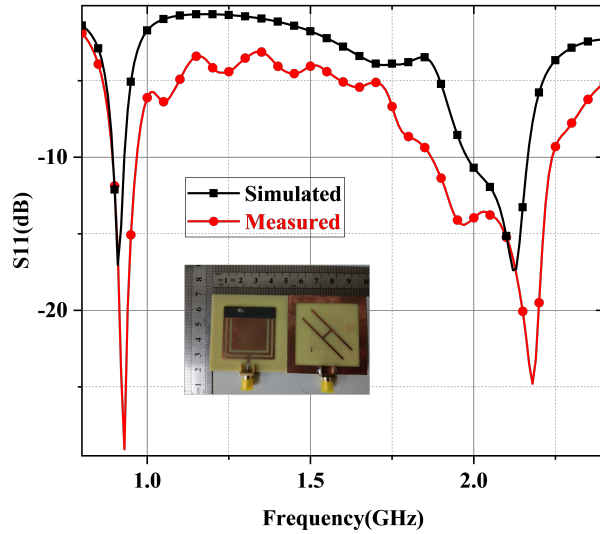


Fig. 6. The simulation and measurement S_{11} of the proposed compact dual band antenna with magnetodielectric ferrite loading.

of ferrite loading on the antenna is not obvious around 2.175 GHz. The S_{11} of the simulation and measurement of the proposed compact dual-band antenna with magnetodielectric ferrite loading is shown in Figure 6. The error between simulation result and measurement result is caused by processing technology and the test environment.

III. RESULTS

The radiating performance of the proposed antenna is measured in Satimo anechoic chamber. As observed, the yoz-plane is the E-plane while the xoy-plane is the H-plane of the antenna. The 2-D radiation patterns (yoz- and xoy-planes) of the antenna simulation and measurement are plotted in Figure 7. It can be seen from Figure 7 that in the low-frequency operation band, the radiation characteristics of the antenna loaded with ferrite are better than that of the antenna without ferrite, while in the high-frequency operation band, the influence of loaded ferrite on the radiation characteristics of the antenna is not significant. It can be seen from Figure 7 (a) that in low-frequency band, the simulation trend of the antenna loaded with ferrite is consistent with the measured radiation patterns of the E-plane, but the measured co-polarization radiation pattern of the antenna shows sawtooth, which is caused by the irregular surface of ferrite material. This is a problem caused by the processing process, which can be avoided by improving the technology. Figure 8 shows the measurement results of the peak gain of the proposed antenna in this letter. Through comparison, it is found that the radiation performance of the antenna with ferrite is more

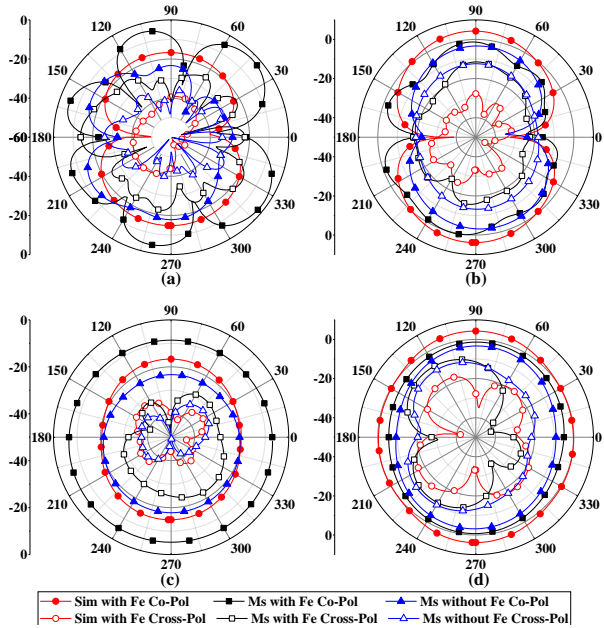


Fig. 7. 2-D radiation patterns of antenna simulation and measurement. (a) E-plane (yoz-plane) at 0.925 GHz, (b) E-plane (yoz-plane) at 2.175 GHz, (c) H-plane (xoy-plane) at 0.925 GHz, (d) H-plane (xoy-plane) at 2.175 GHz.

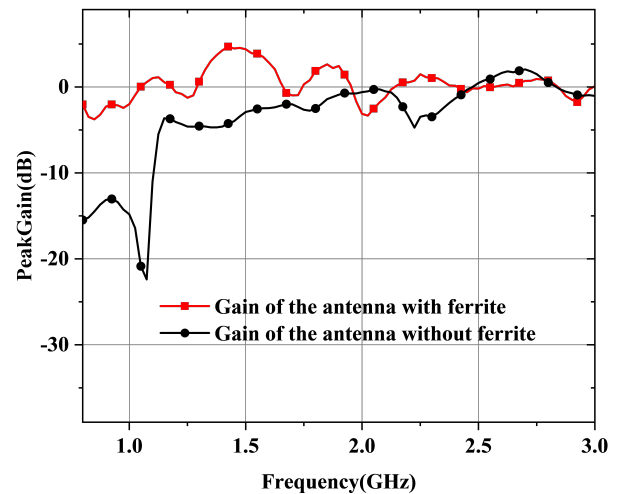


Fig. 8. The measurement peak gain of the proposed antenna.

stable. Furthermore, in Table 1, a comparison of the proposed antenna with the existing multiband antennas is given and it is found that the designed antenna shows improved miniaturized size and fair impedance bandwidth.

Table 1: Performance comparison of the proposed antenna with other reported multi-band antennas

| Ref. | Size | Num. of bands (GHz) | Impedance BW(%) | app | Efficiency(%) |
|-----------|------------------|----------------------|-----------------|----------------------|---------------|
| [9] | $0.093\lambda^2$ | three–1.83, 2.5, 3.1 | 21.4, 12.8, 4.5 | — | 75, 90, 82 |
| [10] | $0.14\lambda^2$ | two–3.74, 5.1 | 13.1, 16.7 | WiMAX/WLAN | 80, 75 |
| [11] | $0.066\lambda^2$ | two–2.56, 4.64 | 7.2, 51.7 | ISM/WiMAX/WLAN | — |
| [12] | $0.054\lambda^2$ | two–1.66, 5.69 | 31.3, 64.85 | Bluetooth/WLAN/WiMAX | — |
| [14] | $0.109\lambda^2$ | two–1.88, 2.5 | 7.5, 12.6 | — | — |
| This work | $0.024\lambda^2$ | two–0.925, 2.175 | 8.6, 18 | ISM/GSM/UMTS | 22, 54 |

λ —wavelength in free space corresponding to the lowest resonant frequency.

IV. CONCLUSION

In this letter, a compact dual-band planar antenna loaded with magnetodielectric ferrite has been fabricated and measured. The characteristic mode analysis (CMA) is used for the modeling, analysis, and optimization of the proposed antenna without ferrite in order to reveal the underlying modal behaviors of each radiating element and to guide the mode excitation. The ferrite used in this paper is a ferrite with high frequency, high permeability, high dielectric, and low loss made by our research group. By studying the simulation and measurement data of the antenna loaded with ferrite and not loaded with ferrite, it is verified that the loaded ferrite has a good influence on the radiation performance of the antenna designed in this paper. At the same time, it is proved that the antenna structure combined with Co₂W hexaferrite can realize the antenna miniaturization.

ACKNOWLEDGMENT

This work is supported by the Key Project of the National Natural Science Foundation of China under Grant 62090012, 62031016, 61831017, the Project Funding under Grant 19-163-21-TS-001-062-01, and the Sichuan Provincial Science and Technology Important Projects under Grant 2019YFG0498, 2020YFG0282, 2020YFG0452 and 2020YFG0028.

REFERENCES

- [1] M. Sonkki, E. Antonino-Daviu, M. Cabedo-Fabres, M. Ferrando-Bataller, and E. T. Salonen, "Improved planar wideband antenna element and its usage in a mobile MIMO system," *IEEE Antennas Wirel. Propag. Lett.*, vol. 11, pp. 826-829, Jul. 2012.
- [2] J. Tao and Q. Y. Feng, "Compact ultrawideband MIMO antenna with half-slot structure," *IEEE Antennas Wirel. Propag. Lett.*, vol. 16, pp. 792-795, Apr. 2017.
- [3] C. Yang, J. Kim, H. Kim, J. Wee, B. Kim, and C. Jung, "Quad-band antenna with high isolation MIMO and broadband SCS for broadcasting and telecommunication services," *IEEE Antennas Wirel. Propag. Lett.*, vol. 9, pp. 584-587, Jul. 2010.
- [4] J. Tao and Q. Y. Feng, "Compact isolation-enhanced UWB MIMO antenna with band-notch character," *J. Electromagn. Waves Appl.*, vol. 30, no. 16, pp. 2206-2214, Jul. 2016.
- [5] J. Guo, Y. Zou, and C. Liu, "Compact broadband crescent moon-shape patch-pair antenna," *IEEE Antennas Wirel. Propag. Lett.*, vol. 10, pp. 435-437, May. 2011.
- [6] T. Wu, H. Su, L. Gan, H. Chen, J. Huang, and H. Zhang, "A compact and broadband microstrip stacked patch antenna with circular polarization for 2.45-GHz mobile RFID reader," *IEEE Antennas Wirel. Propag. Lett.*, vol. 12, pp. 623-626, May. 2013.
- [7] V. P. Sarin, M. S. Nishamol, D. Tony, C. K. Aanandan, P. Mohanan, and K. Vasudevan, "A broadband l-strip fed printed microstrip antenna," *IEEE Trans. Antennas Propag.*, vol. 59, no. 1, pp. 281-284, Jan. 2011.
- [8] J. Li, J. Shi, L. Li, T. A. Khan, J. Chen, Y. Li, A. Zhang, "Dual-band annular slot antenna loaded by reactive components for dual-sense circular polarization with flexible frequency ratio," *IEEE Access*, vol. 6, pp. 64063-64070, Oct. 2018.
- [9] P. M. Paul, K. Kandasamy, and M. S. Sharawi, "A triband circularly polarized strip and SRR-loaded slot antenna," *IEEE Trans. Antennas Propag.*, vol. 66, no. 10, pp. 5569-5573, Oct. 2018.
- [10] R. S. Daniel, R. Pandeewari, and S. Raghavan, "Dual-band monopole antenna loaded with ELC metamaterial resonator for WiMAX and WLAN applications," *Appl. Phys. A-Mater. Sci. Process.*, vol. 124, no. 8, p. 570, Jul. 2018.
- [11] B. Murugeswari, R. S. Daniel, and S. Raghavan, "A compact dual band antenna based on metamaterial-inspired split ring structure and hexagonal complementary split-ring resonator for ISM/WiMAX/WLAN applications," *Appl. Phys. A-Mater. Sci. Process.*, vol. 125, no. 9, p. 628, Aug. 2019.

- [12] B. Bag, P. Biswas, S. Biswas, and P. P. Sarkar, "Wide-bandwidth multifrequency circularly polarized monopole antenna for wireless communication applications," *Int. J. RF Microw. Comput. Eng.*, vol. 29, no. 3, p. e21631, Nov. 2018.
- [13] M. Alam, Mainuddin, B. K. Kanaujia, M. T. Beg, S. Kumar, and K. Rambabu, "A hexa-band dual-sense circularly polarized antenna for WLAN/WiMAX/SDARS and C-band applications," *Int. J. RF Microw. Comput. Eng.*, vol. 29, no. 4, p. e21599, Apr. 2019.
- [14] T. Yue, Z. H. Jiang, and D. H. Werner, "A compact metasurface-enabled dual-band dual-circularly polarized antenna loaded with complementary split ring resonators," *IEEE Trans. Antennas Propag.*, vol. 67, no. 2, pp. 794-803, Feb. 2019.
- [15] A. S. Turk and A. K. Keskin, "Partially dielectric-loaded ridged horn antenna design for ultrawideband gain and radiation performance enhancement," *IEEE Antennas Wirel. Propag. Lett.*, vol. 11, pp. 921-924, Aug. 2012.
- [16] Z. L. Zheng, Y. W. Li, T. Liu, and Q. Y. Feng, "Novel high-frequency magneto-dielectric properties of CaO-SiO₂ Co-Doped NiZnCo spinel ferrites for RF and microwave device applications," *IEEE Trans. Magn.*, vol. 54, no. 11, pp. 1-4, Nov. 2018.
- [17] Z. L. Zheng, Q. Y. Feng, Q. Y. Xiang, Z. X. Di, and V. G. Harris, "Low-loss NiZnCo ferrite processed at low sintering temperature with matching permeability and permittivity for miniaturization of VHF-UHF antennas," *J. Appl. Phys.*, vol. 121, no. 6, p. 063901, Feb. 2017.
- [18] R. Aldhaheri, I. Alruhaili, K. Babu, and M. Sheikh, "A compact CPW-Fed UWB antenna with dual-band notched characteristics for WiMAX/WLAN applications," *Appl. Comput. Electromagn. Soc. J. (ACES)*, vol. 36, no. 2, pp. 145-151, Feb. 2021.
- [19] F. H. Lin and Z. N. Chen, "Low-profile wideband metasurface antennas using characteristic mode analysis," *IEEE Trans. Antennas Propag.*, vol. 65, no. 4, pp. 1706-1713, Apr. 2017.
- [20] J. Monica and P. Jothilakshmi, "Multifold bandwidth improvement in conformal patch antenna for aircraft application using corrugated edge coupling," *Appl. Comput. Electromagn. Soc. J. (ACES)*, vol. 36, no. 5, pp. 577-588, May. 2021.
- [21] Y. Li, W. Li, and R. Mittra, "A compact ACS-FED dual-band meandered monopole antenna for Wlan and WiMax applications," *Microw. Opt. Technol. Lett.*, vol. 55, no. 10, pp. 2370-2373, Oct. 2013.
- [22] Y. Li, W. Li, and Q. Ye, "A compact asymmetric coplanar strip-fed dual-band antenna for 2.4/5.8

GHz Wlan applications," *Microw. Opt. Technol. Lett.*, vol. 55, no. 9, pp. 2066-2070, Sept. 2013.



Yongwei Li received the M.S. degree in computer science and technology from Southwest Jiaotong University, Chengdu, in 2012. He is currently pursuing the Ph.D. degree in information and communication engineering with Southwest Jiaotong University, Chengdu, China.

His current research interests include antenna theory, implantable antennas, antenna miniaturization design, meta material antenna design, multi frequency antenna design, and circularly polarized antenna design.



Quanyuan Feng received the M.S. degree in microelectronics and solid electronics from the University of Electronic Science and Technology of China, Chengdu, China, in 1991 and the Ph.D. degree in electromagnetic field and microwave technology from Southwest Jiaotong University, Chengdu, in 2000.

He is currently the Head of the Institute of Microelectronics, Southwest Jiaotong University. He has been honored as the Excellent Expert and the Leader of Science and Technology of Sichuan Province owing to his outstanding contribution. He has authored or co-authored more than 500 papers published on the IEEE Transactions on Antennas and Propagation, the IEEE Transactions on Microwave Theory and Techniques, and the IEEE Antennas and Wireless Propagation Letters, among which more than 300 papers were registered by the Scientific Citation Index (SCI) and Engineering Index (EI). His current research interests include integrated circuit design, RFID technology, embedded system, wireless communications, antennas and propagation, microwave and millimeter-wave technology, smart information processing, electromagnetic compatibility, and RF/microwave devices and materials.



Zongliang Zheng received the Ph.D. degree in electronic science and technology from the University of Electronic Science and Technology of China, Chengdu, China, in 2016. From 2014 to 2015, he was a visiting scholar at the Department of Electrical and Computer Engineering,

Northeastern University, Boston, USA. In 2016,

he joined the School of Information Science and Technology, Southwest Jiaotong University, Chengdu, China, as an assistant professor and master's supervisor. His research interests include microwave magnetic materials and devices, novel antenna designs, magnetodielectric materials for antenna applications, RFID technology. In recent years, Dr. Zheng has authored or co-authored more than 50 academic papers and invited papers in

international journals and conference proceedings. He has also served as reviewer members for many journals and conferences, such as IEEE T-MTT, IEEE T-MAG, IEEE Access, IEEE INTERMAG Conference, etc. He now acts as the principle investigator for projects of National Natural Science Foundation of China (NSFC) and Sichuan Project of Science and Technology.

A Gain-enhanced Dual-band Microstrip Antenna using Metasurface as Superstrate Configuration

HuQiang Tian, JunLin Wang, Ding Han, and Xin Wang

College of Electronic and Information Engineering
Inner Mongolia University, Hohhot, 010021, China
13240880198@163.com, wangjunlin@imu.edu.cn,
handinghanding@126.com, wangxin219@imu.edu.cn

Abstract – In this paper, antenna gain enhancement using a metasurface (MS) which is designed over the FR4 dielectric by introducing a periodic arrangement of unit cells on a microstrip patch antenna is presented. Combined with the theoretical proof, a method of loading low-frequency MS structure on microstrip antenna is proposed and the antenna gain is improved by using the superposition principle of electric field above the antenna. The proposed antenna is fabricated and measured. It achieves a 4.49 dBi gain enhancement and 8.27 dBi gain enhancement when the superstrate is added over the microstrip antenna at the design frequency of 2.4 GHz and 1.8 GHz, respectively. Since there are a large number of electromagnetic waves in this frequency band in the environment, it can be extended to the study of RF energy collection and other aspects.

Index Terms – antenna gain, microstrip antennas, slotted fractal patch.

I. INTRODUCTION

In the modern technology era, the demand for efficient, low-cost, and high-gain operating antennas is quite high. This can significantly reduce the waste of communication resources. Increasing antenna gain has the advantages of increasing transmission distance and reducing transmitter power consumption [1–5]. One of the methods of increasing the gain is to use an array antenna. However, the loss and complexity of the feed network increase with the increase in the number of antenna units. To overcome the drawbacks of the feeding network, a Fabry–Perot cavity antenna is proposed [6, 7].

In recent years, metasurface (MS) structures have been incorporated into various processes, such as the optical and microwave frequency domain; manipulating incident electromagnetic waves and reaching the phase reflection of the surface wave can be controlled [2–5]. The surface impedance of the MS can be executed by structuring the MS unit cells that also enable beam

shaping [9–11]. In addition, the MS structure with double negative (DNG) electromagnetic characteristics is superior to the MS structure with single negative (SNG) electromagnetic characteristics in terms of gain, bandwidth, and antenna efficiency [8]. Hence, the MS can be found in a broad range of applications, namely surface wave absorbers, surface waveguides, cloaking, polarization converters, antennas, modulators, and so on [9–13].

In this paradigm, a miniaturized and high-gain dual-band microstrip antenna with MS structure is proposed in which the square patch array of 1×5 is designed above and below it and integrate geometric figures with short-circuit via on the surface of the patch [14–16]. So as to achieve the control of the required frequency band parameters. By loading two semi-circular grooves on the ground, reflectance is controlled by merging two semicircular slots on the ground. The antenna gain is enhanced by a 9×9 MS as the upper layer of the antenna [17–22]. The design uses HFSS2020 software to simulate the return loss of 17 dB and 27 dB at 1.8 GHz and 2.4 GHz, respectively. In addition, in this design, the bandwidth of the model under MS coverage increases by 6.9%. At 1.8 GHz, the single radiation gain of the antenna increases to 4.49 dBi, and at 2.4 GHz, the antenna gain increases to 8.27 dBi. Since there are a large number of electromagnetic waves in this frequency band in the environment, it can be extended to the study of RF energy collection and smart sensing.

II. THEORETICAL APPROACH

A. In-phase calculations on different effective permittivity superstrates

The electric-field distribution of the antenna aperture and the radiation pattern have a Fourier transform relationship. To create a high-gain antenna, it is not only necessary to have a larger antenna aperture, but there should also be an in-phase electric field on the aperture. Assume a point source as shown in Figure 1. The phase of the electric field some distance away from the point source is dependent on the distance. The phase difference ($\Delta\epsilon$) between points P1 and P2 can be expressed by

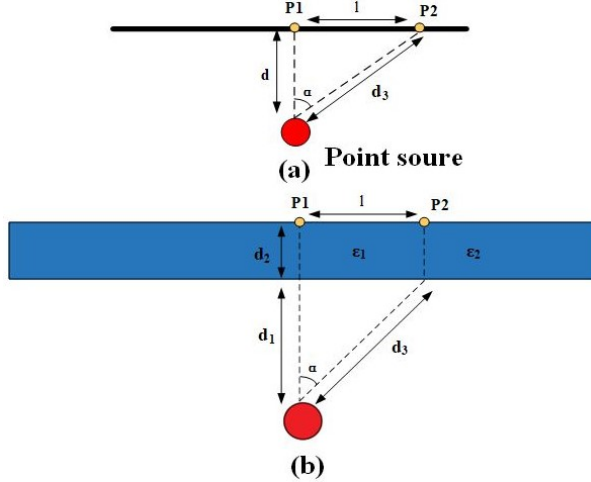


Fig. 1. (a) Phase difference between two points for the air. (b) Proposed superstrate [7].

the following equation [7]

$$2n\pi + \Delta\epsilon = \beta_0 (\sqrt{d_3 - d_1}). \quad (1)$$

Where β_0 is the propagation constant in the air, d is the distance between the point source and P1. l is the distance between P1 and P2. According to Figure 1 (a), the phase difference is always nonzero when the distance l is not zero. When a dielectric layer, which has a thickness of d_2 with a different permittivity determined by its position is located above the point source at a distance of d , the phase difference ($\Delta\epsilon$) between points P1 and P2 can be expressed by the following equation [7], assuming that there is no reflection between the dielectric layer and the air:

$$2n\pi + \Delta\epsilon = \beta_0 (\sqrt{d_3 - d_1}) + d_2\beta_0 (\sqrt{\epsilon_1} - \sqrt{\epsilon_2}), \quad (2)$$

where ϵ_2 is the permittivity at P2 and ϵ_1 is the permittivity at P1. According to Figure 1 (b), the phase difference $\Delta\epsilon$ can be set to zero by changing ϵ_2 .

B. Principle of gain increase

An ideal Fabry–Perot resonator is composed of two parallel infinite uniform and an ideal point antenna. It is assumed that the electromagnetic wave has no loss in the transmission state, and the edge effect is ignored. The radiation source emits electromagnetic waves with a wavelength of λ and a frequency of f . In the case of GND total reflection, its reflection coefficient is $e^{j\varphi_2}$. The reflection coefficient of FSS is p , that is, the reflection coefficient is $pe^{j\varphi_1}$. Since the distance between the radiation plates is d , According to eqn (3) the electric field amplitude E_0 changes to E , after multiple reflections and transmissions [8].

$$E = \sum_{n=0}^{\infty} f(\alpha) E_0 p^n \sqrt{1-p^n} e^{j\varphi_n}. \quad (3)$$

Among them, φ_n is the phase difference between electromagnetic beam n and beam 1, $f(\alpha)$ is the directional pattern in the direction of a degree from the radiation source and the GND normal line, and the electric field amplitude is E_0 . Therefore, the phase difference between any beam and beam 1 can be written as [8]

$$\varphi_n = n\varphi = n \left(-\frac{4\pi}{\lambda} d \cos\alpha - \varphi_1 + \varphi_2 \right). \quad (4)$$

Thus, the far-field energy density S can be obtained as

$$S = \frac{1-p^2}{1+p^2-2p\cos(\varphi_1+\varphi_2-\frac{4\pi}{\lambda}d\cos\alpha)}. \quad (5)$$

So when α is 0, S will be the maximum [8]

$$S_{\max} = \frac{1+p}{1-p} S_0. \quad (6)$$

Where S_0 is the energy density in this direction when the overburden is not load. According to eqn (6), the far-field energy density of the antenna is related to the value of p . Therefore, the antenna gain can be improved by carrying FSS matching with the antenna [9]. In addition, the height of MS distance from the antenna L can also be calculated from eqn (7)

$$L = \frac{c}{2f} \left(\frac{\varphi_1 + \varphi_2}{2\pi} - n \right). \quad (7)$$

III. DESIGN AND SIMULATION OF THE PROPOSED ANTENNA

The designed antenna is fed by a coaxial feeding mode and is divided into the metal–dielectric–metal three-layer structure. GND regulates resonant frequency and increases the impedance bandwidth by slot. The middle metal patch at the top of the antenna is set with four annular slots for parameter regulation, and the square patch with regular arrangement is set up to improve the antenna gain. The primary radiating element and the bottom layer of the antenna are separated by a 1.6 mm thick FR4 dielectric layer (loss tangent = 0.002 and relative permittivity 4.4).

An MS was used in the structure by combining a periodic structure of unit cells which is composed of a symmetric curl structure to significantly improve the gain of the antenna. The MS layer is also organized on the FR4 dielectric with a thickness of 1.6 mm. Moreover, the bottom layer of the antenna is separated by a 1.6 mm thick FR4 dielectric layer (loss tangent = 0.002 and relative permittivity 4.4). The optimized geometric dimensions of the 3-D structure and the back view and top view of the traditional antenna are shown in Figure 2 (a)–(c), respectively.

A 50 Ω lumping feed was fed into this antenna using an SMA connector through the substrate and ground layer. The designed antenna works in WIFI and GSM

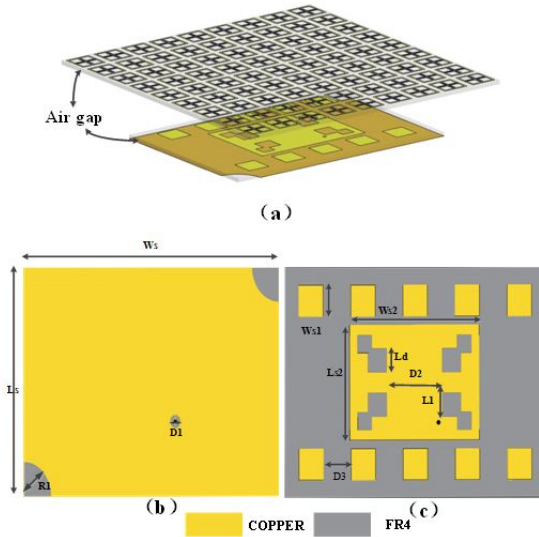


Fig. 2. (a) 3-D antenna model, (b) Conventional antenna back view, (c) Top view of the conventional patch (Design optimization parameters: $W_s = 74.52$ mm, $L_s = 51.8$ mm, $D_1 = 3.0$ mm, $R_1 = 8$ mm, $W_{s1} = 7$ mm, $W_{s2} = 37.26$ mm, $L_d = 5.3$ mm, $L_{s2} = 25.9$ mm, $D_2 = 16.06$ mm, $D_3 = 8$ mm, $L_1 = 6$ mm).

1800 MHz, two regions in which the operational band can be tuned by just adjusting the location of the shorting via and dimensions of the periodic slots. The designed evolution. Further study is carried out to identify the effects of various parameters in terms of the impedance bandwidth and return loss.

The designed evolution of the conventional patch antenna and with three different steps. The corresponding return loss responses are shown in Figure 3. It is clear from that the introduction of the MS just above the conventional patch results in the lowering of the operating frequency of the antenna. In the low frequency band, the bandwidth changes from 1.83–1.87 GHz to 1.79–1.83 GHz without significant reduction. Further study shows that the bandwidth of the proposed antenna at 2.4 GHz increases by 4.1%, and the return loss reaches 27 dB. It is further observed that the introduction of the 9×9 order of the MS improves the bandwidth of the proposed antenna. For further study, the parametric studies are carried out to identify the effects of various parameters in terms of the impedance bandwidth and return loss.

A. Layout of the microstrip patch

Initially, microstrip patch antenna was patterned on a 1.6 mm thick low-cost FR4 substrate, which is shown in Figure 2 (c). Antenna operates at 2.4 GHz with a –10 dB impedance bandwidth of 3.2% and a realized gain of 5.07 dBi. The microstrip patch was reformed into a

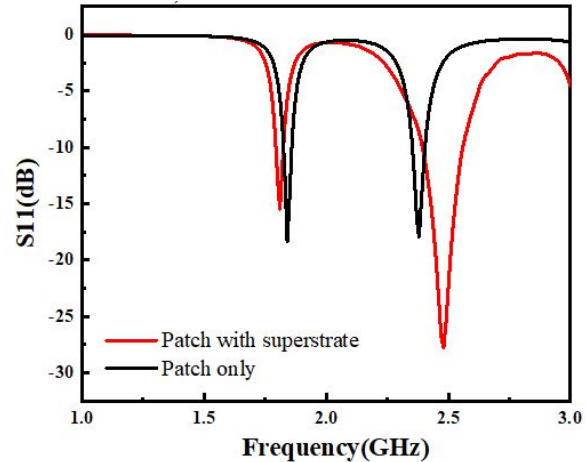


Fig. 3. Plot of S_{11} (dB) with respect to the frequency (GHz) of the proposed antenna.

fractal shape by etching the four different fractal square-shaped slots, the antenna gain increases to 5.27 dBi. The impedance bandwidth is increased by 3.02% at 2.4 GHz.

Under this arrangement, as shown in Figure 4 (a), firstly, change the feeding position to achieve impedance matching. Then adjust the patch size to the experimental band as shown in Figure 4 (b). Finally, the antenna parameters are further optimized to obtain better far-field gain.

B. Layout of the MS unit design

In this design, the performance of the conventional patch antenna shown as in Figure 2 was enhanced by the inclusion of the MS. Initially, the MS layer is separated from the conventional patch by an air spacer and is further replaced by the insulation pillar.

The MS consists of periodic unit cells with a 9×9 order. The unit cell consists of a centrosymmetric curl structure as shown in Figure 5 (a), (b). According to the directional coefficient ΔD of the previously designed antenna, the theoretical reflection coefficient p that the reflector should reach is about 0.57 from the eqn (8) [8].

$$p = \frac{10^{\Delta D/10} - 1}{10^{\Delta D/10} + 1}. \quad (8)$$

Then the corresponding structure of the metamaterial is obtained by LC equivalent circuit analysis as shown in Figure 5 (a), (b) and the optimization simulation results are close to the theoretical calculation results. The primitive electromagnetic properties, such as the effective permittivity and permeability, the concerned MS layer have been studied. The real and imaginary parts of the effective permittivity are shown in Figure 5 (c), while the same for effective permeability are shown in Figure 4 (d). At the left and right resonant

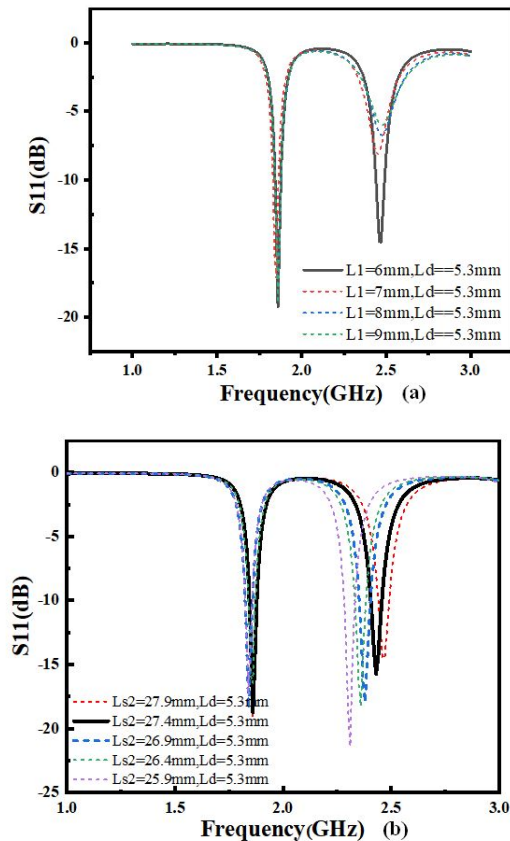


Fig. 4. (a) Plot of S_{11} (dB) with respect to the frequency at constant $L_d = 5.3$ mm and L_1 variations. (b) Plot of S_{11} (dB) with respect to the frequency at constant $L_d = 5.3$ mm and L_{s2} variations.

frequency band of 3.3 GHz metamaterial, its effective permeability and effective permittivity are negative, that is (DNG) structure.

It can be clearly observed from Figure 5 (c) and (d) that the MS layer about 3.3 GHz is DNG material. DNG material is suitable for producing narrow beam radiation in far field. As a consequence, the engineered structures can be utilized for making small and reconfigurable antennas.

C. Design antenna combined simulation with MS

Due to the low frequency of the antenna, this experiment needs to achieve the design of metamaterial unit miniaturization according to theoretical derivation. By adjusting the shape of the metamaterial, the FSS material can reduce the stopband to a lower frequency band in a limited space. It is found that the FSS material can be miniaturized by bending the patch and increasing the effective electric length of the patch.

Under this arrangement, as shown in Figure 6, firstly, the gap GS of the symmetric metamaterial struc-

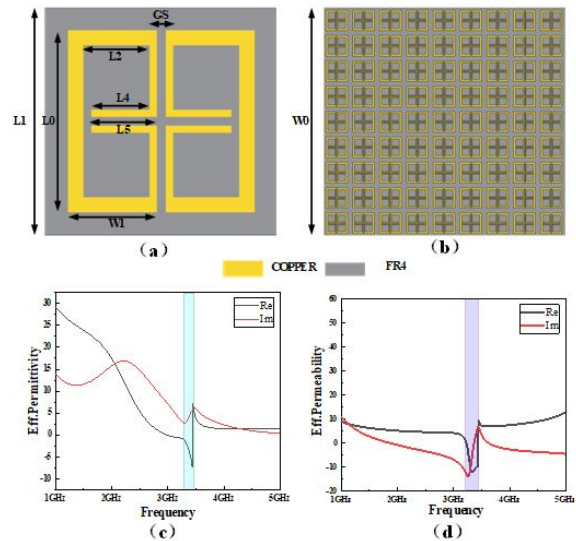


Fig. 5. (a) Unit cell of MS (designed parameters: $L_0 = 8$ mm, $W_1 = 3.8$ mm, $G_s = 0.4$ mm, $L_2 = 3.1$ mm, $L_4 = 2.5$ mm, $L_5 = 2.8$ mm) with (b) 9×9 order MS, (c) effective permittivity of the unit cell, and (d) effective permeability of the unit cell.

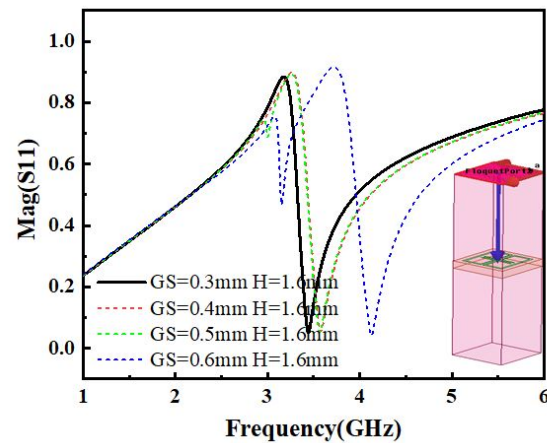


Fig. 6. Plot of mag with respect to the frequency at constant $H = 5.3$ mm and G_s variations.

ture was changed to make the simulation data coincide with the theoretical calculation data. Then, the model was simulated by using the master-slave boundary to achieve the appropriate reflection amplitude. Combined with theoretical derivation and simulation results, the MS reflection coefficient is about 0.57 at 2.4 GHz, and according to eqn (7), the MS coverage height L is about 15.5 mm.

The electric field distributions of the top and bottom surfaces of the conventional patch antenna at various

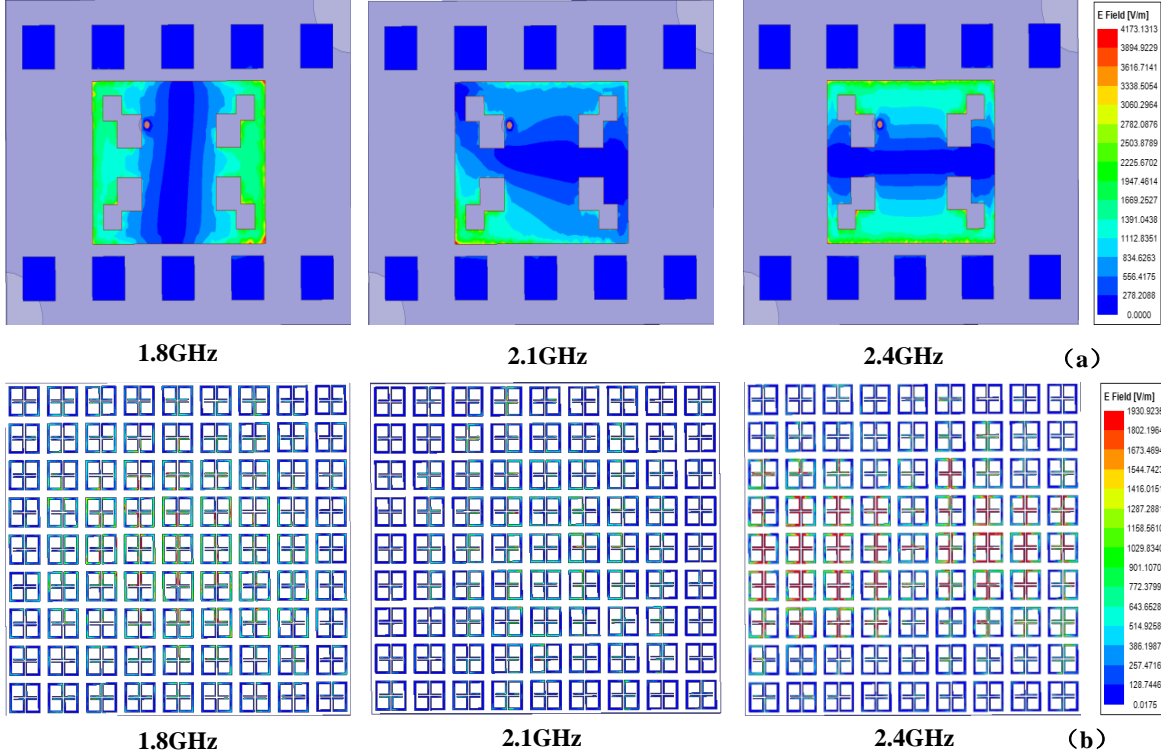


Fig. 7. Surface current distributions at (a) top and (b) 9×9 order MS at different operating frequencies within the proposed structure.

operating frequencies of 1.8 GHz, 2.1 GHz, and 2.4 GHz are shown in Figure 7 (a), respectively. With the increase of antenna frequency, the distribution of the antenna electric field shifts from the left and right edges of the antenna to the upper and lower edges [8, 9]. The electric field distributions in the top MS layer at the aforementioned frequencies are also shown in Figure 7 (b). It is observed from Figure 7 that the field distribution is maximum along the edge of the antenna and the intensity of the fields is very high among the unit cells of the MS layer.

In Figure 7 (a), (b), as shown in the same frequency, we also studied respectively on the surface of the patch antenna designed three surface current [23, 24]. The results show that the surface currents around the antenna feed and MS layer are stronger at the corresponding frequencies. The current distribution path on the top surface increased as the four-unit cell slot of the fields is very high among the unit cells of the MS layer.

IV. FABRICATION AND TEST OF THE PROPOSED ANTENNA

The antenna prototype shown in Figure 2 was fabricated using the PCB prototyping instrument [25]. The top and rear views of the fabricated sample are shown in Figure 8 (a), (b), respectively. The complete 3-D sam-

ple is shown in Figure 8 (c). The antenna prototype was tested by HP Network Analyzer as shown in Figure 8 (e). The return loss profile of the prepared sample as shown in Figure 8 (e) was measured, and it can be seen that the 10 dB impedance bandwidth measured by the experiment in the range of 1.8 GHz and 2.4 GHz matched well with the corresponding simulation.

The E-plane and H-plane radiation pattern measurements of the fabricated antenna were carried out within the anechoic chamber. The test environment is shown in Figure 9 (a), (b). The far-field antenna gains of the proposed prototype with respect to frequencies are shown in Figure 10. It can be seen that the gain of the simulated quantity increased nearly three times before and after adding MS, and the simulated quantity was basically consistent with the real measurement.

As shown in Table 1, the maximum gain of analog image and measured image of antenna at 1.8 GHz is 4.49 dBi and 4.13 dBi, respectively. The maximum gain in 2.4 GHz analog mode and measurement mode is 8.27 dBi and 6.32 dBi. The maximum efficiency of analog image and measured image at 1.8 GHz is 45.15% and 41.31%, respectively. The maximum efficiency in 2.4 GHz analog mode and measurement mode is 69.15% and 62.17%, respectively. Table 2 shows the performance comparison between the proposed antenna and other antennas. It can

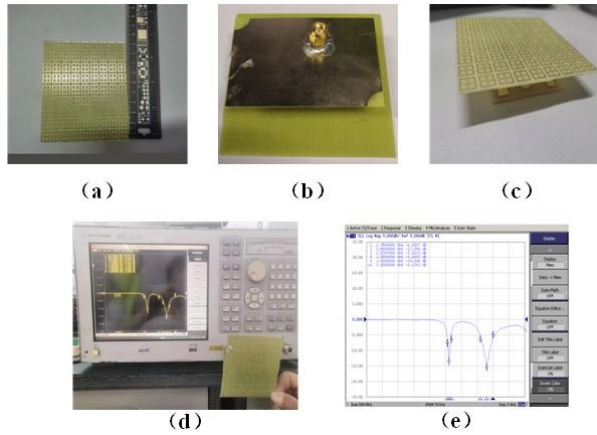


Fig. 8. (a) Top view. (b) Rear view. (c) 3-D view of the proposed antenna. (d) S-parameter measurement using VNA (e) Plot of measured S11(dB) with respect to frequency.

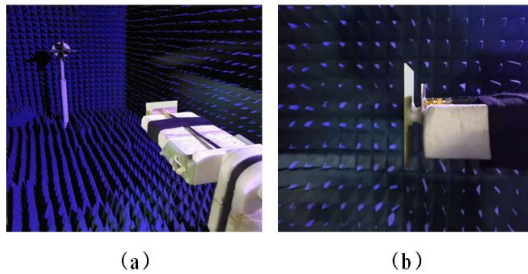


Fig. 9. (a) Microwave anechoic chamber measures far-field radiation. (b) The transmitting antenna serves as the signal source.

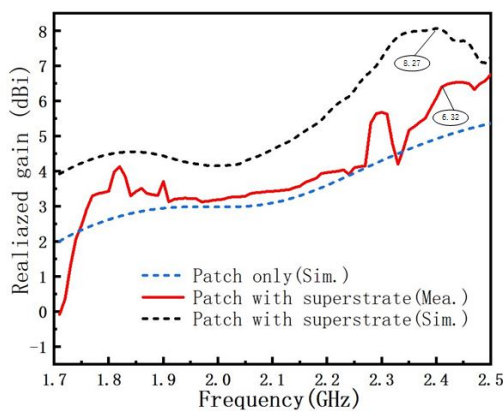


Fig. 10. Gain in the antenna bandwidth for the patch antenna with and without the superstrate.

be concluded from the table that the proposed TA has the advantages of high gain and reflection efficiency. Most importantly, it has dual frequency characteristics.

Table 1: The simulation results are compared with the measured results

| Results | Frequency (GHz) | Return loss (dB) | Max. gain (dBi) | Efficiency (%) |
|-----------|-----------------|------------------|-----------------|----------------|
| Simulated | 1.8 | 17.1 | 4.49 | 45.15 |
| Measured | 1.8 | 14.3 | 4.13 | 41.31 |
| Simulated | 2.4 | 27.1 | 8.27 | 69.15 |
| Measured | 2.4 | 17.3 | 6.32 | 62.17 |

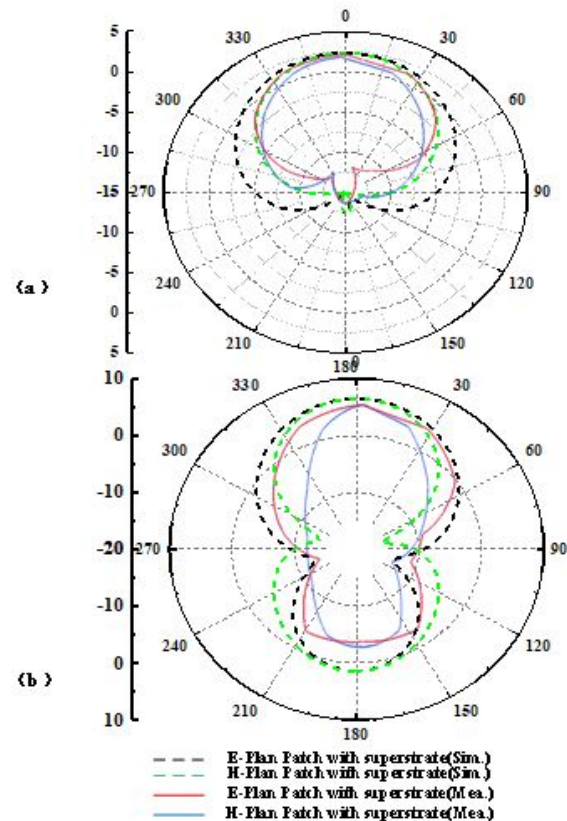


Fig. 11. (a) Antenna far-field simulation and measured figure at 1.8 GHz. (b) Antenna far-field simulation and measured figure at 2.4 GHz.

In addition, as shown in Figure 11, the simulated radiation mode is very consistent with the measured radiation mode.

The difference between the simulation and design results may occur due to the fabrication tolerances (which can be due to the slight air gap between these dielectric layers at the time of fabrication, soldering between the dielectric substrate and the SMA connector, or the copper loss of the FR4 dielectric at the time of polishing). In addition, the shift may be due to the insertion loss of the SMA connector.

Table 2: The comparison between the proposed TA and other published TA

| Ref. | Frequency (GHz) | Return loss (dB) | Max. gain (dBi) | Relative bandwidth (-10dB) (%) |
|-----------|-----------------|------------------|-----------------|--------------------------------|
| [7] | 5.7 | 13 | 8.9 | 3.8 |
| [19] | 10.5 | 24 | 7.57 | 7.6 |
| [23] | 4.5 | 24 | 7.5 | 2.8 |
| This Work | 1.8 | 17.1 | 4.49 | 2 |
| | 2.4 | 27.1 | 8.27 | 7.6 |

V. CONCLUSION

This communication proposed a low-frequency MS structure and the use of a hyperlayer to increase the antenna gain. By adjusting the MS characteristic, the reflection coefficient can be changed to form a large area of in-phase electric field on the hyperlayer surface. The proposed antenna operates at 2.4 GHz frequency with a fractional bandwidth of 6.9% and a significantly enhanced gain of 8.27 dBi at the same operating frequency. The simulated and the experimental results validate well, therefore, demonstrating a good antenna performance. Since there are a large number of electromagnetic waves in this frequency band in the environment, it can be extended to the study of RF energy collection and other aspects.

ACKNOWLEDGMENT

This work was supported and funded by the National Natural Science Foundation of China (51965047), Inner Mongolia Science and Technology Research Project (2020GG0185), Research Startup Fund of High-level Talents Introduction in 2018(21700-5185131, 21700-5185128).

REFERENCES

- [1] M. E. Badawe, T. S. Almoneef, O. M. Ramahi, "A true metasurface antenna," *Sci Rep.* vol. 6, no. 1, pp. 1-8, May 2016.
- [2] S. Zhang, X. Chen, G. F. Pedersen, "Mutual coupling suppression with decoupling ground for massive MIMO antenna arrays," *IEEE Transactions on Vehicular Technology.* vol. 68, no. 8, pp. 7273-7282, Aug. 2019.
- [3] S. Liu, D. Yang, Y. Chen, X. Zhang, Y. Xiang, "High isolation and low cross-polarization of low-profile dual-polarized antennas via metasurface mode optimization," *IEEE Transactions on Antennas and Propagation.*, vol. 69, no. 5, pp. 2999-3004, May 2020.
- [4] J. Su, J. Liu, Z. Li, L. Y. Yang, "Full and independent manipulation of Co- and Cross-polarized waves with metasurface," *Applied Computational Electromagnetics Society Journal*, vol. 34, no. 11, pp. 1653-1661. Nov. 2019.
- [5] F. H. Lin and Z. N. Chen, "Low-profile wideband metasurface antennas using characteristic mode analysis," *IEEE Trans. Antennas Propagation.*, vol. 65, no. 4, pp. 1706-1713, Apr. 2017.
- [6] W. An, Y. Li, H. Fu, J. Ma, W. Chen, and B. Feng, "Low-profile and wideband microstrip antenna with stable gain for 5G wireless applications," *IEEE Antennas and Wireless Propagation Letters.*, vol. 17, no. 4, pp. 621-624, Apr. 2018.
- [7] J. H. Kim, C.-H. Ahn, and J.-K. Bang, "Antenna gain enhancement using a holey superstrate," *IEEE Trans. Antennas Propagation.*, vol. 64, no. 3, pp. 1164-1167, Mar. 2016.
- [8] K. Xingjian, *Antenna Principle and Design.* National Defense Industry Press, 1995.
- [9] F. Liu, J. Guo, L. Zhao, G. L. Huang, and Y. Yin, "Dual-band metasurface-based decoupling method for two closely packed dual-band antennas," *IEEE Transactions on Antennas and Propagation*, vol. 68, no. 1, pp. 552-557, Jan. 2020.
- [10] H.-P. Li, G.-M. Wang, X.-J. Gao, J.-G. Liang, and H.-S. Hou, "A novel metasurface for dual-mode and dual-band flat high-gain antenna application," *IEEE Trans. Antennas Propagation.*, vol. 66, no. 7, pp. 3706-3711, Jul. 2018.
- [11] M. A. Qureshi, A. Aziz, A. Amin, H. F. Rasool, F. Hayat, "Design of a new wideband single-layer reflective metasurface unit cell for 5G-communication," *Applied Computational Electromagnetics Society Journal*, vol. 35, no. 8, pp. 975-978. Oct. 2020.
- [12] J. Ghosh, D. Mitra, and S. Das, "Mutual coupling reduction of slot antenna array by controlling surface wave propagation," *IEEE Trans. Antennas Propagation.*, vol. 67, no. 2, pp. 1352-1357, Feb. 2019.
- [13] W. Yang, L. Gu, W. Che, Q. Meng, Q. Xue, and C. Wan, "A novel steerable dual-beam metasurface antenna based on controllable feeding mechanism," *IEEE Trans. Antennas Propagation.*, vol. 67, no. 2, pp. 784-793, Feb. 2019.
- [14] E. Delihanlar and A. H. Yuzer, "Wearable textile fabric based 3D metamaterials absorber in X-band," *Applied Computational Electromagnetics Society Journal*, vol. 35, no. 2, pp. 230-236, Feb. 2020.
- [15] H. Bai and G. Wang, "A multistate high gain antenna based on metasurface," *International Journal of RF and Microwave Computer-Aided Engineering*, vol. 30, no. 4, 2020.

- [16] S.-H. Zhu, X.S. Yang, J. Wang, N.-S. Nie, and B.-Z. Wang, "Mutual coupling reduction of +45 dual-polarized closely spaced MIMO antenna by topology optimization," *IEEE Access*, vol. 8 pp. 29089-29098, Jan. 2020.
- [17] M. Li, B. G. Zhong, and S. W. Cheung, "Isolation enhancement for MIMO patch antennas using near-field resonators as coupling-mode transducers," *IEEE Trans. Antennas Propagation*, vol. 67, no. 2, pp. 755-764, Feb. 2019.
- [18] D. Samantaray and S. Bhattacharyya, "A gain-enhanced slotted patch antenna using metasurface as superstrate configuration," *IEEE Trans. Antennas Propagation*, vol. 68, no. 9, pp. 6548-6556, Sep. 2020.
- [19] J. Z Tang, X. Chen, F. Fa5raz, Q. Zhang, and S. Zhang, "A metasurface superstrate for mutual coupling reduction of large antenna arrays," *IEEE Access*, vol. 8, pp. 126859-126867, Jul. 2020.
- [20] M. I. Pasha, C. Kumar, and D. Guha, "Simultaneous compensation of microstrip feed and patch by defected ground structure for reduced cross polarized radiation," *IEEE Trans. Antennas Propagation*, vol. 66, no. 12, pp. 7348-7352, Dec. 2018.
- [21] S. Liu, D. Yang, Y. Chen, X. Zhang, and Y. Xiang, "High isolation and low cross-polarization of low-profile dual-polarized antennas via metasurface mode optimization," *IEEE Trans. Antennas Propagation*, vol 69, no. 5, pp. 2999-3004, May 2021.
- [22] T. Li and Z. N. Chen, "Wideband sidelobe-level reduced Ka-band meta-surface antenna array fed by substrate-integrated gap waveguide using characteristic mode analysis," *IEEE Trans. Antennas Propagation*, vol. 68, no. 3, pp. 1356-1365, Mar. 2020.
- [23] P. P. Kumar, K. Sreelakshmi, B. Sangeetha, and S. Narayan, "Metasurface based low profile reconfigurable antenna," *International Conference on Communication and Signal Processing (ICCSP)*, 2017.
- [24] S. Liu, D. Yang, Y. Chen, K. Sun, X. Zhang, and Y. Xiang, "Low-profile broadband metasurface antenna under multimode resonance" *IEEE Antennas and Wireless Propagation Letters*, vol. 20, no. 9, pp. 1696-1700, Sep. 2021.
- [25] A. Sharma, D. Gangwar, B. K. Kanaujia, S. Dwari, and S. Kumar, "Design of a wideband polarisation conversion metasurface and its application for RCS reduction and gain enhancement of a

circularly polarized antenna," *IET Microwaves, Antennas Propagation*, vol. 13, no. 9, pp. 1427-1437, May 2019.



surface.

HuQiang Tian received bachelor degree in Communication Engineering from Inner Mongolia Normal University, Hohhot, China, in 2019. From 2019, he pursued his Master degree in Inner Mongolia University. His research Interest are transmitter antenna and frequency selective



micro nano RF devices (antennas, filters, couplers, etc.), metamaterial antennas.

JunLin Wang received a doctor's degree in engineering in Instrument Science and technology of Zhong-bei University. He is currently working in the College of electronic information engineering, Inner Mongolia University, Hohhot, China. His research interests are



is artificial intelligence.

Ding Han received a doctor's degree in agricultural electrification and automation engineering from Inner Mongolia Agricultural University. At present, he works in the school of electronic information engineering of Inner Mongolia University in Hohhot, China. His research interest



micro nano RF devices (antennas, filters, couplers, etc.), metamaterial antennas.

Xin Wang received a doctor's degree in engineering in Instrument Science and technology of Zhong-bei University. She is currently working at the College of electronic information engineering, Inner Mongolia University, Hohhot, China. Her research interests are

Design Optimization of Ultra-Wideband Vivaldi Antenna using Artificial Intelligence

Peyman Mahouti¹, Ahmet Kızılay², Ozlem Tari³, Aysu Belen⁴, Mehmet A. Belen⁵,
and Alper Çalışkan²

¹Department of Electronics and Automation, İstanbul University- Cerrahpaşa, İstanbul, Turkey
pmahouti@iuc.edu.tr

²Department of Electronic and Communication, Yıldız Technical University, İstanbul, Turkey
akizilay@yildiz.edu.tr, alperc@yildiz.edu.tr

³Department of Mathematics and Computer Science, İstanbul Arel University, İstanbul, Turkey
ozlemilgin@arel.edu.tr

⁴Department of Hybrid and Electric Vehicles Technology, İskenderun Technical University, Hatay, Turkey
aysu.belen@iste.edu.tr

⁵Department of Electric and Electronic, İskenderun Technical University, Hatay, Turkey
mali.belen@iste.edu.tr

Abstract – In this work, computationally efficient design optimization of frequency selective surface (FSS)-loaded ultra-wideband Vivaldi antenna via the use of data-driven surrogate model is studied. The proposed design methodology consists of a multi-layer FSS structure aimed for performance improvement of the Vivaldi design, which makes the design a multi-objective multi-dimensional optimization problem. For having a fast and accurate optimization process, a data-driven surrogate model alongside the metaheuristic optimizer honeybee mating optimization (HBMO) had been used. The optimally designed antenna had been prototyped and its performance characteristics had been measured. The obtained experimental results are compared with the simulated results of the proposed method. Results show that the obtained FSS-loaded structure has enhanced directivity compared with the design without FSS structure, without any performance losses in the return loss characteristics. The FSS-loaded Vivaldi antenna operates at 2–12 GHz band with a maximum gain of 10 dBi at 10 GHz which makes the design a good solution for RADAR applications.

Index Terms – Frequency selective surface, optimization, surrogate modeling, ultra-wideband, Vivaldi antenna.

I. INTRODUCTION

Due to their high-performance characteristics Vivaldi antenna designs are being used in many

communication applications such as microwave imaging and ground penetrating radar (GPR) [1], [2]. In order to analyze the composition of underground soil, GPR requires to propagate high-power EM wave to the ground. In order to have a wide range of characterization of soil the signals need to go deep into the ground and have high resolution. For such capability the GPR antenna requires to operate in low frequency, have ultra-wideband characteristics, and high gain performance [3]. There are different types of antennas suitable for GPR applications with respect to their characteristics such as o GPR antenna dipole [4], bowtie [5], [6], and Vivaldi antennas [7], [8]. Due to its high gain, ultra-wideband characteristic, Vivaldi antenna can be named as one of the most commonly used antenna design for GPR applications. It should be noted that such designs usually require a large design space or smaller size with lower performance measures. Usage of lens structures can be named as one of the methods for performance improvement of antenna designs [9], [10]. However, although the placement of dielectric lens structures can increase the gain performance of antenna but their improvements are limited [11].

Another well-known solution for performance enhancement of antenna designs is the placement of frequency selective surfaces (FSS) to the aperture of the antenna in an optimally determined configuration such as: antenna design with a multi-layer S-type resonator with zero index for gain enhancement [12], design with

multi-layers [13], [14] for gain enhancement, and [15] for sidelobe suppression of the antenna design. Although the application of FSS can provide a significant performance improvement to the design, the placement and the geometrical design of FSS structures must be optimized to reach their full performance of improvement. Achieving such task requires a multi-objective multi-dimensional optimization process, which requires a considerable amount of trial and error. This process usually forces researchers to make a decision for their models. Either they should use a coarse model with low accuracy for achieving fast and computationally efficient design optimization or they must use fine meshed design with high accuracy at expense of relatively long or infeasible design optimization process [16].

One of the most efficient solutions for having an accurate, reliable, and computationally efficient optimization process is the usage of data-driven surrogate models. Data-driven surrogate models had been used by many researches for applications such as parameter tuning [17], statistical analysis [18], [19], and multi-objective design [20]. In literature, there are many Artificial Intelligence (AI)-based methods for surrogate-based modeling of microwave structures such as polynomial regression [21], kriging interpolation [22], radial basis functions [23], support vector regression [24], polynomial chaos expansion [25], and artificial neural networks (ANN) [26].

In this work, for optimal determination of geometrical design variables of an FSS structure to be applied to an antipodal Vivaldi antenna (AVA) for performance improvements have been achieved via the use of data-driven surrogate modeling [27]. Firstly, an FSS-loaded Vivaldi antenna have been presented in Section II, alongside the design variables of FSS structure. By using Latin-hypercube sampling method, a data set generated with a 3D full-wave EM simulator is created to be used for data-driven surrogate model to create a mapping between geometrical design parameters of FSS structure and performance measures of scattering and maximum gain of the FSS-loaded Vivaldi antenna design. In Section III, some of the commonly used state of the art AI regression algorithms had been used and bench marked to obtain a model with best performance for creating a mapping between input and output of the data set. In Section IV, the optimal selected surrogate model will be used to drive the design optimization search alongside a meta-heuristic optimizer. Finally, the work ends with a brief conclusion in Section V.

II. FSS-LOADED VIVALDI ANTENNA

In Figure 1, a typical AVA design modeled in 3D CST MWS environment is presented. AVA is designed on a PLA Filament–Polar White RBX-PLA-WH002 (ϵ_r ,

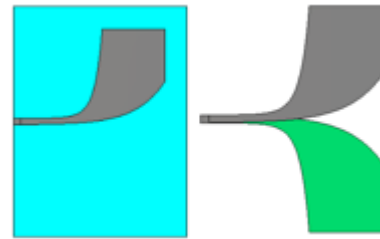


Fig. 1. A typical antipodal vivaldi antenna.

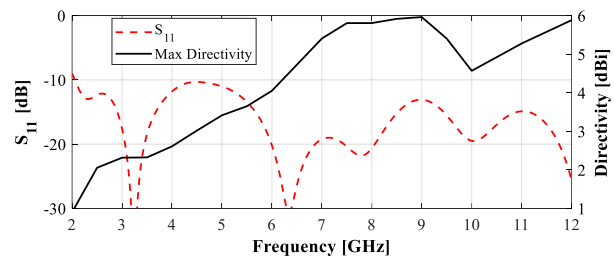


Fig. 2. Simulated performance of the vivaldi antenna.

= 2.5) with two noncoplanar exponentially tapered edge arms on both top and ground plane (symmetrically) of the antenna. The exponentially tapered edges of the design are defined as exponential factor R , $P_1(x_1, y_1)$, and $P_2(x_2, y_2)$, initial and final points of the exponential tapered shape respectively. Design equations are given below as eqn (1)–(3) [28, 29]:

$$y = C_1 e^{Rx} + C_2, \quad (1)$$

where

$$C_1 = \frac{y_2 - y_1}{e^{Rx_2} - e^{Rx_1}} \quad (2)$$

$$C_2 = \frac{y_1 e^{Rx_2} - y_2 e^{Rx_1}}{e^{Rx_2} - e^{Rx_1}} \quad (3)$$

$C_1 = 5$, $C_2 = 0$, $R = 0.03$; and $C_1 = 15$, $C_2 = -8$, $R = 0.1$, respectively. In Figure 2, the simulated performance of the Vivaldi antenna without FSS structure had been presented.

In Figure 3, the schematic of the proposed FSS structure to be placed in top and ground layer sides of Vivaldi antenna is presented. The variables of the FSS structure and their lower and upper limitations are presented in Table 1. For ease of modeling, L_2 is taken as equal to L_1 . Here, for having computationally efficient modeling, the total number of training and test samples are taken as 600 where 500 of the samples are used for

Table 1: Design variables and their variation limits

| Variable | Min | Max | Variable | Min | Max |
|----------|-----|-----|----------|-----|-----|
| W1 | 5 | 15 | L1 | 2 | 8 |
| S1 | 0.5 | 2 | H2 | 2 | 6 |

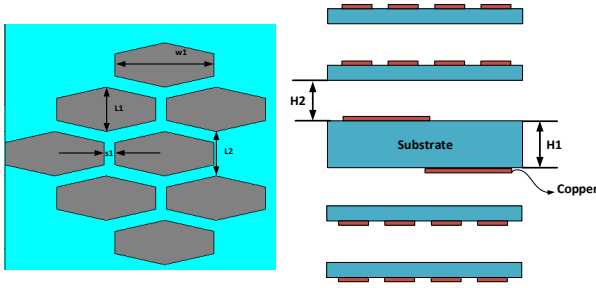


Fig. 3. Schematic of the proposed FSS-loaded Vivaldi antenna.

Table 2: Design variables and their variation limits

| Model | HP | K-fold/Holdout |
|-----------------------------|---|----------------|
| MLP | 2 layers with 15 and 20 neurons, trained with “Levenberg–Marquardt” | 9.1%/10.5% |
| SVRM | Epsilon SVR, Epsilon = 0.15, with radial basis kernel | 7.9%/8.5% |
| Gradient boosted tree | Learning rate of 0.05 1500 number of estimators and depth of 7 | 10.6%/11.5% |
| Random forest | Max depth 10, 200 number of estimators, leaf size of 20 | 11.1%/11.9% |
| Gaussian process regression | Kernel function of “matern3/2,” Prediction method of Block coordinate descent with block size of 2500 | 8.3%/9.0% |

training and 100 are taken as “hold-out” data for evaluation of over-fitting performance of surrogate models. For sampling method, Latin-Hyper cube sampling (LHS) method is used. The frequency range is 1–12 GHz with a step size of 0.1 GHz.

III. SURROGATE MODELING

In this section, some of the commonly used AI regression algorithms have been used for creating a surrogate model for creating a mapping between design variables of FSS structure and the outputs of maximum gain and scattering parameters of the antenna design. For creating the surrogate model of the FSS-loaded Vivaldi antenna, the algorithms given in Table 2 are trained with $K = 5$ K-fold cross validation. Furthermore, a holdout data set with 100 samples is used for testing the over-fitting performance of the models. Relative Mean Error (RME) metric (Eqn (4)) have been used for performance

study of models.

$$RME = \frac{1}{N} \sum_{i=1}^N \frac{|T_i - P_i|}{|T_i|}. \quad (4)$$

Here, T_i is the i th sample targeted value, P_i is the i th sample predicted value, N is the total number of tested samples over the given operation frequency. Here, the obtained RME values are combined values for both S_{11} and maximum gain at each frequency sample. With respect to the obtained results in Table 2, support vector regression machine (SVRM) had been taken as the best surrogate model to be used in the design optimization process due to having the lowest K-fold and hold out RME.

IV. DESIGN OPTIMIZATION

Herein, for determination of optimal design variables of the proposed antenna, a powerful population-based hybrid metaheuristic algorithm HBMO had been used [30, 31]. HBMO is an algorithm based on the mating habits of honey bees in which the new born members of the bee colony (usually assumed that all members are female) are ranked based on their fitness to be the new queen of the colony. The search for the new queen can be considered a global search strategy where there is no initial knowledge of the optimal solution [30]. When, the nurse bee finds a candidate with better fitness values than the current queen the candidate will be crowned as the queen. After the coronation, in order to enhance the development of the new queen and her breeding capabilities, the nurse bees start to feed the queen with “Royal Jelly,” a nutrition that can significantly enhance the fitness of the new queen. This process can be considered as a local search where there is an initial knowledge about a global or local optimum which can be furthered enhanced [31]. It should be noted that, although there are many novel and recently published global search metaheuristic optimization algorithms in literature that might have better convergence speed than the used HBMO algorithm, the main concern of this work is not focused on the convergence performance nor the selection of optimal metaheuristic optimization algorithm. In this work, with the usage of the proposed data-driven surrogate modeling technique, the simulation time required for the prediction of scattering and directivity characteristics of the antenna would be much less than a second while single EM simulation for the selected antenna might take up to 5 minutes or more with respect to the mesh size and the used hardware setup. Thus, in a case that hundreds of function evaluations would took less than a minute the convergence speed of the algorithm can be neglected. Thus, here HBMO algorithm is taken as an example of a metaheuristic optimization algorithm for the selected problem. The cost function that had been used for HBMO

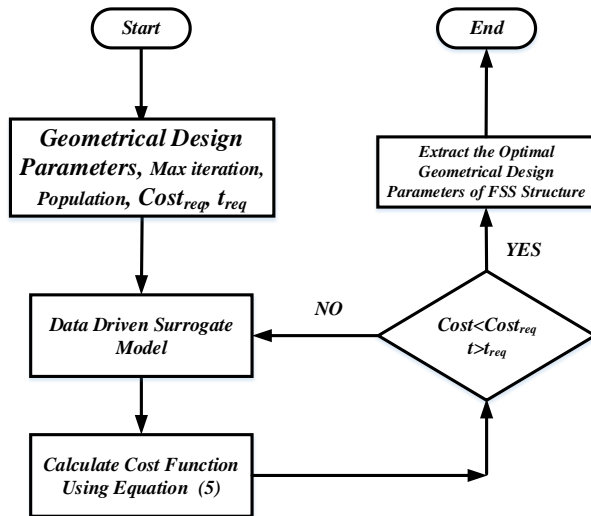


Fig. 4. Flow chart of the proposed optimization process.

search is presented in (5)–(7),

$$x^* = \operatorname{argmin}_x [w_1 C_1(x) + w_2 C_2(x)] \quad (5)$$

$$C_1(x) = \max \{f \in [f_{c1}, f_{c2}] : |S_{11}(x, f)|\} \quad (6)$$

$$C_2(x) = \max \{f \in [f_{c1}, f_{c2}] : \text{Directivity}(x, f)\}, \quad (7)$$

where C is the cost function, x is the input vector of variables of $[W_1 L_1 S_1 H_2]$, f_{c1} and f_{c2} denote the lower and upper frequency determining the target-operating band. The coefficients w_1 and w_2 are weighing of cost functions, these coefficients are taken as $w_1 = 0.7$ while $w_2 = 0.3$, due to the large possible difference between S_{11} , which can have low values such as -30 dB, and directivity for this design might be as high as 10 dBi. Here, the aimed operation bands of FSS-loaded Vivaldi antenna is to achieve an ultra-wideband operation frequency of 2–12 GHz which is an optimal operating range for RADAR applications. The flowchart of the proposed optimization algorithm is given in Figure 4. The optimally selected design variables of the design are as follows: $W_1 = 8.75$, $L_1 = 4$, $S_1 = 1$, $H = 23.7$ all in [mm]. These values are obtained after 15 iterations, 25 Drone bees, and Royal jelly step size of ± 0.1 using HBMO optimization [30].

Furthermore, for justification of the proposed method, the obtained geometrical results are given to 3D EM model in CST and the performance measures of both CST and SVRM surrogate models are compared with each other. As it can be seen from Figure 5, the proposed method has the same performance characteristics as the 3D EM simulator tool.

V. FABRICATION AND MEASUREMENT

In this section, for further evaluation of accuracy and stability of the proposed design optimization method,

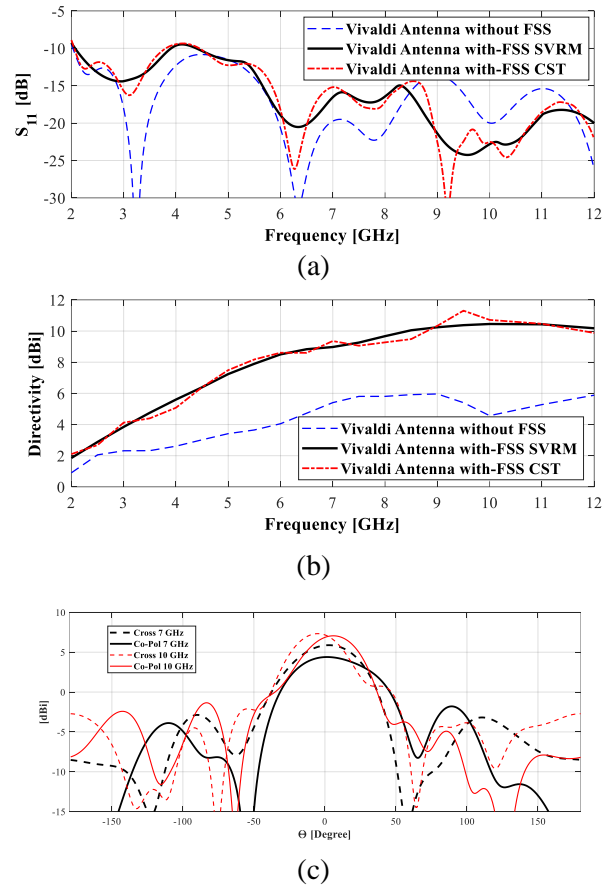


Fig. 5. Simulated (a) scattering, (b) directivity, (c) polarization of FSS loaded, antenna designs.

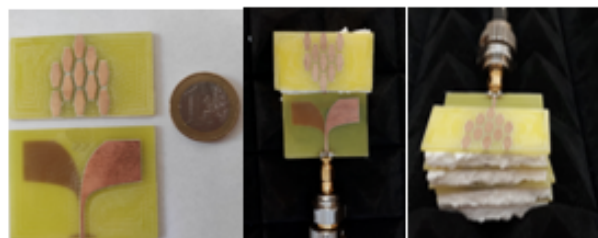


Fig. 6. The prototyped FSS-loaded Vivaldi antenna.

the optimally designed antenna in section IV have been prototyped (Figure 6). The measurement devices (a Network Analyzer with a measurement bandwidth of 9 KHz–13.5 GHz, and LB-8180-NF Broadband Horn Antenna 0.8–18 GHz as reference antenna) available in Microwave Laboratories of Yildiz Technical University had been used.

In Figure 7, the measured experimental results of maximum gain, and scattering parameter of the optimally designed FSS-loaded Vivaldi antenna are

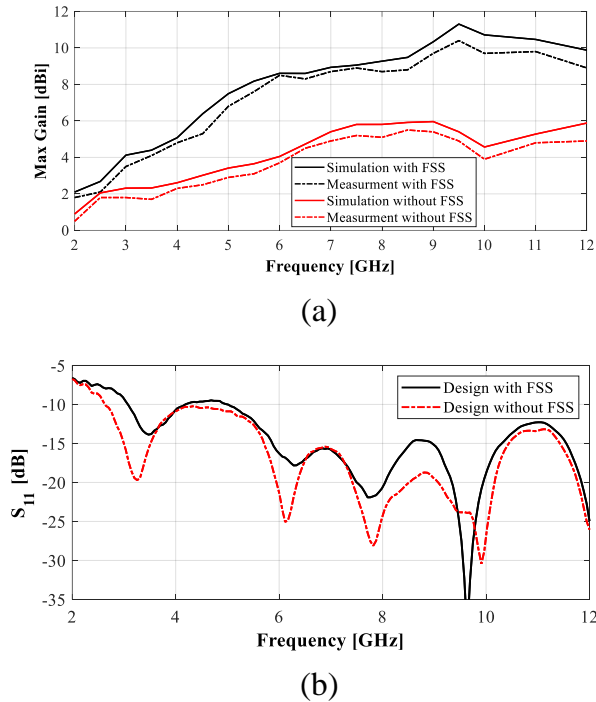


Fig. 7. Measured (a) maximum gain, (b) scattering parameters, over the operating band.

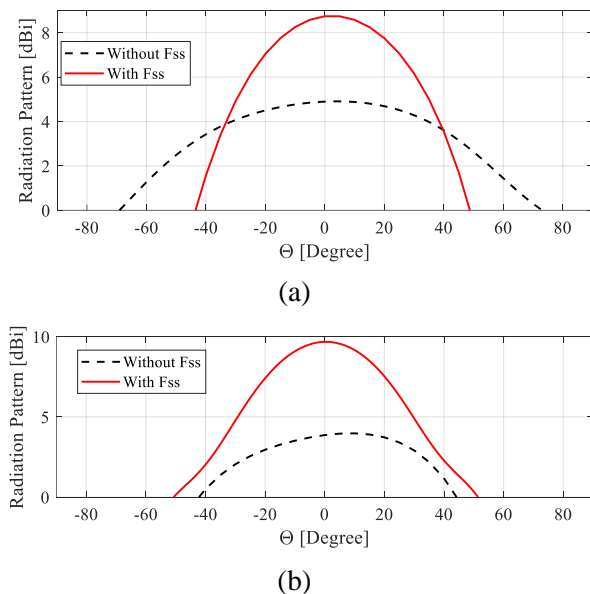


Fig. 8. Measured radiation pattern at (a) 7 GHz, (b) 10 GHz.

presented. As it can be seen from the figure, the measured performances of the antenna are in agreement with the simulated results obtained in previous sections. Fur-

Table 3: RF performance comparison table

| Work | f [GHz] | Gain [dBi] | Material | Size [mm] |
|------|-----------|------------|------------------------|----------------|
| Here | 2–12 | 2–11.8 | FR4 Eps:4.4 | 50×58×1.8 |
| 32 | 3.5–16 | 3.5–12.5 | RO4003C Eps: 3.38 | 80.5×52×14.5 |
| 33 | 1–12 | 1.5–5.1 | FR4 Eps: 4.6 | 45×40×1.6 |
| 34 | 0.8–12 | 6.32 | ARLON 600 Eps: 6.15 | 190×128×1.57 |
| 35 | 1.9–5.5 | 3.6–4.6 | FR4 Eps: 4.4 | 68.3×112.2×0.8 |
| 36 | 2–18 | 3/12.3 | RO4003C Eps: 3.38 | 100×140×0.8 |
| 37 | 1.8/5.2 | -/5.5 | FR4 Eps: 4.3 | 80×60×1.6 |
| 38 | 2.9–11.6 | -/3 | Taconic RF-35 Eps: 3.5 | 26×26×0.76 |
| 39 | 2.4/5.2 | 3.6/2.5 | FR4 Eps: 4.3 | 94.5×100×1.6 |
| 40 | 2.9–14.2 | 5–9 | FR4 Eps: 4.3 | 40×50×1.6 |
| 41 | 0.8–3.4 | 2.4–8.1 | FR4 Eps: 4.4 | 150×150×0.508 |

*Most of the antenna designs have achieved similar S_{11} characteristics. Therefore, in this table S_{11} is not included.

thermore, a performance comparison table of the proposed antenna design with the counterpart designs from the literature [32–40] is presented in Table 3. As it can be deduced from the performance comparison table, the proposed antenna design achieves high gain, wide operation band performance compared to the counterpart designs in the literature with smaller size and lower cost material for substrate.

VI. CONCLUSION

Herein, design optimization of an FSS-loaded Vivaldi antenna had been achieved using both SVRM-based surrogate model and a metaheuristic optimization algorithm HBMO. By using a multi-layer structured FSS design, the performance of a Vivaldi antenna has been increased without a distortion in the gain and scattering performance of the design. Furthermore, for justification of the proposed method the optimally designed antenna had been prototyped and its performance characteristics are measured. As a result, the measured characteristics are found to be in agreement with the simulated results of the proposed method. The proposed design achieves a maximum gain characteristic of 10 dBi with an operation bandwidth of 2–12 GHz which makes this design a suitable candidate for RADAR applications.

VII. ACKNOWLEDGMENT

We would like to express our special thanks of gratitude to the Aktif Nesor Elektronik and DataRobot, for providing researcher licenses for CST and DataRobot. Also, we would like to thank TUBITAK National Observatory for giving partial support under grant number of “119N196.”

REFERENCES

- [1] M. Moosazadeh, S. Kharkovsky, J. T. Case, and B. Samali, “Improved radiation characteristics of small antipodal vivaldi antenna for microwave and millimeter-wave imaging applications,” *IEEE*

- Antennas Wireless Propag. Lett.*, vol. 16, pp. 1961-1964, 2017.
- [2] F. Zhang, G.-Y. Fang, Y.-C. Ji, H.-J. Ju, and J.-J. Shao, "A novel compact double exponentially tapered slot antenna (DETTSA) for GPR applications," *IEEE Antennas Wireless Propag. Lett.*, vol. 10, pp. 195-198, 2011.
- [3] L. Guo, H. Yang, Q. Zhang, and M. Deng, "A compact antipodal tapered slot antenna with artificial material lens and reflector for GPR applications," *IEEE Access*, vol. 6, pp. 44244-44251, 2018.
- [4] K. Kim, W. R. Scott, and S. Member, "Design of a Resistively loaded Vee dipole for radar applications," *IEEE Trans. Antennas Propag.*, vol. 53, no. 8, pp. 2525-2532, Aug. 2005.
- [5] M. Serhir and D. Lesselier, "Wideband reflector-backed folded bowtie antenna for ground penetrating radar," *IEEE Trans. Antennas Propag.*, vol. 66, no. 3, pp. 1056-1063, Mar. 2018.
- [6] L. Guo, B. Xiao, M. Li, H. Yang, and H. Lin, "A high-gain and frequency tunable bow tie antenna with epsilon-negative metasurface," *J. Electromagn. Waves Appl.*, vol. 29, no. 5, pp. 693-702, Mar. 2015.
- [7] L. Sang, X. Li, T. Chen, and G. Lv, "Analysis and design of tapered slot antenna with high gain for ultra-wideband based on optimisation of the metamaterial unit layout," *IET Microw. Antennas Propag.*, vol. 11, no. 6, pp. 907-914, May 2017.
- [8] A. Z. Hood, T. Karacolak, and E. Topsakal, "A small antipodal vivaldi antenna for ultrawide-band applications," *IEEE Antennas Wireless Propag. Lett.*, vol. 7, pp. 656-660, 2008.
- [9] H. Cheng, H. Yang, Y. Li and Y. Chen, "A compact vivaldi antenna with artificial material lens and sidelobe suppressor for GPR applications," *IEEE Access*, vol. 8, pp. 64056-64063, 2020. doi: 10.1109/ACCESS.2020.2984010.
- [10] G. Teni, N. Zhang, J. Qiu, and P. Zhang, "Research on a novel miniaturized antipodal Vivaldi," *IEEE Antennas Wireless Propag. Lett.*, vol. 12, pp. 417-420, 2013.
- [11] J. Bourqui, M. Okoniewski, and E. C. Fear, "Balanced antipodal vivaldi antenna with dielectric director for near-field microwave imaging," *IEEE Trans. Antennas Propag.*, vol. 58, no. 7, pp. 2318-2326, Jul. 2010.
- [12] B. Zhou and T. J. Cui, "Directivity enhancement to vivaldi antennas using compactly anisotropic zero-index metamaterials," *IEEE Antennas Wireless Propag. Lett.*, vol. 10, pp. 326-329, 2011.
- [13] S. Kundu, A. Chatterjee, S. K. Jana, and S. K. Parui, "A compact umbrella-shaped UWB antenna with gain augmentation using frequency selective surface," *Radioengineering*, vol. 27, no. 2, pp. 448-454, Jun. 2018.
- [14] E. Erfani, M. Niroo-jazi, and S. Tatu, "A high-gain broadband gradient refractive index metasurface lens antenna," *IEEE Trans. Antennas Propag.*, vol. 64, no. 5, pp. 1968-1973, May 2016.
- [15] H. Cheng, H. Yang, Y. Li and Y. Chen, "A compact vivaldi antenna with artificial material lens and sidelobe suppressor for GPR applications," *IEEE Access*, vol. 8, pp. 64056-64063, 2020.
- [16] P. Mahouti, "Design optimization of a pattern reconfigurable microstrip antenna using differential evolution and 3D EM simulation-based neural network model," *Int. J. RF Microw. Comput. Aided Eng.*, vol. 29, e21796, 2019. <https://doi.org/10.1002/mmce.21796>.
- [17] J. Wang, X. S. Yang, and B. Z. Wang, "Efficient gradient-based optimization of pixel antenna with large-scale connections," *IET Microwaves Ant. Prop.*, vol. 12, no. 3, pp. 385-389, 2018.
- [18] M. Rossi, A. Dierck, H. Rogier, and D. Vande Ginste, "A stochastic framework for the variability analysis of textile antennas," *IEEE Trans. Ant. Prop.*, vol. 62, no. 16, pp. 6510-6514, 2014.
- [19] J. S. Ochoa and A. C. Cangellaris, "Random-space dimensionality reduction for expedient yield estimation of passive microwave structures," *IEEE Trans. Microwave Theory Techn.*, vol. 61, no. 12, pp. 4313-4321, 2013.
- [20] J. Dong, W. Qin, and M. Wang, "Fast multi-objective optimization of multi-parameter antenna structures based on improved BPNN surrogate model," *IEEE Access*, vol. 7, pp. 77692-77701, 2019.
- [21] J. L. Chávez-Hurtado and J. E. Rayas-Sánchez, "Polynomial-based surrogate modeling of RF and microwave circuits in frequency domain exploiting the multinomial theorem," *IEEE Trans. Microwave Theory Techn.*, vol. 64, no. 12, pp. 4371-4381, 2016.
- [22] N. V. Queipo, R. T. Haftka, W. Shyy, T. Goel, R. Vaidynathan, and P. K. Tucker, "Surrogate-based analysis and optimization," *Progress in Aerospace Sciences*, vol. 41, no. 1, pp. 1-28, 2005.
- [23] P. Barmuta, F. Ferranti, G. P. Gibiino, A. Lewandowski, and D. M. M. P. Schreurs, "Compact behavioral models of nonlinear active devices using response surface methodology," *IEEE Trans. Microwave Theory and Tech.*, vol. 63, no. 1, pp. 56-64, 2015.
- [24] J. Cai, J. King, C. Yu, J. Liu, and L. Sun, "Support vector regression based behavioral modeling technique for RF power transistors," *IEEE Microwave and Wireless Comp. Lett.*, vol. 28, no. 5, pp. 428-430, 2018.

- [25] A. Petrocchi, A. Kaintura, G. Avolio, D. Spina, T. Dhaene, A. Raffo, and D. M. P.-P. Schreurs, "Measurement uncertainty propagation in transistor model parameters via polynomial chaos expansion," *IEEE Microwave Wireless Comp. Lett.*, vol. 27, no. 6, pp. 572-574, 2017.
- [26] J. E. Rayas-Sanchez and V. Gutierrez-Ayala, "EM-based statistical analysis and yield estimation using linear-input and neural-output space mapping," *IEEE MTT-S Int. Microwave Symp. Digest (IMS)*, pp. 1597-1600, 2006.
- [27] P. Mahouti, A. Kızılay, O. Tari, A. Belen, M. A. Belen, "Design optimization of ultra wide band vivaldi antenna using artificial intelligence," *International Applied Computational Electromagnetics Society (ACES) Symposium*, pp. 1-4, 2021. doi: 10.1109/ACES53325.2021.00164.
- [28] X. Zhang, Y. Chen, M. Tian, J. Liu, and H. Liu, "A compact wide-band antipodal Vivaldi antenna design," *Int. J. RF Microw. Comput. Aided Eng.*, vol. 29, e21598, 2019. <https://doi.org/10.1002/mmce.21598>.
- [29] F. Güneş, İ. Ö. Evranos, M. A. Belen, P. Mahouti, and M. Palandöken, "A compact triband antipodal vivaldi antenna with frequency selective surface inspired director for IoT/WLAN applications," *Wireless Netw.*, vol. 27, pp. 3195-3205, 2021.
- [30] F. Güneş, S. Demirel, and P. Mahouti, "A simple and efficient honey bee mating optimization approach to performance characterization of a microwave transistor for the maximum power delivery and required noise," *Int. J. Numer. Model.*, vol. 29, pp. 4-20, 2016.
- [31] F. Güneş, S. Demirel, and P. Mahouti, "Design of a front-end amplifier for the maximum power delivery and required noise by HBMO with support vector microstrip model," *Radioengineering*, vol. 23, no. 1, pp. 134-143, 2014.
- [32] X. Li, G. Liu, Y. Zhang, L. Sang, G. Lv, "A compact multi-layer phase correcting lens to improve directive radiation of Vivaldi antenna," *Int. J. RF Microw. Comput. Aided Eng.*, 2017.
- [33] D. M. Elsheakh, E. A. Abdallah, "Ultrawideband vivaldi antenna for DVB-T, WLAN, and WiMAX applications," *International Journal of Antennas and Propagation*, vol. 8, pp. 1-7, 2014.
- [34] J. Schneider, M. Mrnka, J. Gamec, M. Gamcova, Z. Raida, "Vivaldi antenna for RF energy harvesting," *Radioengineering*, vol. 25, no. 4, pp. 666-671, 2016.
- [35] R. Bulgaroni, W. M. Torres, H. X. de Araujo, I. R. S. Casella, C. E. Capovilla, "Low-cost quad-band dual antipodal Vivaldi antenna using microstrip to CPS transition," *Microw. Opt. Technol. Lett.*, vol. 60, pp. 2315-2320, 2018.
- [36] A. S. Arezoomand, R. A. Sadeghzadeh, M. N. Moghadasi, "Investigation and improvement of the phase-center characteristics of VIVALDI's antenna for UWB applications," *Microw. Opt. Tech. Lett.*, vol. 58, no. 6, pp. 1275-1281, 2016.
- [37] R. Natarajan, M. Kanagasabai, M. Gulam, N. Alsath, "Dual mode antipodal Vivaldi antenna," in *IET Microwaves, Antennas & Propagation*, vol. 10, no. 15, pp. 1643-1647, 2016.
- [38] Z. Li, C. Yin, X. Zhu, "Compact UWB MIMO vivaldi antenna with dual band-notched characteristics," in *IEEE Access*, vol. 7, pp. 38696-38701, 2019.
- [39] H. Zhu, X. Li, L. Yao, and J. Xiao, "A novel dielectric loaded vivaldi antenna with improved radiation characteristics for UWB application" *Applied Computational Electromagnetics Society Journal*, vol. 33, no. 4, pp. 394-399, 2018.
- [40] Y. Zhu, D. Su, W. Xie, Z. Liu, and K. Zuo, "Design of a novel miniaturized vivaldi antenna with loading resistance for ultra wideband (UWB) applications" *Applied Computational Electromagnetics Society Journal*, vol. 32, no. 10, pp. 895-900, 2017.



Peyman Mahouti received his M. Sc. And Ph.D. degree in Electronics and Communication Engineering from the Yıldız Technical University, Turkey, in 2013 and 2016, Respectively. He is currently an Associated Professor with the Department of Electronic and Communication, Istanbul University - Cerrahpasa, Turkey. The main research areas are analytical and numerical modelling of microwave devices, optimization techniques for microwave stages, and application of artificial intelligence-based algorithms. His research interests include analytical and numerical modelling of microwave and antenna structures, surrogate-based optimization, and application of artificial intelligence algorithms.



Ahmet Kizilay was born in Istanbul, Turkey, in 1969. He received B.Sc. degree in Electronics and Communications Engineering from Yildiz University in 1990, M.Sc. and Ph.D. degrees in Electrical Engineering from Michigan State University in 1994 and 2000, respectively.

In July 2001, he joined the Department of Electronics and Communications Engineering at Yıldız Technical University, where he is currently working as Professor. His main research interests include time domain electromagnetic scattering, electromagnetic wave theory, and fiber optics.



Özlem Tari received her B.Sc., M.Sc. and Ph.D. in Physics Engineering from the Istanbul Technical University (ITU). She was the recipient of the Universidad Carlos III de Madrid Research Fellowship award before accepting her position at Istanbul Arel University in 2010. Her research areas are the phase transitions and phase diagram of some physical systems, Multi-Objective Optimization problems and development of Meta-Heuristic Optimization Algorithms.



Aysu Belen received his Ph.D. degree in Electronics and Communication Engineering from the Yıldız Technical University in 2021. Currently, she is a Lecturer in İskenderun Technical University. Her main research areas are optimization of microwave circuits,

circuits, device modeling, and computer aided circuit design and microwave amplifiers.



Mehmet Ali Belen received his Ph.D degree in Electronics and Communication engineering from the Yıldız Technical University in 2016. He is currently an Associated Prof. in İskenderun Technical University. His current activities include teaching and researching

Electromagnetics and Microwaves along with developing Additive Manufacturing 3D Printed Microwave Components for Rapid Prototyping. His current research interests are in the areas of multivariable network theory, device modeling, computer aided microwave circuit design, monolithic microwave integrated circuits, and antenna arrays, active/passive microwave components especially in the field of metamaterial- based antennas and microwave filters.



Alper Çalışkan received his Ph.D. degree in Electronics and Communication Engineering from the Yıldız Technical University in 2019. The main research areas are optimization of microwave circuits, broadband matching circuits, device modeling, and computer aided circuit

design, microwave amplifiers.

Dual-Band Phased Array 5G Mobile-Phone Antenna with Switchable and Hemispherical Beam Pattern Coverage for MIMO-Diversity Communications

Naser Ojaroudi Parchin¹, Osama M. Dardeer², Ahmed S.I. Amar³, Chan Hwang See¹, and Raed Abd-Alhameed⁴

¹School of Engineering and the Built Environment, Edinburgh Napier University, Edinburgh, UK
n.ojaroudiparchin@napier.ac.uk

²Microstrip Department, Electronics Research Institute, Nozha, Cairo, Egypt

³Air Defense College, Alexandria University, Alexandria, Egypt

⁴Faculty of Engineering and Informatics, University of Bradford, Bradford, UK

Abstract – A new design of dual-band antenna array with 3D-coverage beam steering characteristic for millimeter-wave (MM-Wave) communications is proposed in this manuscript. The antenna covers frequency bands of 18 GHz and 28 GHz. Its configuration contains three sub-arrays of patch radiators along the edge area of the smart phone printed circuit board (PCB). Each sub-array contains eight elements of dual-band patch antennas with C-shaped slots. The resonant frequencies of the single element radiator can be adjusted by tuning the sizes of the embedded C-shaped slot and the main patch radiator. The beam-steerable antenna is designed on an N9000 PTFE dielectric. In order to achieve high gain beams and also for covering wider beam-steering area, each sub-array is deployed in different top-sides of the PCB with a dimension of 55×110 mm². Using three uniform linear eight element sub-arrays, hemispherical beam pattern coverages can be achieved. The proposed antenna provides good performances in terms of gain, radiation and total efficiencies, and beam steering properties which make it suitable for use in the fifth generation (5G) mobile-phone platforms.

Index Terms – 5G networks, dual-band patch antenna, hemispherical beam coverage, mobile terminals.

I. INTRODUCTION

In line with the abbreviations of the past and current mobile communication standards (for instance 1G, 2G, 3G, and 4G), the term 5G, used here denotes the next generation mobile communication systems after current 4G systems [1]. One key feature of 5G communications systems is using the millimeter-wave (MM-Wave) spectrum along with beam-steerable array antennas at the user equipment and also the base stations [2, 3]. The

use of MM-Wave spectrum leads to new challenges in the 5G antenna designs for wireless communication systems [4]. To our knowledge, little is known on the design of arrays for 5G mobile terminals [5, 6]. We represent below how to employ MM-Wave for 5G cellular communication systems using microstrip antenna arrays.

In this study, a dual-band array antenna design with beam-steerable property in a standard PCB technology for MM-Wave mobile communications is proposed. The proposed antenna design contains three dual-band sub-arrays located along the edge region of the handset PCB. The array elements are divided into three sub-arrays, and each sub-array is employed in different sides of PCB edge region. S-parameters, realized gain, radiation beams, directivity and beam steering properties of the 5G antenna are studied. The antenna operates at the frequencies of 18 GHz and 28 GHz which are suitable for the 5G mobile communications. This manuscript has been organized as follows: The schematic of the single patch antenna element and its radiation performances along with the measured and simulated S_{11} characteristics are presented in Section II. The performance of the proposed dual-band 5G antenna with hemispherical beam pattern coverage is described in Section III. The last Section is the conclusion.

II. DUAL-BAND PATCH ANTENNA

Printed patch antennas with different feeding types are increasing popularity for use in narrow and band microwave wireless links. They are also often employed in MM-Wave communications as well. A simple microstrip patch antenna configuration is basically composed of a printed conductor on top layer of dielectric with a full metal plane on the back side. The fundamental radiation mechanism from the patch antenna is the same as the small electric dipole [7]. The energization

of the patch will establish a charge pushing the charges from the bottom to the top region of the radiator. Due to this charge-movement, the currents can flow on the upper and lower surfaces of the patch as well as on the surface of the ground plane [8]. In this paper, the 50 Ohm coaxial feeding type has been employed for the antenna elements where the inner-conductor of the coaxial cable is contacting the radiation patch and the outer-conductor is connected to the ground plan. In order to achieve good matching as well as lowest input impedance, we have used a 50 Ohm probe feeding with diameters of 0.5 and 1.72 for inner and outer conductors, respectively. The proposed dual-band patch antenna is designed on N9000 PTFE substrate with thickness, loss tangent, and dielectric constant of 0.787 mm, 0.0018, and 2.2, respectively. The configuration of the antenna is shown in Figure 1. The parameter values of the proposed antenna layout are specified in Table 1.

The essential parameters for designing a probe-fed printed patch antenna are: operation frequency (f_0), thickness, and dielectric constant of the employed substrate [9]. The selected resonant frequency for the proposed antenna design is 18 GHz (lower resonance frequency). Hence, the essential parameters of the dual-band patch antenna design are: $f_0 = 18$ GHz, $\epsilon_r = 2.2$ and $h = 0.787$ mm. The width of the patch can be given by:

$$W_{sub} = \frac{C}{2f_0\sqrt{\frac{\epsilon_r+1}{2}}}, \quad (1)$$

where C , ϵ_r , and f_0 are the speed of light, the dielectric constant (permittivity) of the substrate, and the desired resonant frequency, respectively. For a rectangular microstrip antenna, the value of the effective permittivity (ϵ_{reff}) can be calculated using:

$$\epsilon_{reff} = \frac{(\epsilon_r + 1)}{2} + \frac{(\epsilon_r - 1)}{2} \left[1 + 12 \frac{h_{sub}}{W_{sub}} \right]^{-\frac{1}{2}}. \quad (2)$$

The overall size of the radiation patch along its length is extended on each end by a distance ΔL , which

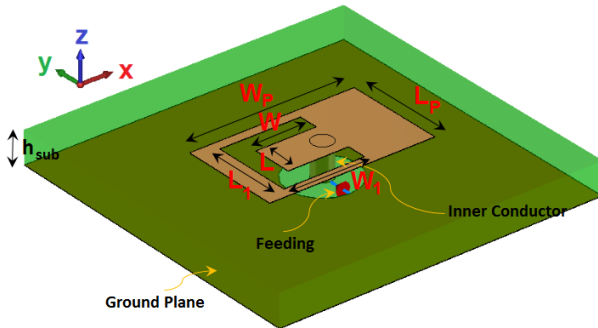


Fig. 1. Transparent schematic of the antenna.

Table 1: Parameter values of the antenna

| Parameter | W_{sub} | L_{sub} | h_{sub} | W_P | L_P |
|------------|-----------|-----------|-----------|-------|-------|
| Value (mm) | 55 | 110 | 0.787 | 4.32 | 2.5 |
| Parameter | W_{P1} | L_{P1} | W | L | W_1 |
| Value (mm) | 4.32 | 2.5 | 4 | 1.5 | 3 |
| Parameter | L_1 | W_2 | W_3 | L_3 | d |
| Value (mm) | 2.25 | 4 | 3 | 2 | 0.8 |
| Parameter | d_r | d_1 | d_{r1} | d_2 | d_s |
| Value (mm) | 1.72 | 4 | 0.5 | 1.7 | 4 |

can be given by:

$$\Delta L = 0.421 h_{sub} \frac{(\epsilon_{eff} + 0.3) \left(\frac{W_{sub}}{h_{sub}} + 0.264 \right)}{(\epsilon_{eff} - 0.258) \left(\frac{W_{sub}}{h_{sub}} + 0.8 \right)}, \quad (3)$$

where h_{sub} is the substrate height and W_{sub} is the substrate width. For the resonant, the effective length is:

$$L_{eff} = \frac{C}{2f\sqrt{\epsilon_{reff}}}, \quad (4)$$

Then, the length of the patch resonator can be calculated as follows:

$$L_{eff} = \frac{C}{2f\sqrt{\epsilon_{reff}}}. \quad (5)$$

The final step of the dual-band patch antenna design is choosing the length of the second resonator element. By cutting a C-shaped slot at the antenna radiating patch, the second resonance at the higher frequencies (28 GHz) is generated. In the proposed design, the optimized length $L_{resonance}$ is set to resonate at $0.25\lambda_{resonance}$, where $L_{resonance} = L_1 + W_1 - 0.5(L_1 - L)$. $\lambda_{resonance}$ corresponds to the second resonance frequency (28 GHz). The S_{11} result of the proposed antenna simulated using CST software [10] is illustrated in Figure 2(a), (b). As illustrated, using the proposed design, a good dual-band function with improved bandwidth has been achieved.

The simulated S_{11} curves of the proposed dual-band patch antenna for different values of radiation patch length (W_P) are plotted in Figure 3 (a). As seen, when the length of the radiation patch (main radiator) increases

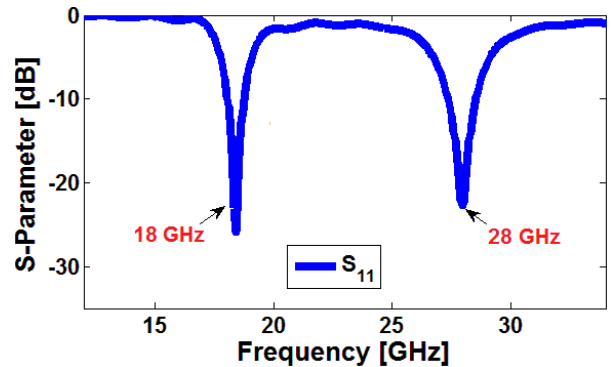


Fig. 2. Simulated S_{11} of the dual-band patch antenna.

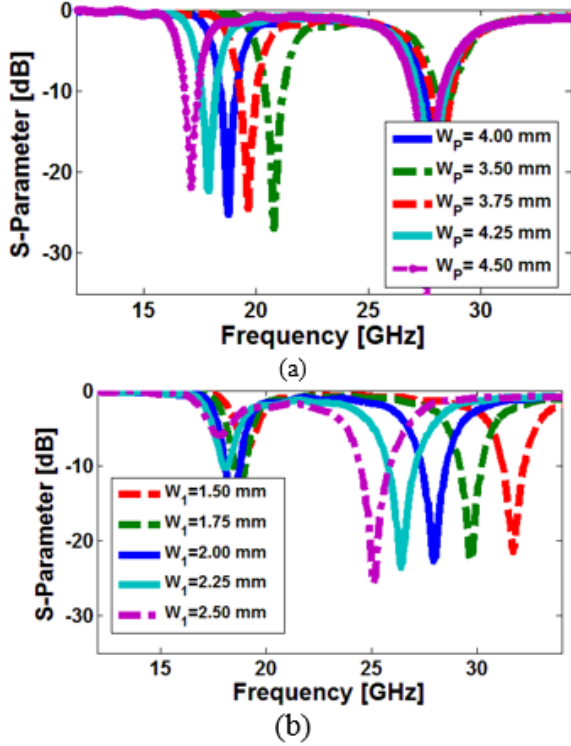


Fig. 3. Simulated S_{11} for values of (a) W_p and (b) W_1 .

from 3.5 to 4.5 mm, the center of the first resonance decreases from 21 to 16 GHz. Based on this result we can conclude that the first resonance can be adjusted by changing the length of the main radiator (patch). Another important parameter of the proposed dual-band design is the C-shaped slot. The main effect of this structure occurs on the second resonance. In the proposed structure, the length of W_1 is the critical parameter to control the upper operation band. Figure 3 (b) shows the simulated S_{11} results of the dual-band antenna with different lengths of W_1 . As the width of the C-shaped slot changes from 1.5 to 2.5 mm, the operation frequency of the second resonance is varied from 25 to 32 GHz. Therefore, the operation frequency of second-resonance is tunable by changing the size of the embedded C-shaped slot.

In order to realize the phenomenon for the dual-band performance of the antenna, the current distributions of the dual-band antenna at 18 and 28 GHz are depicted in Figure 4. As seen, at the first frequency (18 GHz), the current is concentrated on the edge regions of the rectangular radiating patch. Therefore, due to the resonant characteristics of the rectangular patch length, the impedance of the antenna can be tuned at this frequency [10]. As illustrated in Figure 4 (b), at the upper resonance frequency (28 GHz), the currents flow mainly around the modified C-shaped slot structure and justify the impact of the embedded slot on the generation of the

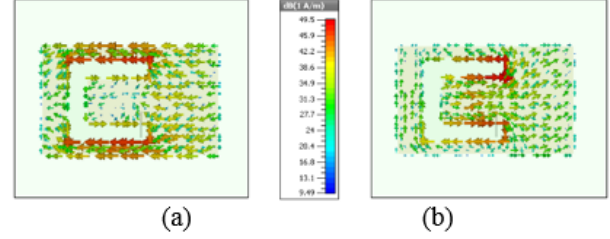


Fig. 4. Current densities at (a) 18 GHz and (b) 28 GHz.

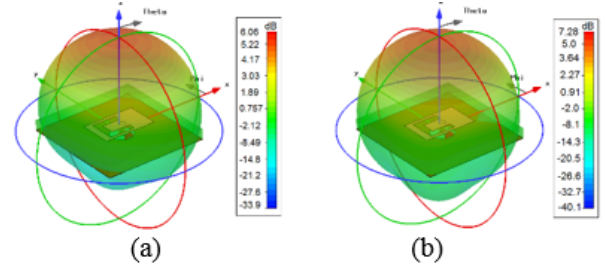


Fig. 5. 3D radiations at (a) 18 GHz and (b) 28 GHz.

second resonance. The simulated radiation patterns at 18 and 28 GHz are represented in Figure 5. As can be seen, the antenna provides a good radiation behavior in both of the operation frequencies. In addition, sufficient realized gains (more than 6 dB) are obtained for the designed dual-band antenna at the operation bands. The antenna element is fabricated and its return loss characteristics are measured. Figure 6 (a) illustrates the fabricated prototype. The measured and simulated S_{11} characteristic of the antenna are illustrated in Figure 6 (b). As seen, the antenna provides a dual-band performance around 18 and 28 GHz.

Figure 7 (a), (b) depicts polar views of the antenna radiation patterns including both, the co-polarized and cross-polarized, x - z plane (E -plane) and y - z plane (H -plane), respectively. As illustrated, the antenna has good radiation performance with stable co-polarization and low-level cross polarization. Furthermore, as can be seen, the effect of the probe feeding on the field pattern shapes at different operation frequencies is insignificant.

The dual-band patch antenna maximum gain, and its efficiencies (radiation and total) over the operation frequency range are shown in Figure 8. In theory, the antenna efficiencies are related according to:

$$e = e_r e_{cd}, \quad (6)$$

and the gain of the radiator can be calculated using the total efficiency and the directivity as follows:

$$G_0(dB) = 10 \log(e_0 D_0), \quad (7)$$

where e_0 is the total efficiency of the antenna, e_r is the reflection efficiency $= (1 - |\Gamma|^2)$, e_{cd} is the radiation effi-

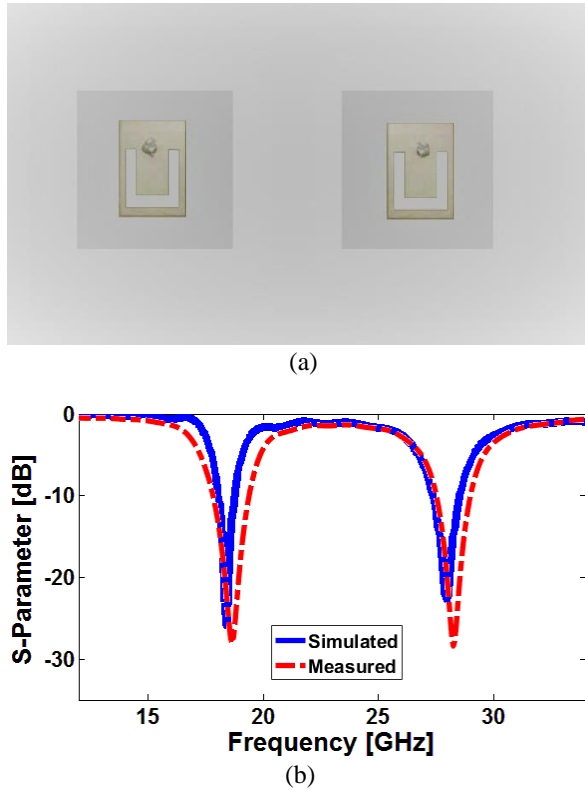


Fig. 6. (a) Top view of the fabricated antenna elements and (b) measured/simulated S_{11} of the single antenna.

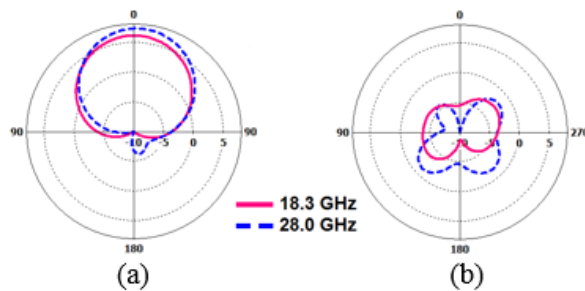


Fig. 7. Simulated 2D radiation patterns of the dual-band antenna, (a) co-polarization, (b) cross-polarization.

ciency, and D_0 is the antenna directivity [11]. As can be seen from Figure 8, the antenna has desirable radiation properties with more than 6 and 7 dBi maximum gains at lower and upper operation frequencies, respectively. Furthermore, the antenna has a high-efficiency function at the frequencies of the antenna operation bands.

III. PROPERTIES OF THE 5G MOBILE PHONE PHASED ARRAY ANTENNA

The schematic of the presented 5G array antenna is illustrated in Figure 9. The design is composed of three

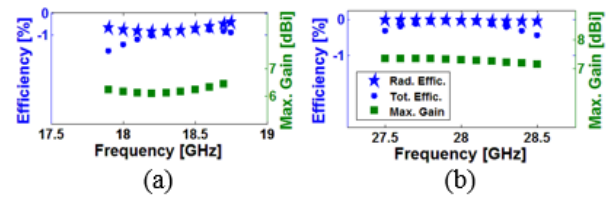


Fig. 8. Simulated efficiencies and maximum gains of the antenna at, (a) lower and (b) upper operation bands.

dual-band patch antenna sub-arrays deployed at different edge regions of smartphone PCB. Eight elements of dual-band microstrip patch antennas are used for each sub-array. For the proposed design λ is the guided wavelength at the middle frequency (23 GHz). As can be observed in Figure 9 (a), the compact antenna package (Fig. 9 (b)) is deployed at the edge side of the PCB. The proposed mobile-phone 5G antenna has a full ground plane. The antenna design has an overall dimension of $W_{sub} \times L_{sub} = 55 \times 110 \text{ mm}^2$.

The simulated S-parameter of a single sub-array is illustrated in Figure 10 (a). As shown, the proposed phased array dual-band antenna provides good S-parameters with low mutual-couplings between antenna elements.

Figure 10 (b) illustrates couplings among the antenna elements. The maximum mutual couplings between radiation elements of the design are occurred among “Antenna_A1-Antenna_A2,” “Antenna_A1-Antenna_B1,” and “Antenna_A1-Antenna_C1.” As illustrated, all of the mutual couplings are less than -25 dB , -13 dB , and -24 dB , respectively. It can be seen

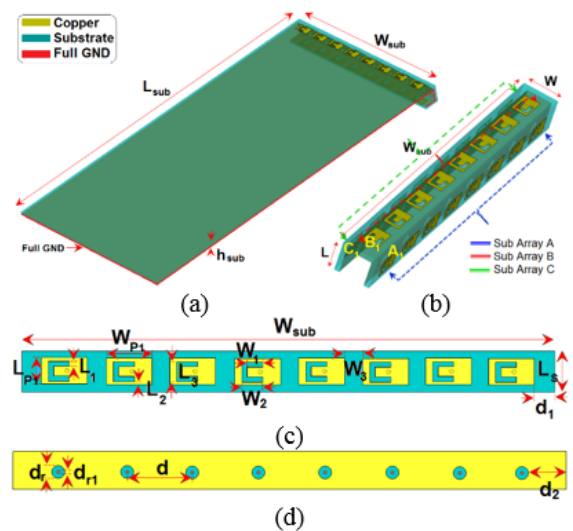


Fig. 9. (a) Side view of the proposed mobile phone antenna, (b) antenna package configuration, (c) top and (d) bottom layers of each sub-array.

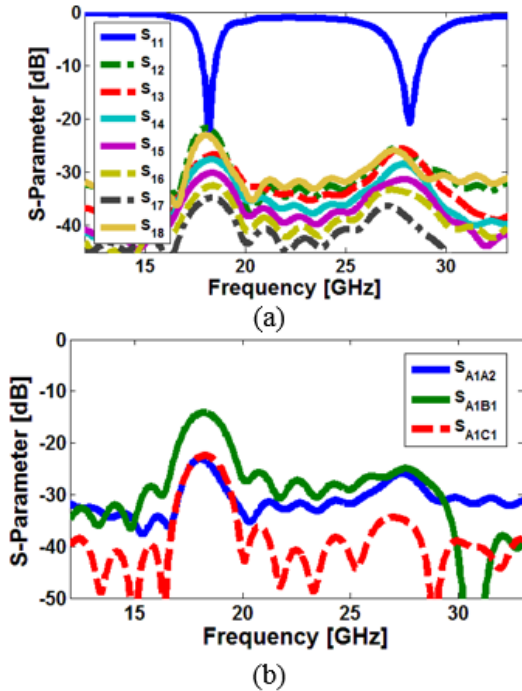


Fig. 10. Simulated (a) S-parameters and (b) mutual couplings of a sub-array.

that the coupling between sub-array A elements and sub-array B elements are higher than the other couplings which occurred mainly because of the distance between two sub-array elements. As seen, the proposed antenna has good S-parameters and also it is not sensitive to the mutual coupling of the radiation elements.

Based on re-simulated results of the proposed design, it should be noted that the mutual coupling on an element within a sub-array when it is scanned and also the coupling between sub-arrays when one sub-array is scanned while monitoring coupling on an adjacent sub-array element have been investigated. According to the results, the antenna provides sufficient and low coupling between the elements and adjacent sub-arrays and its effects in the final conformal array is not significant to lead to a potential multi-path problem [12].

Figure 11 shows the simulated directivity characteristics of the dual-band design for sub-arrays at the main scanning angle (0°). As illustrated, the antenna provides a good directivity property for all of the sub-arrays at 0° . The antenna directivities for different sub-arrays are greater than 13.5 and 15.5 dBi at 18 and 28 GHz, respectively. The efficiencies (radiation and total) of the mobile phone antenna are illustrated in Figure 12. As shown, the antenna efficiencies are greater than -0.3 and -0.7 dB for radiation efficiency and total efficiency, respectively. From these results, it can be seen that the antenna provides good efficiencies at 18 and 28 GHz.

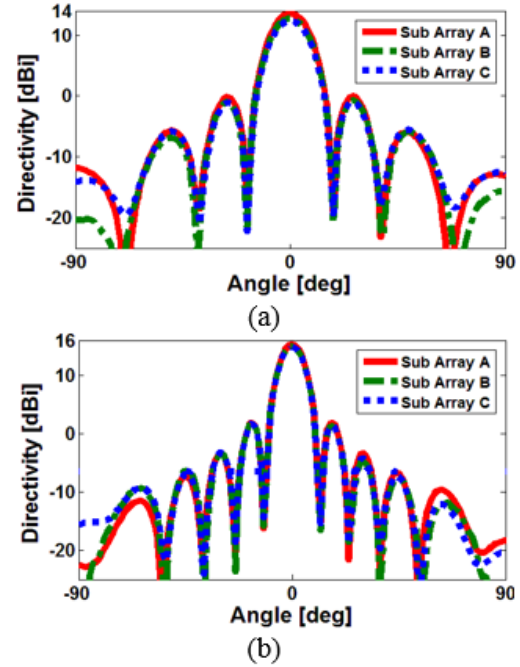


Fig. 11. Directivities of the antenna at 0° for (a) 18 GHz, and (b) 28 GHz of operation bands.

The 3D radiation beams of the proposed dual-band antenna array at 18 and 28 GHz for each sub-array are depicted in Figure 13 (a), (b), respectively. As seen, the proposed 3D beam coverage antenna package with the compact dual-band sub-arrays is highly effective to provide the required beam coverage for 5G handsets.

Figure 14 shows the 3D radiation beams of the dual-band antenna array at 18 and 28 GHz, respectively. As can be seen, the proposed dual-band antenna array provides a wide-scan beam steering function with the high gains for the scanning angles of 0, 30, and 60 degree. In the range of 0 to 30 degrees, the gain values are

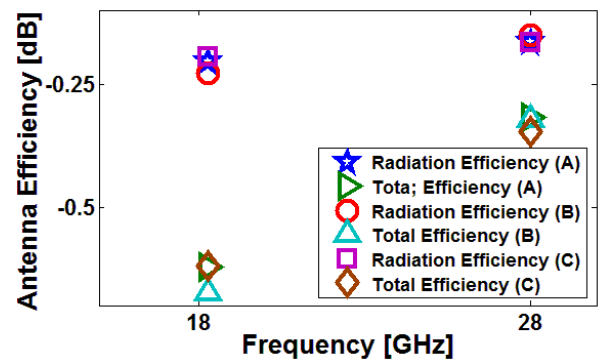


Fig. 12. Simulated efficiencies of the different sub-arrays at 0° scanning angle.

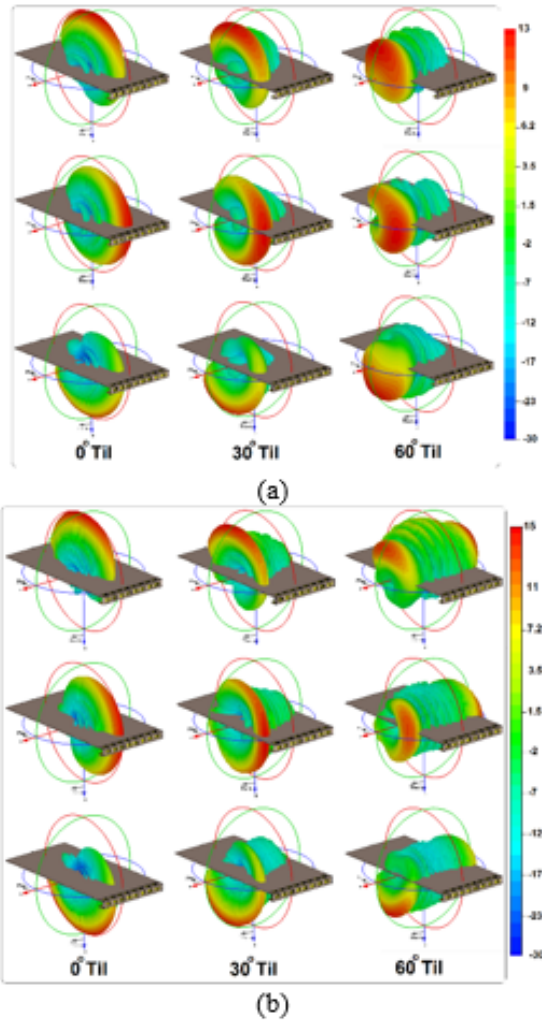


Fig. 13. Radiation beams of each dual-band sub-arrays for different angles, (a) 18 GHz and (b) 28 GHz.

almost stable with the values of 13 dB at 18 GHz and 15 dB at 28 GHz. As shown, the sub-arrays possess relatively low side-lobe levels at the lower frequency (18 GHz). As illustrated, the side-lobe levels in the scanning range of 0° to 60° is less than 0 dB. However, as illustrated in Figure 14 at 28 GHz, the sub-arrays beams provided relatively high side lobes at the scanning degree $<40^\circ$ which is mainly because of the distance of the elements.

In general, the radiation-element distance should be chosen as $\lambda/2$ of the operation frequency [13, 14]. However, as the antenna provides dual-band function, it is difficult to achieve wide-scanning property at both operation frequencies. Therefore, high side-lobe levels will be appeared, especially at higher scanning angles of the lower frequency band.

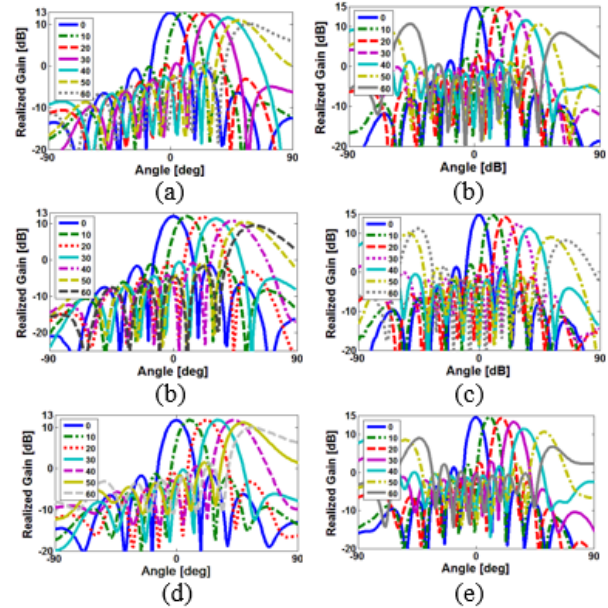


Fig. 14. Simulated realized gains for, (a) sub-array A at 18, (b) sub-array B at 18, (c) sub-array C at 18, (d) sub-array A at 28, (e) sub-array B at 28, and (f) sub-array C at 28 GHz.

IV. CONCLUSION

The design and characteristics of a dual-band microstrip antenna array for 5G cellular communication systems is introduced in this paper. Three uniform linear eight-element dual-band patch antenna sub-arrays are used to achieve hemispherical radiation beams with 3D beam-coverage. The simulated result analysis of the proposed 5G antenna gives good fundamental properties in terms of impedance bandwidth, antenna gain/directivity, radiation pattern, and steering of the radiation beams. The obtained results show that the presented dual-band 5G antenna array could be used in the future 5G cellular communication systems. The proposed mobile phone phased array antenna is strongly effective to cover the required beam-coverage for 5G smart phones.

REFERENCES

- [1] W. Roh, J. -Y. Seol, J. Park, B. Lee, J. Lee, Y. Kim, J. Cho, K. Cheun, and F. Aryanfar, "Millimeter-Wave beamforming as an enabling technology for 5G cellular communications: Theoretical feasibility and prototype results," *IEEE Commun. Mag.*, vol. 52, pp. 106–113, 2014.
- [2] T. S. Rappaport, S. Sun, R. Mayzus, H. Zhao, Y. Azar, K. Wang, G. N. Wong, J. K. Schulz, M. Samimi, and F. Gutierrez, "Millimeter wave mobile communications for 5G cellular: It will work!" *IEEE Access*, vol. 1, pp. 335–349, 2013.

- [3] Y. Wang, J. Li, L. Huang, Y. Jing, A. Georgakopoulos and P. Demestichas, "5G mobile: Spectrum broadening to higher-frequency bands to support high data rates," *IEEE Vehicular Technology Magazine*, vol. 9, pp. 39-46, 2014.
- [4] Y. Azar, G. N. Wong, K. Wang, R. Mayzus, J. K. Schulz, H. Zhao, F. Gutierrez, D. Hwang, T. S. Rappaport, "28 GHz propagation measurements for outdoor cellular communications using steerable beam antennas in New York city," *IEEE ICC*, 2013.
- [5] N. Ojaroudiparchin, M. Shen, and G. F. Pedersen, "Wide-scan phased array antenna fed by coax-to-microstriplines for 5G cell phones," *21st International Conference on Microwave, Radar and Wireless Communications (MIKON)*, 2016.
- [6] W. Hong, K. Baek, Y. Lee, and Y. G. Kim, "Design and analysis of a low-profile 28 GHz beam steering antenna solution for future 5G cellular applications," *IEEE International Microwave Symposium*, 1-6 June, Tampa Bay, Florida, 2014.
- [7] N. O. Parchin, Y. I. A. Al-Yasir, J. M. Noras, and R. A. Abd-Alhameed, "Dual-polarized MIMO antenna array design using miniaturized self-complementary structures for 5G smartphone applications," *EuCAP Conference*, 31 March-5 April, Krakow, Poland, 2019.
- [8] B. F. Wang and Y. T. Lo "Microstrip antenna for dual-frequency operation," *IEEE Trans. Antennas Propag.*, vol. AP-32, no. 9, pp. 938-943, 1984.
- [9] C. A. Balanis, *Antenna Theory Analysis and Design*, 3rd edition, Wiley, New Jersey, 2005.
- [10] *CST Microwave Studio*, ver. 2020, CST, Framingham, MA, USA, 2020.
- [11] R. Garg, P. Bhartia, I. Bahl, A. Ittipiboon, *Microstrip Antenna Design Handbook*, Artech House, Boston – London, 2000.
- [12] N. O. Parchin, R. A. Abd-Alhameed, and M. Shen, "Frequency-switchable patch antenna with parasitic ring load for 5G mobile terminals," *International Symposium on Antennas and Propagation (ISAP)*, Xi'an, China, 2019.
- [13] A. Ullah, N. O. Parchin, R. A. Abd-Alhameed, and P. S. Excell, "Coplanar waveguide antenna with defected ground structure for 5G millimeter-wave communications," *IEEE MENACOMM*, 19-21 Nov., Manama, Bahrain, 2019.
- [14] N. O. Parchin, J. Zhang, R. A. Abd-Alhameed, G. F. Pedersen, and S. Zhang, "A planar dual-polarized phased array with broad bandwidth and quasi-endfire radiation for 5G mobile handsets," *IEEE Trans. Antennas Propag.*, vol. 69, pp. 6410-6419, 2021.



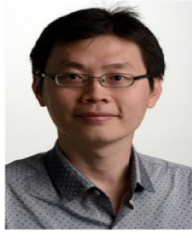
Naser Ojaroudi Parchin is currently an assistant professor (lecturer) at Edinburgh Napier University, UK. He obtained his PhD in Electrical Engineering from University of Bradford, UK, where he was a Postdoctoral Research Assistant at the Faculty of Engineering and Informatics and worked as a research fellow in SAT-NEX V project, funded by European Space Agency. From 2018 to 2020, he was a Marie Curie Research Fellow in H2020-ITN-SECRET project funded by EU Commission. He is author and coauthor of several book chapters, and more than 300 technical journals and conference papers with more than 5200 citations and 40 h-index. His research interests include antennas, phased arrays, MIMO systems, microwave components, and electromagnetic wave propagation.



Osama M. Dardeer was born in 1987. He received the B.S. degree with honor from Menofia University, Egypt, in 2009. He received the M.S. degree in electrical engineering from Ain Shams University, Egypt in 2017. He received the PhD degree in electrical engineering from Ain Shams University, Egypt in 2021. He is currently an Assistant Researcher at Microstrip Department, Electronics Research Institute, Egypt. He has been a member of research projects funded from national agencies such as National Telecommunication Regulatory Authority (NTRA). His research interests include UWB Antennas, Antennas for Mobile Generations, Band stop Filters, Radar Antenna Arrays, Power Dividers, RF Energy Harvesting, Internet of Things applications, and Optical Switching Networks.



Ahmed S. I. Amar received the B.S. degree in electrical engineering from the University of Alexandria, Alexandria, Egypt, in 2008, and the M.Sc. degree in electrical engineering from the Ain Shams University, Cairo, Egypt, in 2016. He is currently an Assistant Researcher at Electromagnetic Fields Department, ADR&D Center, Egypt, and aiming for getting a Ph.D. degree from Ain Shams University. His current research interests include Antennas, RF and Microwave Circuit Design, Power Amplifiers, and Millimeter-wave passive and active circuits Design.



Chan H. See received a first class B.Eng. Honours degree in Electronic, Telecommunication and Computer Engineering and a Ph.D. degree from the University of Bradford, UK. Currently, he is an Associate Professor (Head of Electrical Engineering & Mathematics)

in School of Engineering & the Built Environment, Edinburgh Napier University, UK. Previously, Mr. See was a Senior Lecturer (Programme Leader) in School of Engineering, University of Bolton, UK. His research interests cover wireless sensor network design, acoustic/microwave sensors, antennas and microwave circuits. He was awarded a certificate of excellence for his successful Knowledge Transfer Partnership (KTP) with Yorkshire Water in 2009. He has published over 110 journal articles and over 130 conference papers. He is a co-author for one book and five book chapters. Dr. See is a Chartered Engineer (CEng), Senior member IEEE, Fellow of the IET. He is also a Fellow of The FHEA, a full member of the EPSRC Review College, an Associate Editor for IEEE Access and an Editor for Peerj Computer Science, PLOS ONE and Wireless Power Transfer journals.



Raed Abd-Alhameed is a Professor of Electromagnetic and Radio Frequency Engineering at the University of Bradford, UK. He has long years' research experience in the areas of Radio Frequency, Signal Processing, propagations, antennas and computational techniques, and

has published over 800 academic journal and conference papers; in addition He is the Principal Investigator for several funded applications to EPSRCs and leader of several successful knowledge Transfer Programs He was awarded the business Innovation Award for his successful KTP with Pace and Datong companies on the design and implementation of MIMO sensor systems and antenna array design for service localizations. He is also a research visitor for Wrexham University, Wales covering the wireless and communications research areas. His interests are in 5G Green Communications Systems, computational methods and optimizations, wireless and Mobile communications, sensor design, EMC, MIMO systems, beam steering antennas, Energy efficient PAs, RF pre distorter design applications. He is the Fellow of the Institution of Engineering and Technology, Fellow of Higher Education Academy and a Chartered Engineer.

Design of Planar Directional Coupler using 2-Bit Fragment Structures

Yonghui Tao¹, Wenjuan Zhang², Johan Sidén³, and Gang Wang²

¹Department of Electronic and Information Engineering
Jinling Institute of Technology, Nanjing, 211169, China
yhtao87@jit.edu.cn

²Department of Electronic Engineering and Information Science
University of Science and Technology of China, Hefei, 230027, China
Antenna Design University, City, State Code Zip Code, Country
gwang01@ustc.edu.cn
wjz16@mail.ustc.edu.cn

³Department of Electronics Design
Mid Sweden University, SE-851 70 Sundsvall, Sweden
Johan.Siden@miun.se

Abstract – Automatic design of planar directional coupler can be implemented by multi-objective optimization searching for the optimal planar fragment-type structure (FTS). The 2-bit FTS description scheme may include necessary fine structures in fragments to enhance the FTS design. By coding the coupler design space on PCB in 2-bit FTS, defining the FTS design matrix, and searching for the optimal structure, directional coupler can be designed without any structure presetting or artificial intervention. The scheme is demonstrated by designing 10-dB wideband directional coupler with 2-bit FTS scheme. The designed directional couplers are fabricated and tested to show maximum directivity of 58 dB with 36% operation bandwidth.

Index Terms – directional coupler, fragment-type, directivity, modeling, optimization.

I. INTRODUCTION

Microstrip directional couplers are widely used in RF/microwave systems. Traditional microstrip directional couplers are based on coupled lines, which have limited directivity and bandwidth due to the phase velocity difference between the odd and even modes [1].

In order to improve the directivity and bandwidth, different design techniques have been proposed to seek more appropriate coupler structure. Based on the idea of distributed compensation, planar artificial transmission lines [2] and lumped elements [3–5] have been used to enhance the coupler performance, and generate directivity higher than 20 dB. Multilayer structure is proposed

in [6] to improve the minimum directivity to 20 dB over a bandwidth of 10% for coupling of 14.3 dB. A 10-dB directivity-enhanced coupler is designed in [7] by using epsilon negative transmission line, which yields a directivity above 20 dB in a bandwidth of 8.7%. A 15-dB coupler of directivity higher than 22 dB is designed in [8] by using multiple narrow strips and an open slot on the ground. Asymmetric multi-section stripline is proposed in [9] to improve the minimum directivity to 25 dB over a bandwidth of 55% for 18.5 dB coupling. A 10-dB coupler using multi-mode resonator is reported in [10] to present a minimum directivity of 25 dB within a bandwidth of 24%. Periodic metallic cylinders are set on microstrip lines to design 12dB coupler of directivity of 46 dB in [11]. For all these designs, canonical structures of certain types play important roles in the coupler designs.

Recently, a design scheme by using fragment-type structure (FTS) is proposed in [12] to challenge the high directivity and broad bandwidth. The FTS-based planar directional coupler presents a minimum directivity of 37 dB in a relative bandwidth of 45% for 20 dB coupling, and directivity of 28.7 dB in 29% bandwidth for 10 dB coupling [12]. In the FTS designs, appropriate narrow slots are preset to ensure efficient searching for the optimal FTS structure to define the coupler.

To improve the design performance and optimization efficiency, 2-bit FTS has been considered in planar low-pass filter design [13]. It is shown that the design of low-pass filter with the 2-bit FTS elements can acquire higher roll-off rate, wider stopband width, and higher stopband suppression with shorter optimization time, if

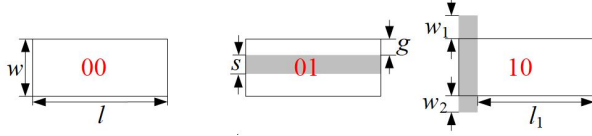


Fig. 1. Elements proposed for the 2-bit FTS scheme.

compared with the design using conventional 1-bit FTS scheme.

In this paper, 2-bit FTS design scheme is proposed for automatic design of high-performance microstrip directional coupler. The appropriate 2-bit FTS elements for directional coupler, the coding for the enhanced FTS design matrixes, and the multi-objective optimization searching for the optimal FTS directional couplers are presented in Section II. In Section III, the proposed 2-bit FTS scheme is demonstrated by challenging the 20 dB and 10 dB planar directional couplers.

II. MULTI-OBJECTIVE OPTIMIZATION SCHEME FOR FTS-BASED DIRECTIONAL COUPLER

With no loss of generality, we consider a design space of dimensions $a \times b$ on PCB for directional coupler. Suppose the design space is to be discretized into cells of dimensions $w \times l$, the design space is gridded into cells of number of $m \times n = (a/w) \times (b/l)$.

When 2-bit FTS is used for high performance design, appropriate fine or subtle structures on FTS elements are required.

A. Structure description with 2-bit FTS

For planar directional coupler, we may choose the 2-bit FTS elements as shown in Figure 1, where two of the FTS elements bear thin metal lines of the width s in vertical and horizontal directions, respectively. By assigning binary codes 00, 01, 10, and 11 to different elements, the 2-bit FTS can be coded.

For the 2-bit FTS elements, different thin lines and slots can be defined by setting different fine structure parameters g and s . The vertical thin line in element “10” is set to extend outside the cell in y -axis direction by w_1 and w_2 , which ensure the connection with the adjacent cell “01.” The gap coupling can be formed between adjacent cells “01” and “11.” Note that the line width s may be set according to the machining precision for PCB processing. In the following design, it is set as $s = 0.2$ mm.

Figure 2 shows the structure coding for the 2-bit FTS description by combining the 1-bit FTS coding and a control matrix, which can be implemented in the following steps:

- i. Discretize the space on PCB reserved for the coupler.

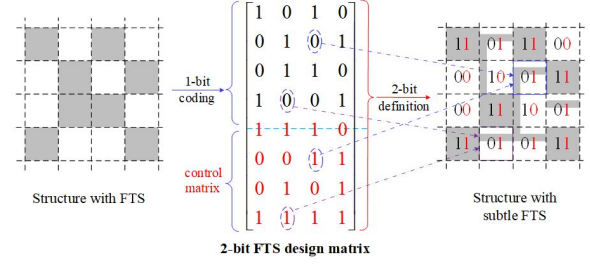


Fig. 2. Structure coding for the 2-bit FTS scheme.

- ii. Assign every cell with either “0” or “1” to form the 1-bit matrix, where “1” = metal and “0” = empty.
- iii. Assign control code “1” or “0” to the 1-bit codes, to form the 2-bit coding: “11” => full metal, “10”=>vertical thin line, “01”=>horizontal thin line, “00”=>empty.
- iv. Define a *control matrix* with the control code “1” and “0”.
- v. Combine the 1-bit design matrix and the control matrix to yield the 2-bit FTS design matrix.

The above 2-bit coding scheme clearly shows that the 2-bit FTS design matrix is always twice the 1-bit design matrix. To include the same thin lines and gaps with the conventional 1-bit scheme, it will need a design matrix enlarged at least to the size of $(w/s) \times (l/s)$, which could be a huge and impractical decision space for multi-objective optimization searching.

B. Objective functions for MOEA/D-GO

Multi-objective optimization searching can be used for design of high-performance planar directional coupler. The specifications of a directional coupler, such as coupling level, return loss (RL) and isolation, can be set as the key indicators for optimization. The objective functions for a directional coupler can be specified as follows [12]:

$$f_1(x) = \max \left(\max_{\omega \in [\omega_1, \omega_2]} |S_{31}|_{dB} - C_0, 0 \right), \quad (1)$$

$$f_2(x) = \max \left(\max_{\omega \in [\omega_1, \omega_2]} |S_{31}|_{dB} - \min_{\omega \in [\omega_1, \omega_2]} |S_{31}|_{dB}, \delta \right), \quad (2)$$

$$f_3(x) = \max \left(Q - \max_{\omega \in [\omega_1, \omega_2]} |S_{41}|_{dB}, 0 \right), \quad (3)$$

$$f_4(x) = \max \left(R_0 - \min_{\omega \in [\omega_1, \omega_2]} |S_{11}|_{dB}, 0 \right), \quad (4)$$

$$f_5(x) = \max \left(BW - \frac{\omega_2 - \omega_1}{\omega_0}, 0 \right), \quad (5)$$

where $[\omega_1, \omega_2]$ defines the desired band of the microstrip directional coupler, $|S_{31}|_{dB}$ indicates the coupling level, $|S_{41}|_{dB}$ indicates the isolation, and $|S_{11}|_{dB}$ indicates the return loss (RL).

Objective function $f_1(x)$ guarantees a coupling level of C_0 (in dB) in the desired band. The objective function $f_2(x)$ ensures the stability of coupling level, and δ is the maximum allowable fluctuation of coupling level. Objective function $f_3(x)$ controls the desired isolation is greater than Q (in dB). Objective function $f_4(x)$ ensures that RL is greater than R_0 (in dB). Objective function $f_5(x)$ assures the operation bandwidth, ω_0 denotes the center frequency and BW is the desired fractional bandwidth.

With the above defined objective functions, the decision matrix for FTS can be optimized to yield the optimal coupler structure. The multi-objective evolutionary algorithm based on decomposition combined with enhanced genetic operators (MOEA/D-GO) for 2-bit FTS [13] can be used to search for the optimal design matrix.

III. COUPLER DESIGNS WITH 2-BIT FTS

For demonstration, the directional coupler is supposed to be printed on a PCB of FR4 substrate ($\epsilon_r = 4.4$, $\tan \delta = 0.02$) and thickness of 1.6 mm. The design space on PCB is 10.3 mm \times 16.4 mm. In addition, the coupler structure on PCB is supposed to have both the horizontal and vertical symmetry so that the real design space for FTS optimization searching is 5.15 mm \times 8.2 mm.

For FTS modeling, the design space 5.15 mm \times 8.2 mm is discretized into 12 \times 6 cells so that the 2-bit FTS scheme needs a design matrix of 12 \times 12, in which 12 \times 6 matrix is the control matrix, as shown in Figure 2.

The parameters defining the 2-bit FTS elements in the Figure 2 are: $w = 0.44$ mm, $l = 1.54$ mm, $l_1 = 1.34$ mm, $s = 0.2$ mm, $g = 0.1$ mm, $w_1 = 0.34$ mm and $w_2 = 0.3$ mm. By setting $w = 0.44$ mm and $l = 1.54$ mm, necessary overlap between the adjacent cells can be guaranteed for side or diagonal connection. In addition, $g = 0.1$ mm ensures a small gap can be yielded.

A. Design of 20-dB directional coupler

For the 20-dB directional coupler, the design objectives are set with $C_0 = 20$ dB in eqn (1), with $\delta = 0.5$ in eqn (2), $Q = 70$ in eqn (3), $R_0 = 40$ in eqn (4), and $BW = 40\%$ in eqn (5) to challenge high performance. The coupler is desired to operate in band $[\omega_1, \omega_2] = [1.6 \text{ GHz}, 2.4 \text{ GHz}]$, which is a quite wide bandwidth for PCB directional coupler. The bandwidth is evaluated in terms of ± 0.5 dB coupling level variation, 20 dB return loss, and 20 dB directivity.

After implementing the MOEA/D-GO optimization with the objectives in eqn (1)–(5), one of the optimal layouts of the FTS-based 20-dB directional coupler is shown in Figure 3. The optimization searching takes 50 iterations (around 65 hours on the computer with Intel Core I7-8700@3.2GHz).

Figure 4 presents the simulated and measured S-parameters. In the operation band, the simulated mini-

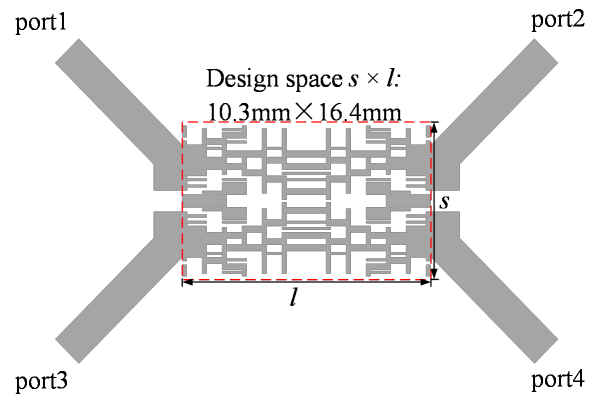


Fig. 3. The layout of 20-dB director with 2-bit FTS scheme.

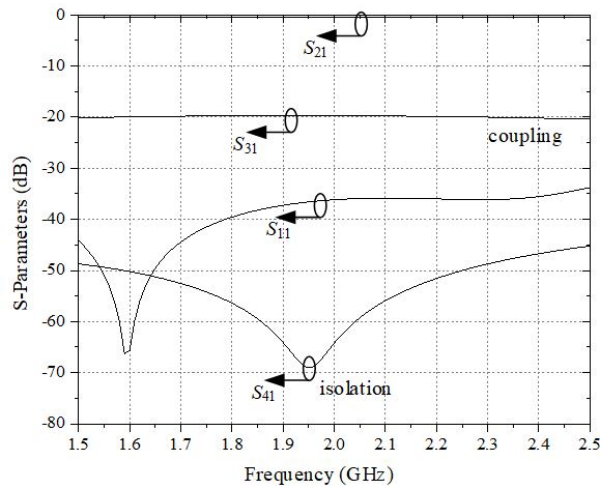


Fig. 4. S-parameters of the 20-dB directional coupler with 2-bit FTS.

imum return loss is 33 dB, the maximum insertion loss is 0.8 dB, the isolation is greater than 45 dB, and the maximum isolation is 69 dB. The coupling level is 20 dB \pm 0.5 dB in frequency band ranging from 1.5 GHz to 2.5 GHz, which gives a fractional bandwidth of 50%.

Directivity of the 20-dB coupler can be calculated from the S-parameters in Figure 4. The minimum directivity is $D_{\min} = 27.5$ dB and the maximum directivity is $D_{\max} = 49$ dB in the operation bandwidth. Therefore, the proposed 2-bit FTS can be used in design of wide-band high-directivity 20-dB directional coupler without any slot presetting.

B. Design of 10-dB directional coupler

For the 10-dB directional coupler, the design objectives are set with $C_0 = 10$ dB in eqn (1), with $\delta = 0.5$ in eqn (2), $Q = 70$ in eqn (3), $R_0 = 40$ in eqn (4), and

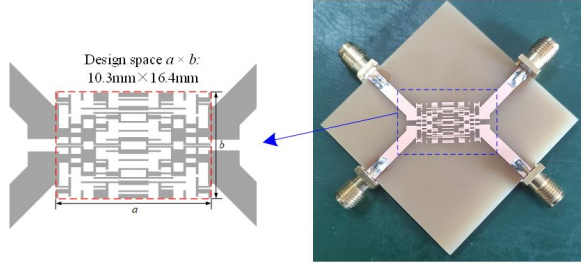


Fig. 5. The 10-dB directional coupler designed with 2-bit FTS.

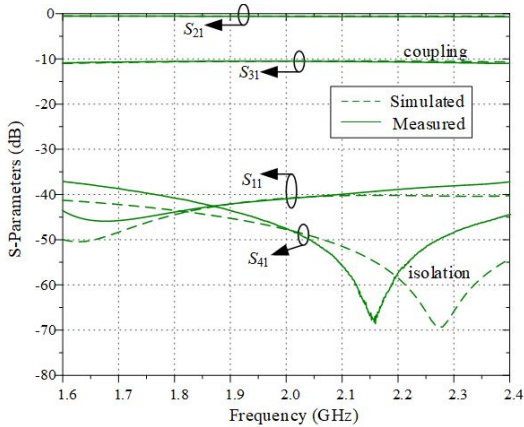


Fig. 6. S-parameters of the 10-dB directional coupler with the 2-bit.

$BW = 40\%$ in eqn (5) to challenge high performance. The coupler is desired to operate in band $[\omega_1, \omega_2] = [1.6 \text{ GHz}, 2.4 \text{ GHz}]$.

After implementing the MOEA/D-GO optimization with the same objectives, optimal layout of the 10-dB directional coupler is obtained and prototype is fabricated, as shown in Figure 5. The optimization searching takes 50 iterations (around 80 hours on the abovementioned computer).

Figure 6 presents the simulated and measured S-parameters. In the operation band, the simulated minimum return loss is 40 dB, the maximum insertion loss is 0.8 dB, the isolation is greater than 41 dB, and the maximum isolation is 69.5 dB. The measured minimum return loss is 37 dB, the isolation is greater than 38 dB, and the maximum isolation is 68 dB.

Directivity of the fabricated coupler is calculated from the measured S-parameters in Figure 6. The minimum directivity is $D_{\min} = 27.5 \text{ dB}$ and the maximum directivity is $D_{\max} = 58 \text{ dB}$ in an operation bandwidth of 36% (from 1.62 GHz to 2.34 GHz).

Table 1: Comparison between different 10-dB directional couplers

| Designs | f_0 (GHz) | Bandwidth | D_{\min} (dB) | D_{\max} (dB) | Design area ($\lambda_g \times \lambda_g$) |
|-----------|-------------|-----------|-----------------|-----------------|--|
| [4] | 1 | 27.7% | 20 | 28 | 0.2×0.03 |
| [7] | 2 | 8.7% | 20 | 40 | 0.35×0.46 |
| [10] | 6.2 | 24% | 15 | 30 | 0.9×0.29 |
| [12]* | 2 | 29% | 28.7 | 44.6 | 0.25×0.1 |
| 2-bit FTS | 2 | 36% | 27.5 | 58 | 0.25×0.1 |

*simulation results only.

The phase difference between Port 2 and Port 3 is $90^\circ \pm 0.5^\circ$.

C. Reference formatting

Since the 20-dB directional coupler design with 1-bit FTS in [12] provides the most competitive performance, we may just compare the designed coupler with the 1-bit FTS coupler in [12]. We find that the 2-bit FTS coupler presented in this paper acquires broader bandwidth of 50%, which is 40% provided by 1-bit FTS coupler in [12]. And the maximum directivity is 49 dB, which is slightly higher than that obtained by 1-bit FTS coupler in [12]. But lower minimum directivity is obtained to be 27.5 dB, which is 37 dB acquired by 1-bit FTS coupler in [12]. However, it is still higher than the minimum directivities (around 20 dB) of wideband planar directional couplers designed by using conventional structures and techniques.

As for the 10-dB coupler, comparison with other 10-dB directional couplers reported in literatures are listed in Table 1. The FTS couplers designed with the 2-bit FTS scheme provide broader bandwidth and higher directivity. In addition, they have a compact size.

IV. CONCLUSION

The 2-bit FTS scheme can be used for automatic design of microstrip directional coupler. With the 2-bit FTS coding, design matrix of size twice that for conventional 1-bit FTS can be acquired, which is very efficient for treating fine or subtle structures in the multi-objective optimization searching. The automatic design of planar directional couplers can complete in days without any apriority about coupler structures, any structure presetting or artificial intervention.

ACKNOWLEDGMENT

This work was funded in part by National Natural Science Foundation of China under Grant 61671421, Natural science fund for colleges and universities in Jiangsu Province (Grant no. 20KJB510005),

and Scientific Research Foundation for Doctors of Jinling Institute of Technology (Grant no. jit-b-201718).

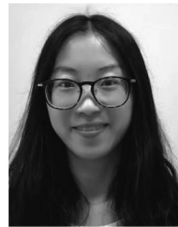
REFERENCES

- [1] M. K. Krage and G. I. Haddad, "Characteristics of coupled microstrip transmission lines-I: Coupled-mode formulation of inhomogeneous lines," *IEEE Trans. Microw. Theory Tech.*, vol. 18, no. 4, pp. 217-222, Apr. 1970.
- [2] C. Liu, T. Yang, K. Huang, and W. Menzel, "Compact capacitive compensated directional coupler using planar artificial transmission lines," *Electron. Lett.*, vol. 47, no. 24, pp. 1321-1323, Nov. 2011.
- [3] J. Ha, W. Shin, and Y. Lee, "An inductive-loading method for directivity enhancement of microstrip coupled-line couplers," *IEEE Microwave and Wireless Components Letters.*, vol. 27, no. 4, pp. 356-358, Apr. 2017.
- [4] R. Phromlongsri, M. Chongcheawchamnan, and I. D. Robertson, "Inductively compensated parallel coupled microstrip lines and their applications," *IEEE Trans. Microw. Theory Techn.*, vol. 54, no. 9, pp. 3571-3582, Sep. 2006.
- [5] M. Akhtar M, M. Zakir, and H. Cheema, "Weakly coupled directional coupler with simultaneous wide bandwidth and high directivity," *Microw Opt Technol Lett.*, vol. 61, pp. 1259-1262, 2019.
- [6] D. Jaisson, "Multilayer microstrip directional coupler with discrete coupling," *IEEE Trans. Microw. Theory Techn.*, vol. 48, no. 9, pp. 1591-1595, Sep. 2000.
- [7] A. Pourzadi, A. R. Attari, and M. S. Majedi, "A directivity-enhanced directional coupler using epsilon negative transmission line," *IEEE Trans. Microw. Theory Techn.*, vol. 60, no. 11, pp. 3395-3402, 2012.
- [8] B. S. Yıldırım and K. Karayahşi, "Broadband UHF directional coupler with high directivity," *Fifth International Electromagnetic Compatibility Conference (EMC Turkiye)*, Sep. 2019.
- [9] A. Agharasuli, M. K. Mehr, O. Manoochehri, and D. Erricolo, "UWB stripline coupler with low loss and ripple," *Proc. International Conference on Electromagnetics in Advanced Applications (ICEAA)*, Sep. 2019.
- [10] P. Mondal and S. Parui, "Multi-mode resonator based asymmetric broadband 10db directional coupler," *3rd International Conference on Microwave and Photonics (ICMAP)*, Feb. 2018.
- [11] J. Shi, X. Y. Zhang, K. W. Lau, J. X. Chen, and Q. Xue, "Directional coupler with high directivity using metallic cylinders on microstrip line," *Electron. Lett.*, vol. 45, no. 8, pp. 415-417, Apr. 2009.
- [12] L. Wang, G. Wang, and J. Siden, "Design of high-directivity wideband microstrip directional coupler with fragment-type structure," *IEEE Trans. Microw. Theory Tech.*, vol. 63, no. 12, pp. 3962-3970, Oct. 2015.
- [13] W. Zhang and G. Wang, "Design of compact planar lowpass filters by using fragment-type structure with multi-bit scheme," *IEEE Access*, vol. 9, pp. 74143-74154, 2021.



Yonghui Tao received the Ph.D. degree from University of Science and Technology of China, Hefei, China, in 2014. From 2015 to 2017, she worked at University of Science and Technology of China as a Post-doctoral Research Fellow supported by the Chinese government.

She is currently an instructor with Jinling Institute of Technology. Her research interests involve radio-frequency identification, microwave hyperthermia, metamaterials and its applications in biomedical engineering.



Wenjuan Zhang received the B.S. degree from Xidian University, Xi'an, China, in 2016. She is currently pursuing the Ph.D. degree in electrical engineering with the University of Science and Technology of China, Hefei, China. Her research interests include microwave/RF circuit theory and design technique, RFID, and sensor design.



Johan Sidén (M'00) received the M.Sc. degree in telecommunication, the Licentiate of Technology degree in electronics, and the Ph.D. degree in electronics from Mid Sweden University, Sundsvall, Sweden, in 2000, 2004, and 2007, respectively.

He is currently an Associate Professor with Mid Sweden University. His current research interests include radio-frequency identification technology, wireless sensor networks, antenna technology, printed passive electronic systems, and optical fiber installation systems.



Gang Wang (M'98) received the B.S. degree from the University of Science and Technology of China, Hefei, China, in 1988, and the M.S. and Ph.D. degrees in electrical engineering from Xidian University, Xi'an, China, in 1991 and 1996, respectively.

From 1996 to 1998, he was with Xi'an Jiaotong University, as a Postdoctoral Research Fellow, supported by the Chinese Government. From 1998 to 2000, he was an Associate Professor with Xi'an Jiaotong University.

In 2001, he was a Visiting Researcher with the Department of ITM, Mid-Sweden University. From 2002 to 2003, he was a Postdoctoral Research Associate with the Department of Electrical and Computer Engineering, University of Florida. From 2003 to 2010, he was with Jiangsu University, China, as a Chair Professor. He is currently a Full Professor with the University of Science and Technology of China. His current research interests include autonomous driving, RFID/sensor technology, and microwave circuit, and antenna design.

Compact Dual-Band Bandpass Filter Based on SSL-SIR With Sharp Roll-Off

Juan Yue, Guanmao Zhang, Zongge Che, Yupeng Lun, Zhihang Li, and Junhong Suo

Institute of Optoelectronics and Electromagnetics Information, School of Information Science and Engineering,
Lanzhou University, Lanzhou 730000, P. R. China
zhanggm@lzu.edu.cn

Abstract – A compact dual-band bandpass filter (DB-BPF) is studied and implemented by using shorted stub-loaded stepped impedance resonator (SSL-SIR) and 0° feed structure in this paper. The resonance frequencies of SSL-SIR can be analyzed and explained by odd–even mode analysis method and it is used in the design of BPF I. Then, the BPF II is created using the theory of 0° feed structure. Finally, the two structures are combined together to form a DB-BPF by reasonably adjusting the coupling between them and the position of the feed points. The simulation results suggest that the center frequencies of the two passbands are 3.45 and 5.2 GHz, respectively, which are suitable for modern wireless communication systems like 5G and WLAN. Compact size, strong passband isolation, and large stopband bandwidth are all advantages of the proposed DB-BPF filter. A prototype is created and constructed to validate this. The simulated results are in good agreement with the measured results.

Index Terms – Dual-band bandpass filter (DB-BPF), 0° feed structure, stub-loaded stepped impedance resonator (SSL-SIR).

I. INTRODUCTION

As we all know, filters play an essential role in many radio frequency (RF) or microwave systems with the development of modern technology. The filters are widely utilized in many sectors such as WiFi, sensing radars, and transceivers due to their great qualities such as compact size, low cost, low insertion loss, superior frequency selectivity, and ease of production. Recently, with the continuous progress of multi-function wireless communication networks, the single band transceiver system has been unable to meet the requirement. Therefore, the diversified function and excellent performance of wireless devices become the focus of attention. To meet various demands, filters that possess multiple functions have been developed by researchers, such as lowpass filters with good out-of-band suppression [1], band-stop filters [2], tunable filters [3], reconfigurable filters [4], and bandpass filters (BPFs) [5].

Dual-band bandpass filters (DB-BPFs) have a lot of promise due to the growing demand for RF transceivers that operate in several frequency bands. Many methods have been developed, and a variety of DB-BPF structures have been proposed using various techniques, such as the DB-BPF based on the hexagonal split ring resonator [6], the dual wide-band BPF based on the cross-shaped resonator [7], the compact DB-BPF based on shorted and open stub-loaded resonators [8, 9], and the DB-BPF based on dual-mode resonators [10].

The DB-BPFs based on the shorted stub-loaded stepped impedance resonator (SSL-SIR) have also been presented in [11–14], in addition to the filters mentioned above. SIRs have the advantages of a simple design, easy manufacture, and a high stopband attenuation level. The DB-BPF in [11] was combined by a pair of open stub-loaded stepped impedance resonators (OSLSIRs) and two SSL-SIRs are embedded between the coupled OSLSIRs to generate quasi-elliptic response at two diverse frequencies, but its whole frame was suffered from great size and complicated structure. In [12], a pair of stub-loaded SIRs and a pair of dual-feedline structures (DFSs) were used to design DB-BPF. However, it was lack of passband selectivity and compactness. A novel compact DB-BPF based on SSL-SIR and a pair of tri-section stepped impedance resonator (T-SIR) was presented in [13], whereas its circuit was not compact enough and simple. In [14], the DB-BPF was constructed by a quad-mode stub-loaded resonator, yet, it occupied a large area.

As previously stated, the DB-BPF built by others required a considerable dimension due to the large number of resonators required. A miniaturized DB-BPF based on SSL-SIR and 0° feed structure is proposed in this paper. First, the theory of odd–even mode analysis is used to analyze SSL-SIR, and then the low passband centered at 3.45 GHz is designed. Based on the theory of 0° feed structure, the upper passband centered at 5.2 GHz is formed. The two passbands are combined together to form a DB-BPF by reasonably adjusting the coupling between them and the position of the feed points. Finally, a prototype is fabricated and

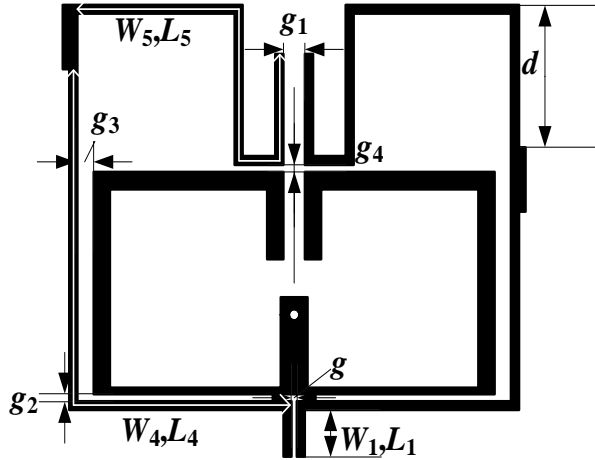


Fig. 1. Geometry of the proposed DB-BPF.

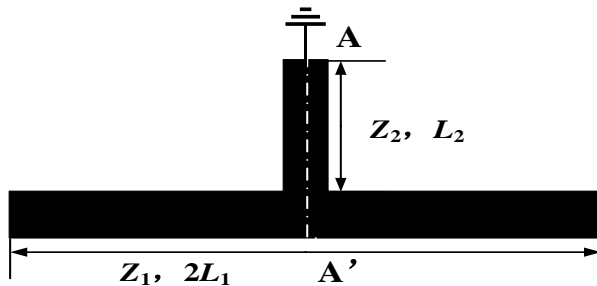


Fig. 2. Diagram of a typical SSLR.

measured, and the measured results verify the rationality of the design.

II. DESIGN OF BPF I

A DB-BPF which composed of SSL-SIR and a two-mode resonator based on a 0° feed structure. Its topology was depicted in Figure 1. The typical SSLR, as shown in Figure 2, is made up of a uniform microstrip line and a shorted stub-loaded resonator in the center, with physical lengths defined as $2L_1$ and L_2 . Its impedances are Z_1 and Z_2 , respectively. By replacing the short one to the open one, the diagram is named OSLR. Due to the symmetrical structures of SSLR and OSLR, the resonant characteristics can be easily analyzed by the odd–even mode analysis method.

Here, the SSL-SIR is used to form BPF I and its topology and the odd–even mode equivalent circuit are shown in Figure 3. The two characteristic impedances and electrical lengths of SIR are Z_1 , Z_2 , $2\theta_1$, and θ_2 . The impedance of the loaded short circuit uniform impedance stub microstrip line is Z_3 , and the electric length of corresponding microstrip line is θ_3 . Since SSL-SIR is symmetric about A, A', the resonant frequency of this structure can also be analyzed by using

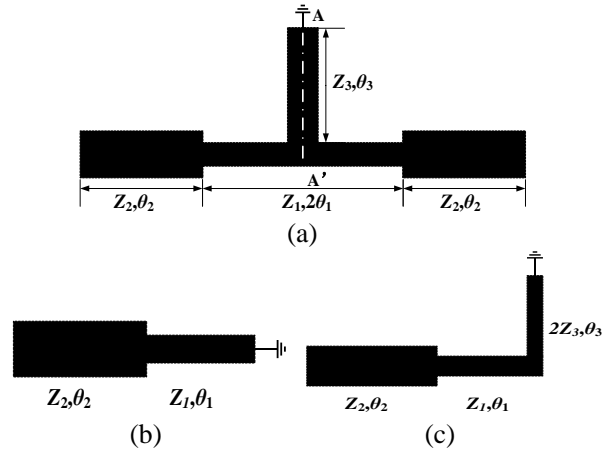


Fig. 3. (a) Structures of SSL-SIR. (b) Odd-mode equivalent circuit of SSL-SIR. (c) Even-mode equivalent circuit of SSL-SIR.

the odd–even mode analysis method. According to the transmission line theory, the input impedance of odd mode can be given by:

$$Z_{ino} = jZ_1 \frac{Z_1 \tan \theta_1 + Z_2 \tan \theta_2}{Z_1 - Z_2 \tan \theta_1 \tan \theta_2}. \quad (1)$$

Based on the resonance condition $1/Z_{ino} = 0$, it can be deduced that when the resonator resonates, its electric length should meet condition (2). Further, define the electric length ratio α , $\theta_T = \theta_1 + \theta_2$, $\alpha = \theta_1/\theta_T$, and formula (2) can be converted into formula (3). The odd-mode equivalent circuit structure is also known as a quarter wavelength SIR.

$$\tan \theta_1 \tan \theta_2 = \frac{Z_1}{Z_2}, \quad (2)$$

$$\tan \alpha \theta_T \tan[(1 - \alpha) \theta_T] = Z_1/Z_2. \quad (3)$$

It can be seen from formula (3), which determines the odd mode resonance frequency (f_{odd}), that when the structural parameters of the loaded shorted uniform impedance stub of microstrip line are changed, the odd-mode resonant frequency will not change at all. It is mainly determined by the impedance ratio Z_1/Z_2 of SIR and the electric lengths θ_1 and θ_2 .

Similarly, the input impedance of even mode can be given by:

$$Z_{ine} = jZ_2 \frac{Z_1^2 \tan \theta_1 + Z_1 Z_2 \tan \theta_2}{Z_1 Z_2 - Z_1^2 \tan \theta_1 \tan \theta_2} + \frac{2Z_1 Z_3 \tan \theta_3 - 2Z_2 Z_3 \tan \theta_1 \tan \theta_2 \tan \theta_3}{-2Z_2 Z_3 \tan \theta_1 \tan \theta_3 - 2Z_1 Z_3 \tan \theta_2 \tan \theta_3}. \quad (4)$$

According to the resonance condition $1/Z_{ine} = 0$, it can be computed that when the resonator resonates, its electric length should meet the following

condition:

$$\begin{aligned} Z_1 Z_2 - Z_1^2 \tan \theta_1 \tan \theta_2 - 2Z_2 Z_3 \tan \theta_1 \tan \theta_3 & \quad (5) \\ - 2Z_1 Z_3 \tan \theta_2 \tan \theta_3 = 0. \end{aligned}$$

Further obtained:

$$\begin{aligned} R_{Z2} \tan \theta_1 \tan \theta_2 + 2R_{Z1} \tan \theta_1 \tan \theta_3 & \quad (6) \\ + 2 \tan \theta_2 \tan \theta_3 = R_{Z1} R_{Z2}, \end{aligned}$$

where $R_{Z1} = Z_2/Z_1$ and $R_{Z2} = Z_1/Z_3$; hence, $Z_2/Z_3 = R_{Z1} R_{Z2}$. From (6), we can see that the even mode resonance condition of SSL-SIR is not only related to the impedance ratio R_{Z1} and the electrical length θ_1 and θ_2 of SIR but also related to the impedance ratio R_{Z2} and the electrical length θ_3 of the loaded shorted stub. We first calculated the electrical parameters based on the f_{odd} and f_{even} determined by formula (3) and formula (6) and then optimized the final electrical parameters in the simulation software. In this study, the impedance ratio of the SSL-SIR R_{Z1} and R_{Z2} are set as 0.8 and 1.6, respectively, and the electric lengths θ_1 , θ_2 , and θ_3 are obtained as 27° , 57° , and 11° independently at 3.45 GHz.

In comparison to a traditional SSLR, the design of a filter employing SSL-SIR will have more flexibility and degrees of freedom, which will considerably improve the adjustable range of filter performance in actual applications.

A small size BPF with a center frequency of 3.45 GHz was designed by reasonably selecting the electrical length, impedance ratio of SSL-SIR and utilizing the coupling of source/load. SSL-SIR bending is designed to reduce the size of the circuit. Simultaneously, the geometry of the proposed filter and its simulation results are shown in Figure 4. The feed lines on the left and right ends are 50Ω . It can be seen that there are two transmission zeros on the left and right sides of the passband. The transmission zeros are introduced through the source load coupling, which can significantly improve the selectivity and out-of-band rejection response of the filter.

III. DESIGN OF BPF II

As shown in Figure 5, the design of BPF II was inspired by [15] based on the theory of 0° feed structure and electric coupling. According to the previous research results, the frequency responses of the filters designed with different tap-line feed points may be significantly different. It has been found in [16] that by using a 0° feed structure, two transmission zeros near the passband can be generated and the stopband rejection has been significantly increased. The electrical delays of the upper and lower paths of the coupling structure in Figure 5 are similar to those at its fundamental resonant frequency which has a 0° difference between the electric delays of the lower and upper paths. Also, the coupling gaps between the two resonators are modeled as π -networks, as shown in the inset of Figure 5, where the values of C_1 and C_2

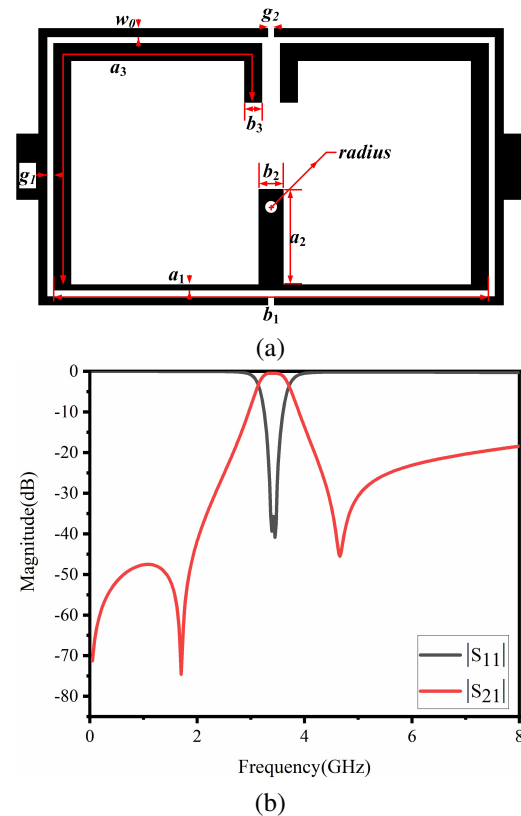


Fig. 4. Geometry of the proposed BPF I and its simulation results. (a) Geometry of the filter ($a_1 = 0.11$, $b_1 = 7.4$, $a_2 = 1.55$, $b_2 = 0.5$, $a_3 = 7.91$, $b_3 = 0.3$, radius = 0.1, $W_0 = 0.15$, $g_1 = 0.1$, and $g_2 = 0.1$ all in millimeter). (b) Simulated S parameters of the passband I.

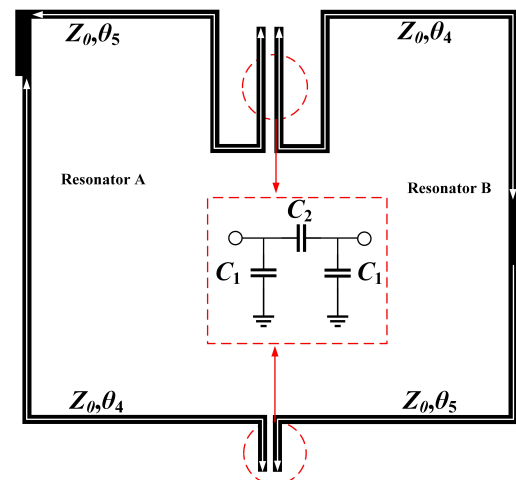


Fig. 5. The topology structure of BPF II.

could be found from [17]. For a lower microwave frequency range, the value of ωC_1 is very small due to $C_1 < 0.01$ pF, and it will be neglected.

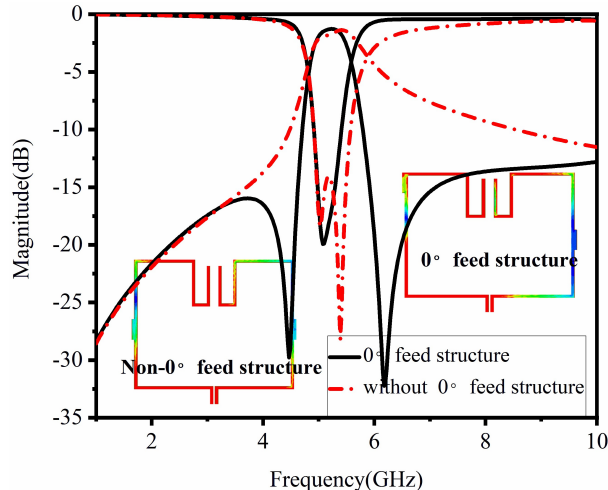


Fig. 6. Simulated results of BPF II with 0° feed structure and without 0° feed structure. (The insets are simulated electric field distribution in 5.2 GHz.)

The transmission matrix of BPF II can be derived from [18], and its transmission coefficient can be further obtained. Figure 6 is the comparison of the BPF2 without 0° feed structure and with 0° feed structure at the center frequency 5.2 GHz. One resonator is resonant at the frequency when θ_4 approaches $\pi/2$ and the other is resonant at the frequency when θ_5 is approximately $\pi/2$.

It can be clearly seen that two transmission zeros which are located at 4.47 and 6.18 GHz, respectively, which are close to the passband and on both sides of the passband; therefore, significant increase has occurred in the stopband injection.

IV. DB-BPF AND EXPERIMENTAL VERIFICATION

A DB-BPF, as shown in Figure 1, is proposed based on the study of the previous two BPFs. The coupling gap between the two filters and the electrical coupling gap of the second filter are tuned by combining the two previously stated BPF I (3.45 GHz) and BPF II (5.2 GHz) together, and the DB-BPF is simply created. The simulated transmission coefficients of the sub-BPF1, sub-BPF2, and DB-BPF are shown in Figure 7. The proposed DB-BPF's two passbands are clearly in good accordance with the passbands of the two sub-filters. At the same time, the selectivity between the two passbands and the isolation between the two passbands are significantly improved. The final optimized dimensions of the DB-BPF demonstrated in Figure 1 are as follows: $g = 0.1$ mm, $g_1 = 0.4$ mm, $g_2 = 0.12$ mm, $g_3 = 0.3$ mm, $d = 2.44$ mm, $W_1 = 0.15$ mm, $L_1 = 0.8$ mm, $W_5 = 0.15$ mm, $L_5 = 8.14$ mm, $W_4 = 0.15$ mm, and $L_4 = 9.78$ mm, where the dimensions of BPF I are the same as Figure 4.

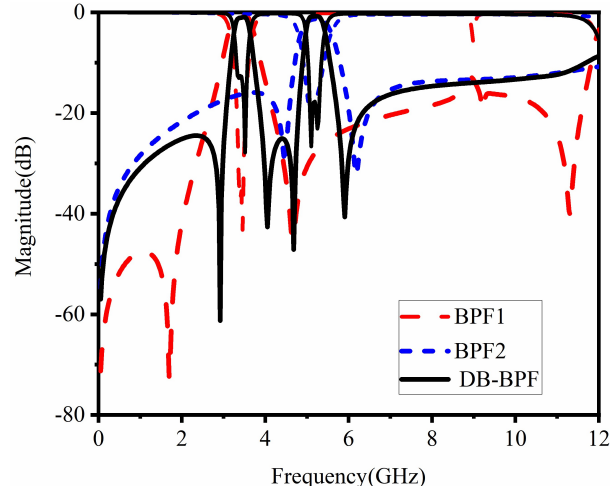


Fig. 7. EM simulated results of transmission coefficients of the proposed DB-BPF and sub-filters.

For verification, a DB-BPF is fabricated and measured. Considering the advantages of dimensional stability, low loss, low water absorption, low cost of printed circuit manufacturing, and easy drilling and plating operations. We used Taconic RF-35 substrate with a relative dielectric permittivity of 3.5 and a thickness of 0.508 mm. Figure 8(a) shows the photograph of the fabricated DB-BPF and the comparison between the simulated DB-BPF and the measured results. Good agreements are obtained between them, while the slight deviation of the upper passband may be due to the fabrication tolerance and soldering errors at the two 50Ω input-output ports.

The two measured passbands are centered at 3.46 and 5.34 GHz with the fractional bandwidths of 6.9% and 4.4%. The measured minimum insertion losses in the passband are 1 and 1.21 dB. Meanwhile, the return losses are better than 11 and 15 dB, respectively. Four transmission zeros that are located at 2.86, 4.05, 4.8, and 6.05 GHz improve the selectivity of each passband and the isolation between the two passbands. Figures 8(b) and (c) show the simulated in-band group delay responses of low passband and high passband, and the minimum group delays in the two passbands are 1.1 and 0.96 ns, respectively. In addition, it has a wide upper stopband ranging from 5.73 to 9.86 GHz with -15 dB injection. The overall size of the filter is 7.74 mm \times 8.54 mm, which occupies $0.15 \lambda_g \times 0.16 \lambda_g$, where λ_g is the guided wavelength at the center frequency of the first passband. A performance comparison between the published DB-BPFs and the proposed one is shown in Table 1. It shows that the proposed DB-BPF has the advantages of compact size, low insertion loss, simple circuit topology, and easy fabrication. Comparing with [13], the

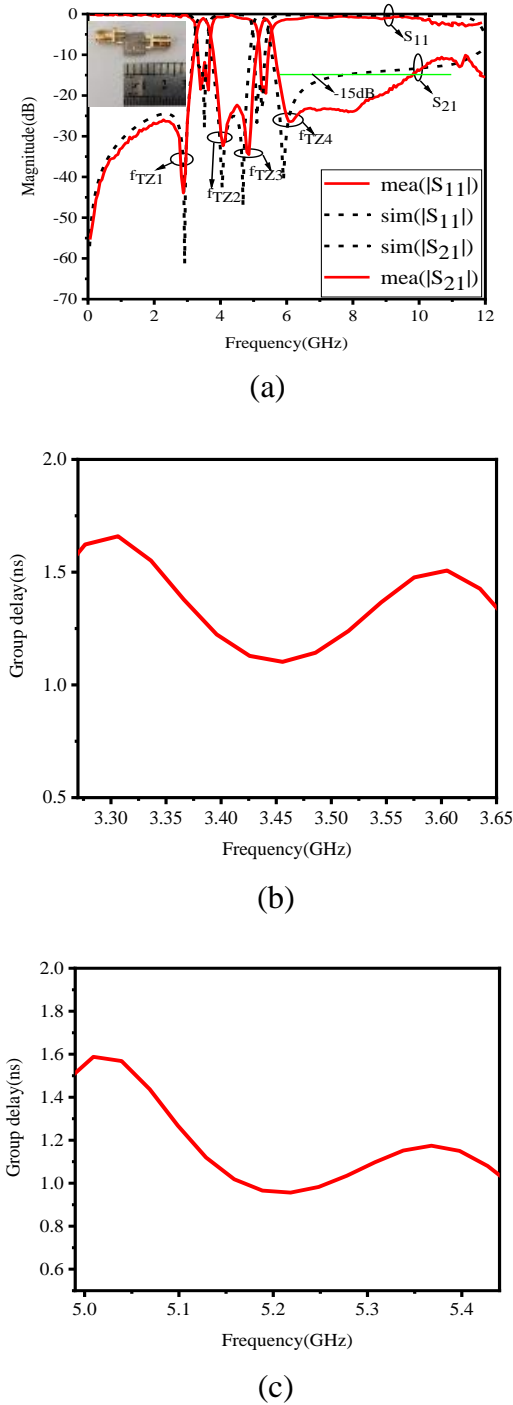


Fig. 8. Responses and group delays of the proposed filter. (a) Simulated and measured S-parameters of the DB-BPF. (b) and (c) Simulated in-band group delay responses of passbands I and II, respectively.

structure required to design the low passband is simpler and easier to design.

Table 1: Comparison of some previous dual-band filters

| | CF (GHz) | FBW (%) | IL (dB) | TZs | Size ($\lambda_g * \lambda_g$) |
|-----------|---------------|---------------|---------------|-----|----------------------------------|
| [11] | 1.63/ 2.73 | 7.5/ 5.1 | 1.5/ 2.15 | 7 | 0.25* 0.25 |
| [12] | 2.3/3.5 | 2.98/ 2.64 | 1.25/ 1.72 | 3 | 0.25* 0.23 |
| [13] | 2.4/3.5 | 15.6/ 5.2 | 1.07/ 1.05 | 4 | 0.32* 0.11 |
| [14] | 2.4/5.2 | 14.8/ 12.9 | 1.43/ 1.34 | 4 | N.A. |
| This work | 3.46/ 5.34 | 6.9/ 4.4 | 1/1.21 | 4 | 0.15* 0.16 |

V. CONCLUSION

A compact DB-BPF which is composed of BPF I and BPF II, based on the SSL-SIR and 0° feed structure, is presented in this article. SSL-SIR is first analyzed using the odd–even mode analysis approach, and then the low passband, centered at 3.46 GHz, is built on this premise. A high-selectivity high passband centered at 5.37 GHz is presented based on the 0° feed structure. Without increasing the size of the circuit, a small DB-BPF with good selectivity is created by combining two independent passbands. After all, a DB-BPF is designed, manufactured, and tested. The measured results are in good agreement with the simulation results. The proposed DB-BPF has the merits of compact size, high selectivity, and independent control of the passband, making it suitable for 5G, WLAN, and narrowband applications.

ACKNOWLEDGMENT

This work is supported by the project of the State Key Program of National Natural Science of China under Grant 61631007, the National Key R&D Program of China under Grant 2019YFA0405403, and the Key Project of Innovation and Entrepreneurship of Lanzhou University under Grant cxcy202002.

REFERENCES

- [1] M. A. Pahlavani, M. Moradkhani, and R. Sayadi, “New design of an adjustable compact microstrip lowpass filter using Z-shaped resonators with low VSWR,” *Microwave and Optical Technology Letters*, vol. 62, no. 11, pp. 3527-3535, Jun. 2020.
- [2] Q. Li, X. Chen, P. L. Chi, and T. Yang, “Tunable bandstop filter using distributed coupling microstrip resonators with capacitive terminal,” *IEEE Microwave and Wireless Components Letters*, vol. 30, no. 1, pp. 35-38, Jan. 2019.
- [3] L. Gao, T. W. Lin, and G. M. Rebeiz, “Design of tunable multi-pole multi-zero bandpass filters and diplexer with high selectivity and isolation,” *IEEE*

- Transactions on Circuits and Systems I: Regular Papers*, vol. 66, no. 99, pp. 3831-3842, Oct. 2019.
- [4] A. Bandyopadhyay, P. Sarkar, T. Mondal, and R. Ghatak, "A Dual Function Reconfigurable Bandpass Filter for Wideband and Tri-band Operations," *IEEE Transactions on Circuits and Systems II: Express Briefs*, vol. 68, no. 6, pp. 1892-1896, Jan. 2021.
- [5] J. Hu, Y. Li, D. Zeng, W. Xu, and G. Lu "Design of a broadband microstrip bandpass filter," *2020 IEEE International Symposium on Antennas and Propagation and North American Radio Science Meeting*, pp. 315-316, Jul. 2020.
- [6] Z. Troudi, Jan Machá, and L. Osman, "Compact dual-band bandpass filter using a modified hexagonal split ring resonator," *Microwave and Optical Technology Letters*, vol. 62, no. 5, pp. 1893-1899, Jan. 2020.
- [7] X. K. Bi, X. Zhang, S. W. Wong, T. Yuan, and S. H. Guo, "Design of equal-ripple dual-wideband bandpass filter with minimum design parameters based on cross-shaped resonator," *IEEE Transactions on Circuits and Systems II: Express Briefs*, vol. 67, no. 10, pp. 1780-1784, Oct. 2019.
- [8] F. Wei, J. H. Yu, C. Y. Zhang, C. Zeng, and X. W. Shi, "Compact balanced DB-BPFs based on short and open stub loaded resonators with wide common-mode suppression," *IEEE Transactions on Circuits and Systems II: Express Briefs*, vol. 67, no. 12, pp. 3043-3047, Dec. 2020.
- [9] C. Liang, Y. Liu, and F. Tai, "Compact bandpass filters using folded quad-mode stub-loaded loop resonators," *Applied Computational Electromagnetics Society (ACES) Journal*, vol. 35, no. 10, pp. 1217-1221, Oct. 2020.
- [10] R. Yin, W. Feng, and W. Che, "High selectivity dual-band bandpass filters using dual-mode resonators," *Applied Computational Electromagnetics Society (ACES) Journal*, vol. 32, no. 9, pp. 800-805, Sep. 2017.
- [11] W. Jiang, W. Shen, T. Wang, Y. M. Huang, Y. Peng, and G. Wang, "Compact dual-band filter using open/short stub loaded stepped impedance resonators (OSLSIRs/SSLSIRs)," *IEEE Microwave and Wireless Components Letters*, vol. 26, no. 9, pp. 672-674, Aug. 2016.
- [12] P. Wen, Z. Ma, H. Liu, S. Zhu, M. Ohira, C. Wang, X. Guan, and B. Ren, "Novel compact DB-BPF using stub-loaded shorted stepped-impedance resonators," *2018 Asia-Pacific Microwave Conference (APMC)*, pp. 22-24, Nov. 2018.
- [13] D. Li, Y. Zhang, X. Feng, K. Song, and Y. Fan, "Dual-band bandpass filter with controllable center frequency and bandwidth using short stub-loaded SIR and tri-section SIR," *AEU-International Journal of Electronics and Communications*, vol. 69, no. 7, pp. 1004-1009, Jul. 2015.
- [14] M. H. Weng, C. Y. Huang, S. W. Dai, and R. Y. Yang, "An improved stopband dual-band filter using quad-mode stub-loaded resonators," *Electronics*, vol. 10, no. 2, pp. 142, Jan. 2021.
- [15] D. Li, J. A. Wang, Y. Liu and Z. Chen, "Miniaturized dual-band bandpass filter with sharp roll-off using ring-loaded resonator," *IEEE Access*, vol. 8, pp. 25588-25595, Feb. 2020.
- [16] S. Y. Lee and C. M. Tsai, "New cross-coupled filter design using improved hairpin resonators," *IEEE Transactions on Microwave Theory Techniques*, vol. 48, no. 12, pp. 2482-2490, Dec. 2000.
- [17] T. C. Edwards and M. B. Steer, "Foundations for microstrip circuit design," John Wiley and Sons, 2016.
- [18] C. M. Tsai, S. Y. Lee and C. C. Tsai, "Performance of a planar filter using a 0° feed structure," *IEEE Transactions on Microwave Theory and Techniques*, vol. 50, no. 10, pp. 2362-2367, Dec. 2002.



Juan Yue received the B.E. degree in communication engineering from Bohai University, Jinzhou, China, in 2018. She is currently working toward the master's degree in information and communication engineering with the School of Information Science and Engineering, Lanzhou University, Lanzhou, China. Her current research interests include microstrip filter and metamaterial absorber.



Guanmao Zhang received the B.S. degree, the M.S. degree in radio physics, and the Ph.D. degree in radio physics from Lanzhou University, Lanzhou, China, in 1995, 1998, and 2007, respectively. He is currently the Director of the Institute of Optoelectronics and Electromagnetic Information, School of Information Science and Engineering, Lanzhou University. His current research interests include surface plasmonics and its communication sensor applications, micro-nano optical device design and application, non-intrusive intelligent photoelectric sensor technology and application, and modern wireless communication technology. As of now, he

has published more than 40 related academic papers, of which more than 20 are included in SCI/EI.



Zongge Che received the B.E. degree in electronic information engineering from Lanzhou Jiaotong University, Lanzhou, China, in 2019. She is currently working toward the master's degree in information and communication engineering with the School of Information Science and Engineering, Lanzhou University. Her current research interests include Terahertz filter, surface plasmonics, metasurface, and metamaterial absorber.



Yupeng Lun received the B.E. degree in communication engineering from Zhengzhou University, Zhengzhou, China, in 2019. He is currently working toward the master's degree in electronic and communication engineering with the School of Information Science and Engineering, Lanzhou University, Lanzhou, China. His current research interests include mobile phone antenna, MIMO antenna, and metamaterial absorber.



Zhihang Li received the B.E. degree in communication engineering from Shandong University, Shandong, China, in 2019. He is currently working toward the master's degree in electronic and communication engineering with the School of Information Science and Engineering, Lanzhou University, Lanzhou, China. His current research interests include frequency selective surface, periodic structures, and metamaterial absorber.



Junhong Suo received the B.E. degree in electronic information science and technology from Heilongjiang University, Haerbin, China, in 2018. He is currently working toward the master's degree in electronic and communication engineering with the School of Information Science and Engineering, Lanzhou University, Lanzhou, China. His current research interests include frequency selective surface, periodic structures, and metamaterial absorber by using the FPGA technology.

Power Changes of Electromagnetic Waves Across the Temporal Boundary in Simple Polar-Molecule Reactions

Xingpeng Liu¹, Song Zhang¹, and Kama Huang²

¹School of Network and Communication Engineering
Chengdu Technological University, Chengdu 610064, China
lxp_herb@163.com, 57101150@qq.com

²College of Electronics and Information Engineering
Sichuan University, Chengdu 611730, China
kmhuang@scu.edu.cn

Abstract – Microwave-assisted chemical reactions have been widely used, but the inhomogeneous heating limits further applications. The aim of this paper is to investigate the power transfer behavior in the simple polar-molecule reactions whose polarization changes with the proceeding of the reactions. At the temporal boundary, based on the continuity of charge and flux and the equivalent transmission line approach of the simple polar-molecule reactions, we discover the power changes in the reactions. The numerical results are in agreement with the theory of the temporal boundary. When the time scale of the component concentration variation is smaller than the wave period, the polarization is not continuous at the temporal boundary. The impedance of the reactions across the temporal boundary changes, and the reflection occurs. Moreover, when the dielectric property of the reactions decreases, the power of the waves increases after the temporal boundary and the waves experience a net energy gain. The results may be helpful in disclosing the non-uniform electromagnetic energy distribution in chemical reactions.

Index Terms – Electromagnetic power propagation, power changes, a temporal boundary, simple polar-molecule reactions.

I. INTRODUCTION

Microwaves have been used increasingly in chemical engineering for a series of advantages, such as improvement in reaction rates, yields, and energy saving [1–3]. However, inhomogeneous heating and hot spots have been limiting the utilization of microwaves in chemical engineering [4, 5]. In order to study these problems, it is essential to investigate the behavior of electromagnetic power transfer in chemical reactions.

The electromagnetic energy propagation through general media with dispersion and loss has been

studied extensively for decades [6, 7]. The previous studies are mainly focused on electromagnetic media characterized by permittivity and permeability. However, most of chemical reactions are non-stationary media, of which dielectric properties are different from the media reported before [8–10]. Recently, the time-varying and dispersive characteristics of chemical reactions have been demonstrated theoretically [11]. Perhaps, the most outstanding features of chemical reactions are time-varying characteristics, which cause changes in the amplitude and frequency of electromagnetic waves. And the reflection and transmission of electromagnetic waves at a temporal boundary have been discussed in chemical reactions [12]. What is more important, the internal reflections caused by time-varying characteristics lead to the non-uniform distribution of electromagnetic waves in chemical reactions. To the best of our knowledge, the effects of time-varying characteristics on electromagnetic energy in chemical reactions are barely mentioned. It is the first time that the simple polar-molecule reactions are chosen as the research object to study the effect of the time-varying characteristics on the power changes. Moreover, the power changes at such temporal characteristics will further stimulate an intense investigation in the non-uniform distribution of electromagnetic energy in spatially homogenous chemical reactions. In order to obtain the power changes across the temporal boundary in the homogenous reactions, the impact of component concentration variation on the conditions and trends of power changes are shown for the first time.

In recent years, the transmission line theory has evolved into a very powerful modeling tool to analyze energy flux in dynamic systems, such as the mechanical and hydraulic systems [13–15]. The unit equivalent circuit of a transmission line can be connected to the resistors, inductors, and capacitors under constraints of a

physical meaning of systems to be modeled [16, 17]. In this approach, electromagnetic field quantities are substituted by the analogous incident and reflected voltage and current propagating through this unit circuit [18, 19]. This conceptually new approach greatly simplifies calculations by the definite physical meaning of circuit elements in the unit circuit. And the fundamental electromagnetic properties of the reactions are reviewed by a unit equivalent circuit approach [20]. The equivalent transmission line approach provides an efficient analysis tool for the power transfer in chemical reactions.

In this letter, we investigate the unique properties of the power transfer through homogenous polar-molecule reactions based on an equivalent transmission line approach. Then the propagation of electromagnetic energy in the reactions is simulated to validate the theoretical results.

II. POWER CHANGES ACROSS A TEMPORAL BOUNDARY IN REACTIONS

The power of electromagnetic waves in media can often be calculated by permittivity. However, many chemical reactions are non-equilibrium process. During this process, the concentrations of reactants and products are changing with time. Based on the modified Smoluchowski–Debye equation, the polarization expression of polar-molecule reactions is indicated by the response function in the time domain. The expression of the polarization in polar-molecule reactions is given as

$$\mathbf{P}(t) = \sum_i \varphi_{A_i}(t) * [c_{A_i}(t)\mathbf{E}(t)] + \sum_j \varphi_{B_j}(t) * [c_{B_j}(t)\mathbf{E}(t)].$$

Here, * denotes the convolution. $\varphi_{A_i}(t)$ and $\varphi_{B_j}(t)$ represent the rotational diffusion properties of the reactant and product, while $c_{A_i}(t)$ and $c_{B_j}(t)$ denote the concentrations of the reactant and product, respectively [10]. To make the polarization expression easily, the simple polar-molecule reactions are considered, in which only one component (X_i) has the polarization

$$\mathbf{P}_{X_i}(t) = \varphi_{X_i}(t) * [c_{X_i}(t)\mathbf{E}(t)]. \quad (1)$$

$\varphi_{X_i}(t)$ and $c_{X_i}(t)$ are the rotational diffusion function and concentration of X_i . * represents the convolution. $\varphi_{X_i}(t) = \varepsilon_0 \chi_{X_i} \exp(-t/\tau_{X_i})/\tau_{X_i}$, where χ_{X_i} is the electric susceptibility, ε_0 is the vacuum permittivity, and τ_{X_i} is the dielectric relaxation time. X_i denotes the reactants or products [10]. Furthermore, the reactions are considered to be more general media of composite dispersive and time-varying characteristics [11]. To show the effects of time-varying characteristics on the power transfer, we consider an instant t_0 as the temporal boundary in chemical process. Figure 1(a) shows the polarization of reaction changes from $\mathbf{P}_{X_i}(t_0^-)$ to $\mathbf{P}_{X_i}(t_0^+)$ between a temporal boundary t_0 , which lead to the intrinsic impedance of the reactions varied from $\eta(t_0^-)$ to $\eta(t_0^+)$.

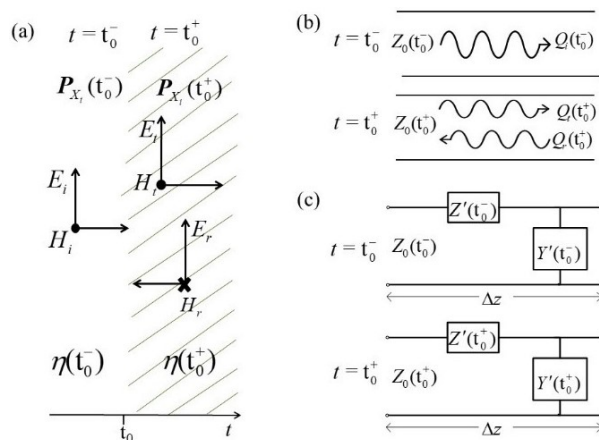


Fig. 1. (a) Propagation processes at the temporal boundary in space-invariant reactions. (b) Schematic of time-varying transmission line. (c) The equivalent circuit unit.

To indicate the features of power changes resulting from the time-varying characteristics of the reactions, the reactions are treated as spatially homogeneous and isotropic nonmagnetic media, being without free charges and currents. The transmission line theory can be employed to explain the electromagnetic propagation behavior in media [21, 22]. The homogenous reactions can be represented by an equivalent transmission line (continuous and invariant along the direction of propagation) to gain an immediate insight into the fundamental properties of reactions. The time-varying transmission line represented in Figure 1(b) corresponds to the model of Figure 1(a). We denote the charge and flux before t_0 with $Q_i(t_0^-)$ and $\phi_i(t_0^-)$. After t_0 , the transmitted and reflected charges are denoted by $Q_t(t_0^+)$ and $Q_r(t_0^+)$, respectively, with a similar notation for the fluxes.

Figure 1(c) shows the unit circuit of the transmission line presenting a per-unit length for media as described by eqn (1). In such a transmission line circuit, the magnetization and polarization are represented by the distributed series impedance (Z') and shunt admittance (Y') per unit length, respectively [16, 17], according to the constitutive relation of the reactions. Since the time-varying characteristics of the reactions, the principle of the time-varying transmission line is to make its characteristic parameters, such as impedance and admittance, being time changing. $Z'(t_0^-)$ and $Z'(t_0^+)$ denote the impedances before and after the temporal boundary located at t_0 , similarly for the admittances $Y'(t_0^-)$ and $Y'(t_0^+)$. The transmission line's characteristic impedance ($Z_0 = \sqrt{Z'/Y'}$) changes from $Z_0(t_0^-)$ to $Z_0(t_0^+)$ at $t = t_0$, which correspond to the reactions' intrinsic impedance. In its unit equivalent circuit, the series

impedance (Z') and shunt admittance (Y') can be represented as the combination of equivalent time-varying resistance ($R(t)$), conductance ($G(t)$), capacitance ($C(t)$), and inductance ($L(t)$) of per-unit length, which can be derived mathematically by Maxwell equations and the constitutive relations of the reactions. The equivalent capacitance changes from $C(t_0^-)$ to $C(t_0^+)$ at $t = t_0$, with a similar notation for the inductance. For a time-varying equivalent circuit, the relationships between charge and voltage is $Q(z, t) = C(t)u(z, t)$ as well as the flux and current is $\phi(z, t) = L(t)i(z, t)$ [23, 24]. Thus, the instantaneous power is given by

$$P(t) = u(t)i(t) = \frac{u^2(t)}{Z_0(t)} = \frac{Q^2(t)}{C^2(t)Z_0(t)}. \quad (2)$$

$\nabla \times \mathbf{E} = -\partial \mathbf{B} / \partial t$ and $\nabla \times \mathbf{H} = \partial \mathbf{D} / \partial t$ indicate that the electric displacement (\mathbf{D}) and magnetic induction (\mathbf{B}) require the continuity at a temporal boundary [25, 26]. As the charge $Q = \int \mathbf{D} \cdot d\mathbf{S}$ and the flux $\phi = \int \mathbf{B} \cdot d\mathbf{S}$, the charge (Q) and flux (ϕ) are conserved at a temporal boundary t_0 [27]. Accordingly, we have

$$Q_i(t_0^-) = Q_r(t_0^+) + Q_t(t_0^+) \quad (3a)$$

and

$$\phi_i(t_0^-) = -\phi_r(t_0^+) + \phi_t(t_0^+). \quad (3b)$$

Thus, the ratio of the reflected power (P_r) and transmitted power (P_t) to the incident power (P_i) at t_0 are derived as

$$\frac{P_r}{P_i} = \frac{C^2(t_0^-)Z_0(t_0^-)}{C^2(t_0^+)Z_0(t_0^+)} \frac{1}{4} \left(1 - \frac{C(t_0^+)Z_0(t_0^+)}{C(t_0^-)Z_0(t_0^-)} \right)^2 \quad (4a)$$

and

$$\frac{P_t}{P_i} = \frac{C^2(t_0^-)Z_0(t_0^-)}{C^2(t_0^+)Z_0(t_0^+)} \frac{1}{4} \left(1 + \frac{C(t_0^+)Z_0(t_0^+)}{C(t_0^-)Z_0(t_0^-)} \right)^2. \quad (4b)$$

To get a deeper insight, we add the eqn (4a) and (4b) and obtain

$$\frac{P_r + P_t}{P_i} = \frac{C(t_0^-)}{C(t_0^+)} \frac{1}{2} \left(\frac{C(t_0^-)Z_0(t_0^-)}{C(t_0^+)Z_0(t_0^+)} + \frac{C(t_0^+)Z_0(t_0^+)}{C(t_0^-)Z_0(t_0^-)} \right). \quad (5)$$

Eqn (4a) and (4b) indicate that the reflected and transmitted powers change due to an abrupt change of impedance. When the time scale of the component concentration variation is greater than the wave period, the time-varying characteristics of the reactions can be neglected and $\mathbf{P}_{X_i}(t_0^-) = \mathbf{P}_{X_i}(t_0^+)$ [11]. The unit parameters of the transmission line circuit do not change at t_0 , that is, $C(t_0^-) = C(t_0^+)$ and $Z_0(t_0^-) = Z_0(t_0^+)$. As shown in eqn (4a) and (4b), $P_r = 0$ and $P_t = P_i$ are obtained subsequently. Thus, $(P_r + P_t)/P_i = 1$ by eqn (5), indicating conservation of energy. It is important to realize that in the absence of the time-varying property of the reactions, $\mathbf{P}_{X_i}(t_0^-) = \mathbf{P}_{X_i}(t_0^+)$ and the temporal boundary is switched off. The reflectivity vanishes and the energy of the waves is conserved.

On the other hand, while the time scale of the component concentration variation is smaller than the

wave period, the time-varying characteristics of the reactions are obvious, and $\mathbf{P}_{X_i}(t_0^-) \neq \mathbf{P}_{X_i}(t_0^+)$ [11]. Thus, $C(t_0^-) \neq C(t_0^+)$ and $Z_0(t_0^-) \neq Z_0(t_0^+)$. The incident power is changed into two parts: the reflected power (P_r) and the transmitted power (P_t). $(P_r + P_t)/P_i \neq 1$ by eqn (5), indicating the non-conservation of energy for the waves. As the energy is conserved for the whole waves and media, eqn (5) can be interpreted as an energy exchange between the waves and the time-varying media [28–30]. Furthermore, an energy exchange occurs between the waves and reactions, which has been demonstrated to lead to either amplification or attenuation of electromagnetic waves depending on whether the dielectric property of the reactions decrease or increases with time [11, 31]. More specially, if the relaxation time of the reactions is much smaller, the characteristic impedance $Z_0(t_0^-)$ and $Z_0(t_0^+)$ are assumed as real numbers approximately. Thus, $\frac{1}{2} \left(\frac{C(t_0^-)Z_0(t_0^-)}{C(t_0^+)Z_0(t_0^+)} + \frac{C(t_0^+)Z_0(t_0^+)}{C(t_0^-)Z_0(t_0^-)} \right) \geq 1$. Particularly, when $C(t_0^-) > C(t_0^+)$, we can get $P_r + P_t > P_i$. Here, it is worth remarking that the sum of the reflected and transmitted power is greater than the incident power. Thus, the reactions bearing the time-varying characteristic act as a source of energy for electromagnetic waves. This fact should be considered in microwave heating to achieve the homogeneous power transfer in the reactions.

To clarify the physical meaning of the derived expression, parametric phenomena of electromagnetic waves in active media can be realized by a time modulation of media parameters [32]. In fact, the number of dipoles would be changed with the proceeding of chemical reactions. It can be inferred that the equivalent time-varying capacitance of the reaction is weakened with the decrease of dipoles' quantity; that is, $C(t_0^-) > C(t_0^+)$. What is more, the electromagnetic waves propagate in the reactions bearing time-varying characteristics, just as if they were in contact with a reservoir (time-dependent background media) [33, 34]. The decrease of the time-varying capacitor leads to reductions of the reservoir energy. This essentially leads to an energy flow from the reservoir to the electromagnetic waves. Therefore, the time-varying capacitors through the bounded discontinuities have an additional contribution as active circuit elements to the electromagnetic power.

III. RESULTS AND DISCUSSIONS

As discussed above, to indicate the unique features of power propagation originating from the time-varying characteristics of the reactions, the effects of component concentration variation on the transmitted power are discussed by the numerical simulations. We consider a monochromatic wave incident into the reactions, so as to understand the influence of the time-varying

characteristics on the transmitted and reflected powers. For the electric field, the single cycle sine wave $E_i(t)$ is employed as

$$E_i(t) = \begin{cases} \sin(2\pi \times 5 \times 10^9 \times t) & t \leq 0.1\text{ns} \\ 0 & t > 0.1\text{ns} \end{cases} \quad (6)$$

In the calculation, the reactions with the electric susceptibility $\chi_{X_i}=10$ and the dielectric relaxation time $\tau_{X_i}=1\text{fs}$ are used. This paper selects an instant t_0 in chemical process and the temporal boundary t_0 is set as 2 ns. To investigate the power changes in the simple polar-molecule reactions, without loss of generality, the reactions are considered as the first-order reaction.

A. Power changes when X_i is the reactant

The normalized concentration $c_{X_i}(t) = \exp(-K_{rate}t)$ can be obtained when X_i is the reactant. K_{rate} is the rate constant of the reactions. The electromagnetic powers in the simple polar-molecule reactions are shown in Figure 2.

When K_{rate} is chosen as 0s^{-1} , $1 \times 10^3\text{s}^{-1}$, and $1 \times 10^8\text{s}^{-1}$, power changes cannot be seen in Figure 2(a)–(c). We find that the reflected power (P_r) is zero and the transmitted power (P_t) is matched with the incident power (P_i). As the time scale of the concentration variation is greater than the wave period, the polarization $P_{X_i}(t)$ is continuous at t_0 . Since the impedance of the reactions does not change at t_0 , no reflection occurs. Moreover, using this condition employed in the unit equivalent circuit of the reactions, $P_r = 0$ and $P_t = P_i$ are obtained by eqn (4a) and (4b), indicating that there are no power changes. When $K_{rate} = 1 \times 10^{11}\text{s}^{-1}$, the reflected power (P_r) is observed clearly, and the transmitted power (P_t) is not equal to the incident power (P_i) in Figure 2(d). As the time scale of the concentration variation is smaller than the wave period, i.e., $c_{X_i}(t)$ changes rapidly with time, the polarization $P_{X_i}(t)$ is not continuous at the temporal boundary, inducing the discontinuous impedance change. For this situation, $P_r \neq 0$ and $P_t \neq P_i$ are obtained by eqn (4a) and (4b), and $(P_r + P_t)/P_i \neq 1$ by eqn (5) indicates power changes. Another phenomenon of interest is that the transmitted power is greater than the incident power.

B. Power changes when X_i is the product

On the other hand, when X_i is the product, the expression of $c_{X_i}(t) = 1 - \exp(-K_{rate}t)$ can be achieved and the electromagnetic powers in the simple polar-molecule reactions are shown in Figure 3. The reflected power is not observed as $K_{rate} = 0\text{s}^{-1}$, $1 \times 10^3\text{s}^{-1}$, and $1 \times 10^8\text{s}^{-1}$ in Figure 3(a)–(c). And we cannot see the power changes. When $K_{rate} = 1 \times 10^{11}\text{s}^{-1}$, the reflected power can be observed, and the transmitted power (P_t) is smaller than the incident power (P_i) in Figure 3(d). We can find the power changes across the temporal boundary in the reactions in Figure 3(d).

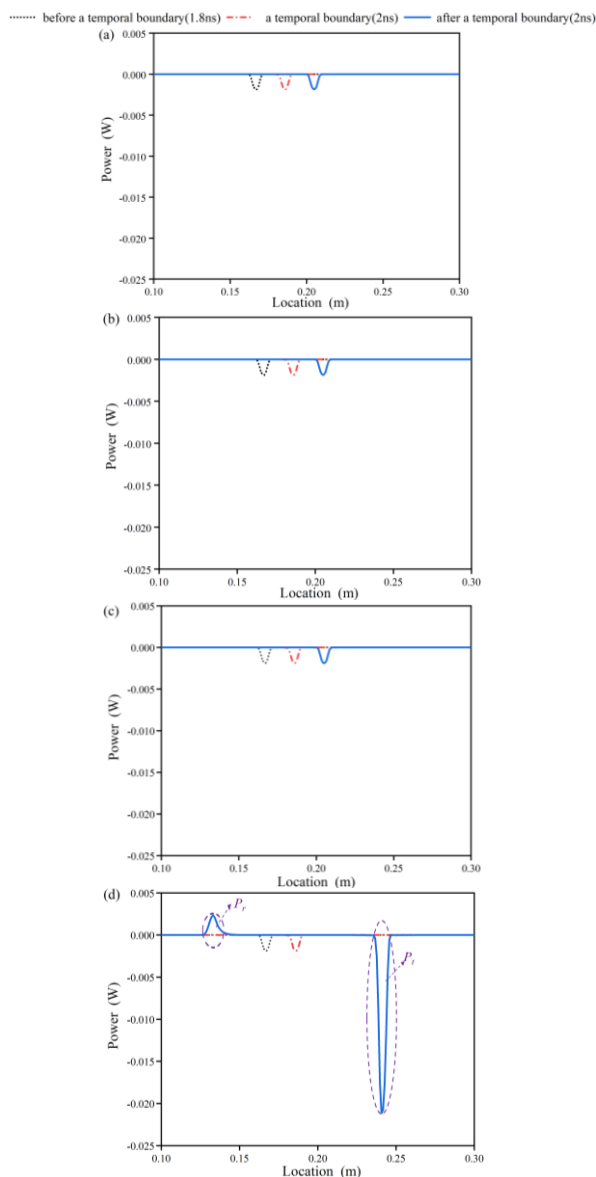


Fig. 2. The electromagnetic powers in the simple polar-molecule reactions when X_i is the reactant. (a) $K_{rate} = 0\text{s}^{-1}$. (b) $K_{rate} = 1 \times 10^3\text{s}^{-1}$. (c) $K_{rate} = 1 \times 10^8\text{s}^{-1}$. (d) $K_{rate} = 1 \times 10^{11}\text{s}^{-1}$.

A temporal variation of the dielectric property is created because the component concentrations change in chemical process. When X_i is the reactant, the component concentration of X_i decreases gradually in the reactions. It can be inferred that the dielectric property is weakened with the decrease of dipoles' quantity when X_i is the reactant. For this situation, the equivalent time-varying capacitance of the reaction decreases as the dielectric property becomes smaller. Based on eqn (5), $P_t + P_r > P_i$ is obtained, indicating the increase of power across the temporal boundary t_0 in the reactions.

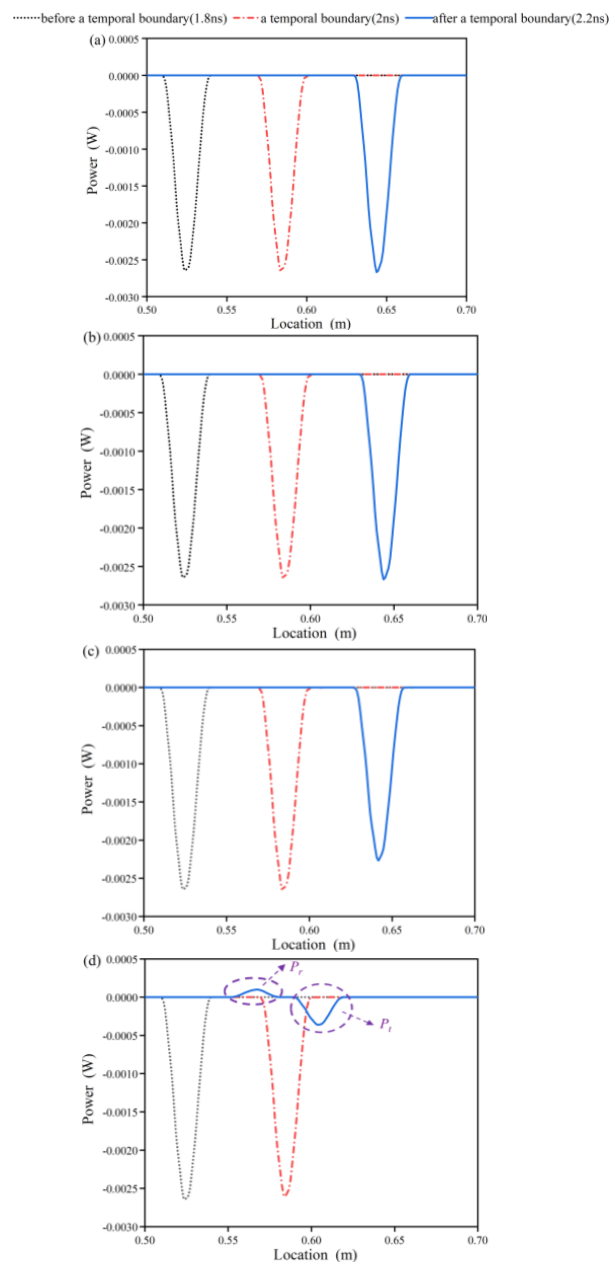


Fig. 3. The electromagnetic powers in the simple polar-molecule reactions when X_i is the product. (a) $K_{rate} = 0\text{s}^{-1}$. (b) $K_{rate} = 1 \times 10^3\text{s}^{-1}$. (c) $K_{rate} = 1 \times 10^8\text{s}^{-1}$. (d) $K_{rate} = 1 \times 10^{11}\text{s}^{-1}$.

When the reactions decrease media's dielectric property, the power of electromagnetic waves increases after the transition, and, thus, the electromagnetic waves experience a net energy gain [35]. This should come as a surprise since decreasing the dielectric property of the reactions is an energy-releasing process. For the reverse case, when X_i is the product, the opposite occurs and the wave experiences a net energy loss because increas-

ing the dielectric property of the reactions consumes energy.

IV. CONCLUSION

Based on the continuity of charge and flux at a temporal boundary and the equivalent transmission line approach of the simple polar-molecule reactions, this paper focuses on the power changes across the temporal boundary. According to the time-varying characteristics of the reactions, the effects of component concentration variation on the power changes are discussed. When the time scale of the concentration variation is smaller than the wave period, the polarization of the reactions is not continuous at the temporal boundary, inducing the discontinuous impedance change. Importantly, when the reactions decrease media's dielectric property, the transmitted power is greater than the incident power; thus, the wave experiences a net energy gain. These results may be helpful in disclosing the non-uniform distribution of electromagnetic energy in chemical reactions.

ACKNOWLEDGMENT

This work was supported by the National Natural Science Foundation of China under Grant 61731013 and the Foundation of Chengdu Technological University under Grant 2020DZ003.

REFERENCES

- [1] X. Zhang, D. O. Hayward, and D. M. P. Mingos, "Effects of microwave dielectric heating on heterogeneous catalysis," *Catalysis Letters*, vol. 88, no. 1, pp. 33-38, 2003.
- [2] M. Bhattacharya, S. K. R. Venkata, and T. Basak, "Role of microwave heating strategies in enhancing the progress of a first-order endothermic reaction," *AIChE Journal*, vol. 59, no. 2, pp. 656-670, 2013.
- [3] M. Irfan, M. Fuchs, T. N. Glasnov, and C. O. Kappe, "Microwave-assisted cross-coupling and hydrogenation chemistry by using heterogeneous transition-metal catalysts: an evaluation of the role of selective catalyst heating," *Chemistry—A European Journal*, vol. 15, no. 43, pp. 11608-11618, 2009.
- [4] M. A. Herrero, J. M. Kremsner, and C. O. Kappe, "Nonthermal microwave effects revisited: on the importance of internal temperature monitoring and agitation in microwave chemistry," *The Journal of Organic Chemistry*, vol. 73, no. 1, pp. 36-47, 2008.
- [5] D. Dallinger, H. Lehmann, J. D. Moseley, A. Stadler, and C. O. Kappe, "Scale-up of microwave-assisted reactions in a multimode bench-top reactor," *Organic Process Research & Development*, vol. 15, no. 4, pp. 841-854, 2011.
- [6] R. Loudon, "The propagation of electromagnetic energy through an absorbing dielectric," *Journal of*

- Physics A: General Physics*, vol. 3, no. 3, pp. 233-245, 1970.
- [7] J. A. Ferreira and J. D. Van Wyk, "Electromagnetic energy propagation in power electronic converters: Toward future electromagnetic integration," *Proceedings of the IEEE*, vol. 89, no. 6, pp. 876-889, 2001.
- [8] H. C. Zhu, X. Q. Yang, and K. M. Huang, "The effective permittivity of reacting mixture solutions for multiphysics calculations," *Journal of Solution Chemistry*, vol. 41, no. 10, pp. 1729-1737, 2012.
- [9] K. Huang, H. Zhu, and L. Wu, "Temperature cycle measurement for effective permittivity of biodiesel reaction," *Bioresource Technology*, vol. 31, pp. 541-544, 2013.
- [10] K. Huang and T. Hong, "Dielectric polarization and electric displacement in polar-molecule reactions," *The Journal of Physical Chemistry A*, vol. 119, no. 33, pp. 8898-8902, 2015.
- [11] X. Liu and K. Huang, "Frequency changes of electromagnetic waves in simple polar-molecule reactions," *The European Physical Journal Applied Physics*, vol. 77, no. 2, pp. 20901, 2017.
- [12] X. Liu, D. Yan, and K. Huang, "Temporal reflection of electromagnetic waves in simple polar-molecule reactions," *COMPEL-The International Journal for Computation and Mathematics in Electrical and Electronic Engineering*, vol. 38, no. 6, pp. 1964-1971, 2019.
- [13] C. Caloz and T. Itoh, *Electromagnetic metamaterials: transmission line theory and microwave applications*, John Wiley & Sons, New Jersey, 2005.
- [14] J. Ma[†] kinen, R. Piche, and A. Ellman, "Fluid transmission line modeling using a variational method," *J. Dyn. Sys., Meas., Control*, vol. 122, no. 1, pp. 153-162, 2000.
- [15] F. Bongard, H. Lissek, and J. R. Mosig, "Acoustic transmission line metamaterial with negative/zero/positive refractive index," *Physical Review B*, vol. 82, no. 9, pp. 094306, 2010.
- [16] A. Sanada, C. Caloz, and T. Itoh, "Characteristics of the composite right/left-handed transmission lines," *IEEE Microwave and Wireless Components Letters*, vol. 14, no. 2, pp. 68-70, 2004.
- [17] G. V. Eleftheriades, O. Siddiqui, and A. K. Iyer, "Transmission line models for negative refractive index media and associated implementations without excess resonators," *IEEE Microwave and Wireless Components Letters*, vol. 13, no. 2, pp. 51-53, 2003.
- [18] J. A. Portí, J. A. Morente, A. Salinas, E. A. Navarro, and M. Rodríguez-Sola, "A generalized dynamic symmetrical condensed TLM node for the modeling of time-varying electromagnetic media," *IEEE Transactions on Antennas and Propagation*, vol. 54, no. 1, pp. 2-11, 2006.
- [19] A. Lai, T. Itoh, and C. Caloz, "Composite right/left-handed transmission line metamaterials," *IEEE Microwave Magazine*, vol. 5, no. 3, pp. 34-50, 2004.
- [20] Y. Liao, S. Zhang, Z. Tang, and X. Liu, "Power loss density of electromagnetic waves in unimolecular reactions," *RSC Advances*, vol. 7, no. 43, pp. 26546-26550, 2017.
- [21] Y. Hadad and A. Shlivinski, "Soft Temporal Switching of Transmission Line Parameters: Wave-Field, Energy Balance, and Applications," *IEEE Transactions on Antennas and Propagation*, vol. 68, no. 3, pp. 1643-1654, 2020.
- [22] A. Scarlatti and C. L. Holloway, "An equivalent transmission-line model containing dispersion for high-speed digital lines-with an FDTD implementation," *IEEE Transactions on Electromagnetic Compatibility*, vol. 43, no. 4, pp. 504-514, 2001.
- [23] J. B. Gunn, "Transformation and reversal of time scale by a time-varying transmission line," *Electronics Letters*, vol. 2, no. 7, pp. 247-248, 1966.
- [24] Z. Li and Z. Yin, "A method for controlling parallel and series RLC circuits with time-varying resistance, inductance and capacitance," *Circuits, Systems, and Signal Processing*, vol. 37, no. 6, pp. 2629-2638, 2018.
- [25] Y. Xiao, D. N. Maywar, and G. P. Agrawal, "Reflection and transmission of electromagnetic waves at a temporal boundary," *Optics Letters*, vol. 39, no. 3, pp. 574-577, 2014.
- [26] M. I. Bakunov and A. V. Maslov, "Reflection and transmission of electromagnetic waves at a temporal boundary: comment," *Optics Letters*, vol. 39, no. 20, pp. 6029-6029, 2014.
- [27] B. A. Auld, J. H. Collins, and H. R. Zapp, "Signal processing in a nonperiodically time-varying magnetoelastic medium," *Proceedings of the IEEE*, vol. 56, no. 3, pp. 258-272, 1968.
- [28] A. G. Hayrapetyan, K. K. Grigoryan, R. G. Petrosyan, and S. Fritzsche, "Propagation of sound waves through a spatially homogeneous but smoothly time-dependent medium," *Annals of Physics*, vol. 333, pp. 47-65, 2013.
- [29] K. B. Tan, H. M. Lu, and W. C. Zuo, "Energy conservation at an optical temporal boundary," *Optics Letters*, vol. 45, no. 23, pp. 6366-6369, 2020.
- [30] T. T. Koutserimpas and R. Fleury, "Electromagnetic fields in a time-varying medium: exceptional points and operator symmetries," *IEEE Transactions on Antennas and Propagation*, vol. 68, no. 9, pp. 6717-6724, 2020.
- [31] A. G. Hayrapetyan, J. B. Götte, K. K. Grigoryan, S. Fritzsche, and R. G. Petrosyan, "Electromagnetic wave propagation in spatially homogeneous yet smoothly time-varying dielectric media," *Journal of Quantitative Spectroscopy and Radiative Transfer*, vol. 178, pp. 158-166, 2016.

- [32] A. Nerukh, N. Sakhnenko, and T. Benson, P. Sewell, *Non-stationary Electromagnetics*, CRC Press, New York, 2012.
- [33] I. A. Pedrosa, "Quantum electromagnetic waves in nonstationary linear media," *Physical Review A*, vol. 83, no. 3, pp. 032108, 2011.
- [34] R. Matloob, "Electromagnetic field quantization in a linear isotropic dielectric," *Physical Review A*, vol. 69, no. 5, pp. 052110, 2004.
- [35] M. Chegnizadeh, K. Mehrany, and M. Memarian, "General solution to wave propagation in media undergoing arbitrary transient or periodic temporal variations of permittivity," *JOSA B*, vol. 35, pp. 2923-2932, 2018.



Xingpeng Liu was born in Hegang, China, in 1985. She received the Ph.D. degree in communication and information system from Sichuan University, Chengdu, China, in 2016.

She is currently an Associate Professor with the School of Network and Communication Engineering, Chengdu Technological University, Chengdu, China. Her research interests are in the areas of electromagnetic theory, microwave heating, and microwave chemistry.



Song Zhang was born in Hefei, China, in 1972. He received the master's degree in communication and information system from Sichuan University, Chengdu, China, in 2004.

He is currently an Associate Professor with the School of Network

and Communication Engineering, Chengdu Technological University, Chengdu, China. His research interests are in the areas of circuit design and signal processing.



Kama Huang (Senior Member, IEEE) was born in Chongqing, China, in 1964. He received the M.S. and Ph.D. degrees in microwave theory and technology from the University of Electronic Science and Technology, Chengdu, China, in 1988 and 1991, respectively.

He has been a Professor with the Department of Radio and Electronics, Sichuan University, Sichuan, China, since 1994 and has been the Director of the department since 1997. In 1996, 1997, 1999, and 2001, he was a Visiting Scientist with the Scientific Research Center "Vidhuk" in Ukraine, Institute of Biophysics CNR in Italy, Technical University Vienna in Austria, and Clemson University in the USA, respectively. At these institutions, he cooperated with the scientists to study the interaction between electromagnetic fields and complex media in biological structure and reaction systems. He has published over 100 papers. His research interests are in the areas of microwave chemistry and electromagnetic theory.

Dr. Huang is the Chief Scientist of the National Basic Research Program of China (973 Program), and he has received several research awards from the Chinese government.